

A STUDY OF THE MOVING FLAME EFFECT IN THREE DIMENSIONS  
AND ITS IMPLICATIONS FOR THE GENERAL CIRCULATION OF THE  
UPPER ATMOSPHERE OF VENUS

by

STEPHEN BRENNER  
B.S., City College of New York  
(1975)

SUBMITTED IN PARTIAL FULFILLMENT  
OF THE REQUIREMENTS FOR THE  
DEGREE OF

DOCTOR OF PHILOSOPHY

at the

MASSACHUSETTS INSTITUTE OF TECHNOLOGY

February 1982

© Massachusetts Institute of Technology 1980

Signature of Author \_\_\_\_\_

Department of Meteorology and Physical  
Oceanography, 28 October 1981

Certified by \_\_\_\_\_

Peter H. Stone  
Thesis Supervisor

Accepted by \_\_\_\_\_

Raymond Pierrehumbert  
Chairman, Departmental Graduate Committee

WITHDRAWN

MAR 6 1982

MIT LIBRARIES

To my dear wife, Nadine

## TABLE OF CONTENTS

	Page
ACKNOWLEDGMENTS	5
VITA	7
LIST OF SYMBOLS	8
ABSTRACT	12
CHAPTER 1: INTRODUCTION	13
1.1 The Moving Flame Effect	13
1.2 Laboratory Experiments	17
1.3 Theoretical Studies	21
1.4 Venus	39
1.5 Objectives and Organization	56
CHAPTER 2: THREE DIMENSIONAL LINEARIZED MODEL	59
2.1 Introduction	59
2.2 Details of the Model	60
2.3 Boundary Conditions	75
2.4 Steady State Mean Meridional Circulation	83
2.5 Large Scale Eddies and the Mean Zonal Wind	111
2.6 Discussion	138
CHAPTER 3: NONLINEAR SPECTRAL MODEL	141
3.1 Introduction	141
3.2 Details of the Model	142
3.3 Numerical Methods	153
3.4 Results	170
3.5 Discussion	210
CHAPTER 4: SUMMARY AND CONCLUSIONS	225
REFERENCES	234

APPENDIX A:	FOURIER ANALYSIS OF THE DIURNAL HEATING FUNCTION	231
APPENDIX B:	PHYSICAL CONSTANTS AND DIMENSIONLESS PARAMETERS FOR VENUS	243
APPENDIX C:	SURFACE SPHERICAL HARMONICS	245
APPENDIX D:	TRANSFORM METHOD FOR COMPUTING NONLINEAR TERMS	252



## ACKNOWLEDGMENTS

I would like to thank my thesis advisor, Professor Peter H. Stone, for his help and guidance during the course of this research. My gratitude is also extended to the other members of my doctoral committee, Professors Reginald E. Newell and Ronald G. Prinn, for reviewing this thesis. I would also like to thank Dr. Eugenia Kálnay de Rivas for serving as my advisor during my earlier years at MIT. Her encouragement and enthusiasm sparked my interest in planetary atmospheres and numerical modelling and provided for the initial development of this thesis topic. Dr. F. Alyea gave me many helpful suggestions concerning the spectral method. I would also like to thank Diana Spiegel for her assistance in solving many of the computer programming problems that arose.

I am grateful to the National Aeronautics and Space Administration for providing financial support during my graduate studies under NASA grant NSG-5113. All of the computations were done on the Amdahl 470 at the Goddard Laboratory for Atmospheric Sciences, Greenbelt, MD.

My appreciation also goes to Liz Manzi for typing the thesis and to Isabelle Kole for drafting the figures.

I am also grateful to many of my fellow students and members of the staff of the department for helpful discussions and for providing the much needed moral support during

some of the more difficult stages of my graduate career.

Finally, I owe the greatest debt of appreciation to my dear wife, Nadine, who was always there when I needed her. Without her love, patience, understanding, encouragement, and financial support this work would never have been completed.

VITA

Born Brooklyn, NY, December 18, 1953

1971-1975 Attended the City College of New York.  
Bachelor of Science degree in Physical  
Oceanography, June 1975.

1975-1981 Research assistant and graduate student  
at the Massachusetts Institute of  
Technology.

## LIST OF SYMBOLS

a	planetary
$c_p$	specific heat at constant pressure
g	gravity
h	vertical length scale
i	$\sqrt{-1}$
j	index for vertical grid
k	horizontal length scale
m	order of spherical harmonic (zonal wavenumber)
n	degree of spherical harmonic
$p$	hydrodynamic pressure
t	time
u	zonal (eastward) velocity
$u_0$	speed of the heat source
v	meridional (northward) velocity
w	vertical (upward) velocity
x	eastward Cartesian coordinate
y	northward Cartesian coordinate
z	vertical (upward) coordinate
$D_n^m$	$\left[ \frac{h^2 - m^2}{4n^2 - 1} \right]^{\frac{1}{2}}$
G	thermal forcing parameter = $\frac{gh}{u_0^2} \frac{\Delta T}{T_0}$
$H_n^m$	$\cos \frac{dP_n^m}{d\phi}$
$L( )$	meridional derivative operator = $\cos \phi \frac{\partial}{\partial \phi}$
$L_m( )$	mth Fourier component of L

M	truncation wavenumber
P	complex amplitude of eddy pressure
$P_n^m$	normalized associated Legendre polynomial
Pr	Prandtl number
Q	dimensionless magnitude of the heat flux boundary condition
R	gas constant
S	weighting function for stretched vertical coordinate
T	complex amplitude of eddy potential temperature
$T_0$	reference value of (potential) temperature
U	$u \cos \phi$ , relative angular momentum
V	$v \cos \phi$
$\underline{v}$	horizontal velocity vector = (u, v)
$Y_n^m$	surface spherical harmonic
$2\gamma^2$	momentum frequency parameter = $\frac{\Omega h^2}{\nu_v}$
$\delta$	$\nabla \cdot \underline{v}$
$\epsilon_v$	$\left(\frac{h}{a}\right)^2 \frac{\nu_H}{\nu_v}$
$\epsilon_k$	$\left(\frac{h}{a}\right)^2 \frac{\kappa_H}{\kappa_v}$
$\zeta$	vertical component of relative vorticity
$2\eta^2$	thermal frequency parameter = $\frac{\Omega h^2}{\kappa_v}$
$\theta$	deviation of potential temperature from reference value
$\kappa_v$	vertical thermal diffusivity
$\kappa_H$	horizontal thermal diffusivity

$\lambda$	longitude
$\mu$	$\sin \phi$
$\nu_v$	vertical kinematic viscosity
$\nu_H$	horizontal kinematic viscosity
$\xi$	stretched vertical coordinate
$\pi$	Pi
$\rho_0$	reference density
$\tau$	iteration variable
$\tau_{\text{DIFF}}$	diffusion time constant
$\phi$	latitude
$\chi$	velocity potential
$\psi$	streamfunction
$\Gamma$	dry adiabatic lapse rate = $\frac{g}{c_p}$
$\Delta_z$ ( )	top to bottom contrast of ( )
$\Delta_\phi$ ( )	equator to pole contrast of ( )
$\Delta p$	pressure scale
$\Delta z$	vertical grid length
$\Delta T$	temperature scale
$\Delta \xi$	stretched vertical grid length
$\Lambda$	Froude number = $gh/u_0^2$
$\Omega$	frequency of the heat source = $ku_0$
$\nabla$	two-dimensional del operator
$(\bar{\quad})$	zonal mean of ( ), = $\frac{1}{2\pi} \int_0^{2\pi} ( ) d\lambda$
$(\quad)'$	deviation from zonal mean

$$\{(\cdot)\}_n^m \text{ transform operator} = \frac{1}{2\pi} \int_0^{2\pi} \int_{-\frac{\pi}{2}}^{\frac{\pi}{2}} (\cdot) P_n^m(\sin\phi) \cos\phi \, d\phi e^{-im\lambda} \, d\lambda$$

$$[(\cdot)] \text{ horizontal mean of } (\cdot), = \frac{1}{P_0} \{(\cdot)\}_0^0$$

$$\langle(\cdot)\rangle \text{ global mean of } (\cdot), = \int_0^1 [(\cdot)] \, dz$$

$\tilde{(\cdot)}$  complex conjugate of  $(\cdot)$

$(\cdot)^*$  dimensional quantity

A STUDY OF THE MOVING FLAME EFFECT IN THREE DIMENSIONS  
AND ITS IMPLICATIONS FOR THE GENERAL CIRCULATION OF THE  
UPPER ATMOSPHERE OF VENUS

by

STEPHEN BRENNER

Submitted to the Department of Meteorology and Physical  
Oceanography on October 28, 1981 in partial fulfillment  
of the requirements for the Degree of Doctor of Philosophy

ABSTRACT

Schubert and Whitehead (1969) suggested that the moving flame effect could possibly explain the rapid retrograde mean zonal flow in the Venus stratosphere because of the relatively slow overhead diurnal motion of the sun. This mechanism is investigated by developing two Boussinesq models with heating supplied as a longitudinally moving periodic heat flux boundary condition at the bottom. Both models are three dimensional so as to allow comparable diurnal and meridional heating contrasts.

The first model is a linearized model derived in Cartesian coordinates. The mean meridional circulation (MMC) driven by the mean meridional heating contrast consists of a Hadley cell. The diurnal motion of the heat source produces tilted eddy convection cells which transport retrograde momentum upward and therefore provide a retrograde mean acceleration of the upper layers of the model. The maximum retrograde mean zonal flow occurs at the latitude of maximum cooling. All of the horizontal velocity components are at most of the same order of magnitude as the phase speed of the heat source.

The second model is nonlinear and derived in spherical coordinates. This model also produces a retrograde mean zonal flow with maximum velocities occurring at the top near the equator. Once again all horizontal velocity components are at most the same order of magnitude as the phase speed of the heat source. It is shown that to obtain meaningful results, a minimum spectral truncation of  $M=6$  is required. From these results it appears unlikely that the moving flame mechanism alone can consistently explain all of the observed features of the circulation of the Venus stratosphere.

Thesis Supervisor: Peter H. Stone

Title: Professor of Meteorology



## CHAPTER 1

INTRODUCTION1.1 The Moving Flame Effect

The concept of fluid motion induced by a moving, periodic heat source is not new to the science of meteorology. Halley (1686) proposed this mechanism in an attempt to explain the existence of the very steady easterly trade winds. According to his theory, the zonal wind would follow the diurnal motion of the sun. Thompson (1892) agreed that a zonal velocity could develop as a result of thermal forcing due to the relative solar motion, but he was not convinced as to the direction of such a flow. To check the validity of Halley's theory, Thompson suggested a simple experiment in which a heat source would be rotated beneath a pan of water and the resulting motions studied. It was not until some 67 years later than Fultz et al. (1959) carried out such a study. They conducted a series of laboratory experiments, using a cylindrical container of water with various heat source arrangements, aimed at simulating various features of the general circulation of the earth's atmosphere. The so-called "moving flame" experiments were actually conducted as will experiments merely to determine what effects, if any, the motion of the heat source might have on their other results. In the course of this investigation, they found a general tendency to develop a weak retrograde mean zonal

flow at the top surface of the water. By retrograde we mean that the fluid flow is in a direction opposite to that of the heat source motion. Fluid flow in the same direction as the heat source motion will be referred to as prograde. The results of Fultz, et al. will be discussed in more detail in section 1.2.

To understand the underlying physics of this process, we begin by considering the simple descriptive model illustrated in Figure 1.1. We assume a channel of infinite horizontal extent bounded above and below by rigid plates with heating applied at the boundaries (as indicated in the diagram) in the form of a periodic source moving to the right. The motion of the heat source will induce a thermal wave in the fluid and this in turn will drive convection cells. Figure 1.1a shows the case of heating from below. The induced thermal wave and resulting convection cells will tilt upward to the left due to the finite thermal diffusion. Reynolds stresses (velocity component correlations) arising from such a pattern will act to transport leftward or retrograde momentum upward thereby driving a retrograde mean zonal flow. For heating from above (Figure 1.1b) the isotherms and convection cells tilt upward to the right resulting in a prograde mean zonal velocity. In addition, there will be phase shifts among the source, the thermal wave, and the velocity wave components which will also contribute to the Reynolds stresses.

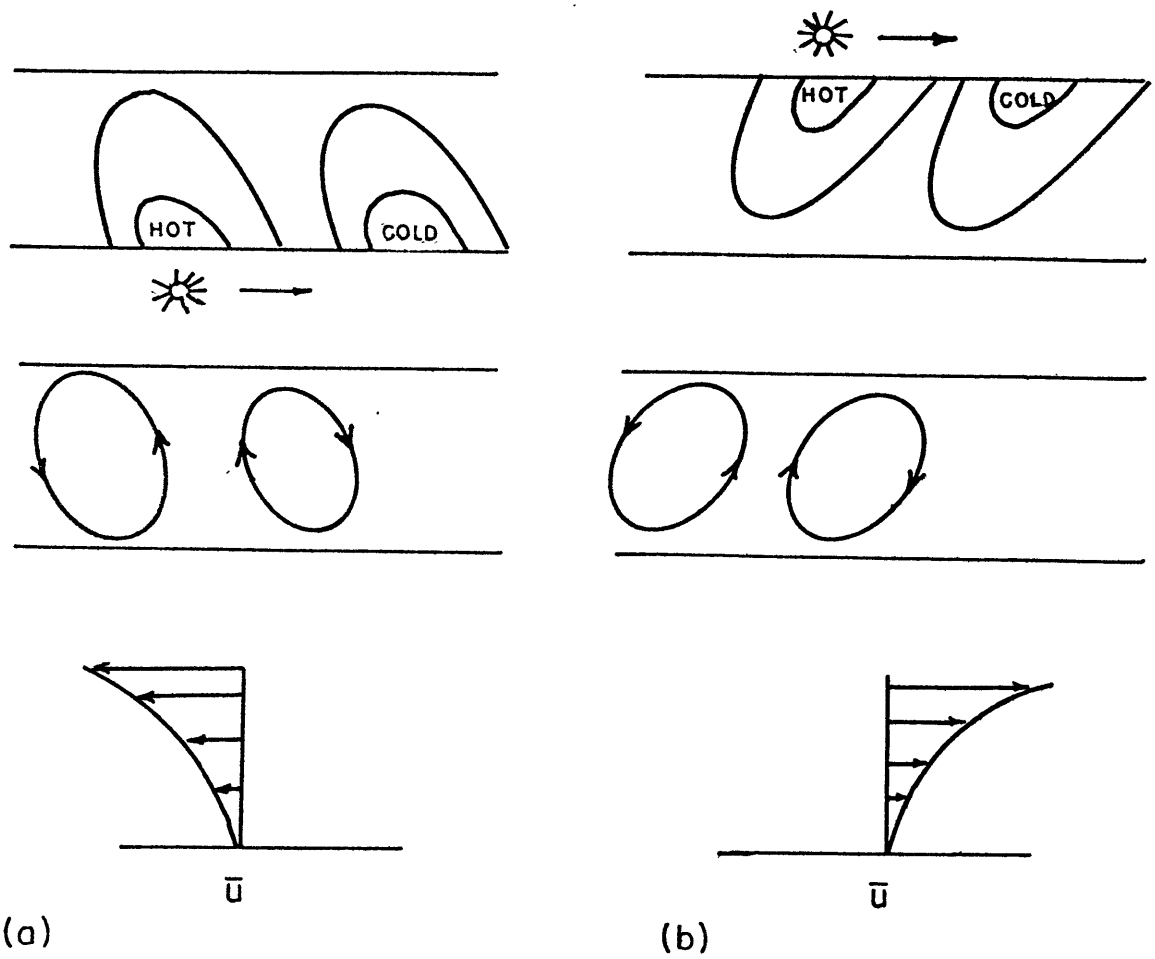


FIGURE 1.1 Moving flame mechanism

(a) heating from below,

(b) heating from above.

In all previously published studies of the moving flame effect, the behavior of the flow has been discussed in terms of certain dimensionless parameters. To facilitate a comparison between our results and the results of others, we will use the following three dimensionless numbers: a thermal forcing parameter,  $G = \frac{gh}{u_0^2} \frac{\Delta T}{T_0}$ , a thermal frequency parameter,  $2\eta^2 = \frac{\Omega h^2}{K}$ , which is the ratio of the vertical heat diffusion time scale to the heat source time scale (i.e. a solar day), and the Prandtl number,  $Pr = \frac{\nu}{K}$  (this introduces the alternative momentum frequency parameter  $2\eta^2 = \frac{\Omega h^2}{\nu} = \frac{2\eta^2}{Pr}$ ). A detailed derivation of the appropriate equations and the parameters mentioned above will be presented in Chapter 2 (also see list of symbols). Qualitatively we should expect the strength of the mean flow to: (a) increase with thermal forcing, (b) increase as the Prandtl number decreases, since large  $Pr$  implies strong momentum diffusion which will tend to eliminate any velocity shears, and (c) reach a maximum for some intermediate value of the frequency parameter, since a very large value (high speed source) allows insufficient time for the fluid to react to the heating contrasts while a small value implies strong diffusion which will reduce temperature and velocity contrasts. Before any further consideration of theoretical aspects of the problem, we will briefly review the experimental results.

## 1.2 Laboratory Experiments

As was mentioned in the previous section, the first moving flame experiments were carried out by Fultz, et al. (1959) as part of their study of the general circulation of the earth's atmosphere. Their apparatus consisted of a cylindrical pan of water heated from below at the outer rim by a rotating Bunsen burner. For varying values of the dimension parameters (see Table 1.1) and for differing initial conditions, their results were always the developments of a mean zonal flow in a direction opposed to the heat source motion. The maximum observed velocities were at most only a few percent of flame speed. The radial profile of the zonal flow indicated a state of roughly constant absolute angular momentum. Finally, the meridional circulation consisted of a Hadley cell, but unfortunately, they neglected to give any numerical values or any comparisons of the relative intensities of the zonal and meridional flows. As a point of interest, we mention that the Hadley cell appeared very quickly, but the mean zonal flow required several flame rotations (i.e. "solar days") to reach a steady state. The fairly small observed magnitude of  $\bar{u}/u_0$  is due to their selection of values of the dimensionless parameters, as discussed in the previous section. Clearly their choices of weak thermal forcing,  $G \sim 0(1)$ , high frequency,  $2\eta^2 \sim 0(10^3)$ , and  $Pr \sim 5$  would all contribute to limiting the strength of the mean zonal velocity.

INVESTIGATOR	$\Lambda$	G	$2\eta^2$	Pr	$2\gamma^2$	$\frac{h}{2\pi a}$	$\frac{\bar{u}}{u_0} \Big _{\max}$
Fultz et al. (1959)	135	2.1	9900	6	1650	0.06	-0.05
Stern (1959)	49	0.5	1100	4.1	270	0.02	-0.01
Schubert and Whitehead (1969)	$1.47 \times 10^5$	7400	0.35	0.027	13	0.02	-4.0
Whitehead (1972)	$6.5 \times 10^4$	9100	0.52	0.027	19	0.02	-4.5
Douglas et al. (1972)	$6.4 \times 10^4$	1400	5500	14	460	0.27	-0.5
Venus	2750	$0(10^3)$	$0(1)^* -$ $0(10)$	$0(.1)^* -$ $0(1)$	$0(1)^* -$ $0(100)$	0.01	-25

TABLE 1.1: Values of the dimensionless parameters for various laboratory experiments and for Venus. All values of  $\frac{\bar{u}}{u_0}$  are retrograde.

\*These values are uncertain; see discussion in Appendix B.

Stern (1959) also conducted some moving flame experiments using a circular annulus filled with water and heated from below. The goal was to eliminate radial (i.e. meridional) convection and to see if a retrograde mean zonal flow would develop in the case of two-dimensional channel flow forced by the motion of the heat source. He observed a retrograde rotation of the water but with maximum speeds of only 0.1 to 1.0 percent of the flame speed. Unfortunately he did not give any details as to the parameter range of his experiments.

Schubert and Whitehead (1969) carried out a series of moving flame experiments using a circular annulus filled with liquid mercury instead of water. The main purpose of their study was to examine the moving flame response of a fluid with a small Prandtl number. In the course of their investigation, they observed retrograde mean zonal velocities that were up to four times as large as the heat source speed. The development of a mean flow that was two to three orders of magnitude larger than previously observed in the water experiments is consistent with their choice of extremely strong thermal forcing, very small Prandtl number, and a thermal frequency of order one. A comparison of the parameter values and the resulting  $\bar{u}$  for the various water and mercury experiments is given in Table 1.1. Based on these results, it was then suggested that the moving flame mechanism might explain the existence of the relatively

rapid retrograde zonal winds in the upper atmosphere of Venus. This would be especially true if radiative transfer is the dominant method of heat transport since in that case, one would expect the effective Prandtl number to be smaller than unity.

Whitehead (1972) repeated and refined the mercury experiments for a wide range of values of the thermal forcing parameter,  $G$ . However, he was still limited to thermal frequencies less than one. Once again, he observed retrograde zonal velocities that increased in magnitude with the thermal forcing. The maximum speed attained by the fluid was more than four times the speed of the heat source. Based on a linearized analysis of the problem, he concluded that surface tension effects, rather than buoyancy induced Reynold's stresses, were responsible for the retrograde flow. He also pointed out that the phase lag of the velocity field (i.e., tilted convection) resulting from either surface tension or buoyancy is qualitatively the same. In his particular apparatus, the surface tension appeared to be the dominant tilting mechanism.

Douglas, et al. (1972) conducted a series of experiments using a relatively deep annulus filled with water and driven by internal (electrical) heating. By deep we mean that the aspect ratio of their apparatus was much larger than any of the others (see Table 1.1). The heating was supplied by passing an electrical current through the fluid. The inner



electrode consisted of the copper wall of the inner cylinder while the outer electrode consisted of several equally spaced vertical tapes connected to a switching network. Each tape was periodically activated by a rotating cam in the switching system. The low resistance of the tapes allowed for a potential difference (heating) that was uniform with height. This arrangement was chosen in an attempt to imitate the strong thermal diffusive properties of a low Prandtl number fluid such as mercury. As expected, they observed a retrograde mean zonal flow with velocities that increased with thermal forcing. In addition, they noted that the maximum mean zonal velocity occurred when the eddy velocities were approximately equal to the speed of the heat source. In this case, the maximum retrograde  $\bar{u}$  was typically one-third to one-half the speed of the heat source.

### 1.3 Theoretical Studies

Over the past two decades, quite a few theoretical studies of the moving flame effect have appeared in the literature. All but two of these followed the experiments of Schubert and Whitehead (1969) and consequently, most of them considered the possible role of the moving flame in driving the four day circulation on Venus. Both linear and nonlinear models have been presented and all have been two-dimensional. As will be indicated in Chapter 2, it becomes convenient to consider the various quantities (temperature,

velocity, etc.) as the sum of a zonal mean part, indicated by an overbar ( $\bar{\phantom{u}}$ ), plus a eddy or perturbation part, indicated by a prime ( $\prime$ ).

### 1.3.1 Linear Models

In a linear model, it is assumed that the dimensionless variables are of at most order one. It is further assumed that mean quantities are smaller than wave quantities and therefore all mean flow self interactions and wave-mean flow interaction can be neglected. Also, in the wave equations, all wave self interactions are neglected.

The first theoretical analysis of the moving flame effect was the linear model presented by Stern (1959), used to explain his experimental results. He considered a two-dimensional, Boussinesq fluid, with small aspect ratio bounded above and below by rigid, no slip surfaces. Heating was supplied as a sinusoidal temperature wave moving with uniform speed at both boundaries. The fluid was also assumed to have infinite thermal conductivity in the vertical ( $Pr \rightarrow 0$ ) so that the induced thermal wave is independent of height. In the limit of very large values of the frequency parameter,  $2\gamma^2 \gg 1$ , he found that the vertically averaged mean zonal velocity was retrograde and given by

$$\frac{\bar{u}}{u_0} = \frac{1}{48} (2\gamma^2)^{1/2} G^2 \quad , \quad 2\gamma^2 \gg 1 \quad (2\eta^2 \rightarrow 0)$$

where the second overbar indicates a vertical average. When applied to his own experiments, this expression yielded a value of  $\frac{\bar{u}}{u_0} \approx 0.1$  which is one to two orders of magnitude larger than actually observed. The main reason for this discrepancy was the unrealistic assumption of  $Pr = 0$  (see Table 1.1).

Davey (1967) reconsidered Stern's problem, but relaxed the assumption of zero Prandtl number. The thermal forcing was applied as a sinusoidal temperature wave at both horizontal, rigid boundaries. For very large values of both frequency parameters,  $2\eta^2, 2\gamma^2 \gg 1$ , the vertically averaged mean zonal velocity was retrograde and given by

$$\frac{\bar{u}}{u_0} = \frac{G^2}{4Pr(1+Pr)} \frac{1}{2\eta^2} \left[ 1 - \frac{3Pr^2 + Pr^{3/2} + 10Pr + Pr^{1/2} + 3}{\sqrt{2}(1+Pr)^{1/2}(1+Pr)} \frac{1}{(2\eta^2)^{1/2}} + O\left(\frac{1}{2\eta^2}\right) \right]$$

$$2\eta^2, 2\gamma^2 \gg 1$$

He also solved the linear problem with heating applied as a temperature wave at the lower rigid, no slip boundary and with a free insulating upper boundary. In this case, the high frequency solution was the same as the rigid-rigid solution but with an extra term in the square brackets

$$- \frac{\text{Pr}}{2(1+\text{Pr})^{1/2}} \frac{1}{(2\eta^2)^{1/2}} \frac{\Lambda}{\Lambda - 1}$$

This corresponds to retrograde flow as long as the Froude number,  $\Lambda$ , is not too close to one. When  $\Lambda = 1$ , resonance occurs at the free boundary in which case surface gravity wave that move at the heat source speed will be generated. The forcing of the mean flow will then be dominated by the gravity waves and not the Reynolds stresses.

Schubert and Young (1970) also approached the problem with a two-dimensional, Boussinesq model with infinite thermal conductivity ( $\text{Pr} \rightarrow 0$ ). To solve the equations, they also considered the limiting cases of very large and very small values of the frequency parameter,  $2\gamma^2$ , and then determined the first and second order terms in an asymptotic series expansion of the eddy velocity components. Their discussion then focused upon the Reynolds stresses that arise from interactions between the first order and second order terms (what they refer to as primary and secondary flows, respectively). For the temperature boundary conditions, the mean zonal velocity varied as

$$\begin{array}{l}
 \overline{u|u} \\
 \sim \left\{ \begin{array}{ll}
 G^2 (2\gamma^2)^{1/2} & 2\gamma^2 \ll 1 \\
 G^2 (2\gamma^2)^2 & 2\gamma^2 \gg 1
 \end{array} \right.
 \end{array}$$

They then pointed out that for the more realistic problem of heat flux boundary conditions, the frequency parameter dependence changes to

$$\frac{\bar{u}}{u_0} \sim G^2 (2\gamma^2)^{-2} \quad 2\gamma^2 \gg 1$$

which implies a very different behavior for the two types of heating. By comparing the relevant parameters for the terrestrial and major planets, they found that the value of  $G$  for Venus was at least four orders of magnitude larger than the others, thus indicating that Venus is the most likely planet to exhibit any significant response to a moving flame type of thermal forcing. The frequency parameter for Venus was estimated to be  $2\gamma^2 \sim 0(100)$  which would therefore classify Venus as a "high frequency" case. The values for the other planets were estimated to be at least two orders of magnitude larger so that when compared to the others, Venus is at the lower end of the high frequency range. If we consider this in view of the variation of  $\bar{u} \sim (2\gamma^2)^{-2}$  for the heat flux boundary conditions, then we once again see that Venus is the most likely planet to develop a retrograde mean zonal flow in response to the motion of the sun (i.e., a moving periodic heat source).

Malkus (1970) solved the linear Boussinesq equations with a rigid, no slip, insulating bottom and a flat, stress

free lid with heating from above specified as a heat flux boundary condition. In the limits of large and small frequency values, he found a retrograde mean zonal flow at the top given by

$$\frac{\bar{u}}{u_0} = \begin{cases} \frac{4}{6} \frac{1}{Pr^4} \left[ \frac{11Pr + 91}{175} \right] G^2 (2\eta^2)^2 & 2\eta^2, 2\gamma^2 \ll 1 \\ \frac{1}{Pr} \frac{1}{2} \left[ \frac{1}{2} + \frac{Pr}{(1+Pr)^{1/2}} \right] G^2 (2\eta^2)^{-2} & 2\eta^2, 2\gamma^2 \gg 1. \end{cases}$$

Although the parameter dependences are correct, the direction of the flow is incorrect due to a sign error in one of his equations. Recalling our simple qualitative model further confirms the directional error since we predicted that heating from above would force a prograde zonal flow. Based on his solution, he then used the Oseen approximation to find a maximum zonal velocity of magnitude  $42 \text{ ms}^{-1} \pm 100\%$ .

Schubert, Young, and Hirsch (1971) reconsidered Malkus' problem (no slip bottom, stress free top, heating from above) and the dependence of the mean zonal flow on heat flux versus temperature boundary conditions. In the limit of both frequency parameters being small ( $2\eta^2, 2\gamma^2 \ll 1$ ) it was found that the direction of the mean zonal velocity at the top and the direction of the vertically averaged mean zonal velocity depended upon the value of Pr. For values greater than the "critical" Prandtl number,  $Pr_c$ , the flow was prograde while for  $Pr < Pr_c$  the flow was retrograde. This

occurred for both temperature and heat flux boundary conditions, and the critical value was always between 0.1 and 0.3. In the limit of large frequencies ( $2\eta^2, 2\gamma^2 \gg 1$ ) the mean flow was always prograde. They also considered the limit of large momentum frequency  $2\gamma^2 \gg 1$  with small Prandtl number so that  $2\eta^2 \ll 1$  (they indicate this case as  $(2\gamma^2)^{-1/2}, 2\eta^2 \ll 1$ ) and again found a direction reversal depending on the Prandtl number for both temperature and heat flux boundary conditions. The explanation for this behavior is that heating from above will tend to tilt the isotherm and convection cells in a prograde sense (Figure 1.1) while momentum diffusion from a lower no slip boundary wall cause a phase lag of the streamfunction in the interior so as to transport retrograde momentum upward. The relative importance of these two effects is indicated by the Prandtl number which is the ratio of the kinematic viscosity to the thermal diffusivity ( $Pr = \nu/k$ ). For small values of  $Pr$ , heat will be well diffused and the thermal tilting effect will be minimal so that momentum diffusion becomes the dominant process in determining the retrograde direction of the mean flow. For large values of  $Pr$ , the opposite is true, so that thermal tilting is the major factor in determining the prograde sense of the mean zonal velocity. In the latter limit of their problem ( $(2\gamma^2)^{-1/2}, 2\eta^2 \ll 1$ ) the critical Prandtl number varied as  $(2\gamma^2)^{-3/2}$  so that extremely large values of the momentum frequency will correspond to retrograde flow

only if the Prandtl number goes to zero. As an example of results, for  $2\gamma^2 = 100$  the critical Prandtl number is  $Pr_c = 0.025$ .

Stern (1971) analyzed the effects of rotation and static stability in the moving flame effect in a cylindrical, radially unbounded fluid. In his model, a Boussenesq fluid with constant static stability ( $s$ ) is initially at rest in a coordinate frame which rotates with angular velocity  $f/2$ . This state is then perturbed by an arbitrary distribution of heat sources and sinks which propagate azimuthally with frequency  $\Omega$ . He found that  $\Omega$ -directed (prograde) angular momentum is pumped to the far field (infinite radius from the axis of rotation) if the quantity  $(\Omega^2 - f^2)/(gs - \Omega^2)$  is positive, and as a result, the fluid near the radius of the heat sources experiences a compensating torque which forces it to rotate in a retrograde sense. Accordingly, retrograde zonal flows could be generated in the case of rapid rotation ( $f^2 > \Omega^2 > gs$ ) or in the case of strong stratification ( $gs > \Omega^2 > f^2$ ).

Upon reviewing all of the above linear solutions, we discover some interesting properties of the problem. We find that within the context of linear theory, the motion of the heat source is able to force a retrograde mean zonal flow under various conditions. Furthermore, the mean zonal velocity increases with the thermal forcing, varying as  $G^2$ , and it increases as the Prandtl number becomes small. Both of these results were qualitatively predicted by the simple



descriptive model illustrated in Figure 1.1. The dependence of  $\bar{u}$  upon the frequency parameters is not quite as simple and obvious. This relationship is a function of the limit of frequency (large or small) and it also varies with the choice of thermal forcing -- i.e. temperature versus heat flux boundary conditions. As an example of this behavior we recall that for large values of momentum and thermal frequency ( $2\gamma^2, 2\eta^2 \gg 1$ ) with heat flux boundary conditions, the dependence is  $\bar{u} \propto (2\gamma^2)^{-2}$ , while for large momentum frequency and small thermal frequency ( $2\gamma^2 \gg 1$  with  $Pr \rightarrow 0$ ) the dependence is  $\bar{u} \propto (2\gamma^2)^{1/2}$ . One of the questions that is not answered by the previous linear solutions is what type of behavior does the mean flow exhibit in the transition from low to high frequency values. This problem will be addressed in Chapter 2 where we present some complete analytical-numerical solutions which are valid for all frequency values.

### 1.3.2 Nonlinear Models

Several nonlinear solutions have already appeared in the literature. Some have dealt with the moving flame effect in general while others have been specifically concerned only with Venus. For simplicity, we will review both types in this section in chronological order of publication.

In their report of experimental results using liquid mercury, Schubert and Whitehead (1969) presented some numerical solutions of the two-dimensional, Boussinesq, mean field

equations subjected to temperature boundary conditions. In the mean field approximation, it is assumed that the zonally averaged variables are larger than the wave amplitudes and thus the wave-mean flow interactions are retained but the wave-wave interactions are neglected in the eddy equations. For fixed values of the thermal forcing parameter and the thermal frequency parameter they found that  $\bar{u}/u_0$  was proportional to  $(Pr)^{-15/4}$  for Prandtl numbers between 1 and 0.1, and  $\bar{u}/u_0 \sim O(1)$  for  $Pr \sim O(.1)$ . Schubert (1969) also solved the mean field equations with rigid no slip boundaries and temperature boundary conditions except he considered the case of  $Pr = 0$ . He found the strongest retrograde mean zonal velocity to be at the center of the channel and that  $\bar{u}/u_0 = 1$  for  $2\gamma^2 = 16$ . For  $2\gamma^2$  between 10 and 16, the dependence of the centerline flow was  $\bar{u}/u_0 \approx 7.5 \exp[-32/2\gamma^2]$ , and based on this relationship, he attempted to extrapolate to larger values of the frequency. Based on our linearized calculations in Chapter 2, we seriously question the validity and real physical meaning of this extrapolation. We find that for the more realistic problem with heat flux boundary conditions,  $\bar{u}$  peaks for some intermediate value of the frequency parameters and then weakens as the frequency gets large.

Gierasch (1970) presented the first nonlinear model designed specifically to study the role of the moving flame effect in driving the four day circulation on Venus. The

major difference between his model and previous studies is that he supplied thermal forcing as internal radiative heating in place of forcing as a boundary condition. The heating term in his thermodynamic equation contained a time constant that decreased exponentially with height and this would cause a prograde tilt in the isotherms, similar to heating from above. The problem was then to find a mechanism that could counteract this tilting and still produce the phase lag between the convection cells and the forcing necessary to drive a retrograde mean zonal flow. He accomplished this by neglecting the viscosity terms in the perturbation and mean zonal velocity equations based on scaling arguments. By considering this inviscid situation, the Reynolds stress term  $\overline{u'w'}$  was effectively forced to be zero and therefore any tilting in the isotherms and convection cells due to heating must be eliminated by a mean zonal flow which advects heat in a retrograde sense in the upper levels of the model. Consequently in his steady state, inviscid solution, Gierasch found that the convection cells and the isotherms had no tilt and were exactly in phase, and the isotherms lagged behind the thermal forcing by  $82^\circ$  at all levels. Since the isotherms would tend to show a smaller phase lag at higher elevations (i.e., the radiative time constant decreases with height) and therefore tilt, the mean zonal velocity must be retrograde and increase with height in order to produce a steady state with untilted isotherms. The main objection to this solution

is that in general a flow with vanishingly small viscosity does not necessarily converge to the inviscid solution (Stone, 1975). Furthermore, this inviscid solution will be unstable to even the slightest amount of viscosity since the introduction of viscosity will allow a prograde tilt in the convection cells and this in turn would produce Reynolds stresses that would act to destroy the retrograde mean zonal flow.

Thompson (1970) proposed an alternative nonlinear instability mechanism by which the necessary Reynolds stresses could be produced. The process begins with steady state, untilted convection cells that have been produced by a stationary heat source (Fig. 1.2b) and if viscosity is not too large, then the mean zonal wind will tilt the convection cells as illustrated in Figure 1.2c. This will result in an upgradient transfer of zonal momentum by Reynolds stresses thereby amplifying the mean zonal wind. The full nonlinear equations for a two-dimensional Boussinesq fluid were solved numerically and the results indicated that a retrograde mean zonal velocity of the correct order of magnitude could develop through this mechanism. Thompson then suggests that the overhead motion of the sun could supply the required initial mean zonal wind and as the instability mechanism takes over, solar motion becomes unimportant. It is not clear from his solutions that the instability mechanism and the moving flame effect will work together effectively since his heating function is equivalent to heating from above and the motion of such a heat source would

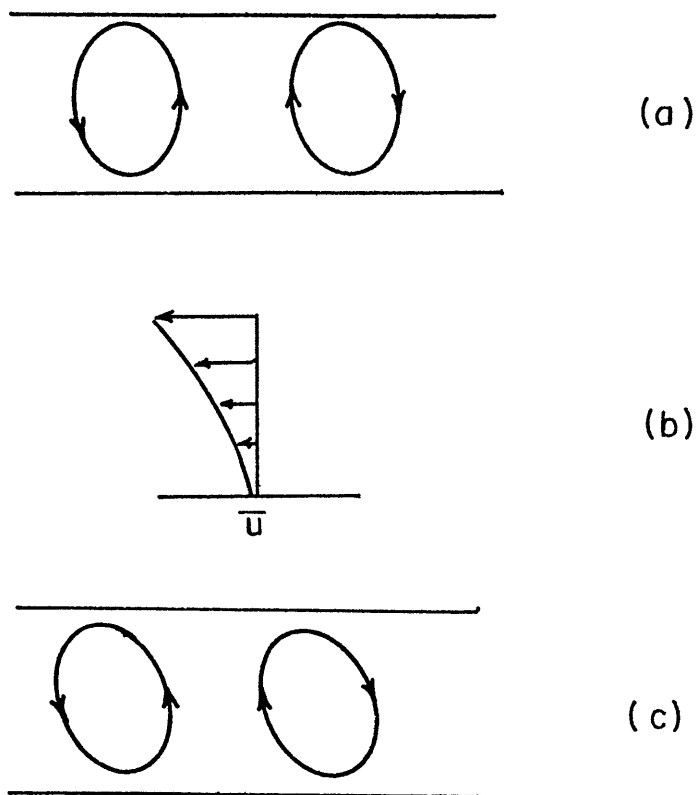


FIGURE 1.2 Nonlinear instability mechanism proposed by Thompson (1970): (a) untilted convection cells, (b) perturbation mean zonal flow, (c) tilted cells due to  $\bar{u}$ .

tend to produce a prograde mean flow and not the required initial retrograde flow. This is evidenced in his inability to achieve any steady retrograde moving flame solutions. Furthermore, even his steady state non-moving flame results are inconclusive because the vertical grid in the model is too coarse to properly resolve the horizontal boundary layers (Stone, 1975). For example, his choice of frequency parameter values  $2\eta^2 = 2\gamma^2 = 100$  implies a dimensionless boundary layer thickness of  $O(10^{-1})$  while his first grid point is at a dimensionless height of 0.1 which is roughly the top of the boundary layer.

Hinch and Schubert (1971) considered the same problem as Schubert (1969), i.e., the mean field equations for a Boussinesq fluid with  $Pr = 0$  and with heating specified as temperature boundary conditions. By using the method of matched asymptotic expansion, they also found that strong retrograde flow would be possible only in the limit of large values of the momentum frequency parameter,  $2\gamma^2 \gg 1$ . In fact, their mean field solution predicted exactly the same behavior as the linear solution considered by Schubert and Young (1970), i.e.,

$$\frac{\bar{u}}{u_0} \sim G^2 (2\gamma^2)^{1/2} \quad 2\gamma^2 \gg 1 \quad .$$

Once again we contrast this solution to the solution with heat flux boundary conditions which in the high frequency limit predicts a decrease in  $\bar{u}$  as the frequency parameter increases. For the stratosphere of Venus, the frequency parameters appear to be within the intermediate range of values (i.e., 0 (1) - 0 (10)), or at most at the low end of the high frequency range. Therefore the temperature boundary conditions can only force a strong zonal flow for frequency values that are irrelevant to Venus. Consequently, any further attempts at simulating the role of the moving flame effect in driving the four day circulation should incorporate the more realistic heat flux boundary conditions.

Young, Schubert, and Torrance (1972) presented some numerical solutions of the full nonlinear equations for a Boussinesq fluid. They considered the effects of varying parameter values and dynamical boundary conditions by solving the equations for various situations and were able to produce only weak retrograde mean zonal velocities. In all of the cases, the dependence of  $\bar{u}$  on the thermal forcing was rather close to the  $G^2$  behavior predicted by linear theory. The sets of boundary conditions they used were both boundaries rigid and no slip subjected to the same temperature wave; both boundaries rigid and stress free subjected to the same temperature wave; a no slip, isothermal bottom and a stress free top subjected to a temperature wave. For the two symmetric cases, the maximum retrograde mean zonal velocity occurred at the channel center

with the rigid-rigid flow being roughly three times as strong as the free-free flow. This is due to the fact that in the free-free case, the fluid cannot acquire any net momentum if there is none initially and thus the retrograde flow at the channel center must be balanced by an equal amount of prograde flow at the edges. In the rigid-rigid case, however, the flow is retrograde at all levels, except at the boundaries where  $\bar{u} = 0$ . It is clear that in both of these cases, the symmetric heating causes a tilt that supports retrograde momentum transport towards the channel center. Both symmetric solutions were fairly insensitive to the value of the Prandtl number. The free-rigid case exhibited the same Prandtl number dependence as in the linear problem considered by Schubert, Young, and Hinch (1971). In this case, the direction of the mean zonal velocity was found to be retrograde for  $Pr$  less than the critical value,  $Pr_c$ , and prograde for  $Pr$  greater than  $Pr_c$  as explained above. The maximum value of  $\bar{u}$  showed a weak increase as the momentum frequency parameter was increased from 10 to 50. This behavior is undoubtedly due to the use of temperature boundary conditions rather than heat flux forcing. Unfortunately they did not perform any computations for the more realistic problem with heat flux boundary conditions. In all of the cases they considered, the maximum horizontal eddy velocity,  $|u'_{\max}|$ , turned out to be larger than the mean zonal velocity,  $\bar{u}$ . For  $G = 1$  (i.e., weak forcing),  $|u'_{\max}|$  was typically two or



three orders of magnitude larger than  $|\bar{u}_{\max}|$ . For  $G = 100$ , the difference was only one order of magnitude with  $|\bar{u}_{\max}/u_0| \approx 1$ .

Young and Schubert (1973) numerically solved the two-dimensional, mean field equations subjected to thermal forcing in the form of internal radiative heating. The main difference between their model and the one used by Gierasch (1970) was that viscosity was included in their momentum equation. Once again, the structure of their thermal forcing is equivalent to heating from above and consequently, they must rely on some other process to reverse the tilt of the isotherms and convection cells. It appears from their calculations that a strong stratification is able to accomplish the necessary tilt reversal. The numerical marching consisted of starting at small values of the Frönde number,  $\tau$ , and iterating to larger values. Unfortunately, the method failed to converge when  $\tau$  reached values between 200 and 300 (the appropriate value for Venus is 3000); nevertheless, they were able to produce retrograde mean zonal velocities that were ten to fifteen times faster than the overhead speed of the sun. In addition to the numerical problems, there are several assumptions made in their model which may seriously affect the results. First, and most important, is the way they handled the net stratification and the mean temperature of the atmosphere. One inconsistency, which they recognized, was the assumption that the mean temperature,  $\bar{T}$ , is equal to

the constant background temperature while in the thermodynamic equation they assumed a constant mean lapse rate of  $\frac{d\bar{T}}{dz} = -4^\circ\text{C}/\text{km}$ . By making these assumptions, they forced the mean temperature structure to be independent of the dynamics of the circulation, and thereby artificially forced true mean state to remain statically stable. Furthermore, upon noting the inconsistency between a constant mean temperature and a constant non-zero lapse rate, they comment that "the only place this discrepancy is likely to be important is in the net stratification term of" the thermodynamic equation; but this positive static stability is precisely the process they relied on to reverse the tilt of the isotherms. Furthermore, while the positive net stratification may provide the required tilt reversal, it will also tend to suppress the intensity of the convection and therefore limit the effectiveness of the Reynolds stress momentum transport. The other questionable assumption in their model, which may be partially responsible for the numerical difficulties, was the neglecting of thermal diffusion. This is valid only if the thermal diffusivity is less than  $10^4 \text{ cm}^2 \text{ s}^{-1}$ . Prinn (1974) has shown that the eddy diffusion coefficients above the visible cloud deck may be as large as  $2 \times 10^5 \text{ cm}^2 \text{ s}^{-1}$ . Such a value would make thermal diffusion at least as effective as radiative heating in vertically transporting heat. It could also force the development of a significant thermal boundary layer.

Table 1.2 - Information about the atmospheres of the Earth and its nearest planetary neighbors (adapted from Houghton, 1977)

	Venus	Earth	Mars	Jupiter
Mean surface temperature (K)	750	288	240	134 <sup>a</sup>
Surface pressure (atm)	90	1	0.007	2 <sup>a</sup>
Free fall acceleration due to gravity (cm s <sup>-2</sup> )	880	980	376	2600
Main constituents	> 95% CO <sub>2</sub>	78% N <sub>2</sub> , 21% O <sub>2</sub>	> 95% CO <sub>2</sub>	H <sub>2</sub> , He
Clouds	Deep H <sub>2</sub> SO <sub>4</sub> clouds complete cover	H <sub>2</sub> O clouds ~50% cover	Some thin H <sub>2</sub> O clouds	NH <sub>3</sub> clouds
Distance from sun (astronomical units)	0.72	1.00	1.52	5.20
Albedo	0.77	0.30	0.15	0.58
Equilibrium temp. T <sub>e</sub> (K)	227	256	216	98
Period of rotation (terrestrial days)	243 <sup>b</sup>	1.00	1.03	0.41
Solar constant (W m <sup>-2</sup> )	2643	1370	593	51
Absorbed solar radiation (W m <sup>-2</sup> ) <sup>c</sup>	608	959	504	21 <sup>d</sup>
Inclination of equator to orbital plane (deg)	< 2	23	24	?

- a values at cloud top since Jupiter has no solid surface
- b The combination of retrograde planetary rotation and orbit around the sun give Venus a solar day of 117 terrestrial days
- c computed from  $(1-A)Q_0$  where A = albedo and Q<sub>0</sub> = solar constant
- d Jupiter has internal heat source comparable to the solar constant

1.4 Venus

While Venus and the planet Earth differ only slightly in size and in magnitude of thermal forcing in the form of net absorbed solar radiation, the other physical parameters that determine the general circulation of these atmospheres show quite a large contrast (see Table 1.2). The very long Venus rotation period of 243 days leads one to expect that Coriolis forces will be relatively unimportant in shaping the atmospheric motions. Consequently, approximations such as quasigeostrophic flow do not apply, and the balance in the equations of motion will be primarily among the non linear terms. Since Venus' axis of rotation is very close to being perpendicular to its orbital plane, seasonal variations and their effects on the state of the atmosphere should also be negligible.

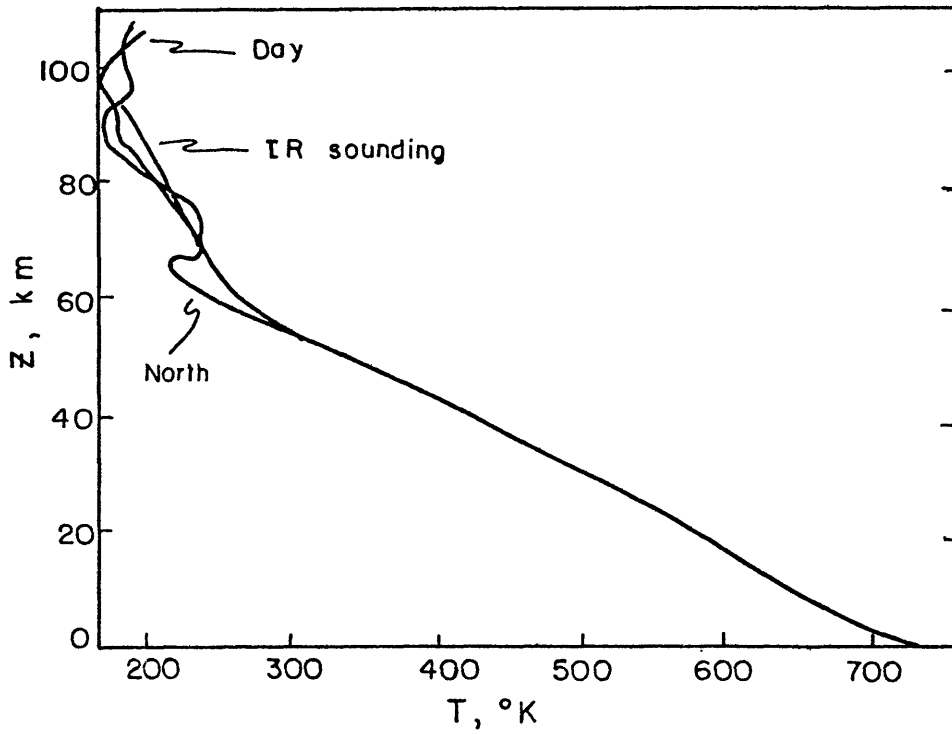
Based on a time scale analysis (radiative, dynamical, and length of a solar day), Stone (1975) divided the atmosphere of Venus into two distinct dynamical regimes. Below an altitude of 56 km , and especially below 40 km, the radiative time constant is longer than the length of a solar day and thus diurnal effects will be relatively unimportant in the lower atmosphere. The deep atmosphere will be driven primarily by equator to pole temperature contrasts associated with latitudinal variations in solar heating. The global circulation should consist of a weak Hadley cell with rising in equatorial regions and sinking in the polar regions. This

hypothesis is consistent with the observed near adiabatic temperature structure (Figure 1.3). The high surface temperature is most likely maintained by a strong greenhouse effect.

Above 56 km, the radiative time scale becomes less than or equal to the length of a solar day, the lapse rate is sub-adiabatic, and horizontal motions are very strong. At these elevations, diurnal and latitudinal temperature contrasts are comparable, and are both important in driving the observed rapid zonal flow (i.e., the Four Day Circulation). For this reason, three-dimensional modelling is necessary if we are to understand the general circulation of the atmosphere of Venus.

At all elevations below 80 km the dynamical time scale is shorter than both the radiative time constant and the length of a solar day. Consequently we should expect advective processes (nonlinear terms) to play a major role in determining the thermal structure of the entire atmosphere (See Figure 1.4).

The latest data from the Pioneer Venus probes has confirmed the existence of several distinct cloud layers below 70 km. Knollenberg and Hunten (1979) have identified four regions referred to as upper (68-58 km), middle (58-52 km), and lower (52-48 km) clouds, and lower haze (48-31 km). Each region contains particles of various sizes consisting of mostly elemental sulfur and sulfuric acid droplets (except no sulfuric acid in the lower haze).



1.3

FIGURE 1.3 Temperature profiles in the Venus atmosphere from Pioneer Venus measurements (from Seiff et. al., 1979).

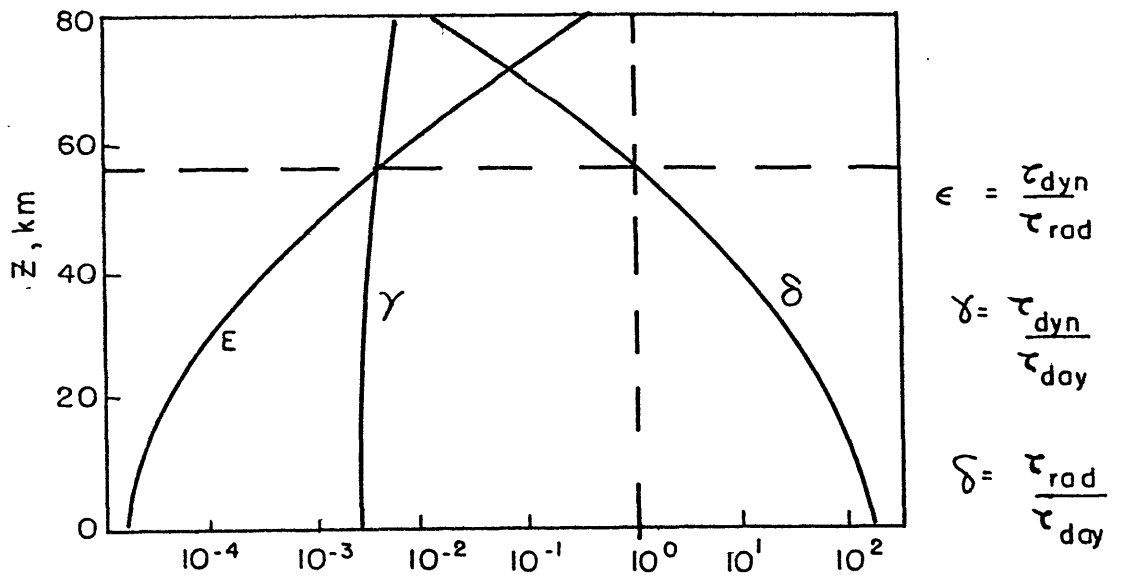


FIGURE 1.4 Ratios of time scales in the Venus atmosphere (from Stone, 1975).

#### 1.4.1 Observational evidence for the 4-day circulation

During the past twenty years, the existence of the retrograde superotation of the upper atmosphere of Venus, commonly referred to as the four day circulation, has been confirmed through several independent methods of observation. Dollfus (1975) has summarized the results of the many earth-based ultraviolet images of Venus. These photographs show the presence of several Y- or psi-shaped dark cloud features with lifetimes of several weeks. These features move in a retrograde direction and reoccur every four days. If in fact this is an indication of fluid motion, then the wind speeds at the cloud tops must be on the order of  $100 \text{ m s}^{-1}$ . On the other hand, Young (1975) has shown that the motion of these UV markings could also reflect the presence of some type of wave phenomenon propagating with a phase speed of  $100 \text{ m s}^{-1}$ , and this motion is therefore not necessarily indicative of high wind speeds. Consequently, additional and alternative observations would be necessary to confirm the existence of the four day circulation. Murray et al. (1974) also found these Y features in the Mariner 10 images of Venus. Because of the greater resolution of the satellite photographs, they were also able to indentify several small scale cloud features which also move with retrograde speeds of about  $100 \text{ m s}^{-1}$ . The general picture painted by the Mariner 10 data indicated the presence of strong retrograde zonal winds near the equator, increasing

in magnitude to a jet in mid-latitudes (possibly exhibiting a conservation of angular momentum), and then decreasing magnitude in high latitudes (solid body rotation). The meridional component of the wind was much smaller and highly variable.

Traub and Carleton (1975), also detected retrograde mean zonal winds of  $83 \text{ m s}^{-1}$  by analyzing spectroscopic observations of Doppler shifts of  $\text{CO}_2$  lines. The meridional velocities were found to be much weaker ( $30 \text{ m s}^{-1}$ ) than the zonal flow. Further conclusions about the meridional flow could not be drawn since the magnitude of the velocity was comparable to the measurement uncertainties.

The other method available to measure wind velocities involves atmospheric entry. The spacecraft is tracked during its descent by means of measuring the Doppler shift of a continuous radio signal that it transmits. From this information, the horizontal component of the probe's drift (presumably due to wind) can be determined. Using this method with Venera 8 data, Marov et al. (1973) measured wind speeds as high as  $100 \text{ m s}^{-1}$ . The strongest velocities were found above an altitude of 50 km.

More recently, the Pioneer Venus spacecraft has confirmed the presence of strong zonal winds through UV cloud photographs from the Orbiter and through radio tracking of the entry probes. Rossow et al. (1980a) have presented a detailed analysis of the UV cloud images for a three



month period. By tracking small scale features, they were able to deduce a retrograde zonal flow with speeds of roughly  $100 \text{ m s}^{-1}$  near the equator and decreasing in magnitude with increasing latitude. The latitudinal profile of the zonal wind is very close to the theoretical profile of solid body rotation (Fig 1.5). Furthermore, the mid-latitude jet observed in the Mariner 10 photographs was not present, thus suggesting a temporal change in the structure of the four day circulation possibly due to some instability mechanism. The meridional flow was poleward and weak with velocities of  $2 \text{ m s}^{-1}$  and  $5 \text{ m s}^{-1}$  in the southern and northern hemispheres respectively. Counselman et al. (1979) have presented preliminary results from the radio tracking of two of the Pioneer Venus entry probes. The measurements reveal fairly large retrograde zonal winds ( $50 \text{ m s}^{-1}$ ) at altitudes as low as 30 km, and velocities of up to  $200 \text{ m s}^{-1}$  near cloud top levels. This data tends to confirm the original hypothesis of a four day circulation as suggested by the motion of cloud features observed in the various UV images.

#### 1.4.2 Other theoretical studies of the Venus atmospheres

In addition to the moving flame studies discussed above, there have been several other theoretical studies of the atmosphere of Venus. These include a few general circulation models and some investigations of other mechanisms

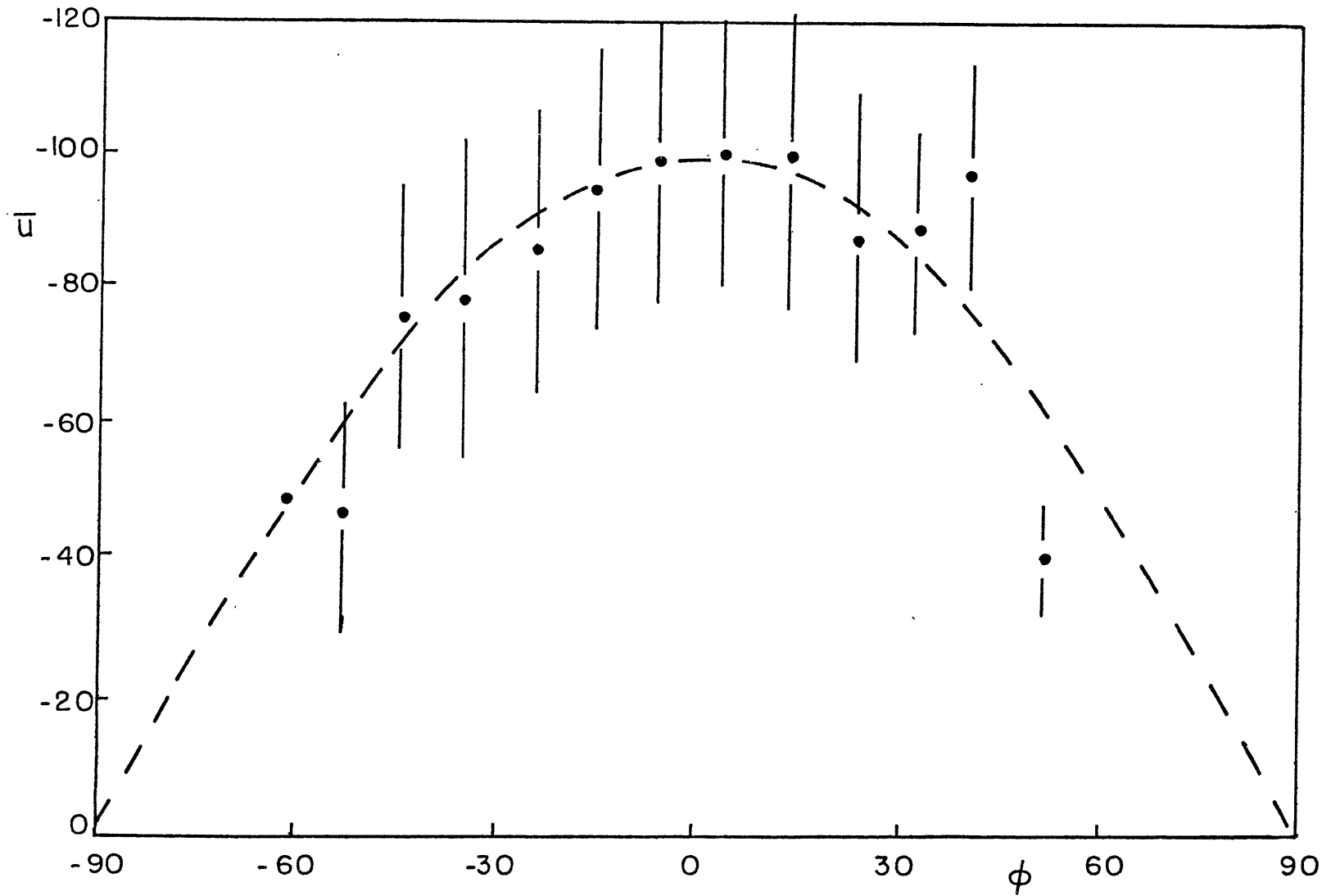


FIGURE 1.5 Meridional profile of  $\bar{u}$  at the cloud tops from Pioneer Venus Orbiter (Rossow et al., 1980a). Dashed line is  $\cos$  (solid body rotation).

that might drive the four day circulation.

Kalnay de Rivas (1973, 1975) presented some results from a series of two-dimensional Boussinesq and quasi-Boussinesq general circulation models. Because of the two-dimensional nature of these studies, they are only valid for the lower atmosphere (i.e., well below the cloud tops) where diurnal heating contrasts are negligible. In general, the flow consisted of a Hadley cell between the subsolar and antisolar points in the nonrotating cases and between the equator and pole in the rotating cases. The intensity, vertical extent, and other smaller scale features of the flow depended upon the choice of parameter values such as eddy viscosity coefficients and total optical depth of the atmosphere. Retrograde zonal velocities appeared only in the rotating models as a result of the presence of a small coriolis force. The maximum speeds attained were less than  $20 \text{ m s}^{-1}$ , and in most cases, the zonal flow consisted of a polar jet confined to the top of the atmosphere. Unfortunately, these models could not be used to examine the role of forcing mechanisms that are asymmetric in longitude. The three-dimensional model that was described (Kalnay de Rivas, 1975) has not yet been fully developed and tested.

Chalikov et al. (1975) reported on some three-dimensional simulations of the lower atmosphere of Venus. Their model was also incapable of producing a four day circulation. Two of the major reasons for this are the very

limited vertical resolution (only two or three levels for most runs), and the relatively low altitude of the upper boundary (38 km). The maximum integration period was only two solar days which is very short, especially for the lower atmosphere.

The only other general circulation model for Venus that is currently in use was developed by Pollack and Young (1975). The rather large values of the vertical and horizontal diffusion coefficients ( $4 \times 10^5 \text{ cm}^2 \text{ s}^{-1}$  and  $4 \times 10^8 \text{ cm}^2 \text{ s}^{-1}$  respectively) and the relatively short integration time (1.4 solar days) prevented the development of any significant mean zonal velocities. In a more recent version of their model (Young and Pollack, 1977), the diffusion terms were modified in such a way as to provide damping that increases according to roughly the fourth power of the wavenumber.\*\* Consequently, this formulation applies very strong dissipation to the shortest resolved scales, an effect which is somewhat desirable since it helps in eliminating the problem of energy cascade to the highest wavenumbers. However, in the Young and Pollack (YP) model the truncation value of total wavenumber four means that a significant part of their spectrum is subjected to extremely strong

\*\*Ordinary viscosity can be expressed in terms of  $\nabla^2 u$  while Young and Pollack formulate diffusion as  $-\nabla^4 u$ . In a spherical harmonic expansion, the Laplacian has the simple form  $\nabla^2 U_n^m = -n(n+1) U_n^m$  where  $m$  is the order (zonal wavenumber) and  $n$  is the degree of the harmonic, and thus viscosity depends on  $n(n+1)$ . The Young-Pollack diffusion operator becomes  $-\nabla^4 U_n^m = -\nabla^2 (\nabla^2 U_n^m) = -[n(n+1)]^2 U_n^m$  and therefore depends on roughly  $n^4$ .

dissipation. A simple calculation (Table 1.3) shows that for truncation at wavenumber four, more than one half of the retained modes are being subjected to Y-P dissipation which is one order of magnitude larger than ordinary viscosity. Because of this diffusion formulation, it is also not surprising to find that their results are relatively insensitive to a moderate increase in horizontal resolution (i.e., from wavenumber 4 to 6). The reason is that in the higher resolution experiments, wavenumbers 3 and 4 are damped at the same rate as in the lower resolution computations and thus the presence of wavenumbers 5 and 6 (which experience

---

Zonal Wavenumber (m)	$\frac{\text{YP diffusion}}{\text{Viscosity}} = \frac{-\nabla^4 U_n^m}{\nabla^2 U_n^m} = n(n+1)$
1	2
2	6
3	12
4	20
5	30
6	42

---

TABLE 1.3: Ratio of YP diffusion to ordinary viscosity as a function of zonal wavenumber. These ratios are the minimum values, since for any fixed  $m$ , we have the relationship  $n \geq |m|$ .

---

even stronger dissipation) will be of little important. An attractive alternative, which we will use in Chapter 3, is to periodically apply a filter which can selectively eliminate the shortest waves without adversely effecting the long waves. Another difficulty with the YP model arises from the  $\frac{\partial^4 u}{\partial z^4}$  form of the vertical diffusion and the required additional boundary conditions. Rossow et al. (1980b) showed that spurious forces could be generated as a result of an error made by YP in specifying the extra upper boundary condition (for a full discussion of these problems, the reader is referred to Rossow et al. (1980b), and Young and Pollack, 1980). Nevertheless, under certain conditions, the model was able to produce retrograde zonal winds as large as  $90 \text{ m s}^{-1}$ . On the basis of their computations, Young and Pollack have tentatively indentified the driving mechanism as a nonlinear instability involving the mean meridional circulation and the planetary scale eddies. Planetary rotation appears to be the source of the initial retrograde flow necessary for the instability. We will present a more detailed discussion of their results in Chapter 3 by comparing them to our nonlinear solutions.

Several driving mechanisms for the four day circulation other than the moving flame effect have also been proposed. Thompson's (1970) nonlinear shear instability theory has already been discussed above in section 1.3.2. Gold and Soter (1971) considered the possible role of solar

thermal tides in driving the observed zonal winds. This mechanism depends on the effect of the semidiurnal tide on the atmospheric mass distribution. If the magnitude and the phase lead of the induced wavenumber 2 mass wave are within the proper range, then a net retrograde torque could develop and accelerate the atmosphere in the correct direction. Unfortunately, neither of these quantities are known for Venus. Furthermore, their computations of the required torque are very sensitive to the value of the kinematic viscosity, and in fact, the mechanism can only operate if the diffusive momentum transport is molecular. For large scale motions and turbulence, it is more likely that eddy viscosity will be the dominant form of diffusion. In this case, the appropriate values of the coefficients would reduce the effectiveness of the tidal forcing by several orders of magnitude.

Fels and Lindzen (1975) proposed another possible mechanism which involves vertical momentum transport by thermally excited internal gravity waves in a vertically semi-infinite atmosphere. They found that these waves will carry prograde (i.e., direction of solar motion) momentum away from the level at which solar heating occurs and thus cause a net retrograde acceleration of that layer. The prograde flow that develops in the adjacent layers will not grow beyond the phase speed of the waves because of critical layer absorption. As the shear increased, further wave

activity will produce turbulence and a tendency for the critical layers to converge towards the level of maximum retrograde velocity and therefore inhibit the further growth of the retrograde flow. While this mechanism can account for a significant amount of retrograde acceleration, it can generate  $100 \text{ m s}^{-1}$  winds only in the presence of an initial retrograde mean zonal flow of  $25 \text{ m s}^{-1}$ .

The approach taken by Leovy (1973) and Gierasch (1975) to explain the four day circulation is quite different from the above mechanisms. They have considered the role of meridional temperature contrasts rather than longitudinal contrasts in maintaining the mean zonal flow. Leovy suggested that the four day circulation represents cyclostrophic balance between the meridional pressure gradient and centrifugal force. In Leovy's model, an initial latitudinal temperature contrast would drive a Hadley cell. It is known (e.g., Starr, 1968), that a Hadley cell on a slowly rotating sphere will produce a mean zonal circulation in which the zonal flow in the upper levels of the fluid will be in the same direction as planetary rotation. For Venus, the retrograde rotation is the source of the initial retrograde zonal flow. The next stage in the development of the rapid retrograde flow requires some alternative mechanism to continually accelerate the upper atmosphere. Unfortunately Leovy skipped this part and proceeded directly to the equilibrium flow. Since the mean zonal flow is now in



cyclostropic balance, any small deviations that arise will excite gravity waves as part of an adjustment process (analogous to geostrophic adjustment). He then suggested that these gravity waves would be similar to equatorial Kelvin waves on earth and could therefore transport retrograde momentum upward. This would occur because Kelvin waves provide an upward transport of momentum of the same direction as atmospheric rotation, which in this case is retrograde.

In an extension of Leovy's theory, Gierasch (1975) showed that under certain conditions, the meridional Hadley cell could supply the upward momentum flux necessary to support the rapid rotation of the upper atmosphere. This requires the presence of some other mechanism that can maintain a retrograde angular momentum surplus in equatorial regions relative to polar regions. In the steady state, there would be a vertical balance between the upward transport by the Hadley cell and the downward transport by eddy and diffusive processes. There would also be a horizontal balance between the poleward flux of angular momentum by the upper branch of the Hadley cell and the equatorward flux by the unspecified process mentioned above. Two possible mechanisms that were briefly discussed are vorticity mixing and momentum transport by horizontal Reynolds stresses. Eventually, Gierasch decided to model this unknown process by an unrealistically strong horizontal diffusion. Kálnay

de Rivas (1975) conducted some numerical experiments to test this mechanism and found that very strong horizontal diffusion would weaken the meridional temperature gradient and consequently suppress the Hadley cell and its resulting momentum flux. This mechanism was also shown to work only if the effective Prandtl number of the horizontal mixing process is several orders of magnitude larger than unity.

The most recent theoretical study of the Venus stratosphere by Rossow and Williams (1979) focused on the possible role of two-dimensional (horizontal) turbulence and barotropic instability in maintaining the four day circulation. Based on scale analysis, they argued that the circulation of the Venus stratosphere is quasi-nondivergent and that the forcing that maintains the circulation is only weakly coupled to the flow. Consequently, they studied the properties of two-dimensional vorticity conserving flows as well as the solutions of the two-dimensional vorticity equation with various types of simple forcing functions (e.g., axisymmetric, localized, etc.). In the former case, the free inertial development of an initial flow field led to a relaxed state of solid body rotation with weak planetary scale waves.

For the forced solutions, the model was subjected to continuous forcing, drag, and dissipation. In the experiments labeled "strong forcing", an equilibrated flow developed as a result of a balance between the forcing and the drag. The nonlinear inertial effects were only of minor importance.

On the other hand, in the "weak forcing" cases, the final flow field consisted of a relaxed state similar to a vorticity conserving flow in which the nonlinear inertial effects shaped the solution. Once again, the relaxed state was predominated by the largest scales of motion.

Based on these results and the differences between the meridional profiles of  $\bar{u}$  in the Pioneer Venus and in the Mariner 10 observations, Rossow et al., (1980a) have proposed a cyclic mechanism involving the mean meridional circulation and barotropic instability which could explain many of the features of the four day circulation. In the first step of the process, the Hadley cell in the lower atmosphere (driven by equator to pole heating contrasts) provides an upward transport of retrograde angular momentum (Gierasch, 1975). The lower atmosphere receives its retrograde angular momentum from frictional coupling to the slowly (retrograde) rotating solid planetary surface. The Hadley cell will also transport retrograde angular momentum poleward, leading to the development of a mid-latitude jet. This point in the cycle corresponds to the Mariner 10 observations (Murray, et al., 1974). As the jet grows, it becomes barotropically unstable, breaks down, and supplies kinetic energy to the large scale eddies. The eddies transport retrograde angular momentum equatorward and lead to the relaxed state of solid body rotation as in the Rossow and Williams model. This corresponds to the Pioneer Venus

observations. As this cycle reoccurs, the upper atmosphere will slowly be accelerated in a retrograde sense so that over a long enough period of time, the rapid zonal winds associated with the four day circulation could develop and be maintained.

Even though Pioneer Venus has brought us one step closer to understanding some of the features of the general circulation of the atmosphere of Venus, it is quite clear that many more extensive observations and numerical simulations will be necessary to help us identify the actual processes that are forcing and maintaining the flow. This is especially true if the circulation is dominated by inertial effects as suggested by Rossow and Williams.

### 1.5 Objectives and Organization

From our discussions of the many experimental, observational, and theoretical studies, it is evident that our knowledge and understanding of the Venus atmosphere is rather limited and that each new piece of information brings us one step closer to solving the puzzle. Within the context of this investigation we certainly could not hope to devise an overly complex general circulation model of a poorly understood planetary atmosphere. What we can do however, is to examine one very particular forcing mechanism (i.e., the moving flame effect) and to determine whether or not it plays a significant role in driving the four day

circulation.

In the past, all of the theoretical moving flame investigations have been restricted to two space dimensions and have concentrated exclusively on the effects of diurnal heating contrasts. Our main objective in this thesis is to consider the more realistic problem in three dimensions with both diurnal and equator to pole differential heating. We are interested in studying the role of the meridional circulation and its interaction with the zonal flow.

To accomplish our goal, we develop two models of different complexity. In Chapter 2 we consider a linearized model of a Boussinesq fluid in Cartesian coordinates. The thermal forcing, in the form of a moving (in longitude) periodic heat source with meridional variations, is specified as a heat flux boundary condition. Our linearization consists of neglecting the eddy self interaction terms in the equations for the mean meridional circulation and in the equations for the eddies. All wave-mean flow interaction and mean flow self interactions are retained. To obtain the steady state circulation, we first solve for the steady state mean meridional circulation that is driven exclusively by equator to pole differential heating. This solution is then used in the remaining equations to solve for the large scale eddies and the mean zonal velocity.

In an effort to more closely model the role of the moving flame mechanism in a planetary atmosphere, we next

develop the more complex model of Chapter 3. We derive the equations in spherical coordinates also with a boundary heating function. We numerically solve the fully nonlinear equations and allow for greater horizontal resolution as compared to the linearized model.

In both cases we find that the moving flame mechanism does in fact drive a retrograde mean zonal flow but with horizontal velocities that are only of the same order of magnitude as the speed of the heat source. It appears therefore that the moving flame mechanism alone cannot adequately explain the very rapid motions that are associated with the four day circulation of the stratosphere of Venus.

## CHAPTER 2

THREE-DIMENSIONAL LINEARIZED MODEL2.1 Introduction

The general circulation of the atmosphere of Venus, especially the four day retrograde rotation of the stratosphere, is indeed a quite complex system that cannot be accurately simulated until much more observational data is gathered. The difficulties in this respect are twofold. First, the extremely slow planetary rotation rate implies that the dominant terms in the equations of motion are associated with nonlinear advective processes. Second, our limited knowledge of the atmosphere of Venus does not allow us to precisely identify the nature of the physical and dynamical processes (e.g., barotropic vs. baroclinic instability) that control the circulation. Nevertheless, we can still speculate about some of the phenomena that might play a role in maintaining the observed dynamical state of the atmosphere. As was discussed in the previous chapter, Schubert and Whitehead (1969) suggested that the relatively slow overhead motion of the sun may in fact produce planetary scale convection cells which would in turn drive a retrograde mean zonal flow that could exceed the speed of the sun by one or two orders of magnitude. All of the subsequent theoretical investigations of this phenomenon concentrated exclusively on the importance of the diurnal

heating contrasts and thus neglected the effects of the meridional circulation that would inevitably exist in a planetary atmosphere. It is therefore one of the main goals of this thesis to examine the meridional circulation that will develop in a simple three-dimensional model with latitudinal heating contrasts and to study the interactions that will occur between a steady mean meridional circulation and the longitudinal convection cells of the two-dimensional moving flame mechanism. It should once again be emphasized that this is a study of only one very specific physical process and therefore cannot completely explain all of the observed features of the dynamical state of the upper atmosphere of Venus.

## 2.2 Details of the Model

In this section we describe the linearized model that is used for our initial investigation of the moving flame mechanism. The equations are derived and solved for a three-dimensional channel of fluid in rectangular coordinates. We realize that by using this geometry the model is not directly applicable to a planetary atmosphere. It also implicitly neglects certain effects, such as cyclostrophic flow, which appear only in spherical geometry. Nevertheless, our simple model will still give us some interesting insight into the relative importance of day-night and equator-pole heating contrasts in forcing a moving flame type



circulation. The investigation consists of two stages. First, we determine the steady state mean meridional circulation (MMC) driven exclusively by the analog of an equator to pole heating contrast. This part of the solution is similar to the various axisymmetric models of Hadley type circulations that have appeared in the literature (e.g., Stone, 1968 and Kalnay de Rivas, 1973). The MMC is solved for in the absence of planetary scale waves and with no planetary rotation. Thus the first part of our linearization consists of neglecting the wave-wave interaction terms in the MMC equations. For this approximation to be strictly valid, we require the following relationships between the zonal (and time) mean variables, indicated by an overbar ( $\bar{\quad}$ ), and the eddy variables, indicated by a prime ( $\prime$ ):

$$|\bar{v}| \gg |v'| \quad , \quad |\bar{w}| \gg |w'| \quad , \quad |\bar{\theta}| \gtrsim |\theta'| \quad .$$

While eddy momentum and heat fluxes might modify the MMC, we will verify a posteriori that these fluxes are of minor importance when compared to advection by the MMC (Figure 2.19). Therefore the equator to pole differential heating and the mean flow self interactions are the dominant processes that force and shape the steady state MMC, and as a first approximation we may solve for the MMC that is independent of the eddies. Having determined the steady state MMC, we then use these solutions as fixed coefficients in the equations for

the large scale eddies and the mean zonal velocity. The wave equations will also be linearized according to the mean field approximation so that any terms that are nonlinear in the eddy variables are neglected. In the equation for the mean zonal flow, however, we must retain the second order wave terms (the so-called Reynold's stresses) since they provide the forcing function for  $\bar{u}$ .

An alternative way of approaching the linearization process is to consider a low order spectral representation of the dependent variables. If the truncation is set at zonal wavenumber 1 ( $M=1$ ), then the wave-wave interaction terms in the eddy equations are automatically eliminated since such terms can only produce higher harmonics. The wavenumber 1 self interactions which contribute to  $m = 0$  are exactly the Reynolds stress terms that we wish to examine and are therefore retained in the  $\bar{u}$  equation. The Reynolds stress terms in the MMC equations are neglected since, as mentioned above, we are concerned only with the first order MMC driven by equator to pole heating contrasts.

We begin with the equations of motion in rectangular coordinates for a fluid confined between two flat horizontal plates. The channel is assumed infinite and periodic in both horizontal coordinate directions. The model geometry is illustrated in Figure 2.1. The heating varies as  $\cos y$  (latitude), corresponding to a subsolar point at  $y = 0$

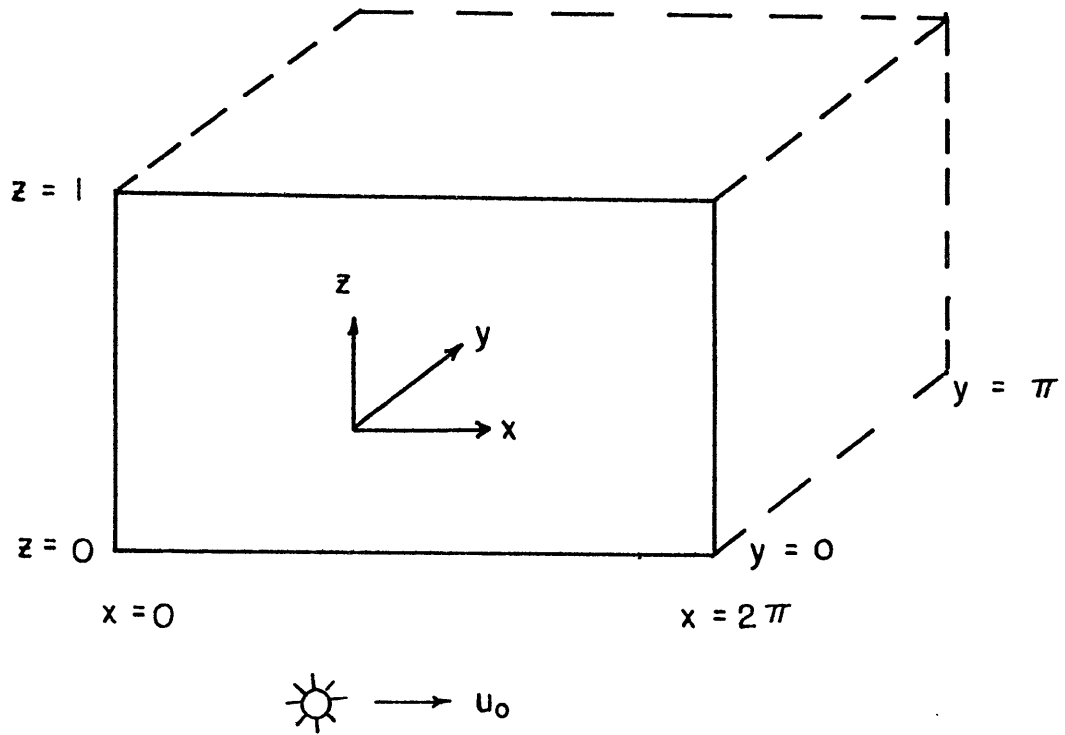


FIGURE 2.1 Model geometry for the linearized model

and an antisolar point at  $y = \pi$ . A zonal Fourier analysis of the heat flux (Appendix A) provides the  $m = 0$  component which drives the MMC and the  $m = 1$  component which is the moving flame type forcing. With reference to Figure 2.1, the periodic motion of the heat source is in the positive X direction (prograde) with speed  $u_0$ , wavelength  $L = 2\pi a$  (or wavenumber  $k = 2\pi/L$ ), and frequency  $\Omega = ku_0$ .

We will also use the following simplifying assumption: no planetary rotation, the Boussinesq approximation, and the hydrostatic approximation.

Planetary rotation is neglected based on the observation that Venus requires 243 terrestrial days to rotate once on its axis. For this reason, Venus has always been considered the classical example of a nonrotating planet.

Ogura and Phillips (1962) have shown that the Boussinesq approximation is appropriate in situations where the vertical scale of the motion is less than the density scale height. Clearly, the deep atmosphere of Venus cannot be precisely simulated with an incompressible model. However, a Boussinesq model is attractive for two reasons. First, the Boussinesq equations take on a rather simple format. And second, previous experience has shown that a Boussinesq model provides a qualitatively good first approximation to the more complicated problem of compressible fluid flow (e.g., Kalnay de Rivas, 1973). By using the Boussinesq

approximation, we neglect density variations except when associated with bouyancy forces. For convenience and simplicity we will consider a neutrally stratified basic state and we will replace density fluctuations with potential temperature fluctuations according to the equation of state for a Boussinesq fluid, i.e.,

$$\frac{\rho}{\rho_0} = \frac{T}{T_0} = \frac{\theta}{\theta_0}$$

where  $\rho$ ,  $T$ , and  $\theta$  are the deviations of density, temperature, and potential temperature from their respective reference values  $\rho_0$ ,  $T_0$ ,  $\theta_0$ . The upward heat flux at the bottom is assumed to be a result of turbulent processes and therefore related to the gradient of potential temperature. Finally, within the context of the Boussinesq approximation we will use constant values for the coefficients of eddy viscosity and thermal diffusivity.

The hydrostatic approximation is used since we are considering only the largest horizontal scales of motion in a fluid layer with small aspect ratio.

With this, we begin by writing the equations in dimensional form (an asterisk indicating a dimensional quantity):

horizontal momentum equations

$$\frac{\partial u^*}{\partial t^*} + \frac{\partial u^* u^*}{\partial x^*} + \frac{\partial v^* u^*}{\partial y^*} + \frac{\partial w^* u^*}{\partial z^*} = -\frac{1}{\rho_0} \frac{\partial p^*}{\partial x^*} + \nu \frac{\partial^2 u^*}{\partial z^{*2}} \quad (2.2.1)$$

$$+ \nu_H \left[ \frac{\partial^2 u^*}{\partial x^{*2}} + \frac{\partial^2 v^*}{\partial y^{*2}} \right]$$

$$\frac{\partial v^*}{\partial t^*} + \frac{\partial u^* v^*}{\partial x^*} + \frac{\partial v^* v^*}{\partial y^*} + \frac{\partial w^* v^*}{\partial z^*} = -\frac{1}{\rho_0} \frac{\partial p^*}{\partial y^*} + \nu \frac{\partial^2 v^*}{\partial z^{*2}} \quad (2.2.2)$$

$$+ \nu_H \left[ \frac{\partial^2 v^*}{\partial x^{*2}} + \frac{\partial^2 v^*}{\partial y^{*2}} \right]$$

continuity equation

$$\frac{\partial u^*}{\partial x^*} + \frac{\partial v^*}{\partial y^*} + \frac{\partial w^*}{\partial z^*} = 0 \quad (2.2.3)$$

thermodynamic equation

$$\frac{\partial \theta^*}{\partial t^*} + \frac{\partial u^* \theta^*}{\partial x^*} + \frac{\partial v^* \theta^*}{\partial y^*} + \frac{\partial w^* \theta^*}{\partial z^*} \quad (2.2.4)$$

$$= K_H \left[ \frac{\partial^2 \theta^*}{\partial x^{*2}} + \frac{\partial^2 \theta^*}{\partial y^{*2}} \right] + K_V \frac{\partial^2 \theta^*}{\partial z^{*2}}$$

hydrostatic equation

$$\frac{\partial p^*}{\partial z^*} = \frac{\theta^*}{T_0} \rho_0 g \quad (2.2.5)$$

where  $u^*$ ,  $v^*$ ,  $w^*$  are the velocity components in the  $x^*$ ,  $y^*$ ,  $z^*$  directions respectively, and  $\theta^*$  and  $p^*$  are the departures of potential temperature and pressure from the constant reference values  $T_0$  and  $p_0$  respectively. There is no

internal heating term in the thermodynamic equation since the thermal forcing will be supplied through the boundary conditions.

We next proceed to put the equations into dimensionless form and thereby develop the dimensionless parameters appropriate to the problem. The variables in the equations are scaled as follows (quantities without an asterisk are dimensionless):

$$\begin{aligned} (x, y) &= k (x^*, y^*) & w &= \frac{w^*}{k h u_0} \\ z &= \frac{z^*}{h} & \theta &= \frac{\theta^*}{\Delta T} \\ t &= \Omega t^* & p &= \frac{p^*}{\Delta p} \\ (u, v) &= \frac{1}{u_0} (u^*, v^*) \end{aligned}$$

where  $u_0$ ,  $k$ ,  $\Omega (= k u_0)$  are the speed, wavenumber ( $= 2\pi (\text{wavelength})^{-1}$ ), and frequency of the moving heat source, and  $h$  is the depth of the fluid. The scale for the vertical velocity is naturally suggested by the continuity equation. The pressure scale,  $\Delta p$ , is suggested by the hydrostatic equation, i.e.,

$$\Delta p = \rho_0 g h \frac{\Delta T}{T_0}$$

The temperature scale,  $\Delta T$ , will be determined from the magnitude of the heating in section 2.3 where the boundary conditions are discussed. Upon performing the appropriate substitutions and divisions in equations (2.2.1) - (2.2.5), we obtain the following set of dimensionless equations:

$$\frac{\partial u}{\partial t} + \frac{\partial uv}{\partial x} + \frac{\partial wv}{\partial y} + \frac{\partial wu}{\partial z} = -G \frac{\partial p}{\partial x} + \frac{1}{2\gamma^2} \left[ \frac{\partial^2 u}{\partial z^2} + \epsilon_v \left( \frac{\partial^2 u}{\partial x^2} + \frac{\partial^2 u}{\partial y^2} \right) \right] \quad (2.2.1a)$$

$$\frac{\partial v}{\partial t} + \frac{\partial uv}{\partial x} + \frac{\partial vv}{\partial y} + \frac{\partial wv}{\partial z} = -G \frac{\partial p}{\partial y} + \frac{1}{2\gamma^2} \left[ \frac{\partial^2 v}{\partial z^2} + \epsilon_v \left( \frac{\partial^2 v}{\partial x^2} + \frac{\partial^2 v}{\partial y^2} \right) \right] \quad (2.2.2a)$$

$$\frac{\partial u}{\partial x} + \frac{\partial v}{\partial y} + \frac{\partial w}{\partial z} = 0 \quad (2.2.3a)$$

$$\frac{\partial \theta}{\partial t} + \frac{\partial u\theta}{\partial x} + \frac{\partial v\theta}{\partial y} + \frac{\partial w\theta}{\partial z} = \frac{1}{2\gamma^2} \left[ \frac{\partial^2 \theta}{\partial z^2} + \epsilon_x \left( \frac{\partial^2 \theta}{\partial x^2} + \frac{\partial^2 \theta}{\partial y^2} \right) \right] \quad (2.2.4a)$$

$$\frac{\partial p}{\partial z} = 0 \quad (2.2.5a)$$

where  $\epsilon_v = (kh)^2 \frac{\nu_H}{\nu_v}$ ,  $\epsilon_x = (kh)^2 \frac{\kappa_H}{\kappa_v}$

and the three dimensionless parameters appearing on the right-hand sides of the momentum and thermodynamic equations are given by



$$G = \frac{gh}{u_0^2} \frac{\Delta T}{T_0}, \quad 2\eta^2 = \frac{\Omega h^2}{\kappa_v}, \quad 2\gamma^2 = \frac{\Omega h^2}{\nu}$$

which are the three parameters that formed the basis of our discussion of the moving flame effect in Chapter 1. The thermal forcing parameter,  $G$ , is the ratio of buoyancy forces to inertial forces. Some authors have considered  $G$  to be two separate parameters - an inverse Froude number,  $\Lambda = gh/u_0^2$  times a thermal forcing parameter,  $\frac{\Delta T}{T_0}$ . The thermal frequency parameter,  $2\eta^2$ , represents the ratio of the vertical heat diffusion time scale to the period of the heat source; the viscous frequency is similar except it contains momentum diffusion in place of thermal diffusion. The Prandtl number,  $Pr = \frac{\nu}{\kappa_v}$ , is simply the ratio of the thermal and viscous frequencies,  $Pr = 2\eta^2/2\gamma^2$ .

We continue by expanding each of the five dependent variables into a zonal (and temporal) mean part plus a perturbation which is a function of time and of all three space variables, so for example  $u(x,y,z,t) = \bar{u}(y,z) + u'(x,y,z,t)$ . The equations for the mean variables can be obtained by making the appropriate substitutions in equations (2.2.2a) - (2.2.5a) and then averaging over  $x$  and  $t$ . Upon noting that the zonal average of a perturbation is zero, we find that

$$\frac{\partial \bar{v}\bar{u}}{\partial y} + \frac{\partial \bar{w}\bar{u}}{\partial z} + \frac{\partial \overline{v'u'}}{\partial y} + \frac{\partial \overline{w'u'}}{\partial z} = \frac{1}{2\gamma^2} \left[ \frac{\partial^2 \bar{u}}{\partial z^2} + \epsilon_v \frac{\partial^2 \bar{u}}{\partial y^2} \right] \quad (2.2.6)$$

$$\frac{\partial \bar{v}\bar{v}}{\partial y} + \frac{\partial \bar{w}\bar{v}}{\partial z} + \frac{\partial \overline{v'v'}}{\partial y} + \frac{\partial \overline{w'v'}}{\partial z} = \frac{1}{2\gamma^2} \left[ \frac{\partial^2 \bar{v}}{\partial z^2} + \epsilon_v \frac{\partial^2 \bar{v}}{\partial y^2} \right] - G \frac{\partial \bar{v}}{\partial y} \quad (2.2.7)$$

$$\frac{\partial \bar{v}}{\partial y} + \frac{\partial \bar{w}}{\partial z} = 0 \quad (2.2.8)$$

$$\frac{\partial \bar{v}\bar{\theta}}{\partial y} + \frac{\partial \bar{w}\bar{\theta}}{\partial z} + \frac{\partial \overline{v'\theta'}}{\partial y} + \frac{\partial \overline{w'\theta'}}{\partial z} = \frac{1}{2\gamma^2} \left[ \frac{\partial^2 \bar{\theta}}{\partial z^2} + \epsilon_v \frac{\partial^2 \bar{\theta}}{\partial y^2} \right] \quad (2.2.9)$$

$$(2.2.10)$$

where the terms that are an average of the correlation of two perturbations are called Reynolds stresses and they represent the transport of momentum and heat by the eddies. If equations (2.2.6) - (2.2.10) are subtracted from the expanded equations (2.2.1a) - (2.2.5a), we obtain the following for the perturbations:

$$\begin{aligned} & \frac{\partial u'}{\partial t} + \frac{\partial \bar{u}u'}{\partial x} + \frac{\partial \bar{v}u'}{\partial y} + \frac{\partial \bar{w}u'}{\partial z} + \frac{\partial u'\bar{u}}{\partial x} + \frac{\partial v'u'}{\partial y} + \frac{\partial w'u'}{\partial z} \\ & + \frac{\partial (u'u')'}{\partial x} + \frac{\partial (v'u')'}{\partial y} + \frac{\partial (w'u')'}{\partial z} \\ & = -G \frac{\partial p'}{\partial x} + \frac{1}{2\gamma^2} \left[ \frac{\partial^2 u'}{\partial z^2} + \epsilon_v \left( \frac{\partial^2 u'}{\partial x^2} + \frac{\partial^2 u'}{\partial y^2} \right) \right] \end{aligned} \quad (2.2.11)$$

$$\begin{aligned} & \frac{\partial v'}{\partial t} + \frac{\partial \bar{u}v'}{\partial x} + \frac{\partial \bar{v}v'}{\partial y} + \frac{\partial \bar{w}v'}{\partial z} + \frac{\partial u'v'}{\partial x} + \frac{\partial v'v'}{\partial y} + \frac{\partial w'v'}{\partial z} \\ & + \frac{\partial (u'v')'}{\partial x} + \frac{\partial (v'v')'}{\partial y} + \frac{\partial (w'v')'}{\partial z} \\ & = -G \frac{\partial p'}{\partial y} + \frac{1}{2\gamma^2} \left[ \frac{\partial^2 v'}{\partial z^2} + \epsilon_v \left( \frac{\partial^2 v'}{\partial x^2} + \frac{\partial^2 v'}{\partial y^2} \right) \right] \end{aligned} \quad (2.2.12)$$

$$\frac{\partial u'}{\partial x} + \frac{\partial v'}{\partial y} + \frac{\partial w'}{\partial z} = 0 \quad (2.2.13)$$

$$\begin{aligned} \frac{\partial \theta'}{\partial t} + \frac{\partial \bar{u} \theta'}{\partial x} + \frac{\partial \bar{v} \theta'}{\partial y} + \frac{\partial \bar{w} \theta'}{\partial z} + \frac{\partial u' \bar{\theta}}{\partial x} + \frac{\partial v' \bar{\theta}}{\partial y} + \frac{\partial w' \bar{\theta}}{\partial z} \\ + \frac{\partial (u' \theta')'}{\partial x} + \frac{\partial (v' \theta')'}{\partial y} + \frac{\partial (w' \theta')'}{\partial z} \\ = \frac{1}{2\eta^2} \left[ \frac{\partial^2 \theta'}{\partial z^2} + \epsilon_x \left( \frac{\partial^2 \theta'}{\partial x^2} + \frac{\partial^2 \theta'}{\partial y^2} \right) \right] \end{aligned} \quad (2.2.14)$$

$$\frac{\partial \theta'}{\partial z} = \theta' \quad (2.2.15)$$

We now apply our linearization process (i.e., neglecting terms nonlinear in the perturbations) to (2.2.7) - (2.2.10) to obtain the equations for the steady state MMC

$$\bar{v} \frac{\partial \bar{\theta}}{\partial y} + \bar{w} \frac{\partial \bar{\theta}}{\partial z} = \frac{1}{2\eta^2} \left[ \frac{\partial^2 \bar{\theta}}{\partial z^2} + \epsilon_x \frac{\partial^2 \bar{\theta}}{\partial y^2} \right] \quad (2.2.16)$$

$$\frac{\partial \bar{p}}{\partial z} = \bar{\theta} \quad (2.2.17)$$

$$\bar{v} \frac{\partial \bar{v}}{\partial y} + \bar{w} \frac{\partial \bar{v}}{\partial z} = -G \frac{\partial \bar{p}}{\partial y} + \frac{1}{2\nu^2} \left[ \frac{\partial^2 \bar{v}}{\partial z^2} + \epsilon_y \frac{\partial^2 \bar{v}}{\partial y^2} \right] \quad (2.2.18)$$

$$\frac{\partial \bar{v}}{\partial y} + \frac{\partial \bar{w}}{\partial z} = 0$$

(2.2.19)

in which the advective flux terms (e.g.,  $\frac{\partial \bar{v} \bar{v}}{\partial y}$ ) have been expanded with the aid of the continuity equation. The method of solution of these equations will be described in detail in section 2.4.

The next step is to expand each of the eddy variables as a truncated Fourier series of the phase  $(x-t)$ , so for example

$$u' = \sum_{m=1}^M \left[ U(y,z) e^{im(x-t)} + \tilde{U}(y,z) e^{-im(x-t)} \right]$$

where  $U(y,z)$  is the complex amplitude and  $\tilde{U}$  represent the complex conjugate of  $U$ . If we pick the truncation value  $M = 1$ , then we retrieve the mean field equations for the eddies in which terms that are nonlinear in the perturbations drop out. Therefore forced solutions for the waves will exist in the form

$$\begin{bmatrix} u' \\ v' \\ w' \\ \theta' \\ p' \end{bmatrix} = \begin{bmatrix} U \\ V \\ W \\ T \\ P \end{bmatrix} e^{im(x-t)} + \begin{bmatrix} \tilde{U} \\ \tilde{V} \\ \tilde{W} \\ \tilde{T} \\ \tilde{P} \end{bmatrix} e^{-im(x-t)}$$

Thus we have the simple relationships

$$\frac{\partial(\cdot)'}{\partial x} = i(\cdot)' \quad , \quad \frac{\partial(\cdot)'}{\partial t} = -i(\cdot)'$$

and the perturbation equations (2.2.11) - (2.2.15) can now be written in their "linearized" form

$$\begin{aligned} i(\bar{u}-1)U + \bar{v} \frac{\partial U}{\partial y} + \bar{w} \frac{\partial U}{\partial z} + W \frac{\partial \bar{u}}{\partial z} + V \frac{\partial \bar{u}}{\partial y} \\ = -iGP + \frac{1}{2\gamma^2} \left[ \frac{\partial^2 U}{\partial z^2} + \epsilon_v \left( \frac{\partial^2 U}{\partial y^2} - U \right) \right] \end{aligned} \quad (2.2.20)$$

$$\begin{aligned} i(\bar{u}-1)V + \bar{v} \frac{\partial V}{\partial y} + \bar{w} \frac{\partial V}{\partial z} + W \frac{\partial \bar{v}}{\partial z} + V \frac{\partial \bar{v}}{\partial y} \\ = -G \frac{\partial P}{\partial y} + \frac{1}{2\gamma^2} \left[ \frac{\partial^2 V}{\partial z^2} + \epsilon_v \left( \frac{\partial^2 V}{\partial y^2} - V \right) \right] \end{aligned} \quad (2.2.21)$$

$$iU + \frac{\partial V}{\partial y} + \frac{\partial W}{\partial z} = 0 \quad (2.2.22)$$

$$\begin{aligned} i(\bar{u}-1)T + \bar{v} \frac{\partial T}{\partial y} + \bar{w} \frac{\partial T}{\partial z} + V \frac{\partial \bar{\theta}}{\partial y} + W \frac{\partial \bar{\theta}}{\partial z} \\ = \frac{1}{2\gamma^2} \left[ \frac{\partial^2 T}{\partial z^2} + \epsilon_v \left( \frac{\partial^2 T}{\partial y^2} - T \right) \right] \end{aligned} \quad (2.2.23)$$

$$\frac{\partial P}{\partial z} = T \quad (2.2.24)$$

These equations along with the necessary boundary conditions (see section 2.3) will be solved in section 2.5 (note that the advective flux <sup>terms</sup> ~~times~~ have been expanded).

The eddies as determined by (2.2.20) - (2.2.24) can now be used to compute the Reynolds stresses  $\overline{u'v'}$  and  $\overline{u'w'}$  that appear in equation (2.2.6) for the mean zonal velocity  $\bar{u}$ . The assumed harmonic form for the eddies allows us to determine the Reynolds stresses directly from the complex amplitudes according to the relationships

$$\overline{u'v'} = 2 \operatorname{Re} (U\check{V}) , \quad \overline{u'w'} = 2 \operatorname{Re} (U\check{W})$$

where  $\operatorname{Re}$  indicates the real part of a complex quantity. Thus our set of model equations is completed by the following equation for  $\bar{u}$

$$\begin{aligned} \bar{v} \frac{\partial \bar{u}}{\partial y} + \bar{w} \frac{\partial \bar{u}}{\partial z} + 2 \operatorname{Re} \left[ \frac{\partial U\check{V}}{\partial y} + \frac{\partial U\check{W}}{\partial z} \right] \\ = \frac{1}{2r^2} \left[ \frac{\partial^2 \bar{u}}{\partial z^2} + \epsilon_v \frac{\partial^2 \bar{u}}{\partial y^2} \right] \end{aligned} \quad (2.2.25)$$

To summarize our procedure, we first solve for the steady state MMC (section 2.4) as determined by equations (2.2.16) - (2.2.19) and the necessary boundary conditions which include the thermal forcing. We then solve the linearized equations (2.2.20) - (2.2.24) for the large scale eddies

and equation (2.2.25) for the mean zonal velocity (section 2.5). Once again, our linearization consists of neglecting wave-wave interaction terms in the MMC equations as well as in the eddy equations. The former part of this linearization essentially means that we are specifying a fixed MMC which is unaffected by the presence of planetary waves. This assumption will be verified a posteriori by comparing eddy fluxes and MMC advection (Figure 2.19). The latter part of the linearization is simply a consequence of the low zonal resolution. In all other respects, the equations are nonlinear.

### 2.3 Boundary Conditions

To complete our model, we must specify thermal and dynamical boundary conditions at the horizontal and vertical boundaries of the channel. We first consider the boundary conditions for the thermodynamic equation since therein will be the only source of thermal forcing for the model. It will be assumed that the moving periodic heat source supplies heating at the lower boundary in the form of a heat flux. The top is taken to be an insulating surface. This type of thermal forcing at the bottom is quite obviously relevant to the laboratory studies. For Venus, we must present additional justification. Because of the rather deep extent of the atmosphere of Venus, our model is designed and limited to simulating the region of the atmosphere that includes

the cloud tops (our lower boundary and sunlight absorbing surface) and the adjacent layer of the stratosphere. By considering only heating from below, we are in effect assuming that the stratosphere is transparent to solar radiation and that a major portion of the unreflected sunlight is absorbed in the upper cloud layer. Many of the available observations confirm this hypothesis. Using earth based and Venera 8 measurements, Lacis (1975) found the maximum heating rate due to solar energy deposition to occur near the top of the visible cloud deck. More recently, an analysis of the Pioneer Venus LSFR (solar net flux radiometer) data reveals that the net solar flux decreases by roughly seventy percent in the <sup>layer</sup> from 47 to 65km (Tomasko et al., 1980). Finally, the presence of a statically unstable layer between 52 and 56km (Seiff et al., 1979), and the presence of a turbulent layer at 60km (Woo, 1975) tend to indicate strong absorption of sunlight at these altitudes.

In our model, the thermal forcing at the heated boundary can be transmitted to the fluid only through vertical diffusion. As mentioned above in section 2.2 we will assume that this heat transfer is accomplished by turbulent processes and therefore the heat flux is directly related to the vertical gradient of potential temperature. At and above the Venus cloud tops, radiative processes most likely account for a significant portion of the vertical heat flux. However,



it is not our intention to develop a highly complicated general circulation model for the Venus stratosphere. Our goal is to investigate only the role of a moving periodic heat source with both diurnal and meridional differential heating and the capability of such a heat source to force a retrograde mean zonal flow. Thus we ignore differences between the radiative and turbulent transport mechanisms, and for simplicity we choose the turbulent heat flux and eddy diffusion parameterization.

We can estimate the magnitude of the differential heat flux from observations of the thermal emissions from the Venus cloud tops. Apt et al., (1980) found horizontal variations in the thermal emissions that are typically 10% of the mean flux. This corresponds to a fluctuation<sup>ing</sup> amplitude of roughly  $10^4 \text{ erg cm}^{-2} \text{ s}^{-1}$  (or  $10 \text{ W m}^{-2}$ ). The relationship between the heat flux perturbation,  $F(x, y, t)$ , and the fluctuating potential temperature gradient is simply

$$F(x, y, t) = -\rho_0 c_p K_v \frac{\partial \theta^*}{\partial z^*} \quad (2.3.1)$$

(recall that an asterisk stands for a dimensional quantity). For diurnal variations, we will assume that  $F$  has the structure of a moving localized heat source analogous to the sun or a laboratory heat source (bunsen burner), i.e.,

$$F(x,y,t) = \begin{cases} F(y) \cos(x-t) & |x-t| \leq \frac{\pi}{2} \\ 0 & |x-t| > \frac{\pi}{2} \end{cases}$$

(2.3.2)

where  $(x-t)$  is the local time of day measured from zero at local noon (note that time has already been scaled by the period of the heat source,  $\Omega$ ). Finally, to introduce meridional differential heating that is of the same magnitude as the diurnal heating we simply assume that  $F(y)$  varies as the cosine of latitude. Combining (2.3.1), (2.3.2) and the assumed latitudinal variation provides the lower boundary condition for our model

$$\frac{\partial \theta^*}{\partial z^*} = \begin{cases} -Q^* \cos(x-t) \cos y & |x-t| \leq \frac{\pi}{2} \\ 0 & |x-t| > \frac{\pi}{2} \end{cases} \quad (2.3.3)$$

where the amplitude  $Q^*$  is given by

$$Q^* = \frac{F_0}{\rho_0 c_p \kappa_v}$$

and  $F_0$  is the magnitude of the observed flux variations.

If we nondimensionalize (2.3.3) using  $h$  as a scale for  $z^*$ ,  $\Delta T$

as a scale for  $\theta^*$  and if we assume that the dimensionless boundary condition is  $O(1)$ , we obtain

$$\frac{\partial \theta}{\partial z} = \begin{cases} -\cos(x-t) \cos y & |x-t| \leq \frac{\pi}{2} \\ 0 & |x-t| > \frac{\pi}{2} \end{cases} \quad (2.3.4)$$

as well as an estimate for the potential temperature scale

$$\Delta T \sim \frac{F_0 h}{\rho_0 c_p K_v}$$

which for the Venus values of the physical constants is roughly  $\Delta T \simeq 120^\circ \text{K}$ . We also note that because of the rectangular geometry of our model,  $y$  ranges from 0 to  $\pi$ . This means that the heating from  $y = 0$  to  $y = \pi/2$  is balanced by an equal amount of cooling between  $y = \pi/2$  and  $y = \pi$  and thus the global mean potential temperature fluctuation,  $\langle \theta \rangle = 0$ , will be preserved.

In all cases, we assume there is no heat flux across the top so that  $\frac{\partial \theta}{\partial z} = 0$ . Finally, a zonal Fourier analysis of (2.3.4) (see Appendix A) provides the necessary mean and eddy boundary conditions

$$\frac{\partial \bar{\theta}}{\partial z} = \begin{cases} -\frac{1}{\pi} \cos y & \text{at } z=0 \\ 0 & \text{at } z=1 \end{cases} \quad (2.3.5a)$$

$$\frac{\partial \tau}{\partial z} = \begin{cases} -\frac{1}{4} \cos y & \text{at } z=0 \\ 0 & \text{at } z=1 \end{cases} \quad (2.3.5b)$$

where  $T(y, z)$  is the complex amplitude of  $\theta' = T(y, z)e^{i(\kappa x - t)} + \tilde{T}e^{-i(\kappa x - t)}$  and  $\tilde{T}(y, z)$  is the complex conjugate of  $T$ .

The dynamical boundary conditions required for modeling only a relatively thin layer of the upper atmosphere are not quite as easy to determine. Ideally, one would prefer to impose boundary conditions only where real physical boundaries exist (i.e., at the planet's surface). Unfortunately, within the context of our Boussinesq model, we cannot accurately treat a very deep atmosphere, such as the one on Venus, and thus it becomes necessary to impose artificial horizontal boundaries which hopefully have some physical relevance to the real situation. We will concentrate on the results obtained using the free-rigid boundary conditions where the bottom is a rigid, no slip surface and the top is a flat, stress free surface so that

$$\bar{u} = \bar{v} = \bar{w} = u' = v' = w' = 0 \quad \text{at } z = 0$$

$$\frac{\partial \bar{u}}{\partial z} = \frac{\partial \bar{v}}{\partial z} = \bar{w} = \frac{\partial u'}{\partial z} = \frac{\partial v'}{\partial z} = w' = 0 \quad \text{at } z = 1$$

(2.3.6)

These boundary conditions are immediately applicable to a laboratory experiment but require some justification for Venus. The best argument that we can present is based on observations. Recent data collected by the Pioneer Venus probes indicate the presence of a zone of strong wind shear in the upper and middle cloud layers so that the winds at the base of the middle cloud layer (52km) are weaker than the winds above by a factor of at least two or three (Counselman et al., 1979). By assuming a no-slip bottom, we are confining the entire wind shear to the region at and above the cloud tops. Furthermore, the use of a rigid, no-slip bottom will effectively eliminate any interactions that might occur between the stratosphere and the troposphere (e.g., vertically propagating waves) and thus we can be confident that the circulation that develops in the model will be a result of only the moving flame type thermal forcing. This isolation of the stratosphere can also

partially justified by the apparent natural separation of the Venus atmosphere into two distinct dynamical regimes (Stone, 1975). The assumed periodicity of the forcing and the resulting flow implicitly includes boundary conditions at the imaginary vertical walls (i.e., at  $x = 0, 2\pi$  and at  $y = 0, \pi$ ). All of the eddy variables are periodic in  $x$  with period  $2\pi$ . Since the forcing is symmetric about the points  $y = 0$  and  $\pi$ , the potential temperature, zonal velocity and vertical velocity will all preserve symmetry while the meridional velocity will be antisymmetric. Thus we have the conditions

$$\bar{v} = v' = \frac{\partial \bar{\theta}}{\partial y} = \frac{\partial \theta'}{\partial y} = \frac{\partial \bar{u}}{\partial y} = \frac{\partial u'}{\partial y} = \frac{\partial \bar{w}}{\partial y} = \frac{\partial w'}{\partial y} = 0 \quad \text{at } y = 0, \pi .$$

We conclude this section by once again mentioning that our model is designed to simulate only one very specific physical process (i.e., the moving flame) and is not intended to be a general circulation model for Venus. It would appear that our model more closely resembles a laboratory experiment than the stratosphere of Venus. Or, we can even view our model as simulating a thin transparent atmosphere lying over a deep quiescent ocean that absorbs solar radiation in a thin layer near its surface. The only interaction between the atmosphere and this ocean is the upward turbulent heat flux that drives the atmospheric circulation. While this <sup>e</sup>description may not exactly simulate the relationship between the stratosphere and troposphere

of Venus, we have nevertheless presented some justifications for the relevance and applicability of our model as at least a first approximation to the dynamical state of the upper atmosphere of Venus.

## 2.4. Steady State Mean Meridional Circulation

### 2.4.1 Method of Solution

Having described the necessary equations and boundary conditions, we are now ready to proceed with obtaining the solutions. The first step we take is to determine the steady state mean meridional circulation (MMC) that is driven by a latitudinal heating contrast. Equations (2.2.16) - (2.2.19) along with boundary conditions (2.3.4) and the appropriate parts of (2.3.7) comprise this part of the problem. We begin by expanding each of the dependent mean variables in a series of orthogonal functions of  $y$ . The rectangular coordinate system allows us to use complex Fourier series and thus the variables can be written in the form

$$\begin{bmatrix} \bar{\theta}(y, z) \\ \bar{p} \\ \bar{v} \\ \bar{w} \end{bmatrix} = \sum_{n=-N}^N \begin{bmatrix} \bar{\theta}_n(z) \\ \bar{p}_n \\ \bar{v}_n \\ \bar{w}_n \end{bmatrix} e^{iny}$$

Substitution of these expansions into (2.2.16) - (2.2.14) reduces the equations to a system of ordinary differential equations in  $z$  for the harmonic coefficients  $\bar{\theta}_n, \bar{p}_n, \bar{v}_n, \bar{w}_n$ . The nonlinear terms can be simply computed as follows: given any two functions, say  $p(y)$  and  $q(y)$ , that can be expanded in Fourier series

$$p(y) = \sum_{n_1=-N}^N \bar{p}_{n_1} e^{in_1 y}, \quad q(y) = \sum_{n_2=-N}^N \bar{q}_{n_2} e^{in_2 y}$$

then their product can also be written as a Fourier series

$$r(y) = p(y) q(y) = \sum_{n=-2N}^{2N} r_n e^{iny}$$

where the coefficients  $r_n$  are given by the formula

$$r_n = \sum_{l=n-N}^N \bar{p}_l \bar{q}_{n-l} .$$

Strictly speaking, the summation limit should be  $N = \infty$ , however, since we are interested in the largest scales of



motion we will truncate our series at  $N = 2$ . The choice of this value limits the number of equations and computations yet it still allows simulation of the first order effects of nonlinear distortion. By nonlinear distortion we mean that the MMC need not be symmetric about the line  $y = \frac{\pi}{2}$ . In a completely linear system (i.e., no advection terms in the equations) the MMC must be symmetric about  $y = \frac{\pi}{2}$ . We also note here that our approach is equivalent to the first order asymptotic solutions obtained by Stone (1968). In both methods, the horizontal resolution is exactly the same and the results are quite similar as we will shortly see.

Equations (2.2.16) - (2.2.19) can now be written in spectral form:

$$\sum_{n_1=n-N}^N [i(n-n_1)\bar{v}_{n_1}\bar{\theta}_{n-n_1} + \bar{w}_{n_1}\frac{\partial\bar{\theta}_{n-n_1}}{\partial z}] = \frac{1}{2\eta^2} \left[ \frac{\partial^2\bar{\theta}_n}{\partial z^2} - \epsilon_K n^2 \bar{\theta}_n \right] \quad (2.4.1)$$

$$\frac{\partial\bar{p}_n}{\partial z} = \bar{\theta}_n \quad (2.4.2)$$

$$\sum_{n_1=n-N}^N [i(n-n_1) \bar{v}_n \bar{v}_{n-n_1} + \bar{w}_n \frac{\partial \bar{v}_{n-n_1}}{\partial \bar{z}}] = -inG\bar{P}_n + \frac{1}{2\gamma^2} \left[ \frac{\partial^2 \bar{v}_n}{\partial \bar{z}^2} - \epsilon_\nu n^2 \bar{v}_n \right] \quad (2.4.3)$$

$$in \bar{v}_n + \frac{\partial \bar{w}_n}{\partial \bar{z}} = 0 \quad (2.4.4)$$

and the boundary conditions are

$$\frac{\partial \bar{\theta}_n}{\partial \bar{z}} = \begin{cases} \left. \begin{array}{l} -\frac{1}{2\pi} \\ 0 \end{array} \right\} & \begin{array}{l} n = \pm 1 \\ n \neq \pm 1 \end{array} \text{ at } z=0 \\ 0 & \text{for all } n \text{ at } z=1 \end{cases}$$

$$\bar{v}_n = \bar{w}_n = 0 \quad \text{at } z=0$$

$$\frac{\partial \bar{v}_n}{\partial \bar{z}} = \bar{w}_n = 0 \quad \text{at } z=1 \quad (2.4.5)$$

Even after replacing the  $y$  derivatives with algebraic expressions, we are still left with a quite complicated set of

nonlinear ordinary differential equations in  $z$  for the spectral coefficients. We choose to solve the equations numerically since a numerical model has two major advantages.

First, it produces solutions that are valid for any parameter values (unlike asymptotic or limit solutions which are valid only for extreme values of the parameters). Second, it allows one to quite easily conduct various experiments such as varying parameter values and changing boundary conditions.

To implement the numerical method, we will use an iteration technique in which we introduce a new independent variable,

$\tau$  (the iteration variable which is equivalent to time) and we add the operators  $\frac{\partial \bar{\theta}_n}{\partial \tau}$  and  $\frac{\partial \bar{v}_n}{\partial \tau}$  to the left hand side of equations (2.4.1) and (2.4.3) respectively. The model equations can then be treated as a time marching problem with the "prognostic" variables  $\bar{\theta}_n$ ,  $\bar{v}_n$  and the diagnostic variables  $\bar{p}_n$  and  $\bar{w}_n$ . The time derivatives are approximated by centered differences (the so called leapfrog scheme) so for example we have

$$\begin{aligned} \frac{\partial \bar{\theta}}{\partial \tau} &\approx \frac{\bar{\theta}(\tau + \Delta\tau) - \bar{\theta}(\tau - \Delta\tau)}{2 \Delta\tau} \\ &= -ADV(\tau) + DIFF(\tau - \Delta\tau) \end{aligned}$$

(2.4.6)

where  $ADV(\tau)$  represents the advection terms computed at time  $\tau$  and  $DIFF(\tau - \Delta\tau)$  represents the diffusion terms computed at time  $(\tau - \Delta\tau)$ . By computing the diffusion terms at the backward time step, we avoid the absolute computational instability that is associated with the leap frog solution of the so-called heat<sup>t</sup> or diffusion equation of the form

$$\frac{\partial \bar{\theta}}{\partial \tau} = \frac{\partial^2 \bar{\theta}}{\partial z^2}$$

Every so often, a forward time of the form

$$\frac{\partial \bar{\theta}}{\partial \tau} \approx \frac{\bar{\theta}(\tau + \Delta\tau) - \bar{\theta}(\tau)}{\Delta\tau} \quad (2.4.7)$$

is used. This helps to eliminate the uncoupling of solutions at odd and even time steps which tends to occur when using a leap frog scheme.

The vertical derivatives are also approximated by finite differences. To improve the resolution near the boundaries without drastically increasing the number of levels, we make use of a stretched vertical coordinate and its associated continuously varying grid as suggested by Kálnay de Rivas (1972). Given the appropriate choice of a stretching function, this method can produce a grid with very fine spacing in any desired region of the domain and a coarser spacing elsewhere. This can be especially useful

if one expects the presence of various localized phenomena such as boundary layers. In practice, the stretching is accomplished by defining a function, say  $f$ , which maps the physical space  $z$  into the stretched space  $\xi$  (where a regular grid is used) according to the relationship  $\xi = f(z)$ . The first and second derivatives of any quantity,  $q$ , in the two coordinate systems ( $z$  and  $\xi$ ) are related by

$$\frac{\partial q}{\partial z} = \frac{d\xi}{dz} \frac{\partial q}{\partial \xi}$$

$$\frac{\partial^2 q}{\partial z^2} = \frac{d\xi}{dz} \frac{\partial}{\partial \xi} \left( \frac{d\xi}{dz} \frac{\partial q}{\partial \xi} \right)$$

Kálnay de Rivas (1972) showed that the second order finite difference approximations of these derivatives are given by

$$\frac{\partial q}{\partial z} = \frac{1}{\left(\frac{dz}{d\xi}\right)} \frac{\partial q}{\partial \xi} \approx \frac{q_{j+1} - q_{j-1}}{2\Delta\xi S_j} + O(\Delta\xi^2)$$

$$\begin{aligned} \frac{\partial^2 q}{\partial z^2} &= \frac{1}{\left(\frac{dz}{d\xi}\right)} \frac{\partial}{\partial \xi} \left( \frac{1}{\left(\frac{dz}{d\xi}\right)} \frac{\partial q}{\partial \xi} \right) \\ &\approx \frac{\frac{q_{j+1} - q_j}{S_{j+\frac{1}{2}}} - \frac{q_j - q_{j-1}}{S_{j-\frac{1}{2}}}}{S_j \Delta\xi^2} + O(\Delta\xi^2) \end{aligned}$$

where we have defined  $S = \frac{dz}{d\xi}$ . The relative locations of the three points denoted by  $j - 1$ ,  $j$ , and  $j + 1$  are illustrated in Figure 2.2.

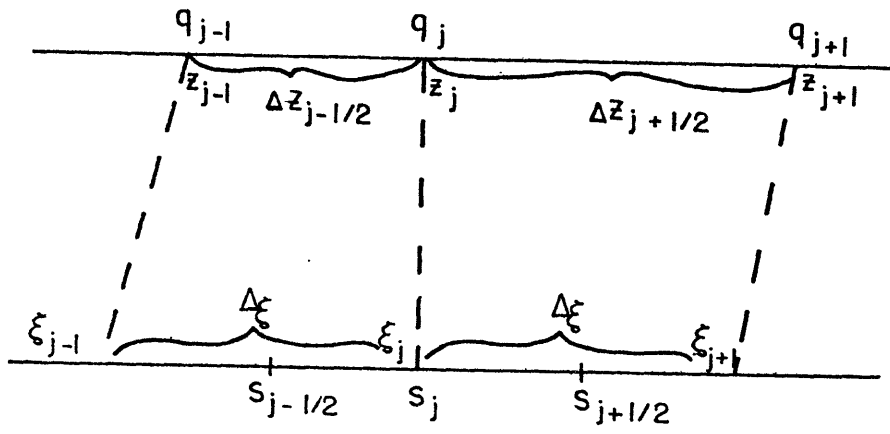


Figure 2.2: Variable grid in  $z$  as defined through the stretched coordinate  $\xi$ . Note regular spacing of the grid in  $\xi$  (from Kálnay de Rivas, 1972).

In our model, we will use the stretched coordinate defined by

$$z = \sin^2 \left( \frac{\pi}{2} \xi \right)$$

$$S = \frac{dz}{d\xi} = \frac{\pi}{2} \sin \left( \pi \xi \right)$$

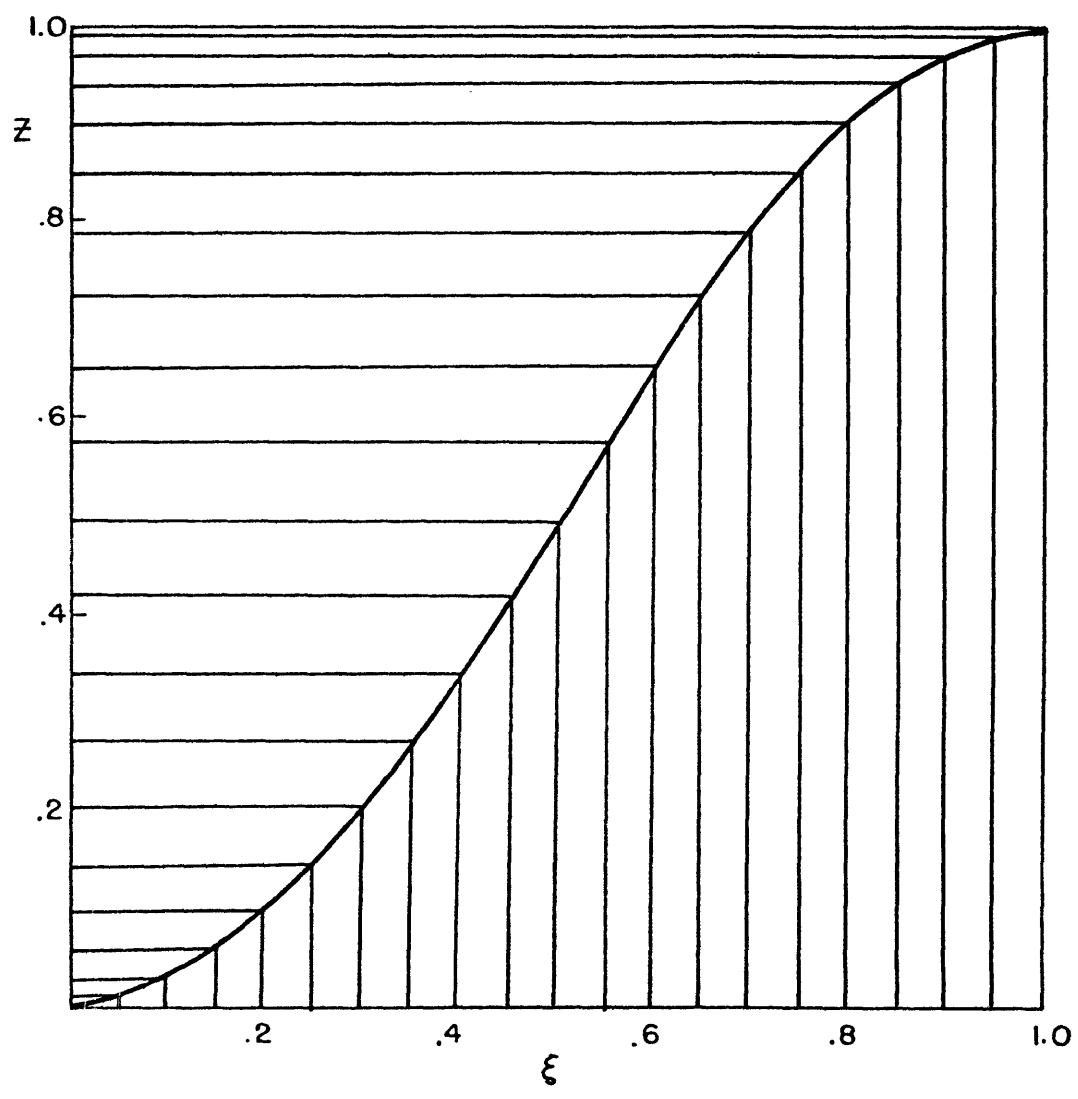


FIGURE 2.3 Physical height,  $z$ , defined by the function  $z = \sin^2(\frac{\xi}{2})$ . Note the regular spacing in  $\xi$ .

Table 2.1: Values of the normal probability density function  $f(z)$  and the cumulative distribution function  $F(z)$  for  $z = \frac{x - \mu}{\sigma}$  ( $\frac{z}{\sigma}$ ),  $\sigma = 10$ .

$z$	$f(z)$	$F(z)$	$S_z$
0	0.0000	0.5000	0
1	0.2420	0.7480	0.242
2	0.0540	0.9772	0.713
3	0.0044	0.9999	0.923
4	0.0001	0.9999	0.994
5	0.0000	0.9999	0.999
6	0.0000	0.9999	0.999
7	0.0000	0.9999	0.999
8	0.0000	0.9999	0.999
9	0.0000	0.9999	0.999
10	0.0000	0.9999	0.999
11	0.0000	0.9999	0.999



which is nearly linear in the interior and provides fine resolution near both the upper and lower boundaries. This behavior is shown clearly in Figure 2.3 and Table 2.1. To increase the computational efficiency, we use a staggered vertical grid (Figure 2.4) in which  $u$ ,  $v$ ,  $\theta$ , and  $p$  are carried at full levels and  $w$  is carried at the half levels. One additional grid level is defined outside of the physical boundaries to easily accommodate derivative boundary conditions.

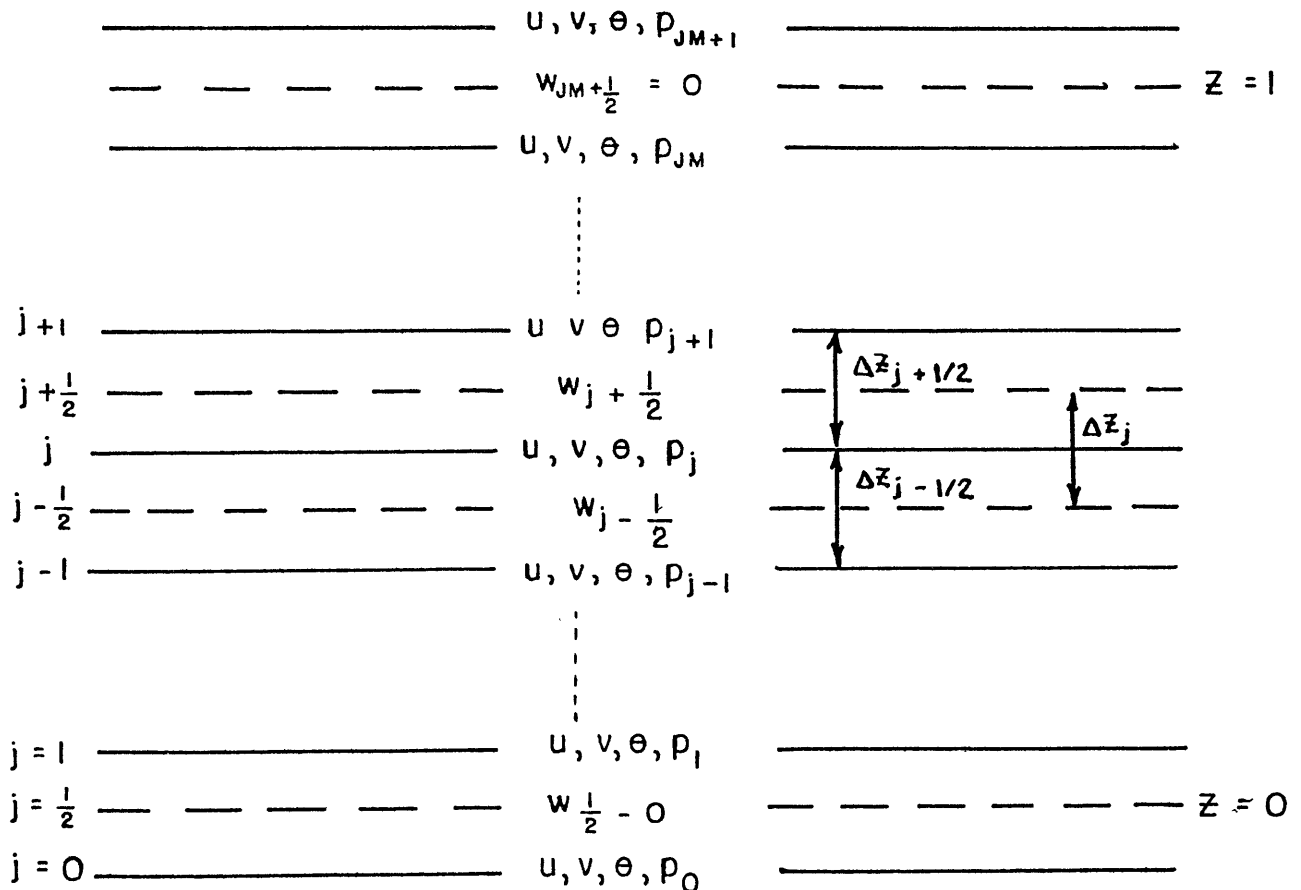


Figure 2.4: Staggered vertical grid

Using the staggered grid of Figure 2.4, we express a typical vertical advective term at level  $j$  as

$$\left[ w \frac{\partial q}{\partial z} \right]_j \approx \frac{1}{2} \left[ \frac{w_{j+\frac{1}{2}} (q_{j+1} - q_j)}{\Delta z_{j+\frac{1}{2}}} + \frac{w_{j-\frac{1}{2}} (q_j - q_{j-1})}{\Delta z_{j-\frac{1}{2}}} \right]$$

(2.4.8)

where  $q$  represents any one of the three prognostic variables  $u$ ,  $v$ ,  $\theta$ . This scheme has been widely used in numerical models because of its quadratic conserving properties (Arakawa and Lamb, 1977). The other advantage of the staggered grid is that (2.4.8), which consists of an average of the advective terms at two adjacent half levels, is second order accurate, i.e., the truncation error is proportional to  $(\Delta z)^2$ .

The procedure we follow is to first advance  $\bar{\theta}_n$  to the new time step. Using these values,  $\bar{p}_n$  is computed diagnostically from the hydrostatic equation (2.4.2). The values of  $\bar{p}_n$  will contain an arbitrary function of  $y$  since we have no boundary condition for the pressure (i.e., in solving the hydrostatic equation, we assume that the boundary value of  $\bar{p}_n$  is zero). This arbitrary function can be determined from mass continuity considerations as described below. We can now use this uncorrected pressure in equation (2.4.3) and determine the uncorrected values of  $\bar{v}_n^u$  at the new time step. The actual value of  $\bar{v}$  and the uncorrected value  $\bar{v}^u$

are related by the expression

$$\bar{v} = \bar{v}^u + \frac{dR}{dy}, \quad \bar{v}_n = \bar{v}_n^u + inR_n \quad (2.4.9)$$

where the arbitrary function  $R(y)$  is given by

$$R(y) = 2G\Delta z \bar{p}(z=1)$$

and  $\bar{p}(z=1)$  is the value of  $\bar{p}$  at the top of the model. From the continuity equation and the boundary conditions on  $\bar{w}$ , we know that

$$\int_0^1 \frac{\partial \bar{v}}{\partial y} dz = - \int_0^1 \frac{\partial \bar{w}}{\partial z} dz = \bar{w}(z=0) - \bar{w}(z=1) = 0$$

Substituting the expression  $\bar{v} = \bar{v}^u + \frac{dR}{dy}$  gives an equation for  $R(y)$

$$\frac{d^2 R}{dy^2} = - \int_0^1 \frac{\partial \bar{v}^u}{\partial y} dz \quad (2.4.10a)$$

or in terms of our harmonic coefficients (recall that

$$\frac{\partial \bar{v}}{\partial y} = \sum_n in \bar{v}_n \quad )$$

$$R_n = \frac{i}{n} \int_0^1 \bar{v}_n^u dz \quad (2.4.10b)$$

and finally, the correct values of  $\bar{v}_n$  are given by

$$\bar{v}_n = \bar{v}_n^u + inR_n$$

This procedure is the equivalent of having a prognostic equation for the "surface" (boundary) pressure. With the new values of  $\bar{v}$  we can now determine  $\bar{w}$ , diagnostically from the continuity equation (2.2.4). Finally, as a convenient tool for presenting the results, we can define a mean meridional streamfunction  $\bar{\psi}$  (based on the two-dimensional form of the mean continuity equation) such that

$$\bar{v} = -\frac{\partial \bar{\psi}}{\partial z} \quad , \quad \bar{w} = \frac{\partial \bar{\psi}}{\partial y}$$

In the numerical model,  $\bar{\psi}$  is defined at the same vertical grid points as  $\bar{w}$ . By using the boundary condition  $\bar{\psi} = 0$  at  $z = 0$  we can easily compute the harmonic coefficients  $\bar{\psi}_n$  from the relationship

$$\bar{\Psi}_n^{j+1} = \bar{\Psi}_n^j - \bar{v}_j S_j \Delta \zeta .$$

#### 2.4.2 Results

The results for the MMC presented in this section are given for the values  $2\eta^2 = 15.5$ ,  $Pr = \frac{1}{2}$ ,  $\epsilon_v = \epsilon_r = 0.1$ . All of these are appropriate for the Venus atmosphere based on the numerical values of the physical parameters listed and discussed in Appendix B. For completeness, we will consider the solutions for several different values of the thermal forcing parameter  $G$  since it is a measure of the importance of nonlinear interactions in shaping the circulation. In all cases, a steady state was reached after the equivalent of 1.5 solar days.

In Figures 2.5, 2.6, and 2.7 we show the steady state MMC for  $G = 10$ , 100 and 1375 (Venus) respectively. Each of the three solutions consists of a single, thermally direct Hadley cell. In general, we notice that the circulation is not symmetric about the point of zero heating ( $y = \pi/2$ ). The rising motion is always confined to regions of heating ( $0 \leq y \leq \pi/2$ ) while the sinking motion tends to occupy the entire region of cooling ( $\frac{\pi}{2} < y \leq \pi$ ) and extends into

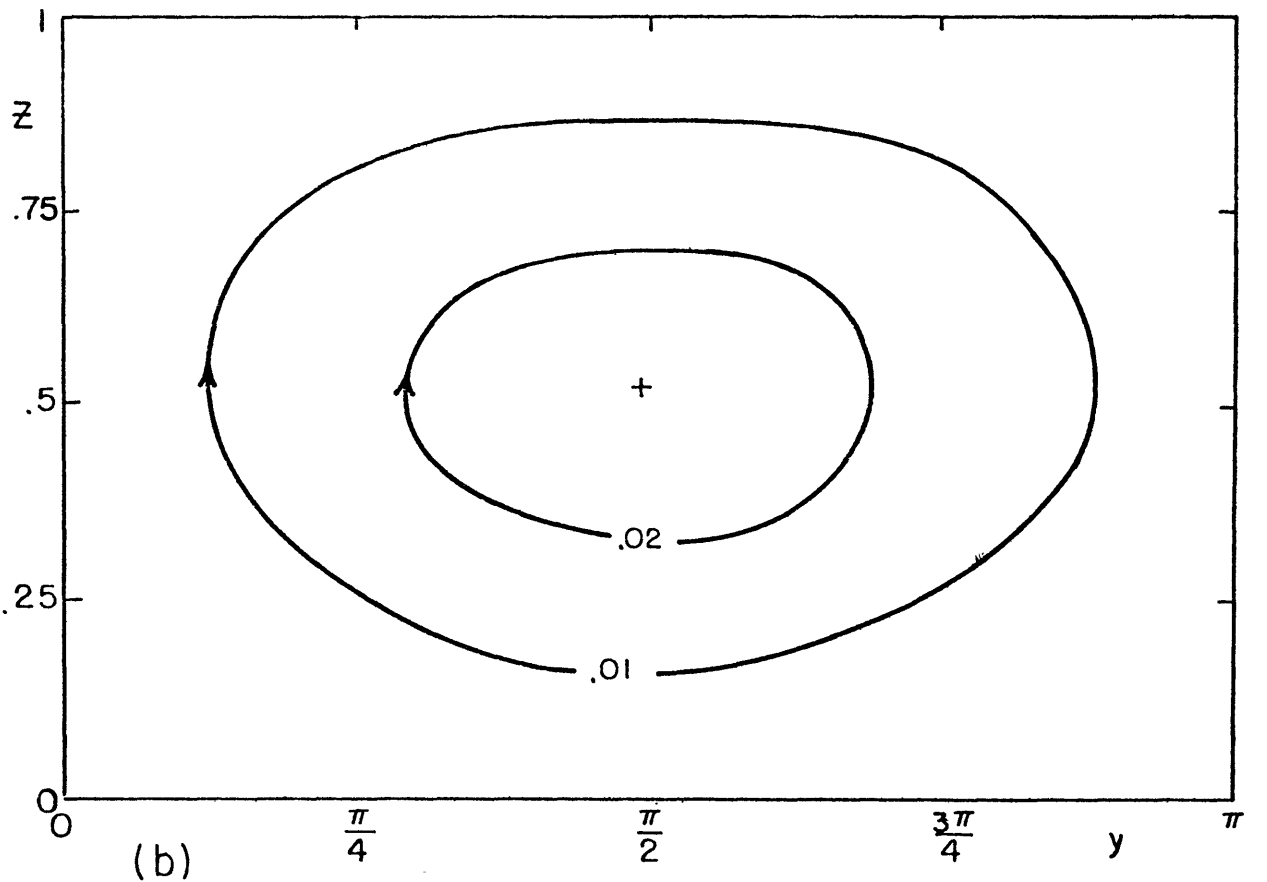
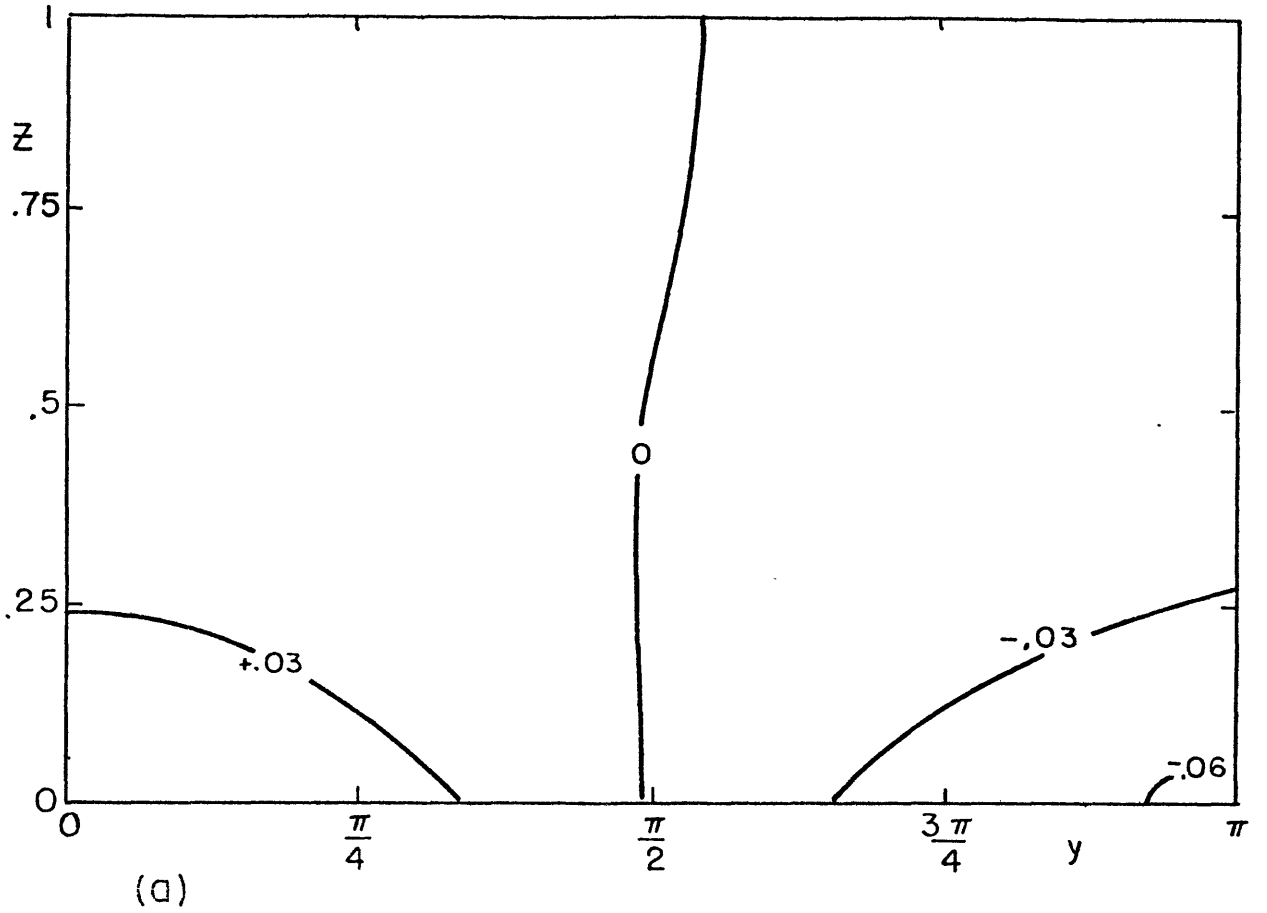
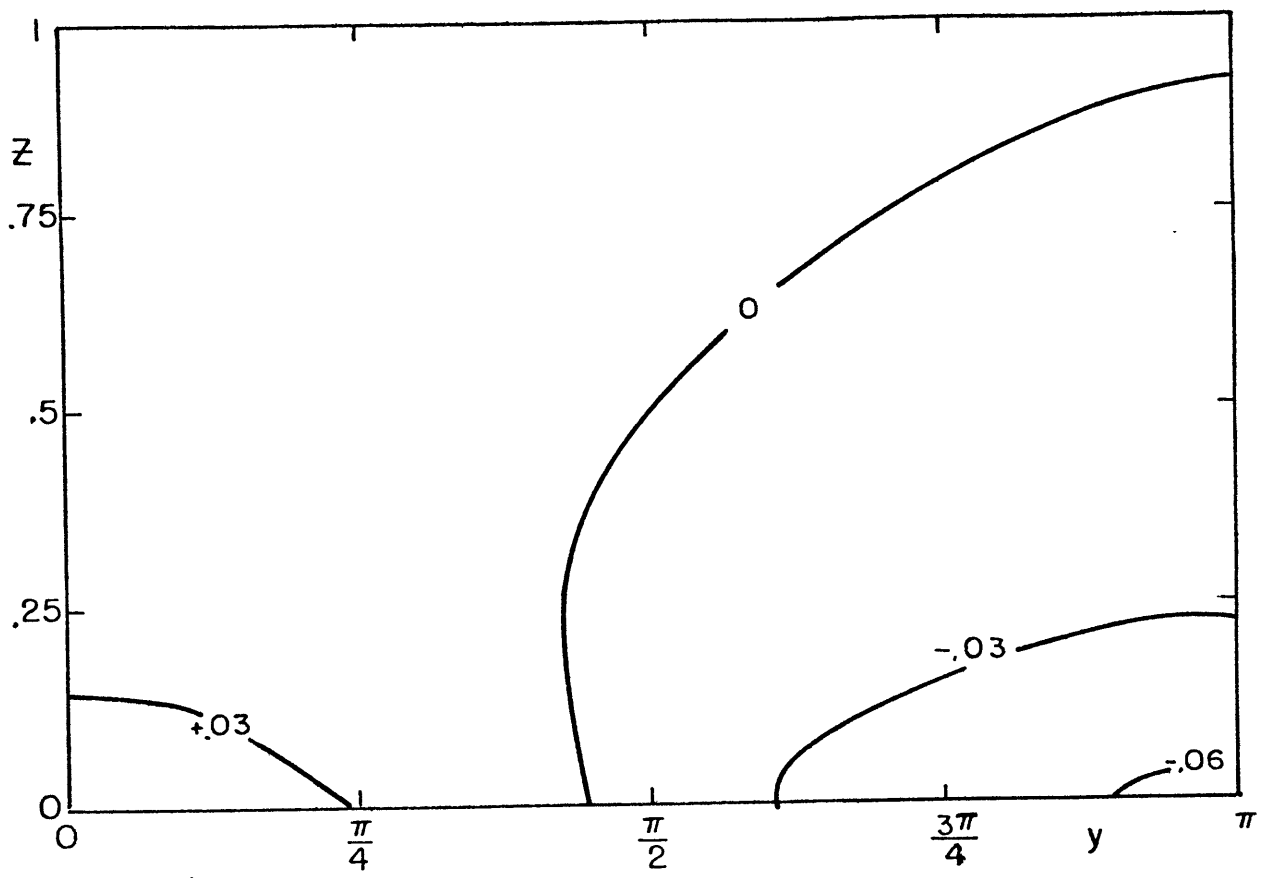
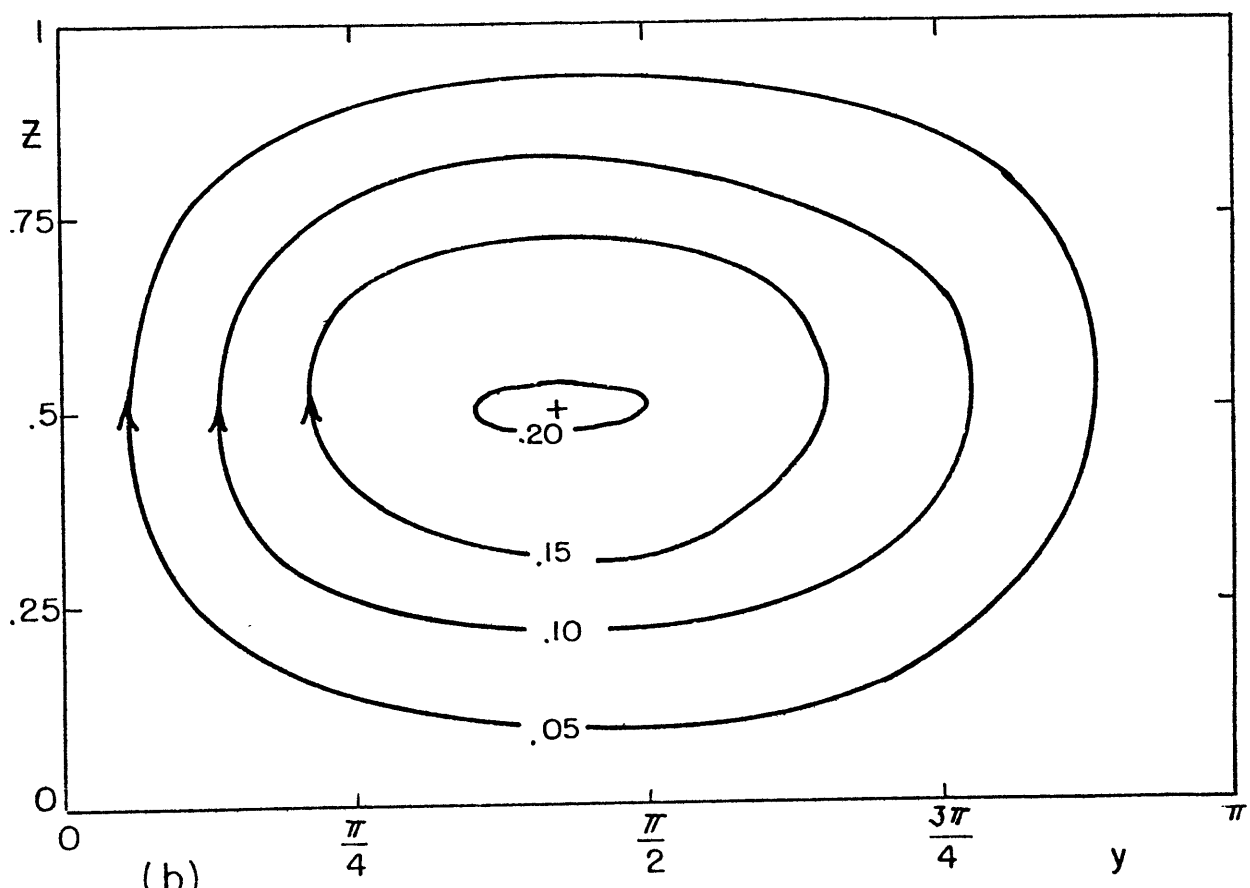


FIGURE 2.5 Steady state dimensionless MMC for  $G = 10$ ,  $2\beta^2 = 15.5$ ,  $Pr = \frac{1}{2}$ : (a) isotherm, (b) streamlines.



(a)



(b)

FIGURE 2.6 As in Figure 2.5 except with  $G = 100$

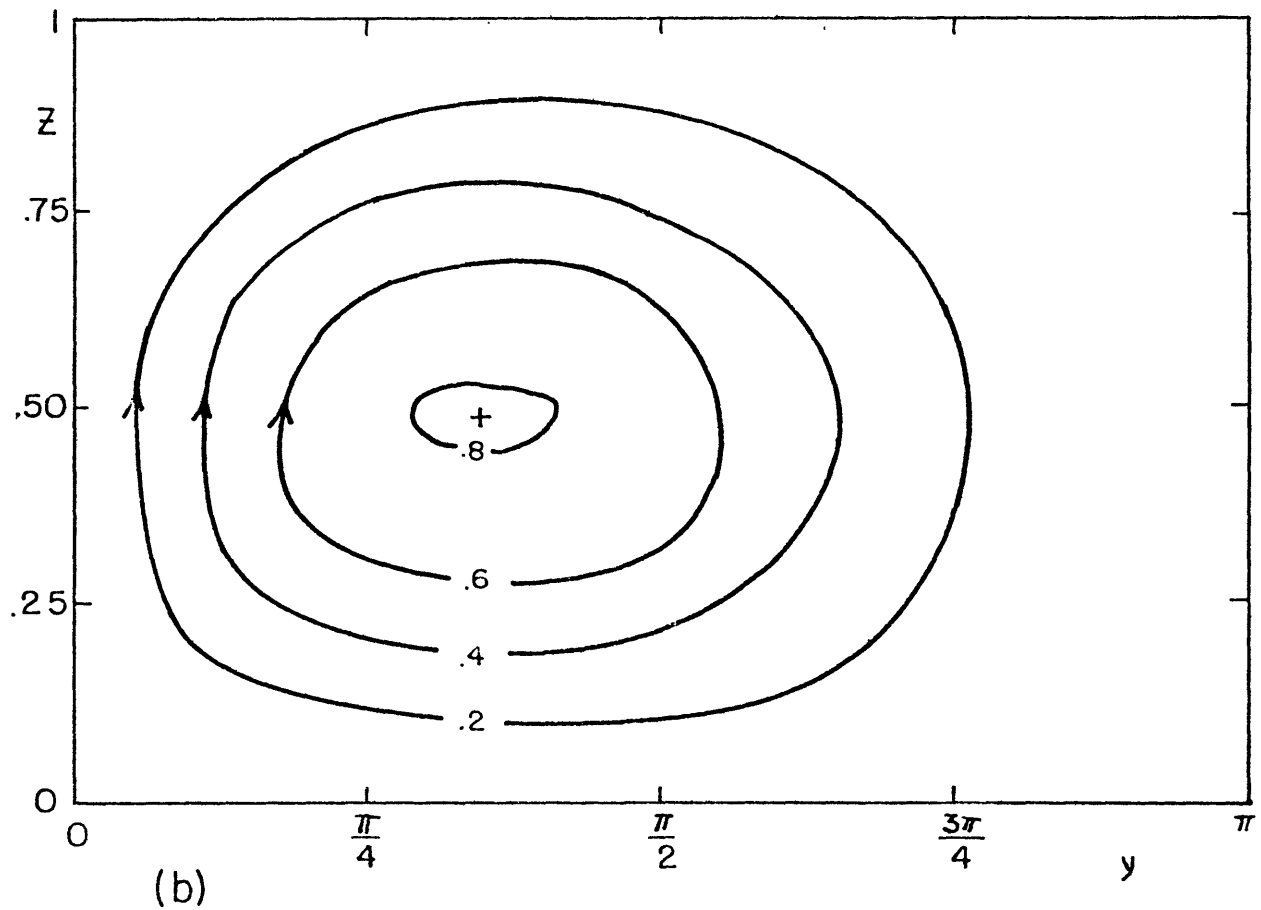
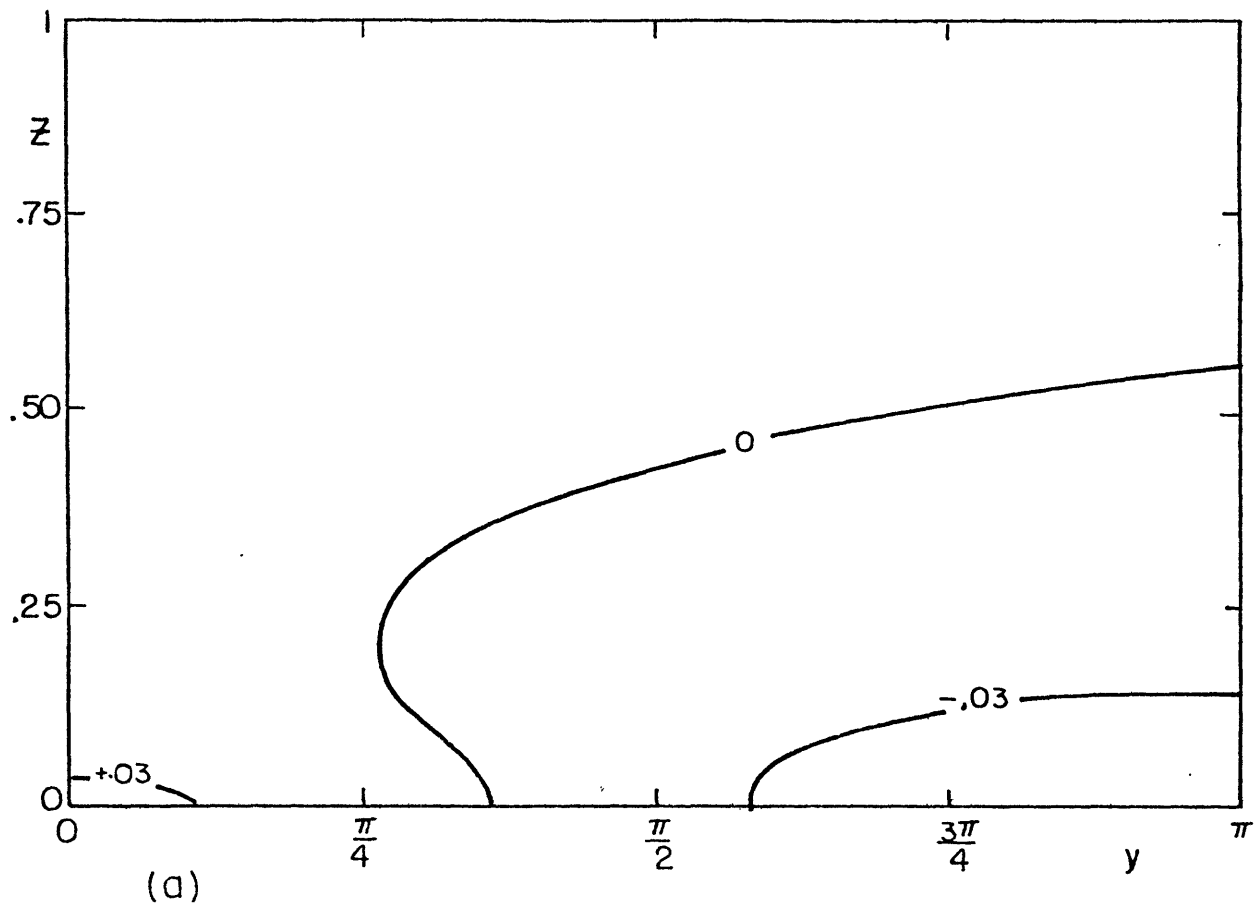


FIGURE 2.7 As in Figure 2.5 except with  $G = 1375$ :  
 (a) isotherms, (b) streamlines, (c)  $\bar{v}$ , (d)  $\bar{w}$ .



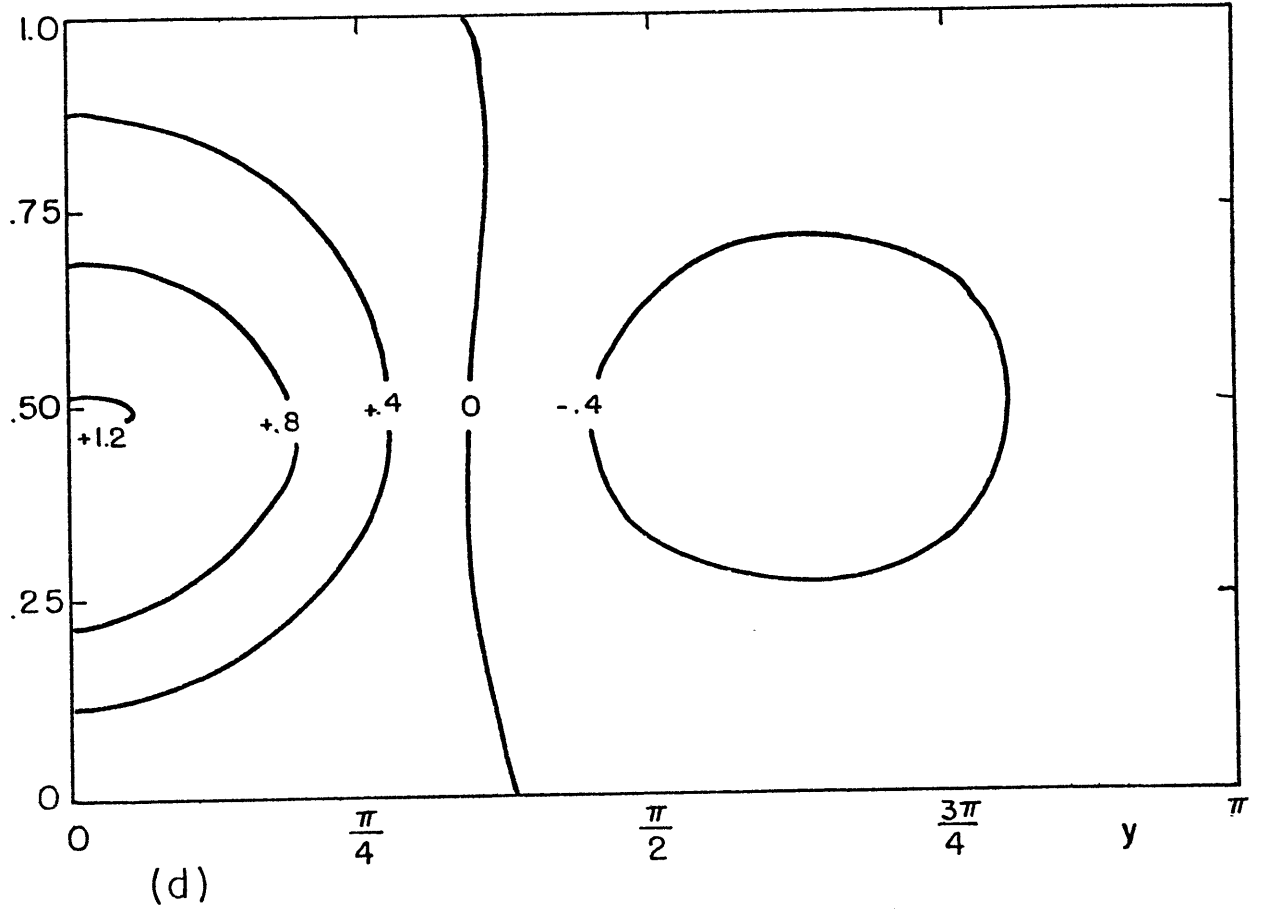
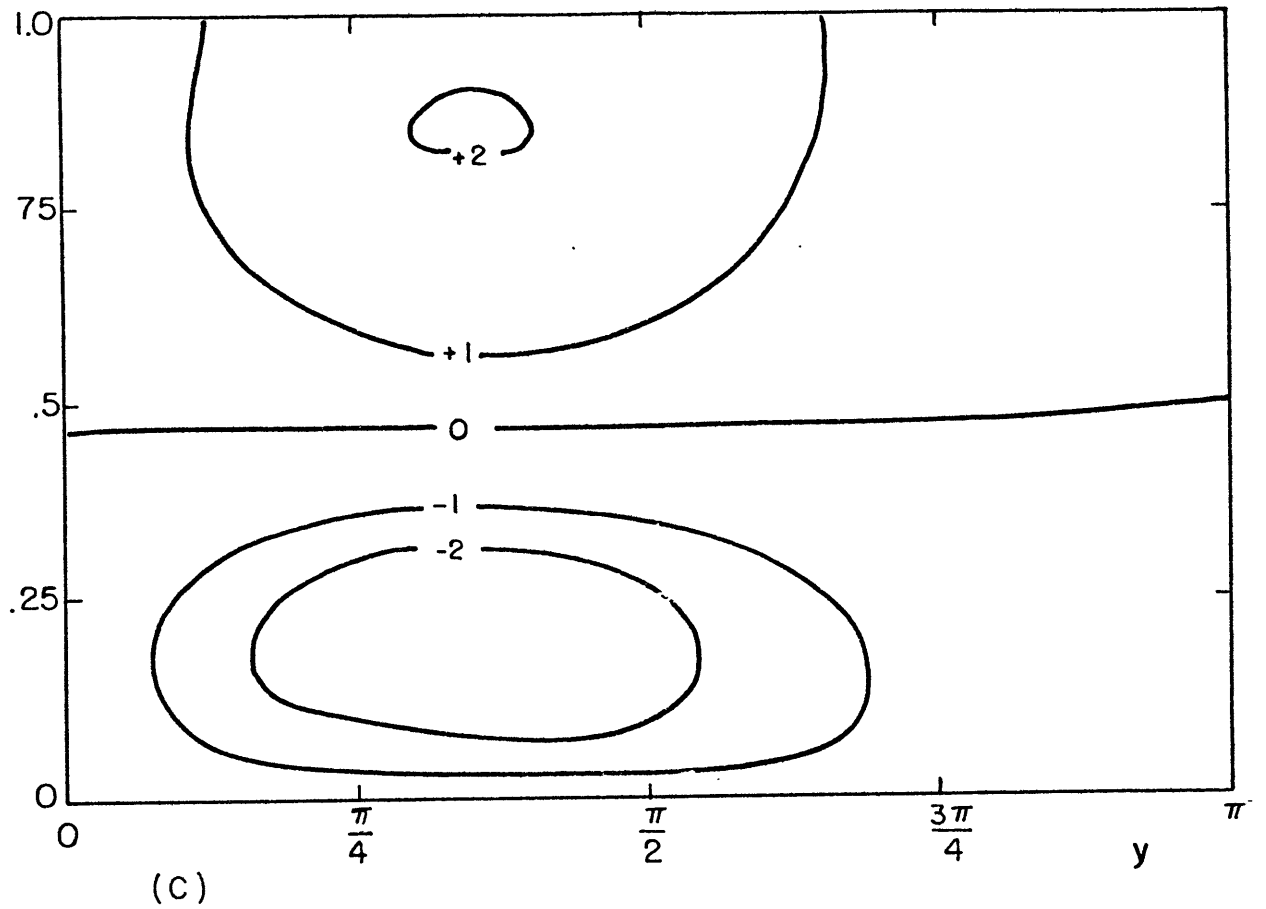


FIGURE 2.7 (continued)

the heated region.

As  $G$  increases, the most noticeable feature is the leftward shift of the streamlines. Stone (1968) demonstrated that this asymmetry is due to nonlinear effects. For heating from above, he found that nonlinear interactions tend to concentrate the horizontal temperature contrasts towards the lower boundary and the point of maximum heating,  $y = 0$ . This effect is further illustrated by the values in the second column of Table 2.2 where we indicate the location of the center of the Hadley cell. For heating from above, the temperature contrasts and the flow are concentrated near the top towards the point of maximum cooling,  $y = \pi$  (see Figure 2.9).

Table 2.2

$G$	Center of Hadley Cell	$\bar{\Psi}_{\max}$	$\Delta_y \bar{\theta}$	$\bar{w}_+ / \bar{w}_-$
10	$y=88^\circ, z=.53$	.025	0.133	1.07
100	$y=76^\circ, z=.50$	.207	0.125	1.40
1375	$y=63^\circ, z=.48$	.828	0.094	1.88

Closely associated with the leftward shift of the streamlines is an increase in the relative intensity of upward velocities. In the last column of Table 2.2 we show the ratio of the maximum upward velocity,  $w_+$ , to the maximum

downward velocity,  $w_-$ . As the area covered by rising motion decreases, mass continuity requires a proportional increase in  $|w_+/w_-|$ . For  $G = 10$ , the solution is very close to being symmetric about  $y = \pi/2$ . Consequently, the maximum upward and downward velocities are roughly the same. By the time we reach  $G = 1375$ ,  $|w_+/w_-|$  is nearly two thus reflecting the decrease in the region of rising.

In Figure 2.8 we have plotted the dimensionless quantities  $\bar{\psi}_{\max}$  (maximum value of the streamfunction) and  $\Delta_y \bar{\theta}$  (Horizontal temperature contrast from  $y = 0$  to  $y = \pi$  at the lower boundary) as functions of the thermal forcing parameter,  $G$ . These values are also listed in Table 2.2. The overall behavior of  $\bar{\psi}_{\max}$  and  $\Delta_y \bar{\theta}$  is as one might expect. The intensity of the circulation (i.e.,  $\bar{\psi}_{\max}$ ) increases with  $G$ . Furthermore, this increase in  $\bar{\psi}$  reflects an increase in the velocity components. We also note that as  $G$  increases  $\Delta_y \bar{\theta}$  decreases. Consequently, as  $G$  becomes larger, the stronger velocities become more effective in mixing the fluid and eliminating the horizontal temperature contrasts. A more detailed examination of these two curves reveals that the most rapid variations occur for  $G \lesssim 500$ . As  $G$  goes to larger values both curves flatten out and it appears that a significant increase in  $G$  causes only a minor strengthening of the circulation. However, we hesitate to extend this conclusion to highly nonlinear cases such as for  $G \gg 1000$ .

We now return to Figure 2.7 for a brief discussion of the MMC solution valid for the Venus values of the dimensionless

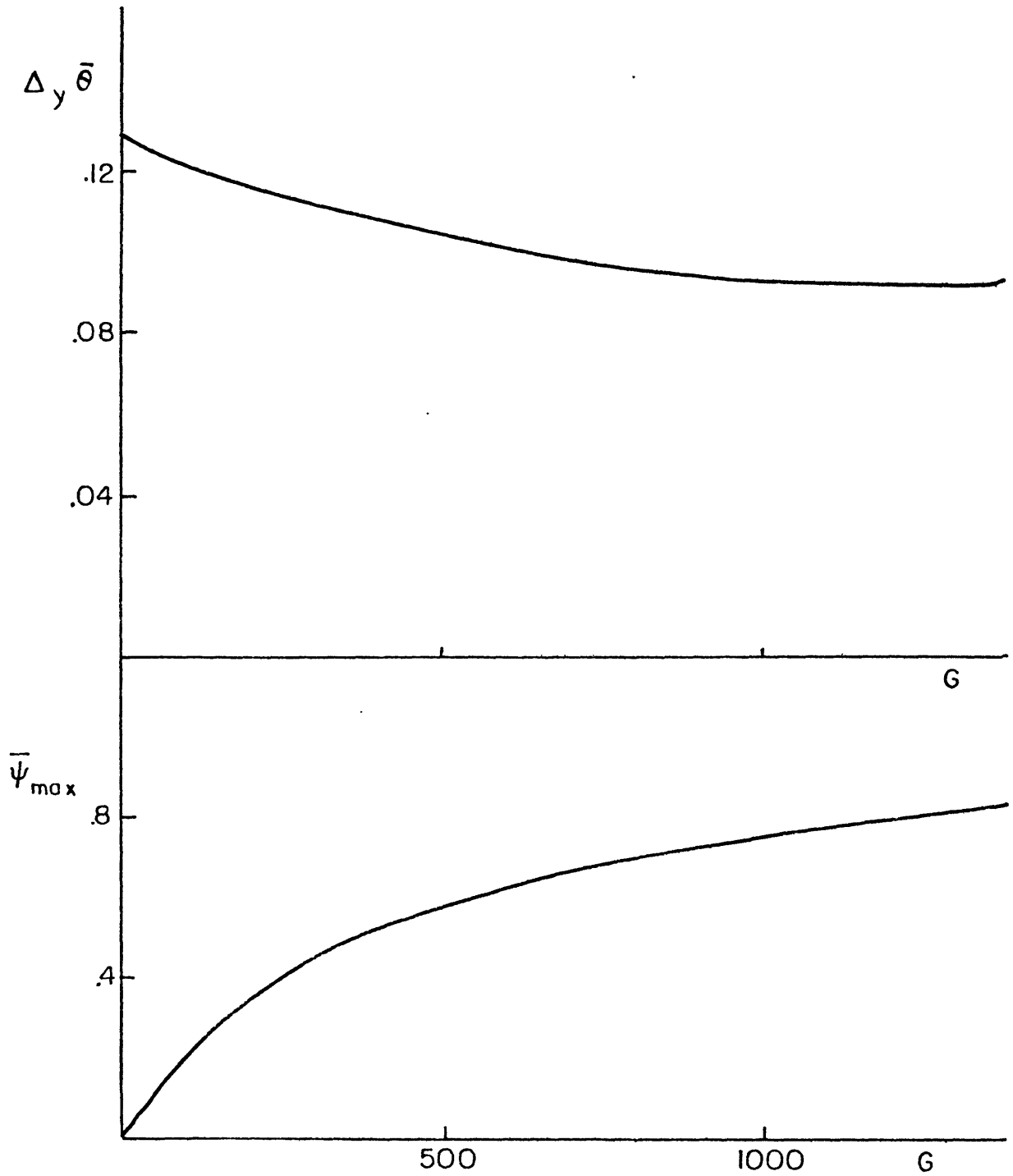


FIGURE 2.8  $\Delta_y \bar{\theta}$  (upper curve) and  $\bar{\psi}_{\max}$  (lower curve) as function of the thermal forcing parameter,  $G$ .

parameters. The concentration of the circulation towards  $y = 0$  has already been explained in terms of the nonlinear effects. In Figure 2.7a we notice that the strong horizontal temperature contrasts appear only in the lower boundary layer ( $z \leq .25$ ) which is understandable since the heating is being applied at the bottom. In the interior, the departures of the temperature from  $T_0$  are quite small thus implying that the model does not deviate significantly from a state of neutral stratification. The solution is statically stable everywhere except in the lower part of the channel in a narrow region around  $y = 0$ . This area of instability will persist since the model has no small scale convective adjustment process to eliminate superadiabatic lapse rates. Nevertheless, the upward heat transport by the MMC (see Figure 2.19 below) will produce a stable horizontally averaged  $\theta$  profile (Figure 2.9). The top to bottom average static stability is  $\Delta_z[\theta] = 0.021$  corresponding to a dimensional value of  $0.5^\circ\text{K}/\text{km}$ . The global average  $\langle \theta \rangle = \int_0^1 \int_0^\pi \bar{\theta} dy dz = 0$  remains zero.

In Figures 2.7c and 2.7d we show the meridional ( $\bar{v}$ ) and vertical ( $\bar{w}$ ) velocities for the Venus values solution. The line between the poleward flow in the upper levels and the equatorward flow in the lower levels appears slightly below the channel center. The strongest meridional velocities occur just below the top of the lower boundary layer with a maximum dimensional magnitude of  $12 \text{ m s}^{-1}$ . The line between upward and downward motions appears near  $y = 60^\circ$  meaning that roughly one third of the atmosphere is rising

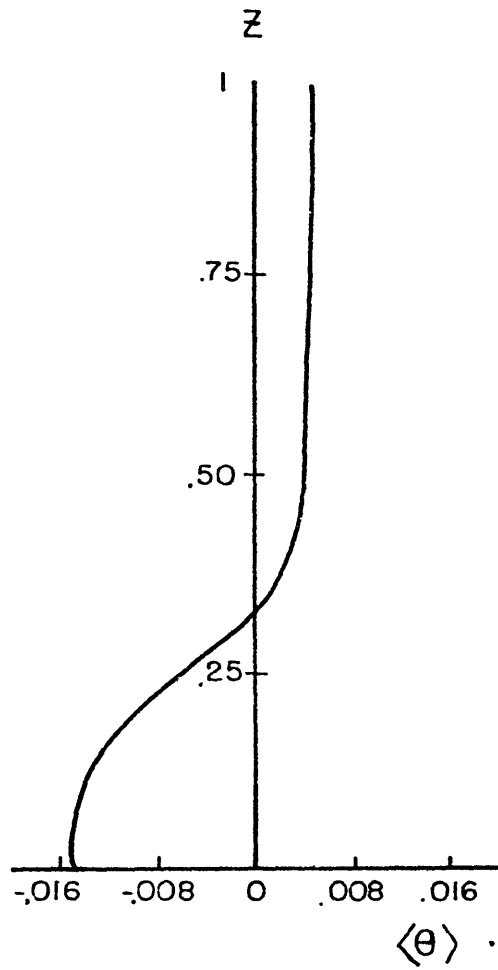


FIGURE 2.9 Horizontally averaged potential temperature as a function of height.

and two-thirds is sinking. The maximum dimensional magnitude of the upward flow is  $0.39 \text{ cm s}^{-1}$ .

Upon comparing our solutions to other Hadley cell studies we find that our model agrees quite well with the theoretical conclusions proposed by Stone (1968) concerning the role of nonlinear interactions and with the nonrotating Boussinesq model developed by Kálnay de Rivas (1971, 1973) (subsequently denoted, EKR). In EKR, the strongest horizontal temperature gradients and the strongest meridional velocities appeared in the upper boundary layer. The vertical velocity field consisted of weak rising motion between  $y = 0$  and  $y = 120^\circ$  and sinking between  $y = 120^\circ$  and  $y = 180$ , with very strong downward motion at the antisolar point. All of these features as compared to our results are easily understood in terms of Stone's nonlinear theory since we use heating from below while Kálnay de Rivas used heating from above. There are also several other differences between the two models. EKR contained a more realistic heating function which consisted of a roughly uniform cooling plus a heating that varied as

$$F \sim \begin{cases} \cos y & 0 \leq y \leq \frac{\pi}{2} \\ 0 & \frac{\pi}{2} < y \leq \pi \end{cases}$$

and thus the resulting meridional heating contrast is only one half of the contrast in our model. On the other hand, the

heat flux boundary condition in EKR was scaled according to the amount of shortwave radiation absorbed by the entire atmosphere which is forty times stronger than our heat flux. However, since EKR considered the entire atmosphere from the surface to the cloud tops, she used a reference density that was approximately 43 times larger than our value. The combination of these two factors means that both our model and EKR's model are forced by comparable heat fluxes.

Since EKR considered a much deeper atmosphere than we do, her height scale was approximately ten times larger than ours. This also means that the thermal forcing parameter,  $G$ , in her model was ten times larger than ours. This would lead one to expect a much more intense circulation in her results. However, the flow in EKR is restricted by relatively strong horizontal diffusion (her horizontal diffusion coefficients are two orders of magnitude larger than ours). One other important difference between her model and ours is the greater horizontal resolution in EKR.

With all of these factors in mind, we find that the results of the two models agree in many respects:

EKR's values

$$\Delta_y \bar{\theta}^* = 23^\circ \text{K}, \quad |\bar{v}_{\max}^*| = 18 \text{ m s}^{-1}, \quad |\bar{w}_{\max}^*| = 60 \text{ cm s}^{-1},$$

$$|\bar{\psi}_{\max}^*| = 7.5 \times 10^8 \text{ cm}^2 \text{ s}^{-1}$$



our values

$$\Delta_y \bar{\theta}^* = 12^\circ \text{K}, \quad |\bar{v}_{\max}^*| = 12 \text{ m s}^{-1}, \quad |\bar{w}_{\max}^*| = 0.4 \text{ cm s}^{-1},$$

$$|\bar{\psi}_{\max}^*| = 2.1 \times 10^8 \text{ cm}^2 \text{ s}^{-1}.$$

The very large difference in the values of  $\bar{w}_{\max}^*$  is directly related to the greater horizontal resolution in EKR. The presence of a very narrow region of strong vertical motion (termed a "mixing region" by Goody and Roberson, 1966) cannot be adequately resolved in our model because of the low order truncation. We also notice the similarity in the overall intensity of the Hadley cell in both models as indicated by the values of  $|\bar{v}_{\max}^*|$  and  $|\bar{\psi}_{\max}^*|$ . It appears that the stronger forcing and stronger dissipation in EKR counteract one another so that both models experience a similar balance between forcing and dissipation. The other factor that contributes to the slightly stronger flow in her solution is that her Hadley cell was concentrated near the upper stress free boundary while ours is displaced towards the lower no-slip boundary.

By comparing these two models we can see that except for missing the "mixing region", our limited model does indeed reproduce many of the features of the results of a set of highly nonlinear computations.

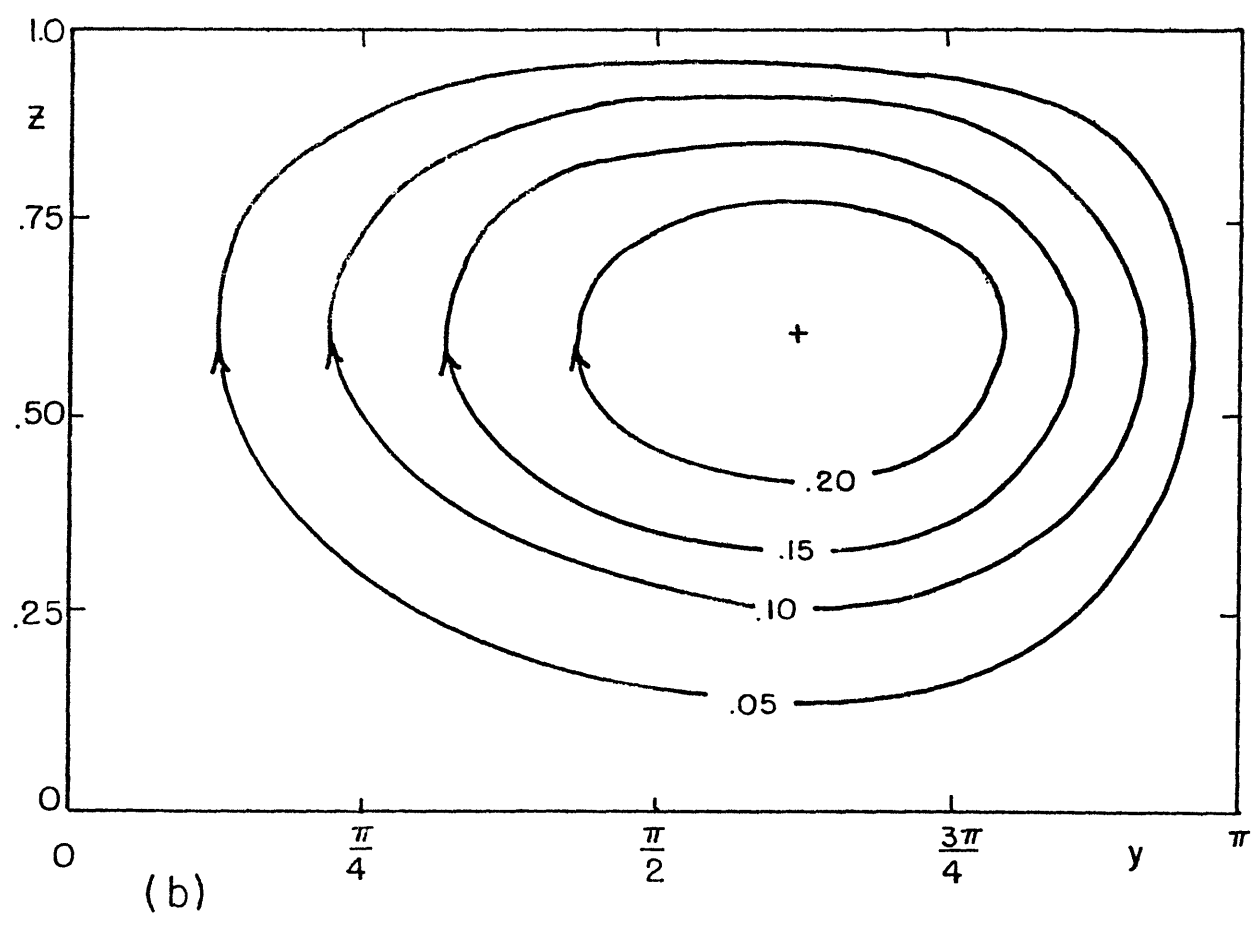
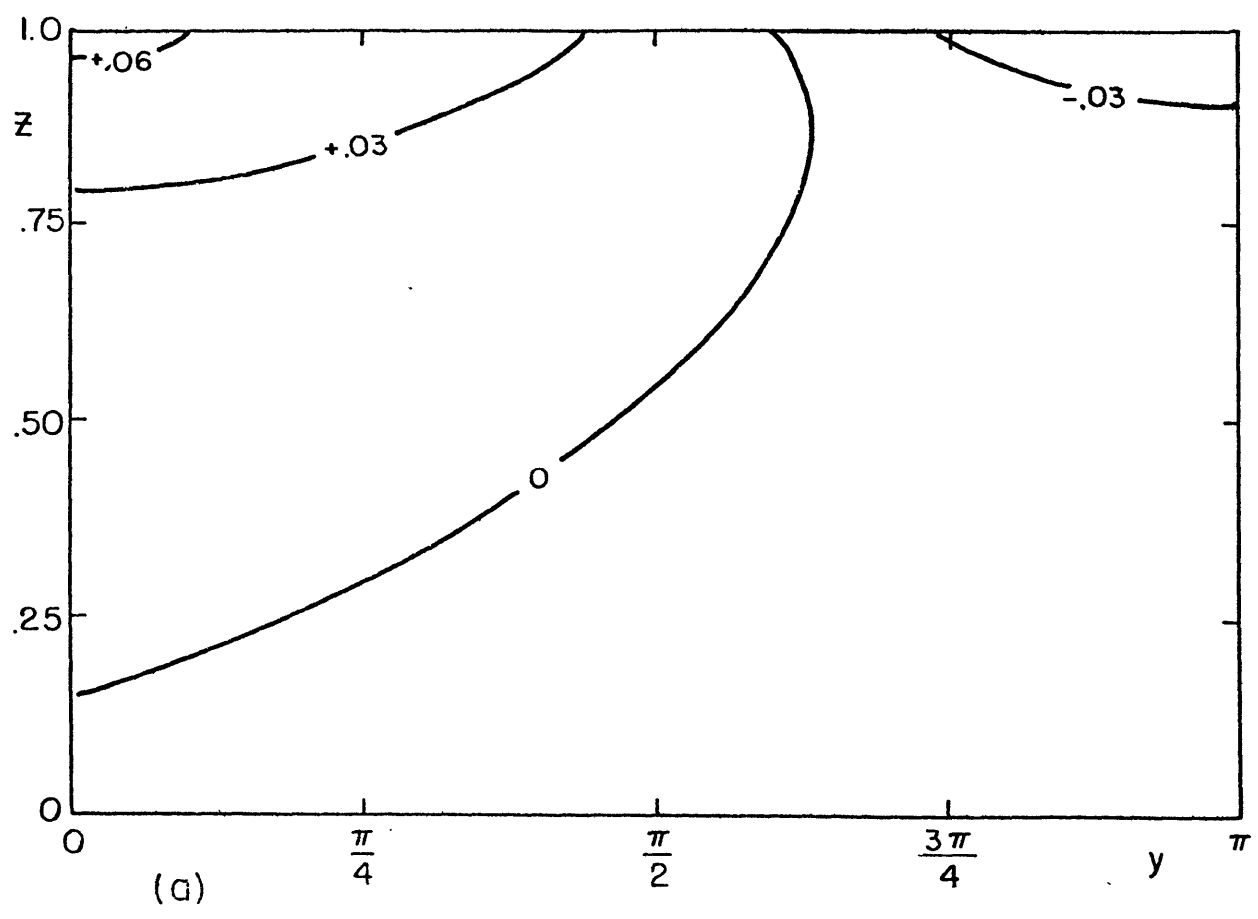


FIGURE 2.10 Steady State Dimensionless MMC with heating from above for  $G=100$ ,  $2\beta^2 = 15.5$ ,  $Pr = 1$

We conclude this section with Figure 2.10 which is the solution for the MMC for heating from above with  $G = 100$ ,  $2\eta^2 = 15.5$ ,  $Pr = \frac{1}{2}$ . Without going into detail, we simply point out that a comparison of Figures 2.9 and 2.6 once again demonstrates the nonlinear concentration effects. The isotherms in the two figures closely resemble a reflection of one another about the lines  $y = \pi/2$  and  $z = .5$ . However, the streamlines for heating from above are not the reflection of those for heating from below. The circulation in Figure 2.9b is slightly more intense and further displaced from the center as compared to its counterpart in Figure 2.6b. The reason once again is related to the fact that the heating from above circulation is concentrated towards the stress free top while the heating from below solution is concentrated near the no-slip bottom.

## 2.5 Large Scale Eddies and the Mean Zonal Wind

### 2.5.1 Method of Solution

From equations (2.2.20) - (2.2.25) we can immediately see that the eddies and the mean zonal wind are coupled to one another by various nonlinear interactions. The eddies provide the forcing for  $\bar{u}$  through the Reynolds stresses  $\overline{u'v'}$  and  $\overline{u'w'}$  while the structure of the waves is affected by the mean zonal flow through the zonal advection term. For this reason, the five eddy variables and  $\bar{u}$  must be determined simultaneously. The numerical method we will use to solve

(2.2.20) - (2.2.25) is quite similar to the one used for the MMC equations in the previous section. We begin by introducing the iteration variable and add the operator  $\frac{\partial}{\partial \tau}$  to the left-hand side of the eddy momentum equations (2.2.20), and (2.2.21), the eddy potential temperature equation (2.2.23), and the  $\bar{u}$  equation (2.2.25). The eddy vertical velocity and pressure are determined diagnostically at each iteration from the continuity equation and the hydrostatic equation, respectively. Latitudinal variations are removed from the equations by expanding each variable in a Fourier series and then performing the appropriate transformation. As in section 2.4, we expand  $\bar{u}$  as a complex Fourier series so that

$$\bar{u}(y, z) = \sum_{n=-N}^N \bar{u}_n(z, z) e^{iny}$$

and we again choose the truncation value  $N = 2$ . For the eddies, we allow comparable zonal and meridional resolutions and thus we retain only meridional wavenumber 1. We will see below in equation (2.5.7) that when the eddies are truncated at  $N = 1$ , they will be able to force up to meridional wavenumber 2 in the expansion of  $\bar{u}$ . This is due to the nonlinear nature of the Reynold's stresses. Since the thermal forcing is symmetric about  $y = 0$  (i.e., the forcing varies as  $\cos y$ ),  $\theta'$ ,  $u'$ , and  $w'$  will preserve symmetry

while  $v'$  will antisymmetric and therefore we can separate the  $y$  dependence as follows

$$\begin{bmatrix} T(y,z) \\ P \\ U \\ W \end{bmatrix} = \begin{bmatrix} T(z) \\ P \\ U \\ W \end{bmatrix} \cos y$$

$$V(y,z) = V(z) \sin y$$

where  $T, P, U, W, V$  are the complex amplitudes of  $\theta', p', u', w', v'$  respectively. If these expansions are substituted into (2.2.20) - (2.2.24) and the appropriate Fourier Transformation is carried out, we obtain the following set of model equations

$$\begin{aligned} \frac{\partial U}{\partial z} = & iU - iU(\bar{u}_0 + \text{Re } \bar{u}_2) - U \text{Im } \bar{v}_2 - \frac{\partial U}{\partial z} \text{Re } \bar{w}_2 \\ & + 2V \text{Re } \bar{u}_2 - W \left( \frac{\partial \bar{u}_0}{\partial z} + \text{Re } \frac{\partial \bar{u}_2}{\partial z} \right) - iGP \\ & + \frac{1}{2r^2} \left[ \frac{\partial^2 U}{\partial z^2} - 2\varepsilon_v U \right] \end{aligned} \quad (2.5.1)$$

$$\begin{aligned} \frac{\partial V}{\partial z} = & iV - iV(\bar{u}_0 - \text{Re } \bar{u}_2) - V \text{Im } \bar{v}_2 + \frac{\partial V}{\partial z} \text{Re } \bar{w}_2 \\ & + W \text{Im } \frac{\partial \bar{v}_2}{\partial z} + GP \\ & + \frac{1}{2r^2} \left[ \frac{\partial^2 V}{\partial z^2} - 2\varepsilon_v V \right] \end{aligned} \quad (2.5.2)$$

$$iU + V + \frac{\partial W}{\partial z} = 0 \quad (2.5.3)$$

$$\begin{aligned} \frac{\partial T}{\partial z} = & iT - iT(\bar{u}_0 + \text{Re } \bar{u}_2) - T \text{Im } \bar{v}_2 - \frac{\partial T}{\partial z} \text{Re } \bar{w}_2 \\ & + 2V \text{Re } \bar{\theta}_2 - W \left( \frac{\partial \bar{\theta}_0}{\partial z} + \text{Re } \frac{\partial \bar{\theta}_2}{\partial z} \right) \\ & + \frac{1}{2\eta^2} \left[ \frac{\partial^2 T}{\partial z^2} - 2\varepsilon_k T \right] \end{aligned} \quad (2.5.4)$$

$$\frac{\partial P}{\partial z} = T \quad (2.5.5)$$

where the complex amplitudes are now functions of only  $z$  and  $\tau$ , and  $\text{Re}(\ )$  and  $\text{Im}(\ )$  stand for the real and imaginary parts, respectively of a complex quantity. The "prognostic" equations for the  $\bar{u}_n$  components are

$$\begin{aligned} \frac{\partial \bar{u}_n}{\partial z} = & - \sum_{n_1=n-N}^N \left[ i(n-n_1) \bar{v}_{n_1} \bar{u}_{n-n_1} + \bar{w}_{n_1} \frac{\partial \bar{u}_{n-n_1}}{\partial z} \right] \\ & + \frac{1}{2\eta^2} \left[ \frac{\partial^2 \bar{u}_n}{\partial z^2} - n^2 \varepsilon_v \bar{u}_n \right] - (RS)_n \end{aligned} \quad (2.5.6)$$

where  $(RS)_n$  is the  $n$ th component of the Reynold's stresses given by

$$(RS)_n = \begin{cases} \frac{\partial}{\partial z} \operatorname{Re}(U\tilde{W}) & \text{for } n=0 \\ 0 & \text{for } n=\pm 1 \\ \frac{1}{2} \frac{\partial}{\partial z} \operatorname{Re}U\tilde{W} + \operatorname{Re}U\tilde{V} & \text{for } n=\pm 2 \end{cases}$$

(2.5.7) .

The spectral coefficients of  $\bar{\theta}$ ,  $\bar{v}$ , and  $\bar{w}$  are already known from the MMC solution. The time stepping of  $T$ ,  $U$ , and  $V$  is performed with the modified leap frog scheme described by equation (2.4.6) with an occasional forward time step. The vertical derivatives and advective terms are computed with the finite difference scheme in stretched coordinates as discussed in section 2.4.

The procedure used here is once again similar to the one used for the MMC. We begin by advancing  $T$  to the new time step  $\tau + \Delta\tau$  by solving the finite difference analog of (2.5.4). We then use the updated values of  $T$  in the hydrostatic equation (2.5.5) to determine the "uncorrected" pressure (uncorrected since it contains a boundary value which is an arbitrary function of  $x$  and  $y$  only). The uncorrected pressure is then used in (2.5.1) and (2.5.2) to compute the uncorrected values  $u'^u$ ,  $v'^u$  at the new time step. The actual values of  $u'$  and  $v'$  are related to the uncorrected values according to

$$u' = u'^u + \frac{dR}{dx} \quad , \quad v' = v'^u + \frac{dR}{dy}$$

where the arbitrary function  $R(x,y)$  is given by

$$R(x,y) = 2G \Delta \tau p'(z=1)$$

and  $p'(z=1)$  is the value of  $p'$  at the top of the model.

From mass continuity and the boundary conditions on  $w'$  we know that

$$\int_0^1 \left( \frac{\partial u'}{\partial x} + \frac{\partial v'}{\partial y} \right) dz = - \int_0^1 \frac{\partial w'}{\partial z} dz = 0$$

If we now replace  $u'$  and  $v'$  by the expressions involving the uncorrected values we find

$$\frac{d^2 R}{dx^2} + \frac{d^2 R}{dy^2} = - \int_0^1 \left( \frac{\partial u'^u}{\partial x} + \frac{\partial v'^u}{\partial y} \right) dz \quad (2.5.8)$$

Recalling the spectral representation of the  $x$  and  $y$  dependences, we find that the coefficient of  $R(x,y)$  is given by



$$R = \frac{1}{2} \int_0^1 [iU^u + V^u] dz$$

and finally the corrected vertical structure of  $u'$  and  $v'$  is given by

$$U(z) = U^u(z) + iR, \quad V(z) = V^u(z) - R.$$

<sup>w</sup>  
We complete the calculations for the eddies at the new time step  $\tau + \Delta\tau$  by solving for  $W$  in (2.5.3).

The time stepping routine for  $\bar{u}$  is straightforward. The Reynolds stresses are computed from the values of  $u'$ ,  $v'$ , and  $w'$  at time  $\tau$ . Equation (2.5.6) is then advanced in time using these Reynolds stresses and the modified leap frog time scheme. There is no correction term analogous to (2.5.8) since the pressure gradient does not appear in the equation for  $\bar{u}$ .

### 2.5.2 Results - Two-Dimensional

We begin the results section by presenting the solution of the two-dimensional moving flame equations in which there are no  $y$  variations. Consequently, equation (2.5.2) is dropped and all terms involving the MMC in the remaining

equations are exactly zero. In Figure 2.11 we show the dimensionless eddy variables  $\theta'$ ,  $w'$ , and  $u'$  for  $G = 1375$ ,  $Pr = \frac{1}{2}$ ,  $2\eta^2 = 15.5$ . The isotherms and the convection cells tilt upward to the left as predicted by our simple qualitative discussion in Chapter 1. This tilting is due to the finite rate of upward diffusion of heat from the heated lower boundary. Not surprisingly, the strongest horizontal temperature gradients are confined to the lower boundary layer with a maximum day-night contrast of  $\Delta_x \theta' = 0.12$ , corresponding to a dimensional values of  $14^\circ\text{K}$ . At the lowest model level  $z = 0.006$  ( $z^* = 30$  m), the highest temperature lags behind the hot spot of the heat source by  $15^\circ$ . The lag in the temperature field increases with height, thus producing the observed tilted isotherms. The maximum lag of  $160^\circ$  occurs at the top of the model.

The large scale eddy circulation, represented by the velocity components  $u'$  and  $w'$ , consists of two large convection cells that move with the heat source. Because of diffusion, the cells tilt upward to the left just as the isotherms. Also due to diffusive processes, the vertical velocity field lags behind both the heat source and the temperature field. The net result is that the cellular overturning is between the terminators with the most intense rising motion near the evening terminator and sinking near the morning terminator. The strongest vertical velocities

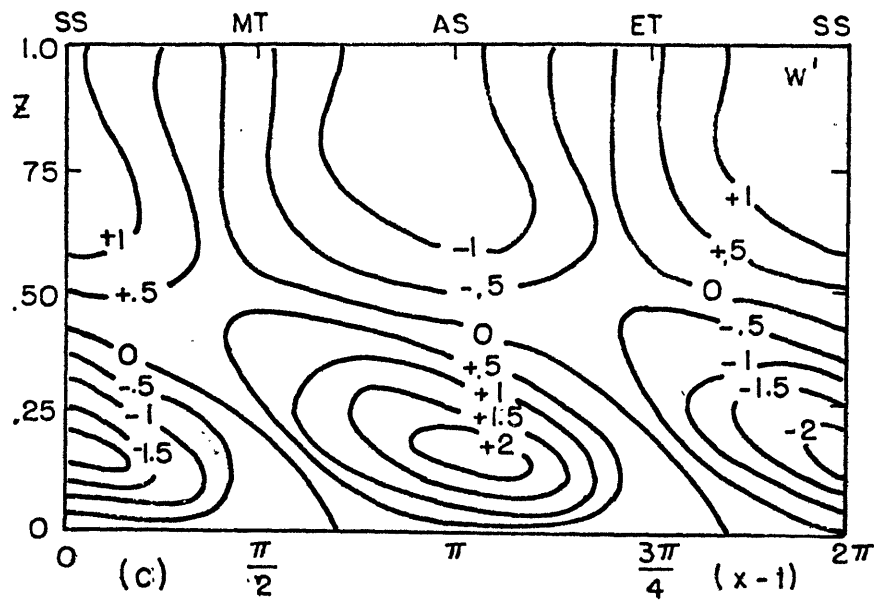
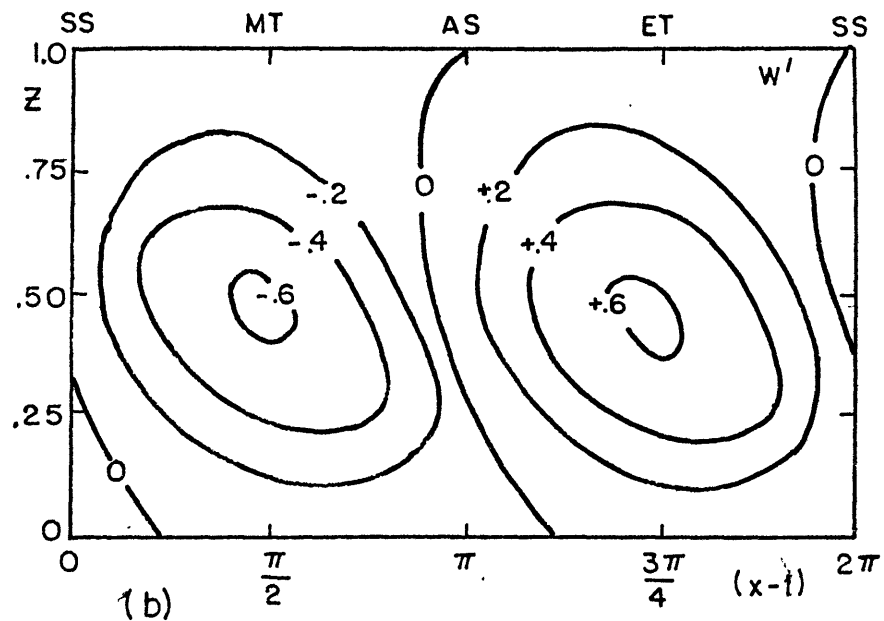
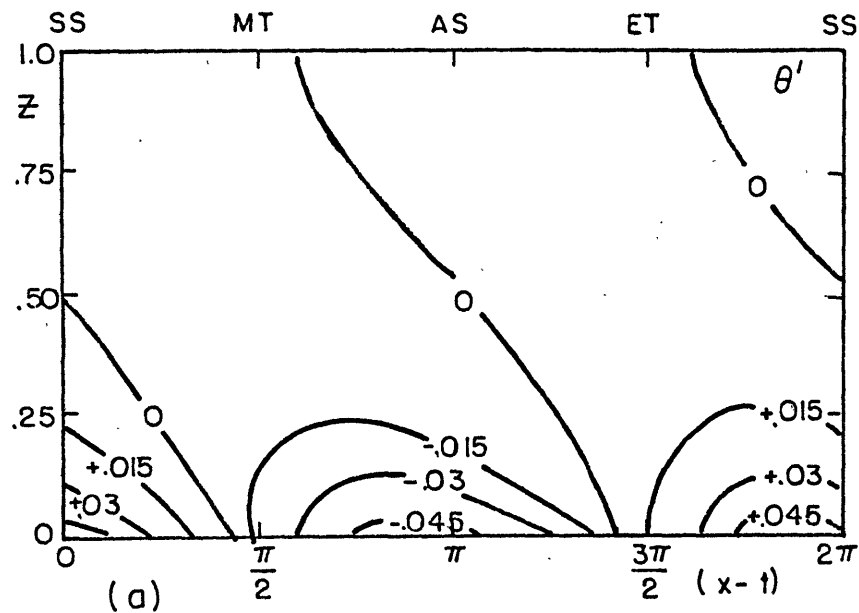


FIGURE 2.11 Steady state two dimensional eddy fields for  $G = 1375$ ,  $2^2 = 15.5$ ,  $Pr = -\frac{1}{2}$ :  
 (a) isotherms,  
 (b) vertical velocity,  
 (c) zonal velocity.

occur near  $z = .50$  with a maximum magnitude of  $w'_{\max} = 0.61$  corresponding to a dimensional value of  $0.20 \text{ cm s}^{-1}$ . Finally, we notice that the eddy zonal velocity field  $u'$ , also demonstrates the tilting of the convection cell. Typical values of  $u'$  are on the order of the speed of the heat source. We notice, however, that the largest values  $|u'_{\max}| = 2.3$  (dimensional value of  $9.2 \text{ m s}^{-1}$ ) appear in the lower boundary layer. This phenomenon, which was also observed in the MMC solution (see Figure 2.7), depends upon the location of the heat source (above or below). The strongest horizontal velocities tend to occur in the boundary layer adjacent to the heated boundary. For a given set of values of the dimensionless parameters, heating from above will produce larger maximum horizontal velocities because of the stress free nature of the upper boundary. A set of computations for the values  $G = 1375$ ,  $Pr = \frac{1}{2}$ ,  $2\eta^2 = 15.5$  with heating from above produced a maximum horizontal eddy velocity at the top boundary with magnitude  $|u'_{\max}| = 4.2$  corresponding to a dimensional value of  $16.8 \text{ m s}^{-1}$ .

We next turn our attention to the solution for  $\bar{u}$  in the two-dimensional problem. In Figure 2.12 we show the vertical profile of  $\bar{u}$  determined in conjunction with the eddies of Figure 2.11. The no-slip bottom and the stress free top are immediately obvious in the profile of  $\bar{u}$ . The

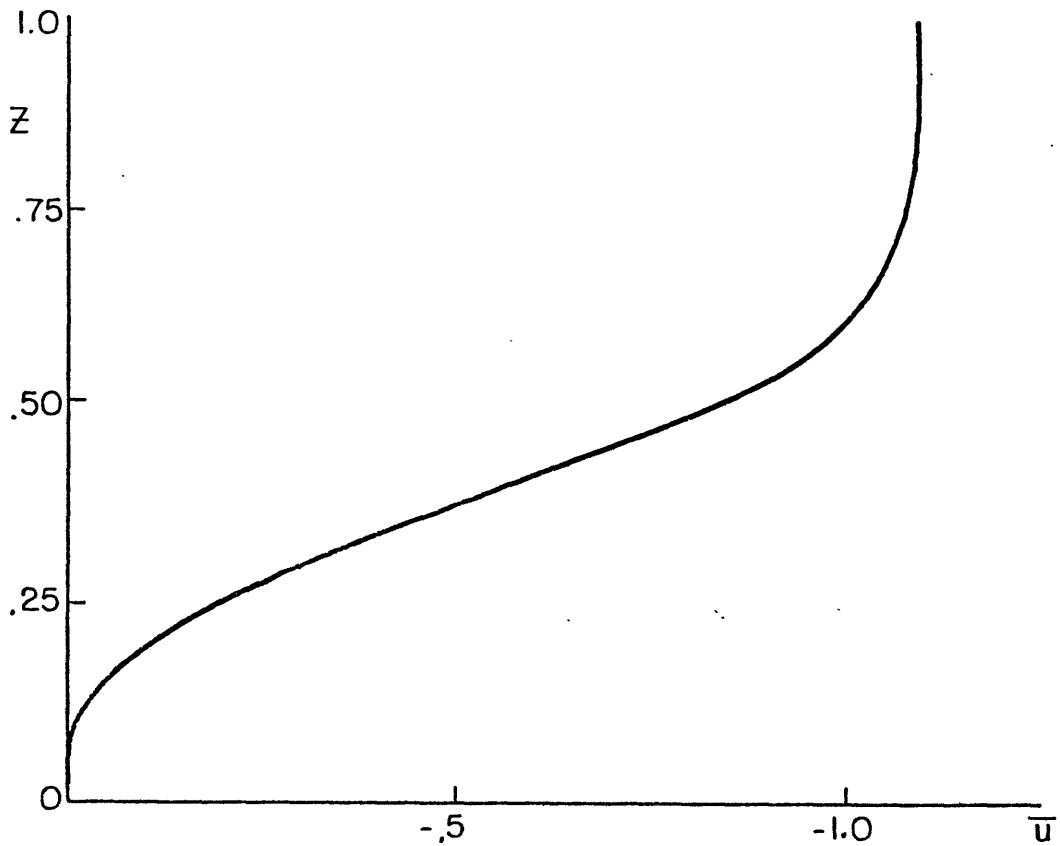


FIGURE 2.12  $\bar{u}$  as a function of height for  $G = 1375, 2\eta^2 = 15.5, Pr = \frac{1}{2}$ .

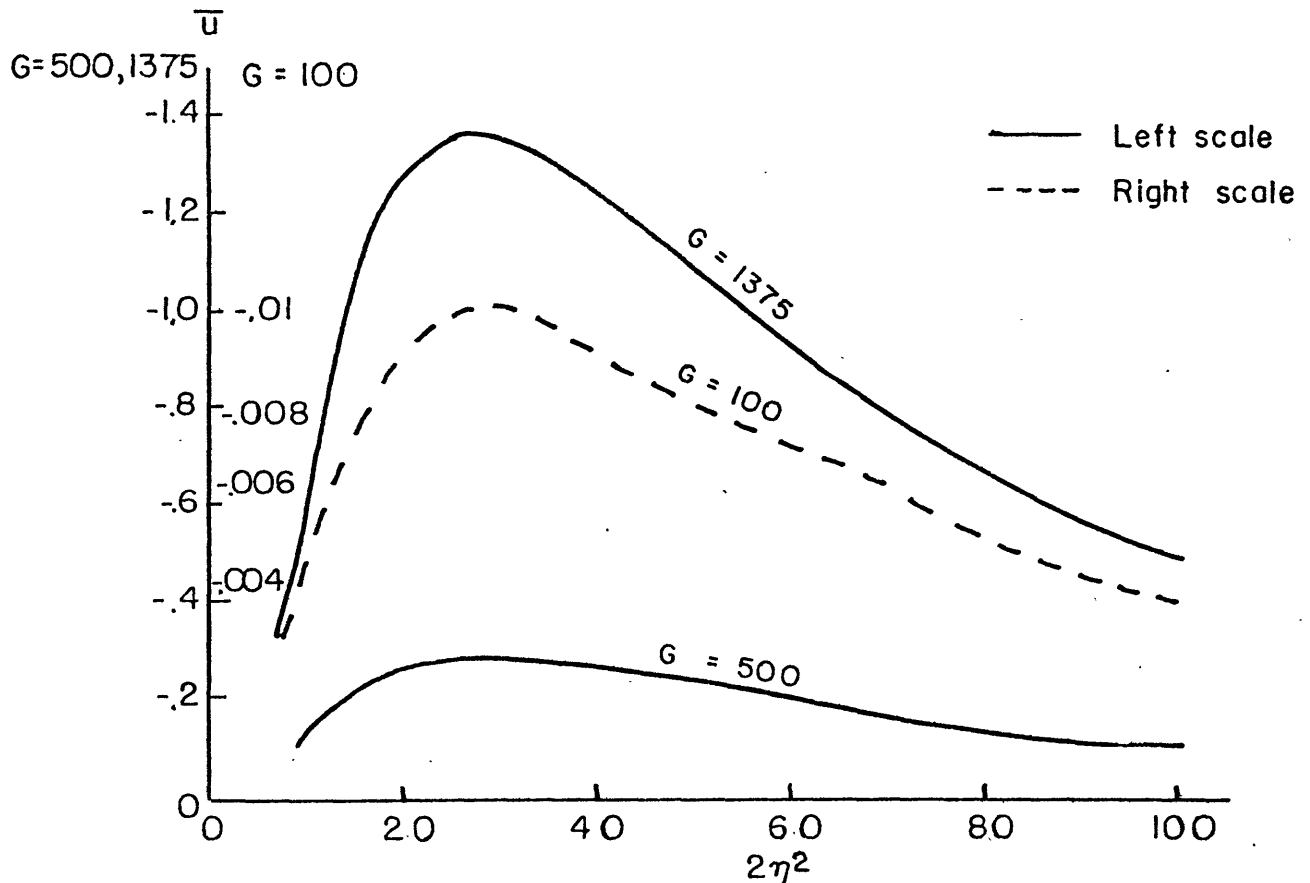


FIGURE 2.13  $\bar{u}$  as a function of the thermal frequency parameter,  $2\eta^2$ , and the thermal forcing parameter,  $G$ .

variation of  $\bar{u}$  within the boundary layers is rather small as compared to the change in the interior. We also notice that in terms of  $\bar{u}$ , the lower boundary is "stress free" in addition to being no-slip. The reason for this can easily be seen from the two-dimensional equation for the steady state mean zonal flow

$$\frac{\partial \overline{u'w'}}{\partial z} = \frac{1}{2r^2} \frac{\partial^2 \bar{u}}{\partial z^2} .$$

In the two-dimensional problem, there is no MMC, no  $v'$ , and no horizontal diffusion of  $\bar{u}$  so that the mean zonal flow represents a balance between the vertical Reynolds stress term and vertical diffusion. Using the stress free top boundary condition, we can integrate this equation once to obtain

$$\overline{u'w'} = \frac{1}{2r^2} \frac{\partial \bar{u}}{\partial z} \quad (2.5.9) .$$

Since the lower boundary is specified as rigid and no-slip, at  $z = 0$  the left-hand side of (2.59) is zero and therefore  $\frac{\partial \bar{u}}{\partial z} = 0$  at  $z = 0$ . We point out, however, that this pseudo-stress-free behavior at the bottom applies only to  $\bar{u}$  and is purely mathematical in nature. In reality, the bottom is not always stress free since  $\frac{\partial \bar{u}}{\partial z}$  is not necessarily zero at  $z = 0$ .

Because of the tilt of the eddy isotherms and convection cells, there will be a net upward flux of retrograde zonal momentum and therefore the strongest retrograde mean zonal flow will appear at the top of the model. The maximum value is  $\bar{u}_{\max} = -1.15$  corresponding to a dimensional value of  $-4.6 \text{ m s}^{-1}$ .

In Figure 2.13 we have plotted the two-dimensional  $\bar{u}(z=1)$  as a function of the thermal frequency parameter,  $2\eta^2$  for several values of the thermal forcing parameter  $G$ . The most obvious feature in all three curves is the peak at  $2\eta^2 = 25$ . As one goes to smaller values of  $2\eta^2$ , the maximum value of  $\bar{u}$  drops off very quickly, especially for  $2\eta^2 \leq 15$ . We recall that as the frequency parameter becomes smaller, viscous forces tend to dominate and weaken the flow. As one goes to larger values of  $2\eta^2$ , the decrease in  $\bar{u}$  is not quite as rapid. In this range,  $\bar{u}$  weakens since the fluid is not able to quickly respond to the rapidly moving heat source, due mainly to the ineffectiveness of the weak diffusive processes. The main point of interest here is that the Venus value of  $2\eta^2 = 15.5$  is fairly close to the peaks in the  $\bar{u}$  curves. As mentioned by Schubert and Young (1970), the value of  $2\eta^2$  for rapidly rotating planets such as the Earth, Mars, and Jupiter is typically on the order of  $10^4$ , and thus of the terrestrial and major planets, Venus is the one most likely to exhibit any significant large scale response to diurnal heating contrasts.

The dependence of  $\bar{u}$  upon the thermal forcing parameter,  $G$  is also as predicted by our discussion in Chapter 1. An

increase in the value of  $G$  represents an increase in the intensity of the physical forcing mechanism and thus results in a stronger flow. Between  $G = 100$  and  $G = 500$ , the variation is  $\bar{u} \sim G^{1.96}$  while between  $G = 500$  and  $G = 1375$ , the variation is  $\bar{u} \sim G^{1.59}$  as compared to the  $G^2$  dependence predicted by the various linear models described in Chapter 1. The change in the  $G$  exponent means that for very large values ( $G \gtrsim 1000$ ), subsequent increases in  $G$  become less effective in increasing the magnitude of  $\bar{u}$ . Once again, we return to Schubert and Young's (1970) estimates of  $G$  for the various planets and we find that the value for Venus is larger than all others by at least two order of magnitude. And once again we are led to the conclusion that the Venus atmosphere is the one most likely to exhibit any significant response to the moving flame type forcing. As to the overall effectiveness of the moving flame mechanism, we have found that it is capable of forcing horizontal velocities (eddy and mean) that are at most of the same order of magnitude as the phase speed of the moving heat source.

### 2.5.3 Results - Three-Dimensional

We have now come to the major focus of this <sup>chapter</sup> investigation - the solution of the moving flame problem in three-dimensions. Using the MMC solution shown in Figure 2.7 (for the Venus values of the parameters  $G = 1375$ ,  $Pr = \frac{1}{2}$ ,  $2\eta^2 = 15.5$ ), we now solve equations (2.5.1) - (2.5.6) for the eddies and the



mean zonal velocity.

In Figures 2.14a - d we show the height-longitude structure of the four, eddy fields  $\vartheta'$ ,  $w'$ ,  $u'$  (at  $y=0$ ) and  $v'$  (at  $y=\pi/2$ ), respectively. Upon comparing the three-dimensional (3D) isotherms and their two-dimensional (2D), counterparts (Figure 2.11a) we note several interesting similarities and differences. In both cases, the strongest horizontal temperature gradients are confined to the lower boundary layer since heating is being supplied from below. The day-night temperature contrasts,  $\Delta_x \theta'$ , are also roughly the same, here having a value of .11 as compared to .12 in the 2D solution.

On the other hand, there are some important differences between the two sets of isotherms. As we will see later, these contrasts will have an important bearing on the resulting convection cells and the mean zonal velocity. At the lowest model level,  $z = 0.006$ , the maximum temperature lags behind the hot spot of the heat source by  $9^\circ$  (longitude) as compared to  $15^\circ$  in the 2D case. We also recall that in the 2D solution, the lag increased with height to a maximum of  $160^\circ$  at the top. Consequently, the 2D isotherms and the convection cells tilted upward to the left throughout the entire vertical extent of the model. In the 3D case, the situation is quite different. Between  $z = 0$  and  $z = 0.3$  the lag between the maximum temperature and the hot spot also increases with height, but only very gradually. The maximum

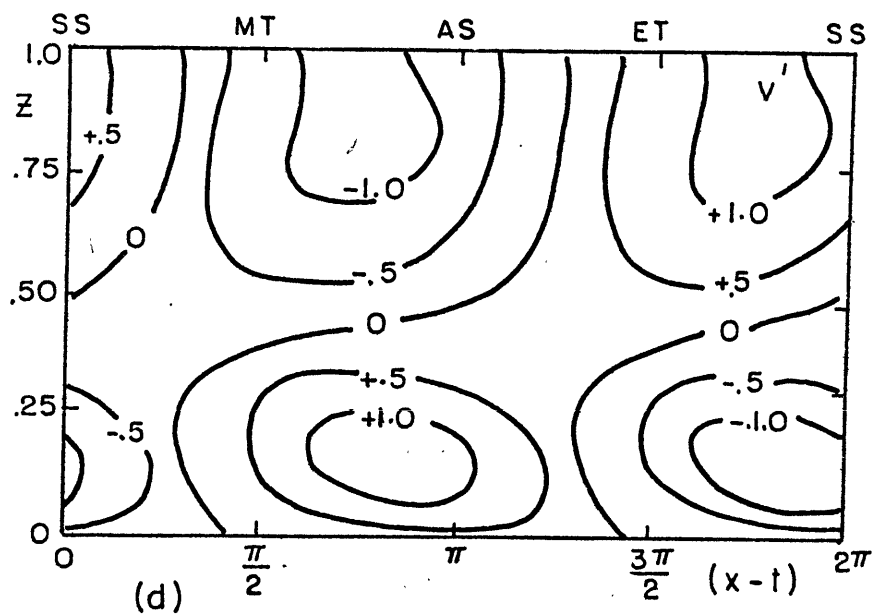
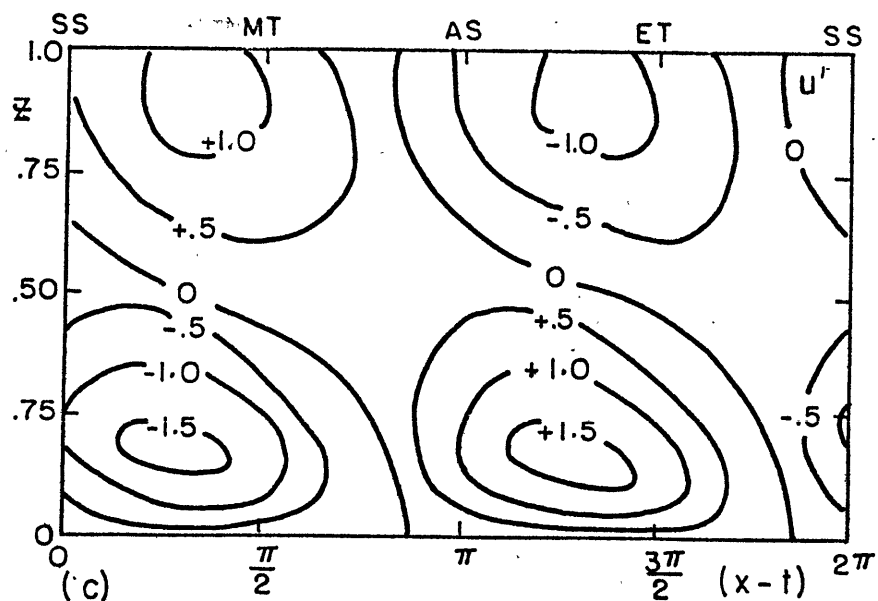
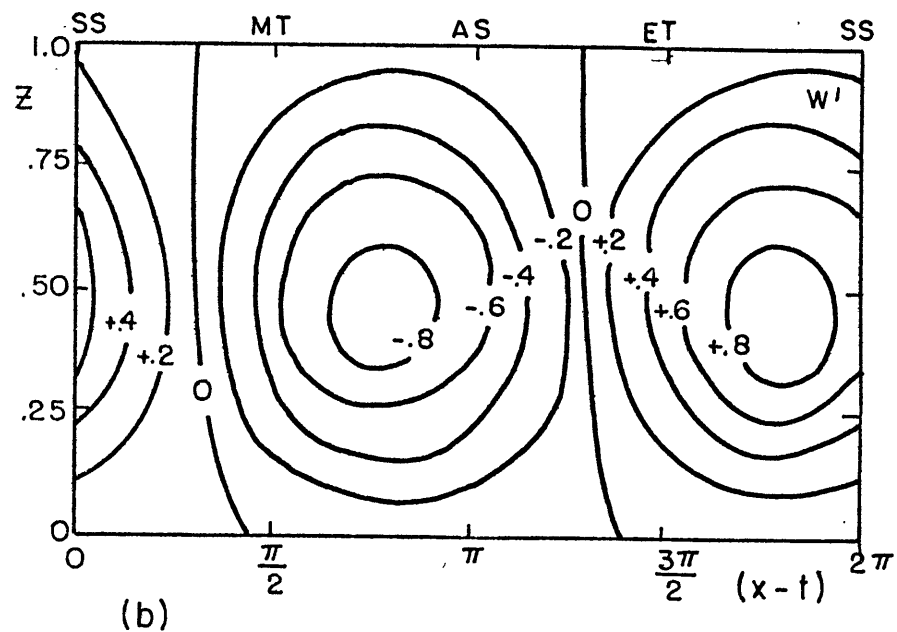
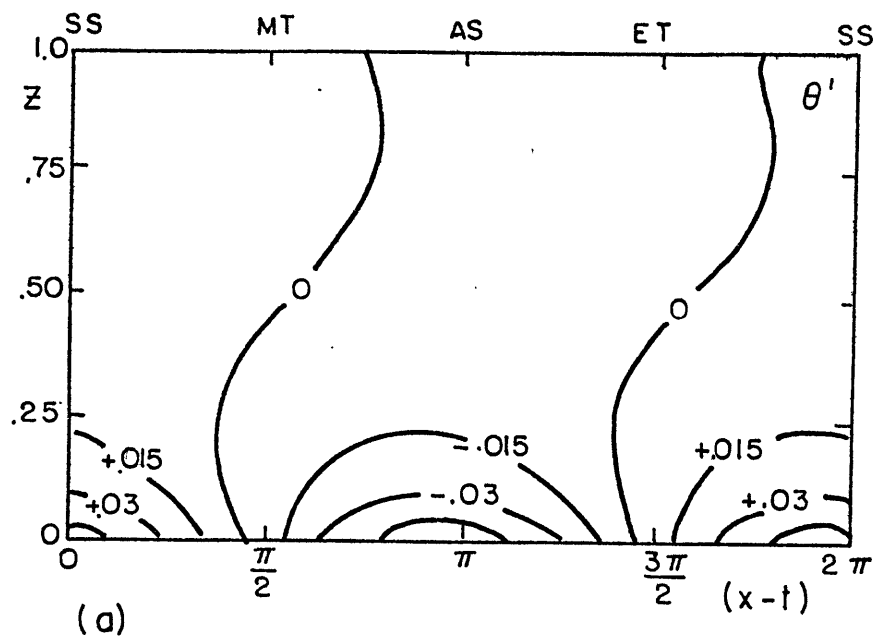


FIGURE 2.14 Three dimensional eddy fields: (a)  $\theta'$ , (b)  $w'$ , (c)  $u'$ , (d)  $v'$ .

lag at  $z = 0.3$  is  $20^\circ$ . Thus the isotherms in the lower portion of the model tilt slightly upward to the left. Above  $z = 0.3$ , however, the sense of the tilt reverses so that the lag in the temperature field decreases with height. In fact at the top of the model, the maximum temperature leads the heat source by  $45^\circ$ . The reason for this tilt reversal is the weak stable mean stratification of the MMC (Figure 2.9). Young and Schubert (1973) observed an analogous behavior in their 2D model with heating from above. In their case, a strong mean static stability was specified for all time. This net stratification was the mechanism responsible for reversing the tilt of the isotherms and convection cells in such a way as to produce Reynolds stresses that would force a retrograde mean zonal flow. We see therefore that the role of stratification in determining the tilt of the convection cells and the direction of the mean zonal flow depends upon the magnitude of the mean (positive) static stability and the location of the heat source (above or below).

In our model, the isotherms in the lower boundary layer retain their tilt upward to the left despite the presence of a positive mean stratification. Since this is the region of maximum thermal forcing (i.e., strongest horizontal temperature contrasts), the resulting longitudinal convection cells will also tilt upward to the left as evidenced by the distribution of  $w'$  and  $u'$  in Figures 2.14b and c. Once again, when

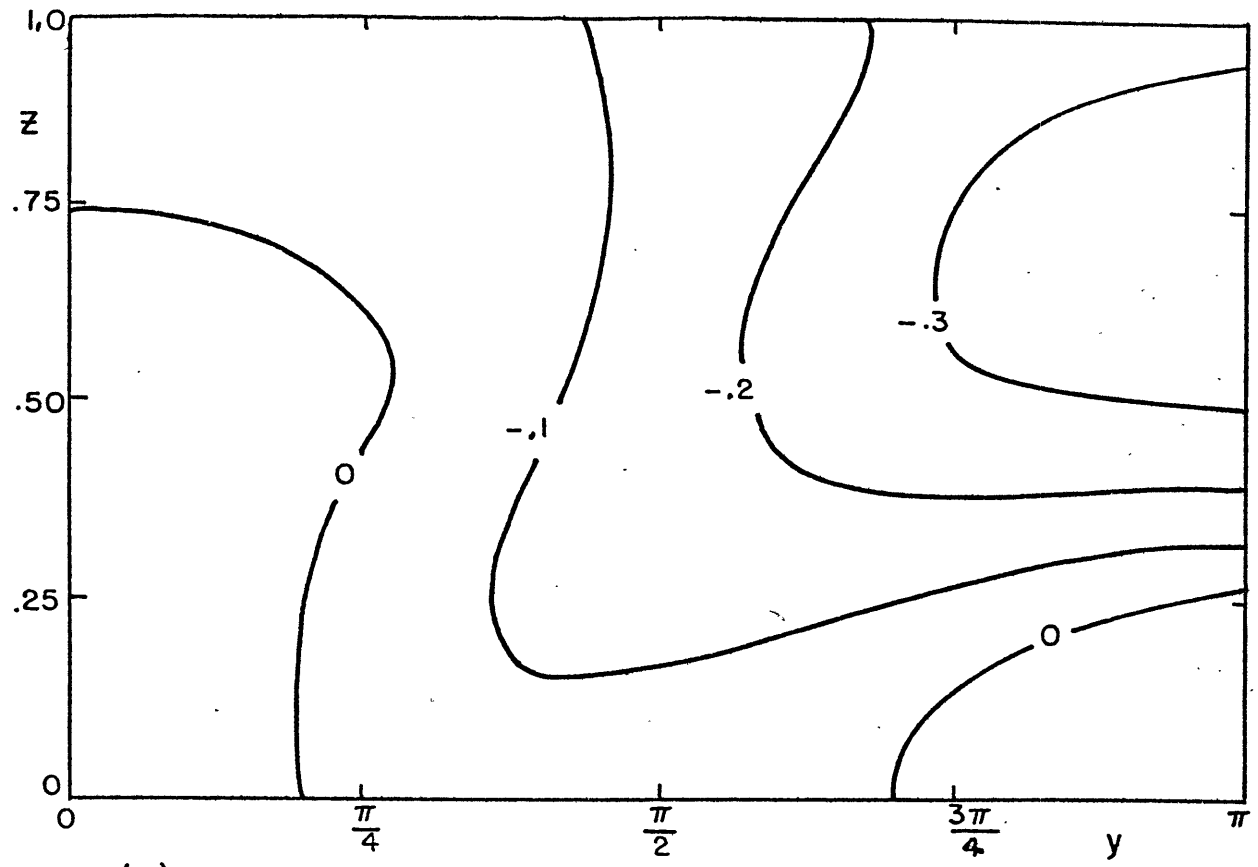
compared to the 2D solution (Figure 2.11), the 3D results show less of a tilt and a smaller phase lag relative to the heat source. In the 2D eddy vertical velocity field, the net tilt, expressed as the phase of  $w'$  near the top relative to the bottom, is approximately  $50^\circ$ . For the 3D  $w'$  the net tilt is only  $18^\circ$ , and thus we expect a weaker forcing of  $\bar{u}$  by the vertical Reynolds stress term  $\overline{u'w'}$ . We also notice that the phase lag of  $w'$  relative to the heat source is roughly  $40^\circ$  (at  $z=.5$ ) as compared to  $90^\circ$  in the 2D case. Thus the longitudinal convection pattern consists of a cellular overturning with the most intense rising motion occurring at the local midafternoon and the most intense sinking motion in the region of local pre-dawn. The above description is valid for  $0 \leq y \leq \pi/2$ . Since  $u'$  and  $w'$  both vary as  $\cos y$ , the longitudinal convection pattern for  $\pi/2 \leq y \leq \pi$  will be similar except for a  $180^\circ$  phase shift. In any event, the maximum vertical velocity is  $w'_{\max} = 0.9$  (dimensional value of  $0.3 \text{ cm s}^{-1}$ ). The strongest eddy zonal velocities appear at the top of the lower boundary layer and have a magnitude of  $u'_{\max} = 1.7$  or  $6.8 \text{ m s}^{-1}$ .

The meridional eddy convection also consists of two large scale convection cells. On the night side, the cell consists of sinking at  $y=0$ , poleward flow in the lower half of the channel, rising at  $y=\pi$  and an equatorward flow in the upper portion of the channel. On the day side, the sense

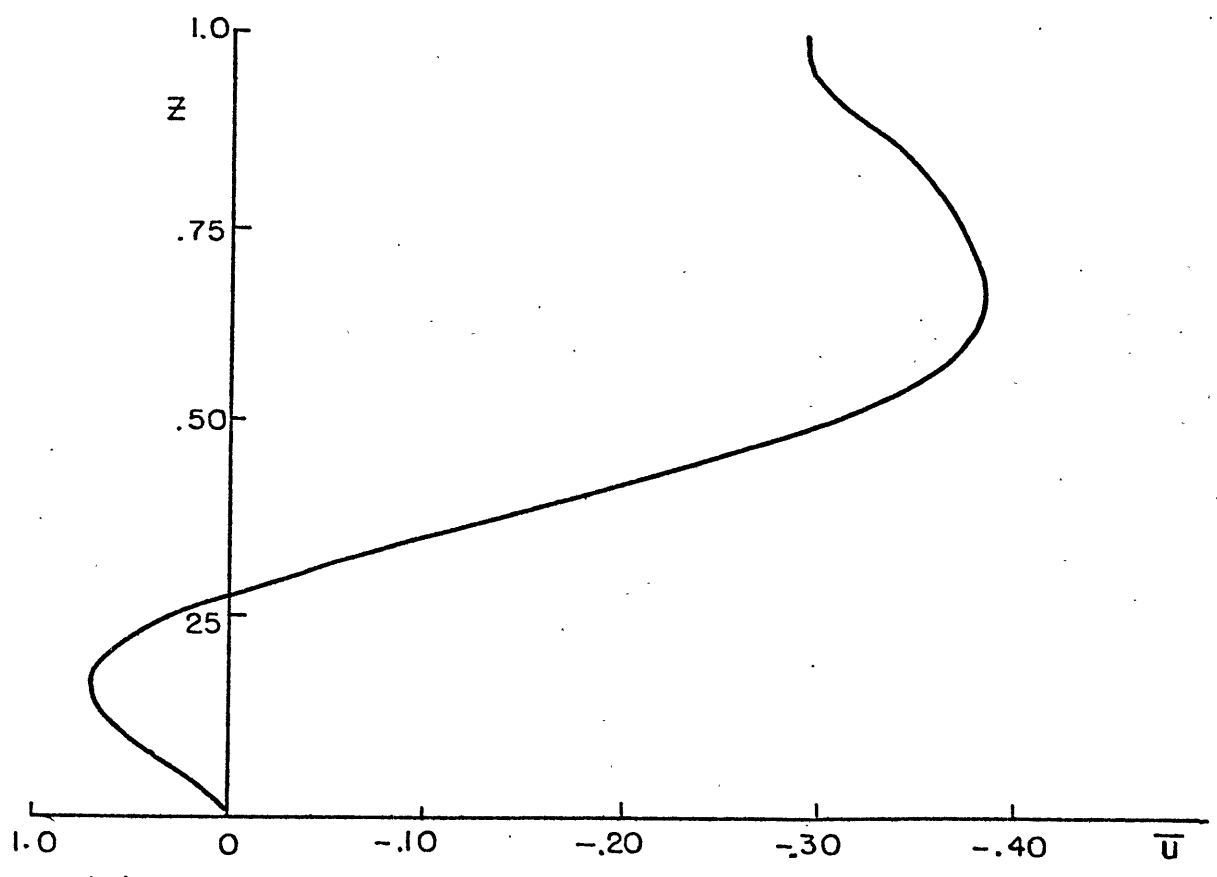
of the circulation is reversed so that rising occurs at  $y=0$  and sinking at  $y=\pi$ . Once again, the strongest horizontal flow appears near the top of the boundary layer with a magnitude of

$$v'_{\max} = 1.4 \text{ or } 5.6 \text{ m s}^{-1}.$$

Having described the MMC and the large scale eddies, we are now ready to examine the mean zonal velocity that develops in our simple three-dimensional model. From equation (2.5.6) we can see that the structure of the mean zonal flow will be strongly influenced by the momentum transporting properties of the MMC and the eddies. In Figure 2.15a  $\bar{u}$  is shown as a function of height and latitude. The velocity is everywhere retrograde except for the two regions of much weaker prograde flow between  $y=0$  and  $y=\pi/4$  and in the lower boundary layer near  $y=\pi$ . The strongest velocities occur at  $y=\pi$  at a height of  $z = .69$ . From Figure 2.15b we see that  $\bar{u}_{\max} = -.38$  or  $1.5 \text{ m s}^{-1}$ . The structure of  $\bar{u}$  can easily be understood in terms of the fluxes of zonal momentum due to the MMC and the eddies. In Figure 2.16 we have plotted the horizontally integrated vertical momentum fluxes as a function of height. The dotted line represents the vertical Reynolds stress term  $\int_0^{\pi} \overline{u'w'} dy$  which clearly corresponds to an upward transport of retrograde momentum at all levels. This is precisely the moving flame effect that arises from the tilt of the eddy convection cells. Obviously the overall effect of the eddies is to force a retrograde mean zonal flow that increases with height.



(a)



(b)

FIGURE 2.15 Three dimensional  $\bar{u}$  for  $G = 1375$   
 $2^2 = 15.5$ ,  $Pr = \dots$  : (a) vertical cross section,  
(b) vertical profile at  $y = \dots$

Since our model is three-dimensional we must also consider the role of the MMC. The dashed line in Figure 2.16 represents the horizontally integrated vertical flux of zonal momentum due to the MMC,  $\int_0^{\pi} \bar{u} \bar{w} dy$ . We can immediately see that this expression corresponds to a downward flux of retrograde momentum. Gierasch (1975) discussed the possibility of an upward flux of retrograde momentum by the MMC. However, this can occur only in the presence of some other mechanism which provides a very strong equatorward flux of retrograde momentum and thus maintains a surplus of retrograde momentum in equatorial regions. Recently, Rossow et. al., (1980) have suggested that barotropic instability in the Venus stratosphere might provide this necessary momentum flux. Base on Mariner 10 photographs of Venus, Travis (1978) has found that the observed zonal wind profile with a midlatitude maximum is barotropically unstable and appears to feed energy to stratospheric eddies with wavenumbers in the range 3-10. Because of limited spectral resolution, the model in this chapter cannot possibly reproduce this behavior.

The solid line in Figure 2.16 represents the total vertical transport of retrograde momentum (i.e., the sum of the eddy and MMC fluxes). From  $z=0$  to  $z = .75$  there is a net upward transport with the strongest flux occurring near the top of the boundary layer which is the level of maximum  $u'$ . Between  $z = .75$  and the top of the model there is an extremely weak downward flux. With this in mind it is easy to

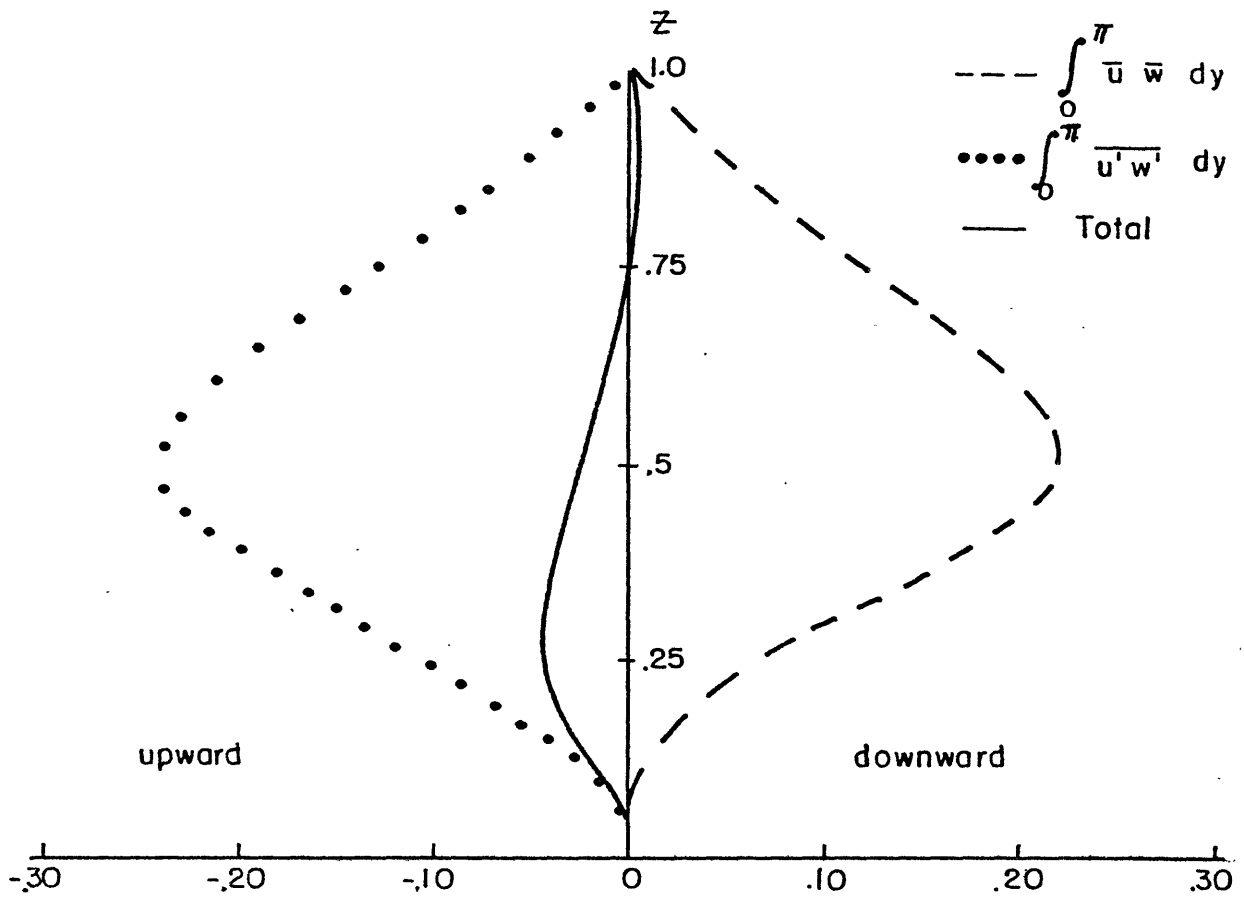


FIGURE 2.16 Vertical transport (horizontally averaged) of zonal momentum. Negative values indicate an upward flux of retrograde momentum.

216

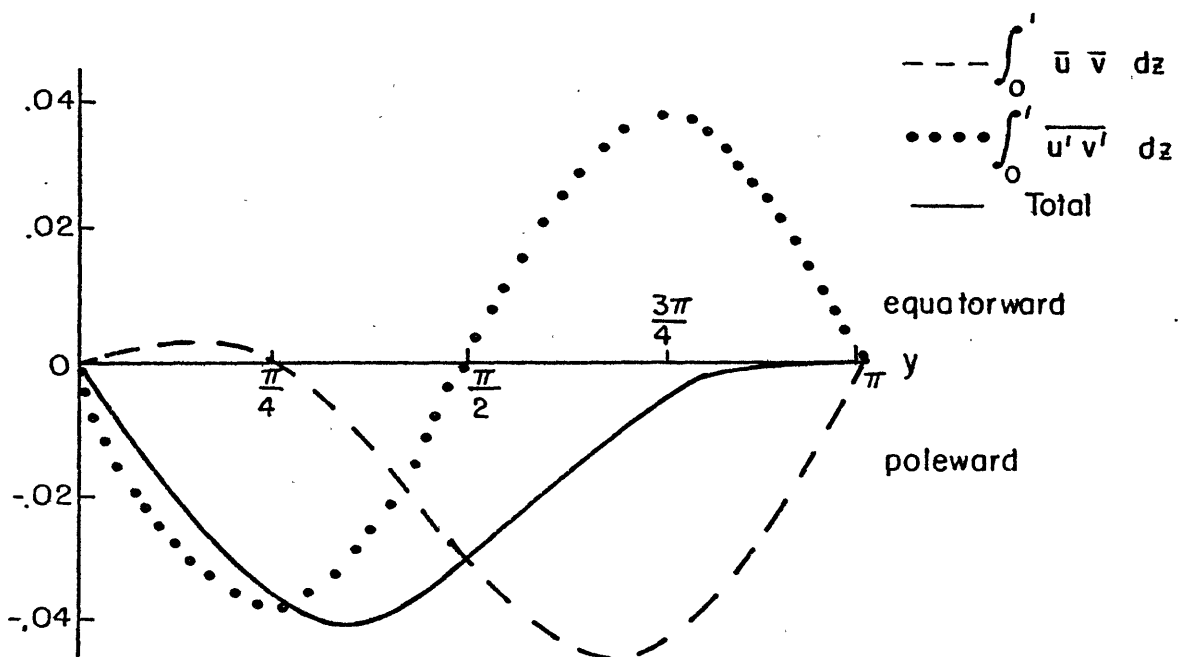


FIGURE 2.17 Horizontal transport (vertically averaged) of zonal momentum. Negative values indicate a poleward flux of retrograde momentum.

217



understand the vertical profile of  $\bar{u}$  shown in Figure 2.15b. The strong upward flux of retrograde momentum in the lower part of the model causes a momentum deficiency below  $z = .25$ , thereby producing a thin layer of prograde flow. These prograde velocities cannot become too large, however, due to the no-slip bottom. The transition from an upward flux to a weak downward flux at  $z = .75$  causes the jet to appear at  $z = .69$ . Comparing Figure 2.15b to the 2D vertical profile of  $\bar{u}$  (Figure 2.12) reveals three differences. The magnitude of  $\bar{u}$  in the 3D case is only one third the size of its 2D counterpart. This is due to the tilt reversal of the 3D isotherms. Next, we notice that the 3D profile does not exhibit the pseudo stress free behavior in the lower boundary layer since the simple relationship

$$\frac{1}{2r^2} \frac{\partial^2 \bar{u}}{\partial z^2} = \frac{\partial \overline{u'w'}}{\partial z}$$

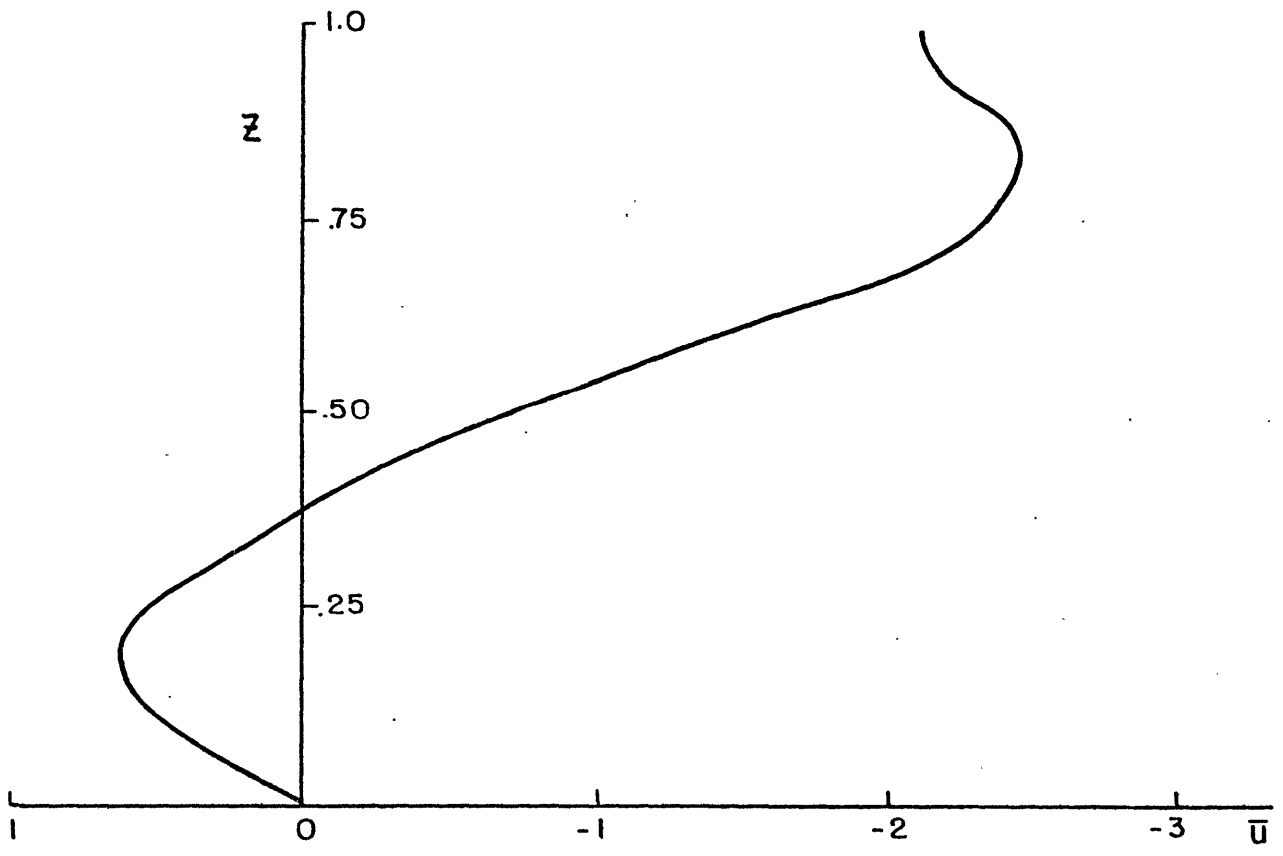
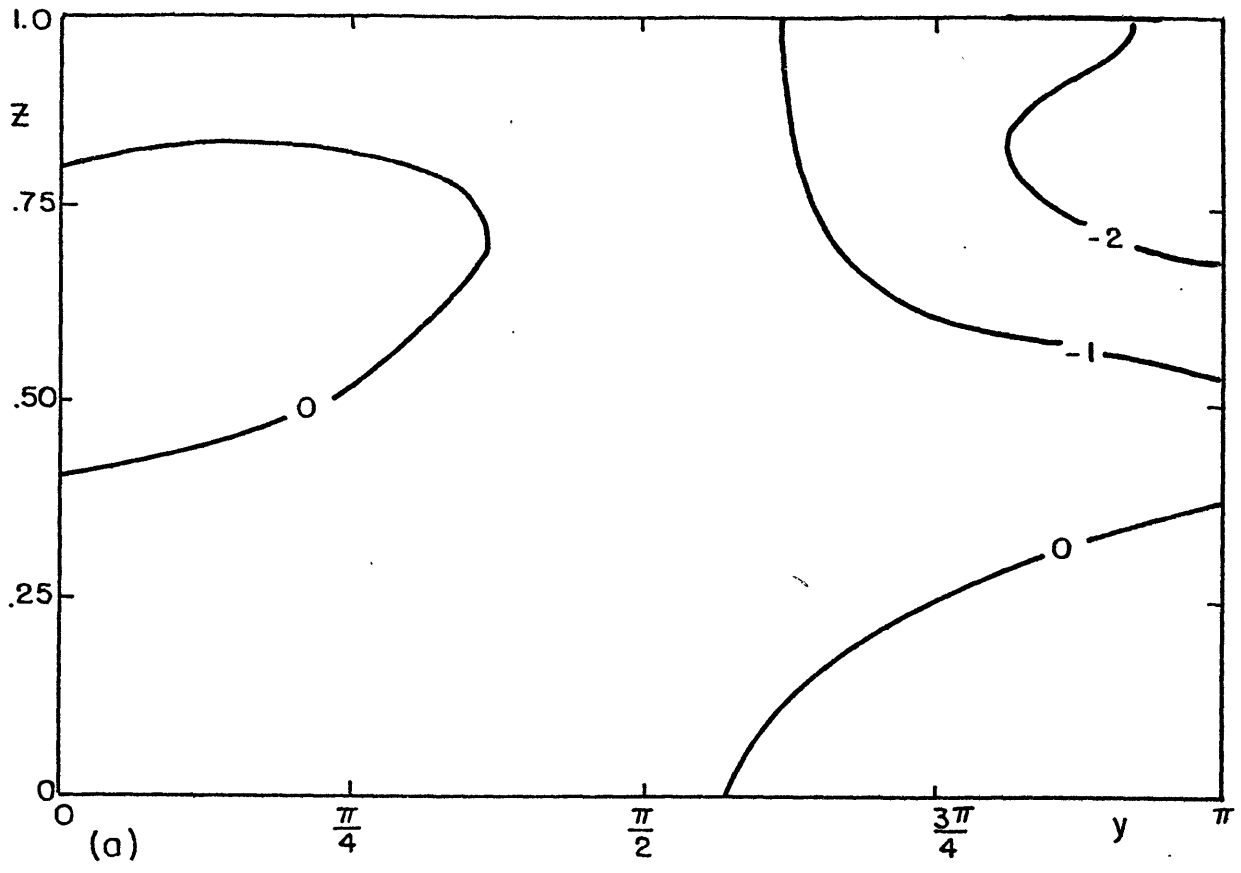
is no longer valid. Finally the 3D jet occurs at  $z = .69$  as compared to the 2D jet which occurred at the top of the model. This again is due to the MMC and its effect on the structure of the eddies.

In Figure 2.17 we have plotted the vertically integrated meridional transport of zonal momentum by the MMC and the eddies as a function of  $y$ . The MMC (dashed line) produces a

poleward flux of retrograde momentum for  $\frac{\pi}{4} \leq y \leq \pi$  and an almost negligible equatorward flux for  $0 \leq y < \frac{\pi}{4}$ . The poleward transport is due to the fact that the maximum retrograde zonal flow occurs in the upper layers and is thus correlated with the poleward branch of the Hadley cell. The dotted curve represents the flux due to the Reynolds stress  $\int_0^1 \overline{u'v'} dz$  and corresponds to a transport of retrograde momentum towards  $y = \frac{\pi}{2}$ . The flux of retrograde momentum is poleward between  $y=0$  and  $\frac{\pi}{2}$  and equatorward between  $\frac{\pi}{2}$  and  $\pi$ . The net flux (solid line) is a poleward transport and thus the largest values of  $\bar{u}$  in Figure 2.15a appear near  $y = \pi$ .

As a comparison, Figure 2.18 shows the mean zonal flow for a 3D case with  $G = 1375$ ,  $2\eta^2 = 15.5$ , and  $Pr = \frac{1}{4}$ . The two main differences between this run and the case of  $Pr = \frac{1}{2}$  are the larger magnitudes of  $\bar{u}$  and the higher altitude of the jet. In this case, the jet occurs at  $z = .83$  with a value of  $\bar{u} = -2.46$  or  $-9.8 \text{ m s}^{-1}$ . The overall solution is qualitatively similar in both cases. Again the main differences are the increased velocities in the case of small Prandtl number. For  $Pr = \frac{1}{4}$  the maximum velocities are listed in the second row of Table 2.3.

We have also run the model for  $Pr = \frac{1}{10}$  with the same values of thermal forcing and thermal frequency as above. Once again we find that all of the velocity components exhibit



(b) FIGURE 2.18  $\bar{u}$  as in Figure 2.15 except for  $Pr = \frac{1}{2}$ :  
 (a) vertical cross section, (b) vertical profile at  $y = \pi$ .

an increase in magnitude as the Prandtl number goes to smaller values. For this case, the maximum velocity magnitudes are listed in the third row of Table 2.3.

	$ \bar{v}_{\max} $	$ \bar{w}_{\max} $	$ u'_{\max} $	$ v'_{\max} $	$ \bar{u}_{\max} $
Pr = .5	2.9 ; 11.6	1.2 ; 0.39	1.7 ; 6.8	1.4 ; 5.6	0.38 ; 1.5
Pr = .25	3.9 ; 15.6	1.6 ; 0.52	2.5 ; 10.0	2.1 ; 8.4	2.5 ; 10.0
Pr = .1	4.9 ; 19.6	2.5 ; 0.82	7.4 ; 29.1	5.3 ; 21.2	5.0 ; 20.0

Table 2.3: Magnitude of maximum velocity components as a function of Pr for  $G = 1375$   $2h^2 = 15.5$ . The first value in each box is the dimensionless magnitude and the second value is the dimensional value. The units for the dimensional values are  $\text{cm s}^{-1}$  for w and  $\text{m s}^{-1}$  for all others.

## 2.6 Discussion

In this chapter, we have developed a highly simplified Boussinesq model for a study of the moving flame mechanism in three dimensions. We began by solving for the steady state mean meridional circulation that develops as a result of equator to pole heating contrasts. As expected, the circulation consists of a thermally direct Hadley cell with rising motion in regions of heating and sinking in regions of cooling. In agreement with other theoretical studies (e.g., Stone, 1968) in the case of heating from below, the nonlinear interactions cause the flow to be concentrated near the lower boundary and near  $y=0$ . This MMC solution was then used to determine the large scale eddies and the mean zonal flow. In all cases considered, we found that the eddies produced an upward flux of retrograde momentum which supported a retrograde mean zonal flow. The MMC produced a weaker downward momentum flux so that the net transport was upward. There was also a net poleward flux of retrograde momentum by the MMC and thus the strongest zonal flow occurred at  $y = \pi$ .

We realize that the model has some simplifications which if removed could alter our conclusions. The two most questionable approximations are the geometry of the model and the low spectral resolution. By considering a rectangular coordinate system we are automatically eliminating certain geometrical phenomena such as cyclostraphic balance. On the

From the values in Table 2.3 we can clearly see that by decreasing the value of the Prandtl number we do indeed increase the magnitude of the retrograde mean zonal velocity. In fact, it was this small Prandtl number behavior of liquid mercury that led Schubert and Whitehead (1969) to suggesting that the moving flame mechanism could drive the four-day circulation on Venus and that the effective Prandtl number of the Venus stratosphere might be quite small. However if we again examine Table 2.3 we find that all other velocity components show a similar increase as the Prandtl number goes to smaller values. For  $Pr = .25$  and  $Pr = .1$ , all of the horizontal velocity components are within a factor of two of each other. For  $Pr = .5$ ,  $\bar{u}$  is smaller than the other components by at least a factor of four.

Since this behavior is contrary to the observed velocity fields on Venus (i.e., for the four-day circulation,  $\bar{u}$  is typically one or two orders of magnitude larger than  $\bar{v}$ ,  $u'$ , or  $v'$ ), we must seriously question the role of the moving flame mechanism in driving the rapid retrograde zonal flow. Furthermore, in all of the cases considered,  $\bar{u}$  was not significantly larger than the speed of the heat source. Consequently, we must conclude that if the moving flame type forcing is confined to the cloud tops, then this mechanism alone cannot adequately explain the observed features of the four-day circulation.

other hand, based on the magnitude of  $\bar{u}$  in the above results, it is unlikely that cyclostrophic balance will occur as a result of moving flame forcing since the motion of the heat source only seems capable of producing velocities that are much too weak.

As discussed in the previous section, the low spectral resolution renders the model incapable of simulating potentially unstable modes with higher wavenumbers. Both the geometric and resolution problems will be eliminated in the next chapter.

Finally we return to the linearization used in this model, namely the neglecting of Reynolds stresses and eddy transport terms in the MMC equations. This linearization allowed us to determine and fix the MMC independent of the eddies and  $\bar{u}$ . In Figure 2.19 we have plotted the vertical heat fluxes due to the MMC (dashed line) and the eddies (dotted line) for the two 3D cases presented above. In both cases, the eddy flux is smaller than the MMC flux by a factor of two so that the neglecting of eddy transport terms in MMC equations should not adversely affect the overall results. If anything, the upward heat flux due to the eddies would probably strengthen the mean static stability and thereby prevent the eddies and  $\bar{u}$  from growing any larger than their current values.

Based on the results of this chapter, we must tentatively

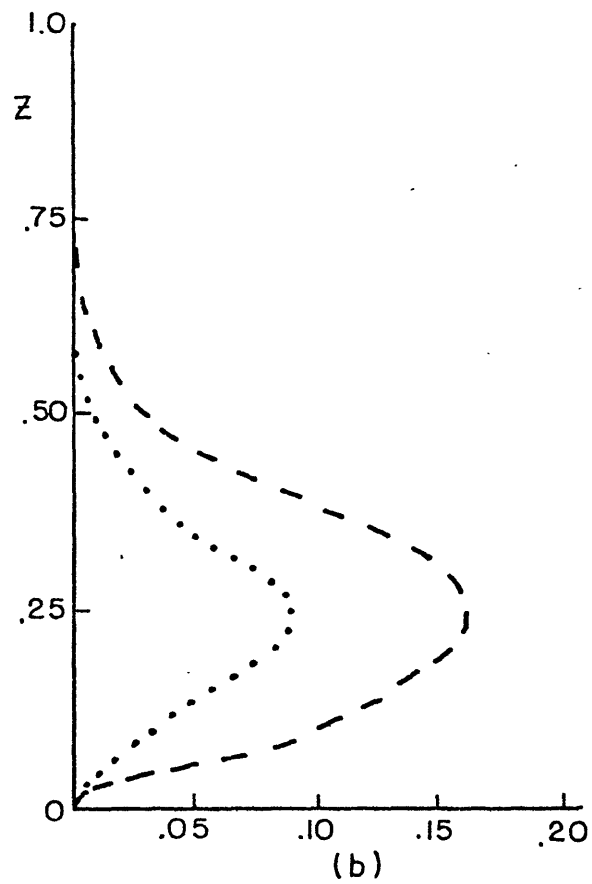
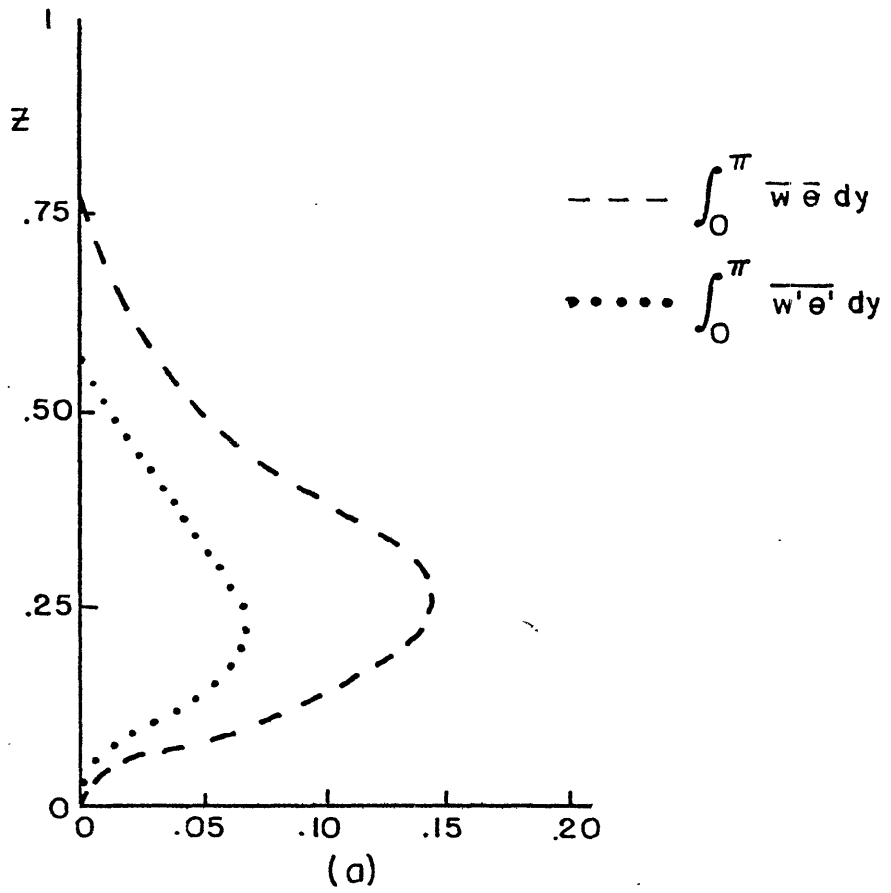


FIGURE 2.19 Vertical heat transport (horizontally averaged) for  $G = 1375$ ,  $2^2 = 15.5$ : (a)  $Pr = \frac{1}{2}$ ,  $Pr = \frac{1}{4}$ .



conclude that if the thermal forcing is confined primarily to the cloud tops, then the moving flame mechanism cannot consistently explain the existence of the rapid retrograde zonal circulation and the weak MMC and eddy velocities observed in the stratosphere of Venus.

## CHAPTER 3

NONLINEAR SPECTRAL MODEL3.1 Introduction

The results of the previous chapter indicate that within the context of a cartesian coordinate system, the moving flame mechanism can maintain a retrograde mean zonal flow. For the parameter values appropriate to the Venus stratosphere, the model produced horizontal velocities that were of the same order of magnitude as the speed of the heat source. In general, however,  $\bar{u}$  tended to be smaller than  $\bar{v}$ ,  $u'$ , and  $v'$  by at least a factor of two. We recall that for the 4-day circulation of the Venus stratosphere,  $\bar{u}$  exceeds the overhead speed of the sun by an order of magnitude. Thus it appears that the moving flame effect by itself cannot completely explain the rapid retrograde flow on Venus.

Among the assumptions used in developing the linearized model, the two that we intend to relax are the restrictions imposed by rectangular geometry and low horizontal resolution. To accomplish this, we will numerically (spectrally) solve the full nonlinear equations written in spherical coordinates. In section 3.2 we will derive the appropriate equations of motion. Section 3.3 contains a description of the numerical methods followed by section 3.4 with the results.

### 3.2 Details of the Model

The model described in this section will be used to investigate the effects of a moving periodic heat source upon a thin spherical shell of fluid. In deriving the equations of motion, we will retain some of the simplifications used in the previous chapter. We still assume:

- (a) the fluid is Boussinesq and in hydrostatic balance;
- (b) no planetary rotation;
- (c) thermal forcing by the moving, periodic heat source is specified as a boundary condition at the bottom;
- (d) a rigid, no-slip bottom and a flat stress free top.

The justification and relevance of these characteristics has already been discussed in Chapter 2. As was mentioned in the introduction to this chapter, the present model represents an improvement over the linearized model in several ways:

- (a) the equations are written for spherical geometry;
- (b) greater horizontal resolution (i.e. higher harmonics);
- (c) a more realistic heating function;
- (d) retains higher order nonlinearities due to greater resolution.

These changes are motivated by the desire to more realistically simulate the applicability of the moving flame mechanism to a planetary atmosphere. The other major difference between the two models is that in the nonlinear spectral model, the

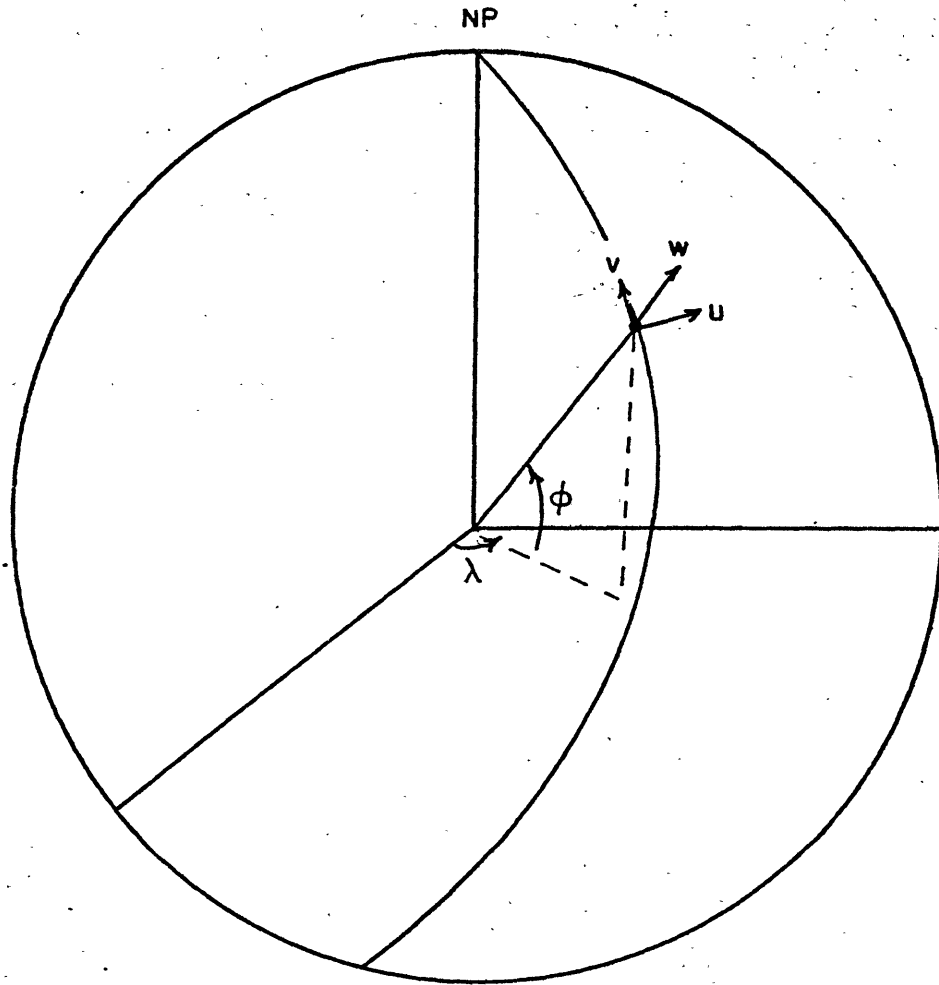


FIGURE 3.1 Coordinate system and velocity compounds for spherical geometry. The heat source moves in the positive direction (i.e., counterclockwise when viewed from the north pole).

horizontal momentum equations are replaced by prognostic equations for the vertical component of vorticity,  $\zeta = \underline{k} \cdot \nabla \times \underline{v}$ , and the horizontal divergence,  $\delta = \nabla \cdot \underline{v}$ . The reason for this is numerical convenience since vorticity and divergence are directly expandable in series of surface spherical harmonics, and the resulting prognostic equations are easier to march in time than are the spectral momentum equations. With these factors in mind, we now proceed with the description of the model and the derivation of the necessary equations.

The coordinate system we use is the standard longitude, latitude, height system,  $(\lambda, \phi, z)$ , where  $\lambda$  is the azimuthal angle measured in the direction of the heat source motion,  $\phi$  is the latitude measured from the equator (positive north and negative south), and  $z$  is the height above the lower boundary (the unit sphere in terms of dimensionless variables). In Figure 3.1, we show the coordinates  $(\lambda, \phi, z)$  and the respective velocity components  $(u, v, w)$ . When viewed from the north pole, the sun (i.e. heat source) moves counter-clockwise and the planet Venus rotates clockwise.

We begin our derivation of the dimensionless vorticity and divergence equations by first writing the dimensionless horizontal momentum equation in vector form

$$\frac{\partial \underline{v}}{\partial t} = - \underline{v} \cdot \nabla \underline{v} - w \frac{\partial \underline{v}}{\partial z} - G \nabla p + \frac{1}{2r^2} \underline{F} \quad (3.2.1)$$

where  $\underline{v} = (u, v)$  is the horizontal velocity,  $\nabla = \left( \frac{1}{\cos \phi} \frac{\partial}{\partial \lambda}, \frac{\partial}{\partial \phi} \right)$  is the horizontal del operator,  $G$  and  $2\gamma^2$  are the thermal forcing and momentum frequency parameters (see Chapter 2), and

$$\underline{F} = \frac{\partial^2 \underline{v}}{\partial z^2} + \epsilon_v \nabla^2 \underline{v}$$

is the diffusion term where  $\nabla^2$  is the horizontal Laplacian operator and  $\epsilon_v = \left( \frac{h}{a} \right)^2 \frac{v_H}{v_v}$ . The procedure and scales for making the equations dimensionless are the same as in the linearized model except for one minor difference. In spherical coordinates, the horizontal length scale must be redefined as  $k = \frac{1}{a \cos \phi}$  and the resulting horizontal velocity scale  $u_0$  is identified as the overhead speed of the sun at the equator.

Following Bourke (1972), we use the vector identity

$$\underline{v} \cdot \nabla \underline{v} = \underline{k} \times \underline{v} \zeta + \nabla \left( \frac{\underline{v} \cdot \underline{v}}{2} \right)$$

to rewrite the momentum equation as

$$\frac{\partial \underline{v}}{\partial t} = - \underline{k} \times \underline{v} \zeta - w \frac{\partial \underline{v}}{\partial z} - \nabla \left( G \rho + \frac{\underline{v} \cdot \underline{v}}{2} \right) + \frac{1}{2\gamma^2} \underline{F} \quad (3.2.2)$$

where  $\underline{k} = (0, 0, 1)$  is the unit vector in the vertical direction and  $\zeta = \underline{k} \cdot \nabla \times \underline{v}$  is the vertical component of relative vorticity. We next apply the operator  $\underline{k} \cdot \nabla \times$  to (3.2.2) and after rearranging terms we are left with the vorticity equation

$$\begin{aligned} \frac{\partial \zeta}{\partial t} = & - \underline{v} \cdot \nabla \zeta - w \frac{\partial \zeta}{\partial z} - \zeta \delta + \underline{k} \cdot \left( \frac{\partial \underline{v}}{\partial z} \times \nabla w \right) \\ & + \frac{1}{2\gamma^2} \left[ \frac{\partial^2 \zeta}{\partial z^2} + \epsilon_v (\nabla^2 \zeta + 2\zeta) \right] \end{aligned} \quad (3.2.3)$$

where  $\delta = \nabla \cdot \underline{v}$  is the horizontal divergence.

To obtain the divergence equation, we apply the operator  $\nabla \cdot$  to (3.2.2) and upon rearranging terms we have

$$\begin{aligned} \frac{\partial \delta}{\partial t} = & - \underline{k} \cdot \nabla \times \underline{v} \zeta - w \frac{\partial \zeta}{\partial z} - \frac{\partial \underline{v}}{\partial z} \cdot \nabla w - \nabla^2 \left( Gp + \frac{\underline{v} \cdot \underline{v}}{2} \right) \\ & + \frac{1}{2\gamma^2} \left[ \frac{\partial^2 \delta}{\partial z^2} + \epsilon_v (\nabla^2 \delta + 2\delta) \right] \end{aligned} \quad (3.2.4)$$

The third prognostic equation for our model is the thermodynamic equation which can immediately be written

$$\frac{\partial \theta}{\partial t} = - \underline{v} \cdot \nabla \theta - w \frac{\partial \theta}{\partial z} + \frac{1}{2\gamma^2} \left[ \frac{\partial^2 \theta}{\partial z^2} + \epsilon_k \nabla^2 \theta \right] \quad (3.2.5)$$

where once again  $\theta$  is the deviation of potential temperature from the reference value  $T_0$ ,  $2\eta^2$  is the thermal frequency parameter and  $\epsilon_k = \left(\frac{h}{a}\right)^2 \frac{\kappa_H}{\kappa_V}$ .

To complete our set of equations we need the following diagnostic relationships for the pressure deviations, velocity components, streamfunction, and velocity potential:

the hydrostatic equation

$$\frac{\partial p}{\partial z} = \theta \quad (3.2.6)$$

the continuity equation

$$\delta + \frac{\partial w}{\partial z} = 0 \quad (3.2.7)$$

the relationships between streamfunction,  $\psi$ , and vorticity and between velocity potential,  $\chi$ , and divergence

$$\zeta = \nabla^2 \psi$$

$$\delta = \nabla^2 \chi \quad (3.2.8)$$

and finally, an expression for  $\underline{v}$



$$\underline{V} = \underline{k} \times \nabla \psi + \nabla \chi \quad (3.2.9)$$

We now proceed with expanding the vector equations in spherical coordinates. At this point we introduce the alternative horizontal velocity components  $U, V$  defined by

$$U = u \cos \phi \quad (3.2.10)$$

$$V = v \cos \phi$$

This substitution was first suggested by Robert (1966) since the scalars  $U, V$  are directly expandable as series of spherical harmonics whereas  $u, v$  are not. This is a consequence of the dependence of  $\underline{V}$  upon  $\psi$  and  $\chi$ , expressed by (3.2.9), and the presence of a factor of  $\cos \phi$  in the denominator of the operator.

Using these new velocity components, we can now write (3.2.3) - (3.2.5) and (3.2.9) in spherical coordinates: vorticity and divergence equations

$$\begin{aligned} \frac{\partial \zeta}{\partial t} = & - \frac{1}{\cos^2 \phi} \left[ U \frac{\partial \zeta}{\partial \lambda} + V \cos \phi \frac{\partial \zeta}{\partial \phi} \right] - w \frac{\partial \zeta}{\partial z} - \zeta \delta \\ & - \frac{1}{\cos^2 \phi} \left[ \frac{\partial V}{\partial z} \frac{\partial w}{\partial \lambda} - \frac{\partial U}{\partial z} \cos \phi \frac{\partial w}{\partial \phi} \right] \\ & + \frac{1}{2\gamma^2} \left[ \frac{\partial^2 \zeta}{\partial z^2} + \epsilon_v (\nabla^2 \zeta + 2\zeta) \right] \end{aligned} \quad (3.2.11)$$

$$\begin{aligned}
\frac{\partial \delta}{\partial t} = & \frac{1}{\cos^2 \phi} \left[ V \frac{\partial \delta}{\partial \lambda} - U \cos \phi \frac{\partial \delta}{\partial \phi} \right] - w \frac{\partial \delta}{\partial z} + \zeta^2 \\
& - \frac{1}{\cos^2 \phi} \left[ \frac{\partial V}{\partial z} \frac{\partial w}{\partial \lambda} + \frac{\partial V}{\partial z} \cos \phi \frac{\partial w}{\partial \phi} \right] - \nabla^2 \left[ \frac{U^2 + V^2}{2 \cos^2 \phi} \right] \\
& - G \nabla^2 \psi + \frac{1}{2\gamma^2} \left[ \frac{\partial^2 \delta}{\partial z^2} + \epsilon_v (\nabla^2 \delta + 2\delta) \right]
\end{aligned}$$

(3.2.12)

thermodynamic equation

$$\begin{aligned}
\frac{\partial \theta}{\partial t} = & - \frac{1}{\cos^2 \phi} \left[ U \frac{\partial \theta}{\partial \lambda} + V \cos \phi \frac{\partial \theta}{\partial \phi} \right] - w \frac{\partial \theta}{\partial z} \\
& + \frac{1}{2\gamma^2} \left[ \frac{\partial^2 \theta}{\partial z^2} + \epsilon_r \nabla^2 \theta \right]
\end{aligned}$$

(3.2.13)

equations for U and V

$$U = - \cos \phi \frac{\partial \psi}{\partial \lambda} + \frac{\partial \chi}{\partial \phi}$$

(3.2.14)

$$V = \frac{\partial \psi}{\partial \phi} + \cos \phi \frac{\partial \chi}{\partial \lambda}$$

The remaining diagnostic equations (3.2.6) - (3.2.8) are left unchanged. In all cases we have not expanded the  $\nabla^2$

operator because of its rather lengthy form. We will see in section 3.3, however, that it has a particularly simple representation in the spectral equations.

### 3.2.1 Boundary Conditions

As was mentioned in the introduction to this chapter, we will assume the same dynamical boundary conditions as in the linearized model. The bottom is taken to be a rigid, no-slip surface and the top is considered to be flat and stress free. This gives us the following conditions:

$$\begin{aligned} w = u = v = 0 & \quad \text{at} \quad z = 0 \\ w = \frac{\partial u}{\partial z} = \frac{\partial v}{\partial z} = 0 & \quad \text{at} \quad z = 1 \end{aligned} \quad (3.2.15)$$

In terms of vorticity, divergence,  $U$ , and  $V$  these boundary conditions are

$$\zeta = \delta = U = V = w = 0 \quad \text{at} \quad z = 0 \quad (3.2.16)$$

$$\frac{\partial \zeta}{\partial z} = \frac{\partial \delta}{\partial z} = \frac{\partial U}{\partial z} = \frac{\partial V}{\partial z} = w = 0 \quad \text{at} \quad z = 1$$

As in the linearized model of Chapter 2 we again assume that the boundary conditions consist of heating from below by a moving periodic heat source and an insulating top. The vertical heat flux is assumed to be due to turbulent processes and therefore related to  $\frac{\partial \theta}{\partial z}$ . Following the discussion in section 2.3 we consider diurnal variations that follow a heat source analogous to the sun and meridional variations following  $\cos \phi$ . Such a flux would be given by

$$F(\lambda, \phi, t) = \begin{cases} -Q^* \cos(\lambda - t) \cos \phi & |\lambda - t| \leq \frac{\pi}{2} \\ 0 & |\lambda - t| > \frac{\pi}{2} \end{cases} .$$

In spherical geometry, however, the range of  $\phi$  is from 0 to  $\frac{\pi}{2}$  so that the horizontal integral of  $F$  is nonzero and thus the global mean value  $\langle \theta \rangle = 0$  would not be preserved. To avoid this unrealistic possibility, we will balance the heating by subtracting out the global mean flux  $\langle F \rangle = -\frac{Q^*}{4}$ . We point out that this is primarily a mathematical tool to maintain an equilibrium state and does not necessarily lend itself to a simple physical interpretation (although the boundary condition to be presented does resemble a balance between uniform longwave cooling and shortwave heating). Furthermore, since we are really interested in the horizontal heating contrasts, removing the global mean flux should not adversely effect our results. The final

dimensionless thermal boundary conditions for the spherical model are therefore given by

$$\frac{\partial \theta}{\partial z} = \left\{ \begin{array}{ll} \frac{1}{4} - \cos(\lambda-t) \cos \phi & |\lambda-t| \leq \frac{\pi}{2} \\ \frac{1}{4} & |\lambda-t| > \frac{\pi}{2} \end{array} \right\} \text{ at } z=0 \quad (3.2.17)$$

at  $z=1$

where  $(\lambda-t)$  is the local time of day measured from zero at local noon. As in Chapter 2 the temperature scale determined from the heat flux boundary condition is

$$\Delta T \sim \frac{F_0}{\rho_0 c_p k_v} = 120^\circ \text{K}$$

From (3.2.17) we immediately notice that the diurnal and meridional differential heating contrasts are of the same order of magnitude so that we might expect comparable zonal and meridional velocities in our results.

Using the zonal Fourier analysis of the diurnal heating from Appendix A, we find that the zonal mean heat flux at the bottom is given by

$$\frac{\partial \bar{\theta}}{\partial z} = \frac{1}{4} - \frac{1}{\pi} \cos \phi \quad (3.2.18)$$

which corresponds to net heating between the equator and  $\phi \simeq 38^\circ$  and net cooling between  $\phi \simeq 38^\circ$  and the pole. If we next apply the operator

$$\int_{-\frac{\pi}{2}}^{\frac{\pi}{2}} ( ) \cos \phi \, d\phi$$

to (3.2.18) we can see that the net horizontally integrated heat flux is zero so that the global mean of  $\langle \theta \rangle = 0$  remains unchanged.

Having now derived the necessary equations and boundary conditions, we may turn our attention to the spectral method of solution.

### 3.3 Numerical Methods

To solve our model equations (3.2.11) - (3.2.14) and (3.2.6) - (3.2.8) we will follow a spectral or Galerkin approach in the horizontal and finite differencing in the vertical. In the spectral method, each of the dependent variables is expanded in a series of orthogonal functions of the two space coordinates  $\lambda$  and  $\phi$ . After expanding the variables, each equation is multiplied by the appropriate

function and integrated over the entire domain. The resulting set of equations for the harmonic coefficients contains derivatives with respect to time and height only since the horizontal derivatives are replaced by algebraic expressions. For our problem, the natural choice of expansion functions is the set of surface spherical harmonics which represents the set of orthonormal eigenfunctions of the two dimensional Laplacian operator on the surface of the unit sphere.

The spherical harmonic of order  $m$  and degree  $n$  is defined as

$$Y_n^m(\lambda, \phi) = P_n^m(\sin \phi) e^{im\lambda} \quad (3.3.1)$$

where  $P_n^m(\sin \phi)$  is the normalized associated Legendre polynomial of order  $m$  and degree  $n$ .

From Appendix C we have the orthonormality condition

$$\frac{1}{2\pi} \int_0^{2\pi} \int_{-\frac{\pi}{2}}^{\frac{\pi}{2}} Y_n^m \widetilde{Y}_q^p \cos \phi \, d\phi \, d\lambda = \begin{cases} 1 & \text{for } (m,n) = (p,q) \\ 0 & \text{for } (m,n) \neq (p,q) \end{cases}$$

where  $\widetilde{(\quad)}$  stands for the complex conjugate. We also have the following expressions for the space derivatives

$$\frac{\partial Y_n^m}{\partial \lambda} = im Y_n^m$$

$$\cos \phi \frac{\partial Y_n^m}{\partial \phi} = (n+1) D_n^m Y_{n-1}^m - n D_{n+1}^m Y_{n+1}^m \quad (3.3.2)$$

where 
$$D_n^m = \left[ \frac{n^2 - m^2}{4n^2 - 1} \right]^{\frac{1}{2}}$$

and we have the very simple expression for the Laplacian

$$\nabla^2 Y_n^m = -n(n+1) Y_n^m \quad (3.3.3)$$

We next expand each of the dependent variables as a truncated series of spherical harmonics

$$\begin{bmatrix} \theta(\lambda, \phi, z, t) \\ \rho \\ \zeta \\ \delta \\ \omega \\ \psi \\ \chi \end{bmatrix} = \sum_{m=-M}^M \sum_{n=|m|}^M \begin{bmatrix} \theta_n^m(z, t) \\ \rho_n^m \\ \zeta_n^m \\ \delta_n^m \\ \omega_n^m \\ \psi_n^m \\ \chi_n^m \end{bmatrix} P_n^m(\sin \phi) e^{im\lambda} \quad (3.3.4)$$



and

$$\begin{bmatrix} U(\lambda, \phi, z, t) \\ V \end{bmatrix} = \sum_{m=-M}^M \sum_{n=|m|}^{M+1} \begin{bmatrix} U_n^m(z, t) \\ V_n^m \end{bmatrix} P_n^m(\sin \phi) e^{im\lambda} \quad (3.3.5)$$

where  $M$  is the truncation wavenumber for triangular truncation. We note that the series for  $U$  and  $V$  are truncated at  $n = M + 1$ . This is a consequence of the fact that  $U$  and  $V$  are determined diagnostically from the streamfunction and velocity potential. The precise reason for this will become clear after we present the spectral equations. In Figure 3.2 we show the domain of the harmonic coefficients in wavenumber,  $(m, n)$ , space for triangular truncation. As an example, for  $M = 6$ , the expansions in (3.3.4) include all components on and within triangle ABD while the expansions in (3.3.5) include all components on and within triangle ACE. The source of the term triangular truncation is now quite obvious from the diagram.

To obtain the equations for the harmonic coefficients, we substitute (3.3.4) and (3.3.5) in the model equations and then apply the transform operator

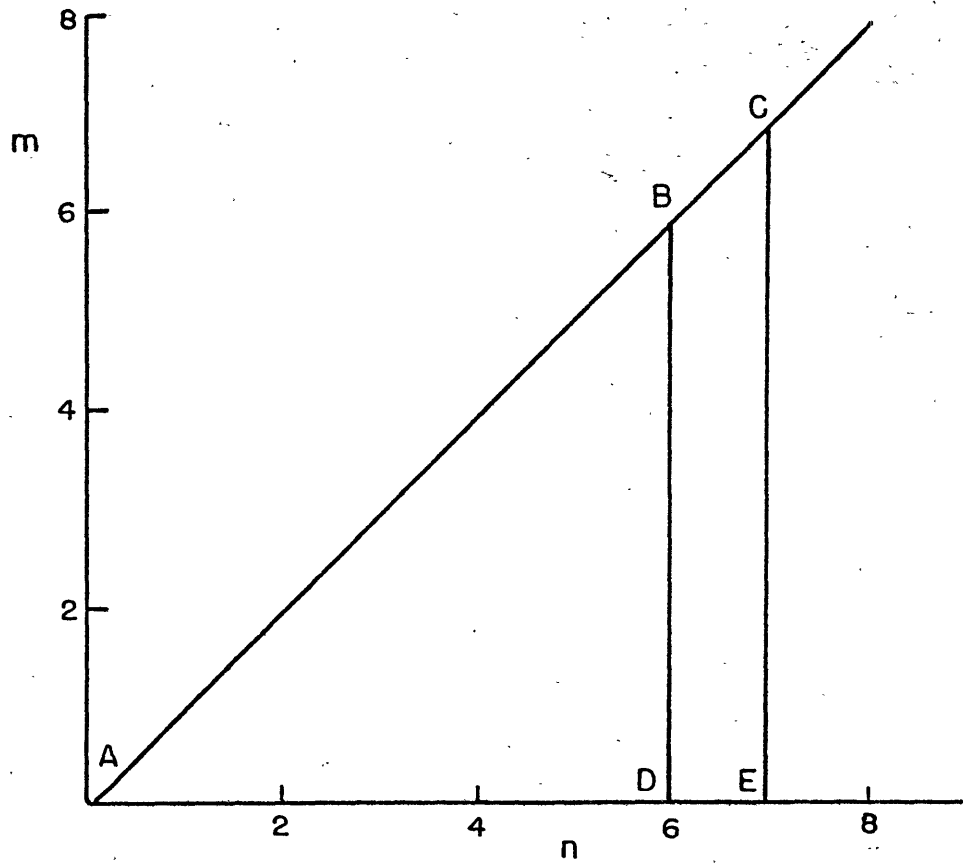


FIGURE 3.2 Domain of spherical harmonic coefficients in wavenumber space for triangular truncation.

$$\left\{ (\ ) \right\}_n^m = \frac{1}{2\pi} \int_0^{2\pi} \int_{-\frac{\pi}{2}}^{\frac{\pi}{2}} (\ ) \tilde{Y}_n^m \cos \phi \, d\phi \, d\lambda \quad (3.3.6)$$

The three prognostic equations in spectral form are:

vorticity equation

$$\begin{aligned} \frac{\partial \zeta_n^m}{\partial t} = & -A_n^m(\zeta) - B_n^m(\zeta) - C_n^m(\delta) - E_n^m(v, -u) \\ & + \frac{1}{2\gamma^2} \left[ \frac{\partial^2}{\partial z^2} + \epsilon_v(-n(n+1)+2) \right] \zeta_n^m \end{aligned} \quad (3.3.7)$$

divergence equation

$$\begin{aligned} \frac{\partial \delta_n^m}{\partial t} = & F_n^m(\zeta) - B_n^m(\delta) + C_n^m(\zeta) - E_n^m(u, v) \\ & + n(n+1) [G_n^m + K_n^m] + \frac{1}{2\gamma^2} \left[ \frac{\partial^2}{\partial z^2} + \epsilon_v(-n(n+1)+2) \right] \delta_n^m \end{aligned} \quad (3.3.8)$$

thermodynamic equation

$$\frac{\partial \theta_n^m}{\partial t} = -A_n^m(\theta) - B_n^m(\theta) + \frac{1}{2\eta^2} \left[ \frac{\partial^2}{\partial z^2} + \epsilon_v(-n(n+1)) \right] \theta_n^m \quad (3.3.9)$$

where the nonlinear terms are given by

$$A_n^m(q) = \left\{ \frac{1}{\cos^2 \phi} \left[ U \frac{\partial q}{\partial \lambda} + V \cos \phi \frac{\partial q}{\partial \phi} \right] \right\}_n^m$$

$$B_n^m(q) = \left\{ w \frac{\partial q}{\partial z} \right\}_n^m$$

$$C_n^m(q) = \left\{ \zeta q \right\}_n^m$$

$$E_n^m(q, r) = \left\{ \frac{1}{\cos^2 \phi} \left[ \frac{\partial q}{\partial z} \frac{\partial w}{\partial \lambda} - \frac{\partial r}{\partial z} \cos \phi \frac{\partial w}{\partial \phi} \right] \right\}_n^m$$

$$F_n^m(q) = \left\{ \frac{1}{\cos^2 \phi} \left[ V \frac{\partial q}{\partial \lambda} - U \cos \phi \frac{\partial q}{\partial \phi} \right] \right\}_n^m \quad (3.3.10)$$

$$K_n^m = \left\{ \frac{U^2 + V^2}{2 \cos^2 \phi} \right\}_n^m$$

where  $q$  and  $r$  are any of the dependent variables and the operator  $\left\{ \right\}_n^m$  is defined in (3.3.6). In general, each of the nonlinear terms will contain an integral over latitude of a product of three different associated Legendre polynomials. Such expressions have been termed interaction coefficients and are rather cumbersome and time consuming to compute. To avoid explicitly calculating these

interaction coefficients, we will evaluate the nonlinear terms according to the transform method as suggested by Elissen et al. (1970) and by Orzag (1970). This method consists of evaluating the nonlinear products in grid space and then transforming the resulting expression into harmonic coefficients. The technique is described in more detail in Appendix D. Next, we present the spectral form of the diagnostic equations of our model. Since all of the equations are linear, application of (3.3.6) is straightforward. The spectral equivalents of (3.2.6) - (3.2.8) and (3.2.14) are

the hydrostatic equation

$$\frac{\partial p_n^m}{\partial z} = \theta_n^m \quad (3.3.11)$$

the continuity equation

$$\delta_n^m + \frac{\partial w_n^m}{\partial z} = 0 \quad (3.3.12)$$

expressions for streamfunction and velocity potential

$$\begin{aligned} \zeta_n^m &= -n(n+1) \psi_n^m \\ \delta_n^m &= -n(n+1) \chi_n^m \end{aligned} \quad (3.3.13)$$

and expressions for U and V

$$\begin{aligned}
 U_n^m &= (n-1) D_n^m \psi_{n-1}^m - (n+2) D_{n+1}^m \psi_{n+1}^m + im \chi_n^m \\
 V_n^m &= -(n-1) D_n^m \chi_{n-1}^m + (n+2) D_{n+1}^m \chi_{n+1}^m + im \psi_n^m \quad (3.3.14)
 \end{aligned}$$

where  $D_n^m = \left[ \frac{n^2 - m^2}{4n^2 - 1} \right]^{\frac{1}{2}}$ . From (3.3.14) we can now see why  $U$  and  $V$  must be truncated at a value of  $n = M + 1$ . If  $n = M + 1$  is substituted into (3.3.13) then there will be a nonzero contribution from the first term on the right-hand side of each equation since these terms are within the truncation limit of  $M$  for  $\psi$  and  $\chi$ .

In the vertical, we once again use the stretched coordinate defined by

$$z = \sin^2 \left( \frac{\pi}{2} \xi \right)$$

along with the staggered grid with ten levels described in Figures 2.3 and 2.4. The vertical derivatives and advective terms are approximated with the finite difference scheme described in section 2.4 and will not be repeated here.

The time integration of the three prognostic equations is performed in accordance with the modified leap-frog scheme described in Chapter 2. The diffusion terms are evaluated at the backward time step to avoid computational instability. Also, a forward time stepping scheme is used

every so often to avoid the separation of the even and odd time step solutions that tends to occur when exclusively using a centered time differencing scheme. The procedure we use is analogous to the method of Chapter 2. First, we advance  $\zeta_n^m$  and  $\theta_n^m$  to the new time using equations (3.3.7) and (3.3.9) respectively, with the nonlinear terms evaluated at the central time step and the diffusion terms evaluated at the backward step, e.g.

$$\zeta_n^m(t+\Delta t) = \zeta_n^m(t-\Delta t) + 2\Delta t \left[ -\text{NONLIN}(t) + \text{DIFF}(t-\Delta t) \right] .$$

Using the latest values of  $\theta_n^m$ , we then diagnose the "uncorrected" pressure from the hydrostatic equation (3.3.11). By "uncorrected" we mean that  $p_n^m$  is computed by assuming that  $p_n^m(z=1) = 0$ . The uncorrected pressure is then substituted into (3.3.8) and we calculate the uncorrected divergence at the new time, i.e.  $\delta_n^m{}^u(t+\Delta t)$ . As in Chapter 2, we use the relationship

$$\delta = \delta^u + \nabla^2 R(\lambda, \phi) \tag{3.3.15}$$

where  $R(\lambda, \phi) = 2G\Delta t p(\lambda, \phi, z=1)$

is an arbitrary function of  $(\lambda, \phi)$  only. In spectral space, this relationship is simply

$$\delta_n^m = \delta_n^m u - n(n+1) R_n^m \quad (3.3.15a)$$

where  $R_n^m$  is the  $(m, n)$ th harmonic coefficient of  $R(\lambda, \phi)$  and  $R_n^m$  is a constant. From mass continuity and the boundary conditions  $w(z=1) = w(z=0) = 0$  we know that if we integrate (3.3.15) or (3.3.15a) over the entire depth of the fluid, the left-hand side must be zero and the second term on the right is independent of  $z$  and thus we have the necessary expression for the correction term

$$n(n+1) R_n^m = \int_0^1 \delta_n^m u \, dz$$

and the actual divergence is obtained by substituting this expression into (3.3.13a). Given the vorticity and divergence, we finally diagnose  $W_n^m$ ,  $U_n^m$ , and  $V_n^m$  from equations (3.3.13) and (3.3.14). We complete the time stepping by applying the spectral equivalents of the boundary conditions on  $\zeta$ ,  $\delta$ , and  $\theta$ .

In this section, we must also address the problem of the spurious growth of the amplitudes



of the harmonics close to the truncation wavenumber. This problem has been termed spectral blocking (Puri and Bourke, 1974) and is the spectral equivalent of the cascade of energy to the smallest scales in a finite difference numerical model. The difficulty is especially noticeable for fairly low truncation values of  $M \lesssim 10$ . The two methods that have been previously used to damp this undesirable growth have both involved the diffusion terms. Upon using a  $\nabla^2$  formulation of diffusion, Pollack and Young (1975) found it necessary to fix the diffusion coefficients at the unrealistically large values of

$$\nu_v = 4 \times 10^5 \text{ cm}^2 \text{ s}^{-1}, \quad \nu_H = 4 \times 10^{11} \text{ cm}^2 \text{ s}^{-1} .$$

The problem here is that such strong diffusion suppresses all scales of motion and therefore only allows a very weak circulation to develop. To make the damping more scale selective, Young and Pollack (1977) tried a  $\nabla^4$  diffusion operator. While they were able to use smaller effective diffusion coefficients ( $\nu_v \sim 10^4 \text{ cm}^2 \text{ s}^{-1}$ ,  $\nu_H \sim 10^9 \text{ cm}^2 \text{ s}^{-1}$ ) the  $\nabla^4$  still provided too much damping of the medium scale waves and artificially stabilized certain potentially unstable modes (see discussion in Chapter 1, especially Table 1.3).

To avoid the problem of excessive long wave damping, we use a  $\nabla^2$  diffusion operator coupled with a linear Shapiro (1970) filter that damps according to the zonal wavenumber. The Shapiro filter is an ideal filter in the sense that it operates only on the amplitude of the wave and thus it does not effect the phase. Consider an arbitrary field represented by a truncated Fourier series, e.g.,

$$\psi(\lambda) = \sum_{m=-M}^M \psi_m e^{im\lambda} \quad (3.3.16)$$

To apply a  $p$ -th order filter, we simply multiply the amplitude of each wave component by the appropriate response function defined by

$$R_p(m) = 1 - \sin^{2p} \left( \frac{m\pi}{2M} \right) \quad (3.3.17)$$

Thus the filtered field,  $\bar{\psi}^\lambda$ , is given by

$$\bar{\psi}^\lambda(\lambda) = \sum_{m=-M}^M \bar{\psi}_m^\lambda e^{im\lambda}$$

where  $\bar{\psi}_m^\lambda = \psi_m R_p(m)$

The main advantage of the Shapiro filter is that one may make the filter as selective as desired by choosing the order of the filter. As an example, in Figure 3.3 we show the response function for an eighth order filter for various spectral truncations. We note that the response function is fairly flat (and close to one) for the long and medium waves and drops off sharply only near the truncation wavenumber. Thus the shortest resolved waves are effectively eliminated while the longer waves are only minimally damped by the filter. We have found that a  $\nabla^2$  diffusion operator coupled with an eighth order zonal filter applied every fifth time step is quite effective in controlling the cascade of energy to the smallest resolved scales and the associated spurious amplitude growth of the short waves (i.e., the problem of spectral blocking). The numerical value of the horizontal diffusion coefficient,  $\nu_H$ , depends upon the truncation wavenumber,  $M$  and it is reduced as  $M$  is increased. For example, for  $M = 6$  we use a value of  $\nu_H = 5 \times 10^9 \text{ cm}^2 \text{ s}^{-1}$ . Since horizontal diffusion is included only as a numerical tool and not necessarily for its physical significance, we will simply set  $\kappa_H = \nu_H$ .

Finally, we point out that since the thermal forcing described by (3.2.17) is symmetric about the equator, the solutions to the equations will also exhibit certain symmetry properties. More specifically,  $\delta$ ,  $\theta$ ,  $p$ ,  $w$ , and  $U$  will be

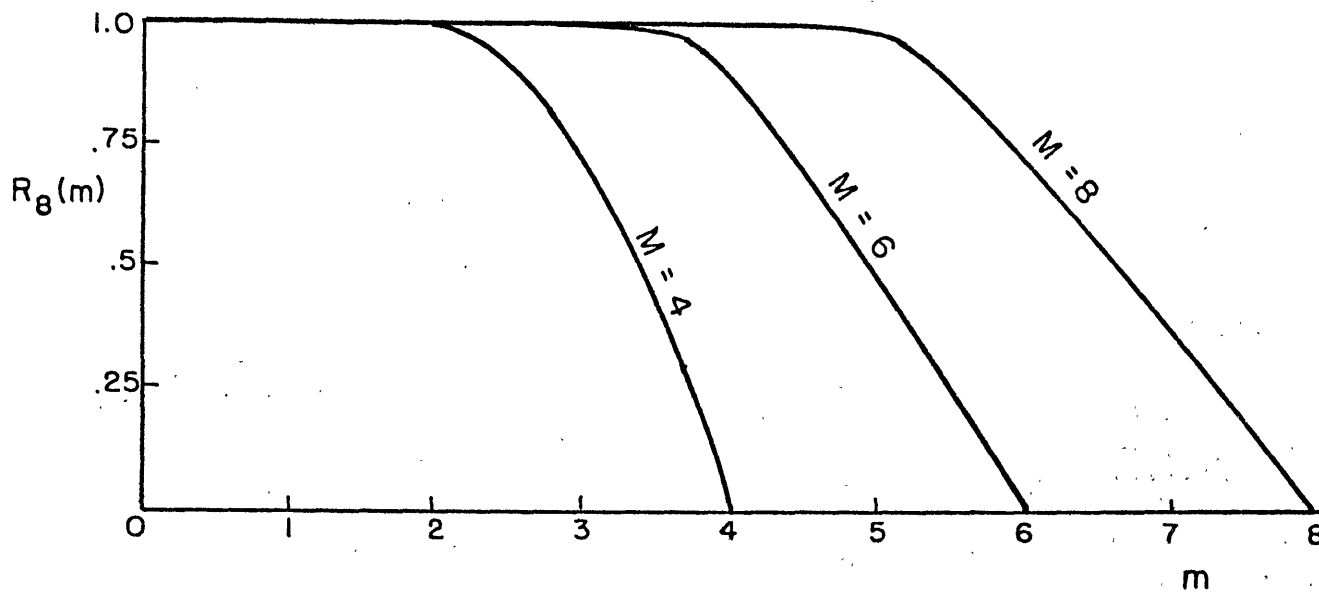


FIGURE 3.3 Response function,  $R_8(m)$ , of an eighth order Shapiro filter for various truncations,  $M$ .

symmetric about the equator while U and V will be anti-symmetric. This allows us to reduce our computation time and memory requirements by a factor of two since the spectral expansions for the symmetric variables will include only even modes (i.e., harmonics for which the sum of the indicies,  $m + n$ , is even). Similarly, the expansions for the antisymmetric variables will include only odd modes (i.e.,  $m + n$  odd). Integrations of this type are commonly referred to as hemispheric as compared to global integrations which retain all harmonics for all variables.

Rossow et al. (1980b) have pointed out that the YP model cannot account for possible barotropic instabilities because of the combined effects of low order truncation ( $M=4$ ), hemispheric representation, and strong damping of any mode with  $n \geq 3$  (their criterion for strong damping is a horizontal diffusion time scale much less than 100 days). This deficiency can be significant if the MMC - barotropic instability cycle discussed by Rossow et al. (1980a) plays a major role in driving the 4-day circulation. Their comments on the YP model were based on the results of Baines (1976) where it was shown that any mode with  $n < 3$  is always barotropically stable. A mode with  $n \geq 3$  will be unstable if its amplitude exceeds a certain critical value.

Furthermore any particular mode can become unstable as a result of interacting with certain other destabilizing modes. Concerning Rossow et al.'s comments on the YP model and their relevance to our model we can make the following statements:

a) the hemispheric representation does indeed eliminate some of the important destabilizing modes.

However if the resolution is high enough and the damping is weak enough some of the retained potentially unstable modes can grow to and beyond the critical amplitude.

b) The resolution and the damping (diffusion) are the key factors that determine whether or not the model allows barotropic instability. Using Rossow et al.'s (1980b) criterion for strong damping ( $\tau_{diff} \lesssim 100$  days) it was shown that in the YP model (M=4) only three of the ten retained modes were not strongly damped. Of these three, none are potentially unstable since  $n < 3$  for all of them. Our M = 4 solution suffers this same deficiency. For our M = 6 solution six of the twenty one modes are not strongly damped. Of these six modes, three are potentially unstable. For the M = 8 solution ten of the thirty-six modes are not strongly damped. Of these ten, seven are potentially unstable. Thus it is clear that our higher resolution experiments (M=6 and 8) do in fact allow for the possibility of barotropic instability. Conversely, we see that M = 6 is the minimum resolution required to simulate any of the

potentially unstable modes.

Having completed our description of the mathematical formulation and the numerical aspects of the model we continue by presenting the results of our computations.

### 3.4 Results

In this section we present the results from our non-linear spectral model. Unless otherwise noted, all variables (e.g. velocity components) are dimensionless. Because of the complexities of a three-dimensional non-linear model and the inherent long time scale nature of our problem we were limited as to the number of numerical experiments that could be conducted. In each case, the computations were stopped when we reached what appeared to be a steady state as determined by the curves in Figure 3.4. From the curves we can see that for  $\bar{u}$  to reach a steady state typically requires an integration time of four solar days ( $\sim 4 \times 10^7$  s or 468 terrestrial days). In our model we have parameterized the vertical heat transport as a diffusion term. Thus we must be sure that the steady state integration period is longer than the vertical diffusive time scale. For our values of  $h = 5 \times 10^5$  cm and  $\kappa_v = 10^4$  cm<sup>2</sup> s<sup>-1</sup> the diffusion time scale is  $\tau = h^2/\kappa = 2.5 \times 10^7$  s. Thus our integrations have exceeded the important time scales in our model (i.e., the length of a

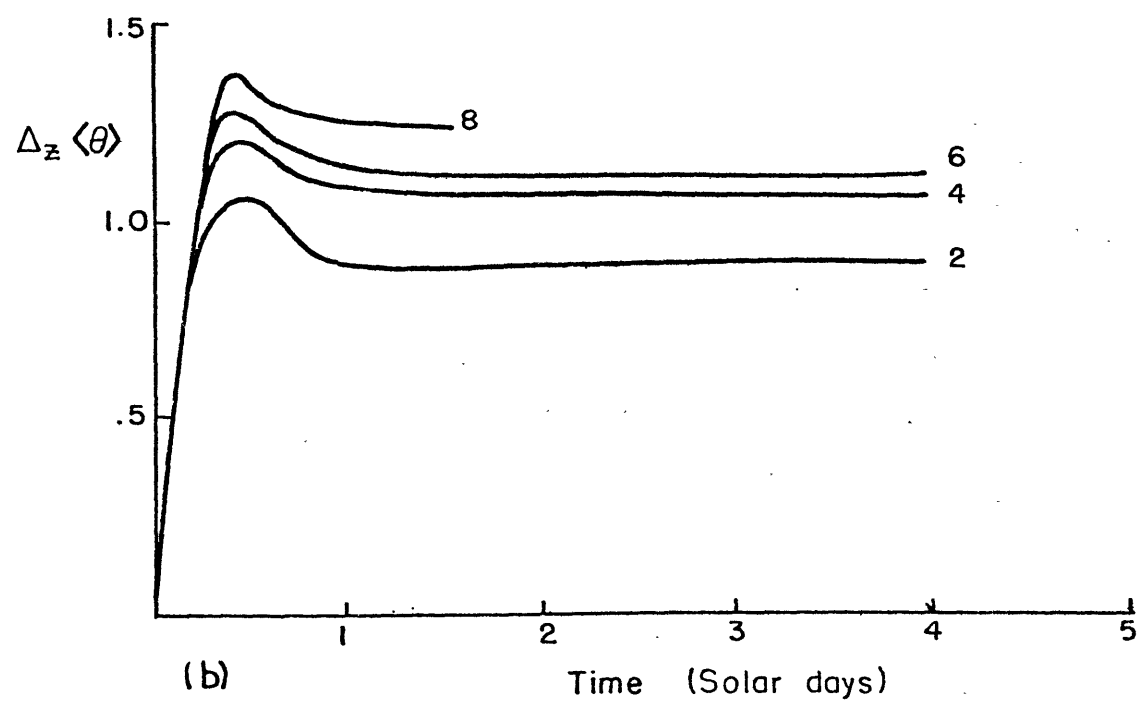
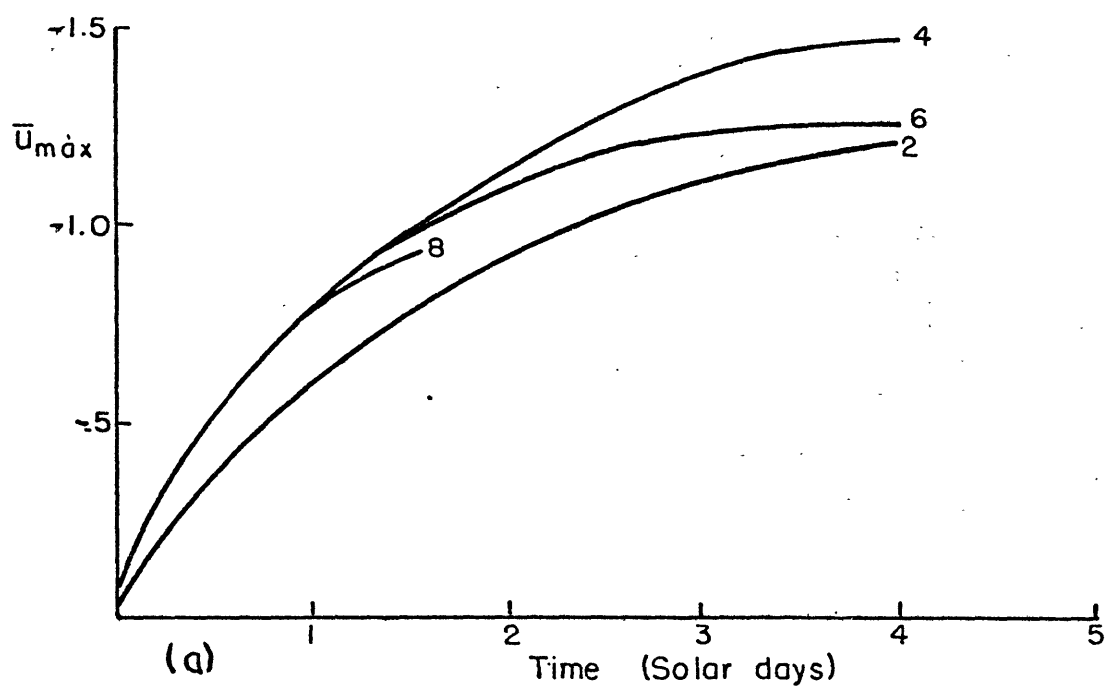


FIGURE 3.4 Time variations of (a)  $\bar{u}_{max}$ , (b)  $\Delta_z \langle \theta \rangle$  . For various truncations,  $M$ .



solar day and the vertical diffusion time).

The strongest retrograde mean zonal velocity in all runs was at the top of the model at the equator. The maximum value of  $\bar{u}$ , as shown in Figure 3.4a, was achieved after 3.5 solar days (SD). On the other hand, the mean meridional circulation (MMC) reached a quasi steady state in less than half of that time, i.e., in 1 to 1.5 SD, as indicated by the top to bottom contrast of the horizontally averaged potential temperature. As a point of interest, we note that Fultz et al. (1959) observed a similar behavior in their laboratory experiments, i.e., the MMC developed rather quickly (less than one flame rotation) while the mean zonal flow required a much longer time to appear (several flame rotations).

Because of the complexities of a three-dimensional nonlinear model and the inherent long time scale nature of our problem, we were limited as to the number of numerical experiments that could be conducted. For the sake of completeness, we carried out a parameter study for only the lowest order spectral truncation of  $M = 2$ . For the higher order truncations, we used our best estimates for the Venus values of the parameters (Appendix B) and focused our investigation on the effects of spectral truncation. Thus, unless otherwise specified, we used  $G = 1375$ ,  $2\eta^2 = 15.5$ ,  $Pr = \frac{1}{2}$ .

Once again, we emphasize that our model is highly simplified and designed to specifically study the moving flame mechanism. It is not meant to be a general circulation model for Venus. Consequently, when we compare our results to the general circulation simulations of Young and Pollack (1977) (referred to as YP) we can make only qualitative comparisons. Nevertheless, the two models do exhibit several important similarities. These are also several interesting differences between the two models which lead us to raise some serious questions as to the validity and relevance of their results.

#### 3.4.1 Low Order (M=2) Computations

As mentioned above, we include these low order computations and parameter studies for completeness. We hesitate to extend these results and conclusions to the higher order nonlinear cases. Since zonal wavenumber 2 is filtered out the eddy fields exhibit only a wavenumber 1 variation and thus do not show any of the interesting higher order nonlinear effects.

In Figure 3.5 we show the maximum retrograde mean zonal velocity as a function of the thermal forcing parameter,  $G$ , for  $2\eta^2 = 15.5$  and  $Pr = \frac{1}{2}$ . For comparison we include the analogous curve for the linearized calculations of section 2.5.2. The most obvious difference between the two curves is that the linearized model exhibits a

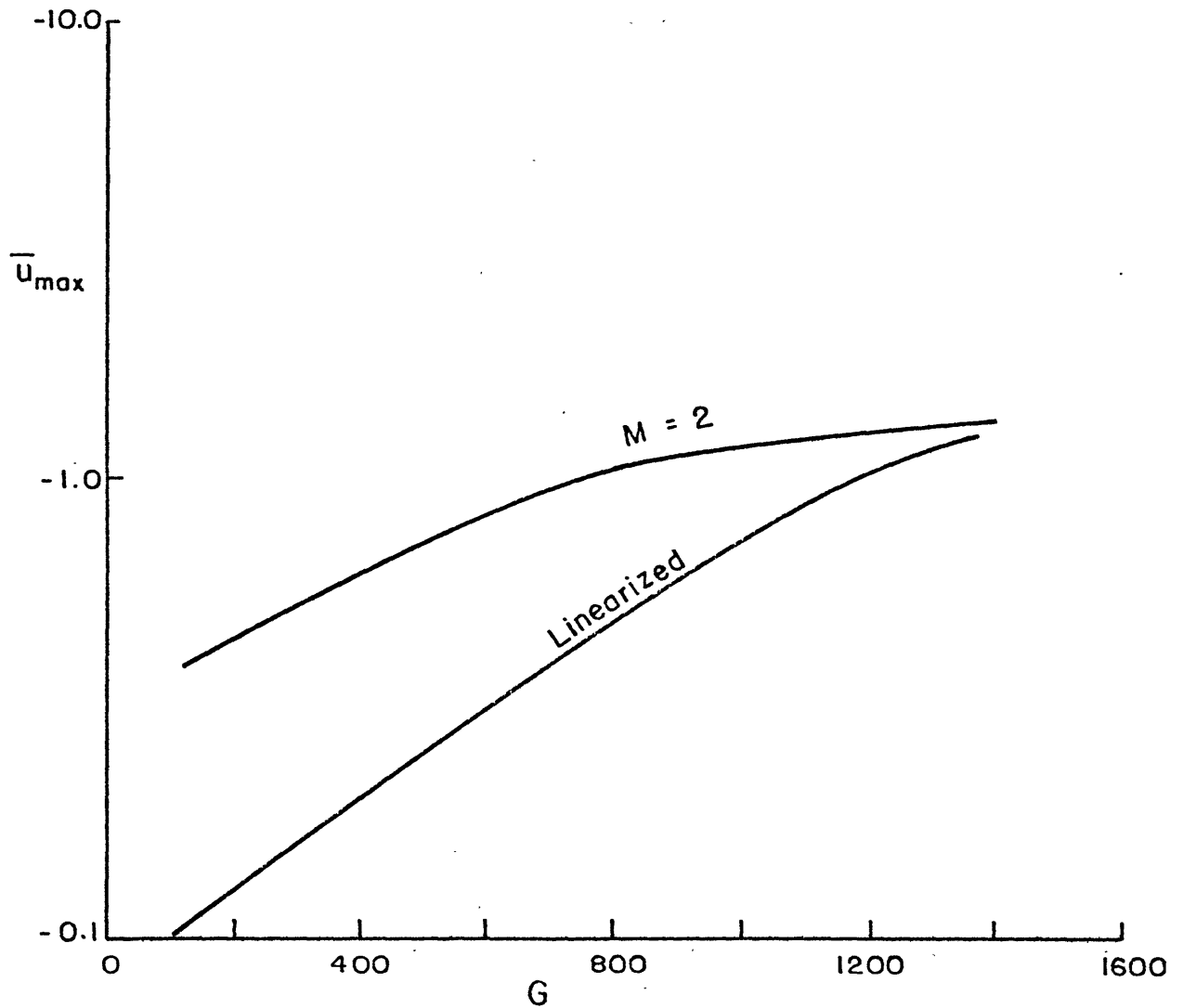


FIGURE 3.5 Maximum retrograde mean zonal velocity  $\bar{u}_{\max}$ , for  $M = 2$  and for the linearized model as a function of the thermal forcing parameter,  $G$ , for  $2^2 = 15.5$ ,  $Pr = \frac{1}{2}$ .

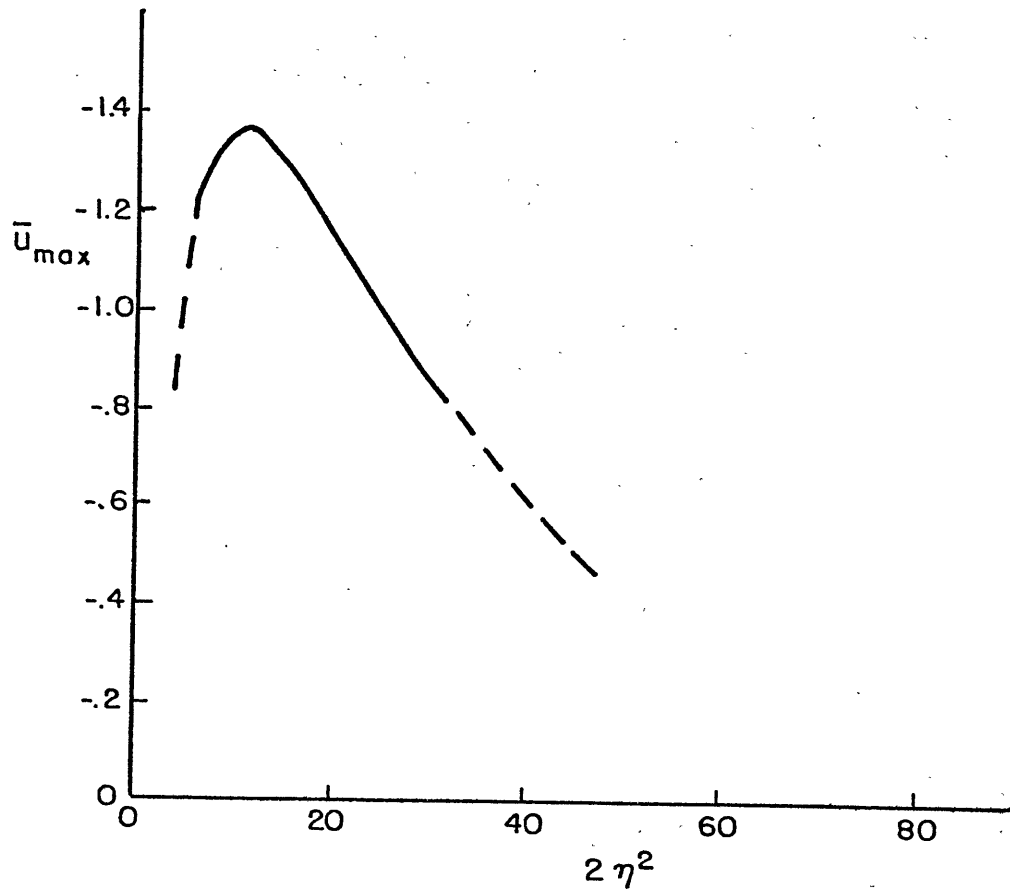


FIGURE 3.6  $\bar{u}_{\max}$  as a function of the thermal frequency parameter,  $2\eta^2$ , for  $G = 1375$ ,  $Pr = \frac{1}{2}$ ,  $M = 2$ .

much steeper slope for  $G \lesssim 1000$ . More specifically for  $G \sim 0(100)$ , the  $M = 2$  curve varies as  $G^{1/2}$  while the linearized curve varies as  $G^{1.6}$ . In both cases, however, as  $G$  exceeds 1000, the curves flatten out implying that in the Venus range of values additional thermal forcing alone will not significantly increase the maximum  $\bar{u}$ .

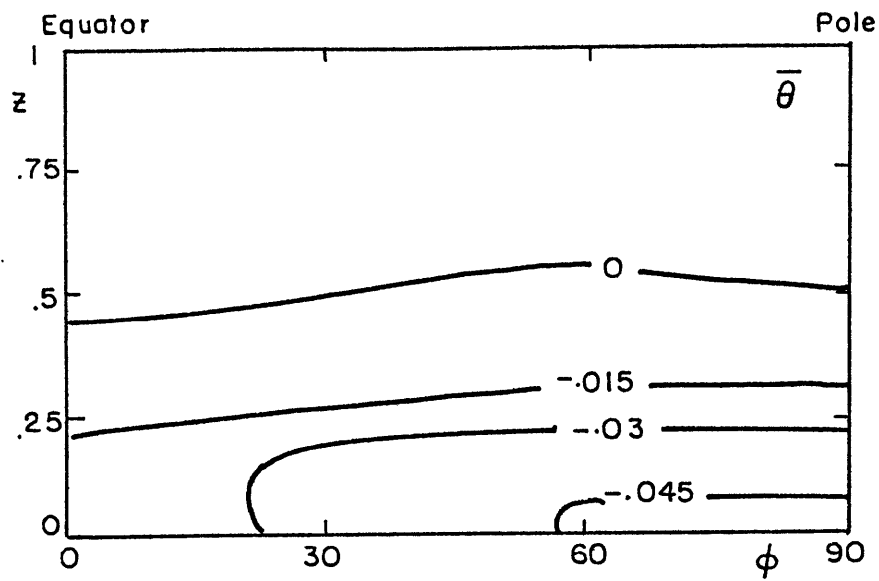
In Figure 3.6 we show the maximum retrograde  $\bar{u}$  as a function of the thermal frequency parameter for  $G = 1375$ ,  $Pr = 1$ . Once again, the behavior is similar to that predicted by our linearized model (Figure 2.13) and by our simple qualitative discussion in section 1.1. The maximum  $\bar{u}$  occurs for some intermediate value of  $2\eta^2 \sim 0(10)$ . In this case it is  $2\eta^2 = 12$  as compared to  $2\eta^2 = 25$  for the linearized case. For  $2\eta^2 \lesssim 10$ , the velocity drops off very quickly. This happens because as  $2\eta^2$  gets smaller, diffusion becomes much more efficient at eliminating temperature contrasts and wind shears. As  $2\eta^2$  increases beyond  $0(10)$  the period of the heat source becomes short compared to the diffusive time scale so that the fluid is not able to significantly react to the relatively rapidly moving heating variations. We note that this process is much more gradual (in terms of changes in  $2\eta^2$ ) than the rapidly increasing effectiveness of diffusion for  $2\eta^2 \lesssim 10$ .

We must mention that the  $M = 2$  parameter study is analogous to the linearized study of Chapter 2. The main difference between the two is that the  $M = 2$  spectral model includes a greater meridional resolution of the zonal wavenumber 1 eddies. Thus by comparing the linearized and  $M = 2$  parameter studies we can see that the behavior of  $\bar{u}$  is determined primarily by  $m = 0$  and  $m = 1$  interactions. Greater meridional resolution of these zonal modes seems to be unimportant. We must also point out that the validity of the  $M = 2$  behavior cannot necessarily be extended to higher truncations.

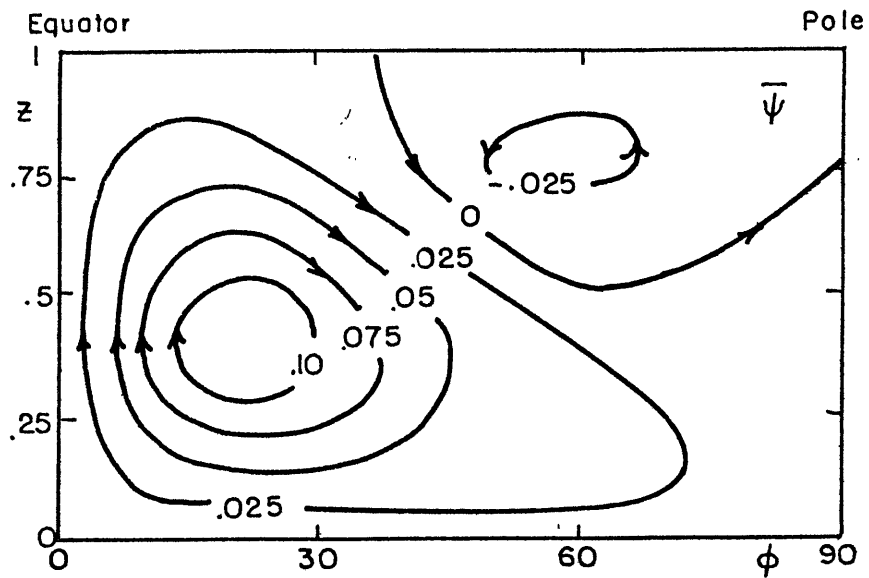
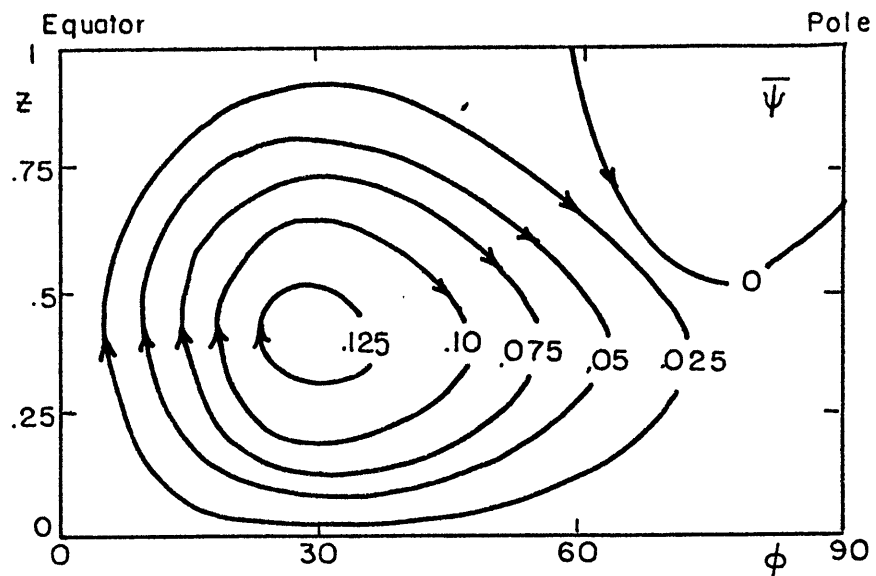
Since the primary goal of this chapter is to investigate the role of nonlinear interactions, we will focus the rest of our discussions on the higher truncation experiments. We will present results for the steady state  $M = 4$  and 6 simulations (approximately 3.5 solar days) and for the  $M = 4, 6,$  and 8 integrations after 1.5 solar days (SD) (time limit on  $M=8$  run).

#### 3.4.2 Mean Meridional Circulation (MMC)

In Figure 3.7 we show the steady state MMC for truncations  $M = 4$  (Figure 3.7a) and  $M = 6$  (Figure 3.7b). In Figure 3.8 we show the MMC after 1.5 SD for  $M = 6$  (Figure 3.8a) and  $M = 8$  (Figure 3.8b). As expected, in all cases the flow is dominated by one large Hadley cell between the equator and the pole. The circulation is driven by



(a)



(b)

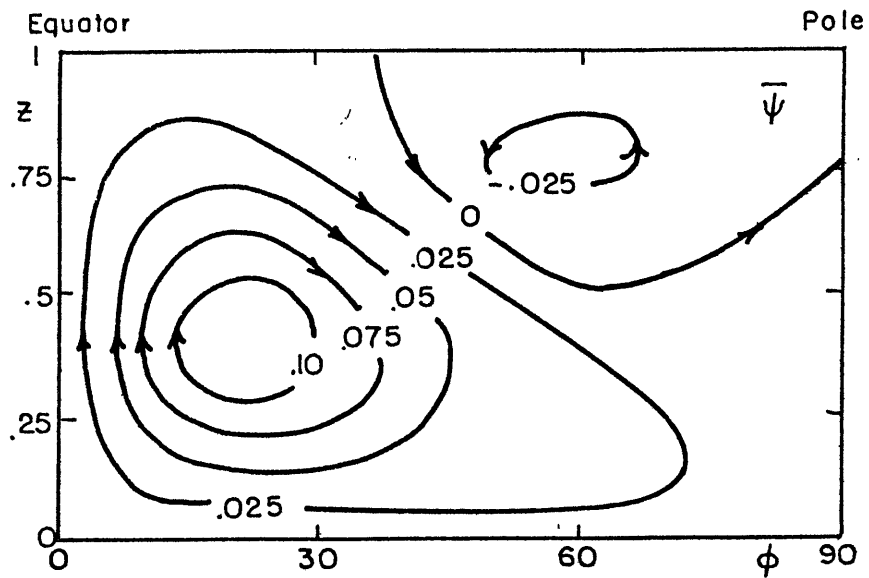
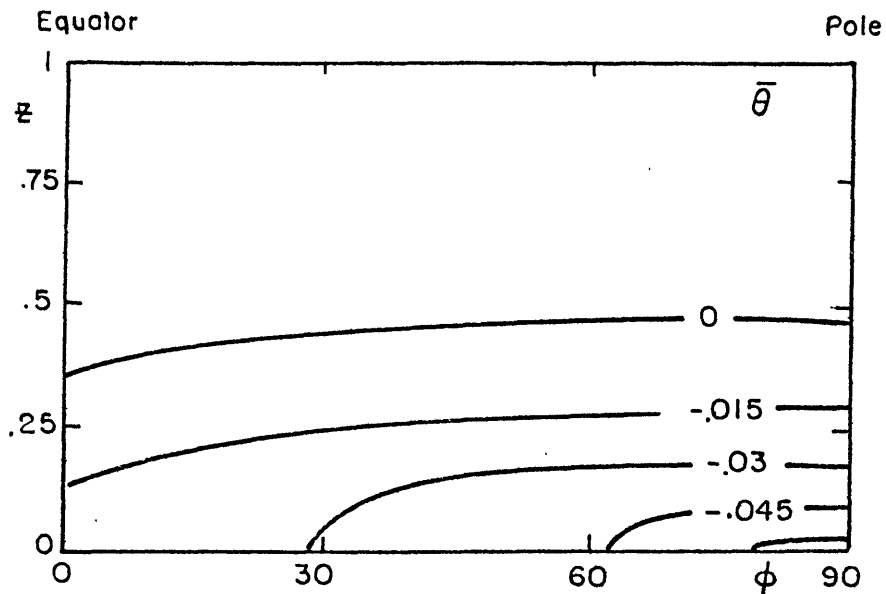
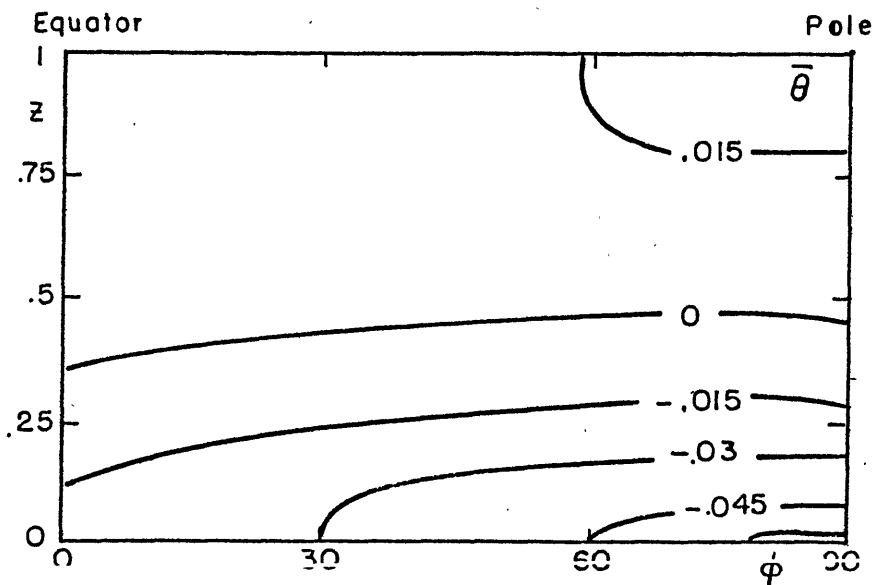
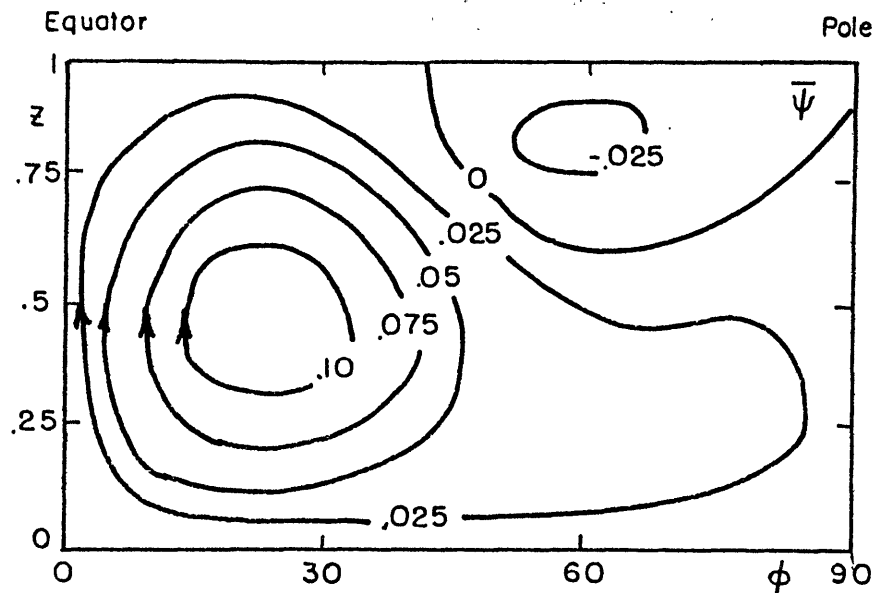


FIGURE 3.7 Steady state MMC ( $\bar{\theta}$  and  $\bar{\psi}$ ) for: (a)  $M = 4$ ,  
(b)  $M = 6$ .



(a)



(b)

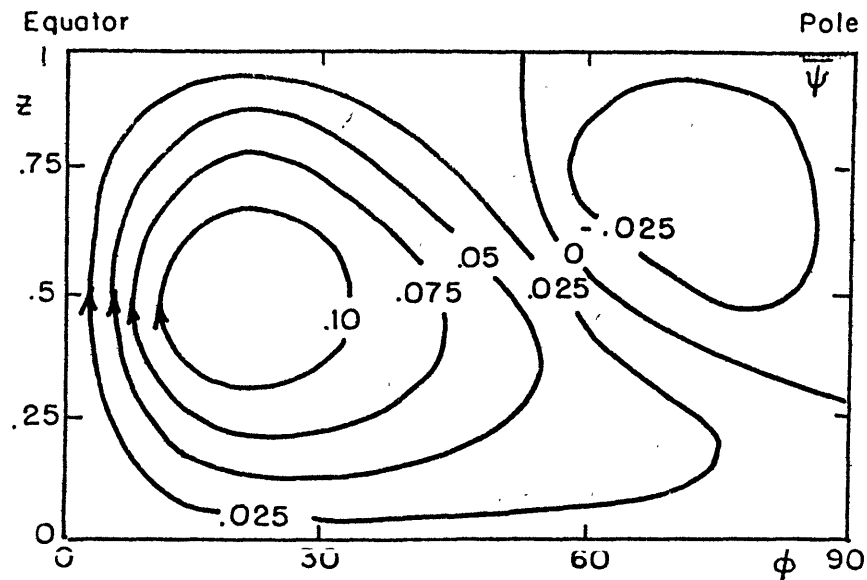


FIGURE 3.8 MMC after 1.5 solar days for: (a)  $M = 6$ , (b)  $M = 8$ .



the meridional flux contrasts at the bottom. The intensity in all cases, as indicated by the streamfunction, is quite similar with a typical value of  $\bar{\Psi}_{\max} = .12$  or  $2.4 \times 10^7 \text{ cm}^2 \text{ s}^{-1}$ . The strongest meridional velocities occur near the top of the lower boundary layer ( $Z \approx .25$ ) and are at most  $2 - 3 \text{ m s}^{-1}$ . Maximum vertical velocities occur at the equator and are typically  $0.15 \text{ cm s}^{-1}$ . The weak reversed cell near the top at high latitudes is driven by a weak reversed temperature gradient at the top (note that this gradient is too weak to appear in our isotherm patterns except in the  $M=8$  case).

Once again, we immediately notice the role of the nonlinear interactions in distorting and concentrating the flow towards the equator and the bottom. This phenomenon was predicted by Stone (1968), as well as others, and by our linearized calculations. It has already been discussed in section 2.4. The main effect of higher resolution on the MMC is to allow for a more pronounced meridional concentration of the flow. In all cases, the cell is centered around  $Z = .4$ . For the steady solutions the  $M = 4$  cell is centered at  $\phi = 30^\circ$  while the  $M = 6$  cell is centered at  $\phi = 22^\circ$ . For the 1.5 SD solutions both the  $M = 6$  and  $M = 8$  cells are centered at  $\phi = 22^\circ$ .

By comparing the four different Hadley cell solution we can draw two important conclusions: 1) the Hadley cell

reaches a quasi steady state in a relatively short time period (roughly 1-1.5 SD), and 2) to properly simulate the important nonlinear interactions we need a minimum resolution of  $M = 6$ .

The mean potential temperature structure in all of the cases is remarkably similar. Once again we find that the strongest gradients (horizontal and vertical) appear in the lowest quarter of the model. The equator to pole temperature contrasts at the bottom are:

M = 4 (steady)	$\Delta_{\phi} \bar{\theta} = .032$	or	$3.8^{\circ}\text{K}$
M = 6 (steady)	.046		$5.5^{\circ}$
M = 6 (1.5 SD)	.048		$5.7^{\circ}$
M = 8 (1.5 SD)	.046		$5.5^{\circ}$

And again we see that  $M = 6$  seems to be the minimum resolution required for accurate simulations even in our simplified model.

### 3.4.3 Large Scale Eddies

We begin this section by showing horizontal maps of the complete flow for the steady state  $M = 4$  and 6 cases (Figures 3.9 and 3.10) and for  $M = 6$  and 8 after 1.5 SD (Figures 3.11 and 3.12). Specifically, we show the zonal velocity,  $u$ , at the top of the model and the vertical velocity,  $w$ , at  $Z = 0.39$ . Starting with Figure 3.9a for  $u$  for the steady  $M = 4$  case we can see that the flow is dominated by the lowest zonal and meridional wavenumbers.

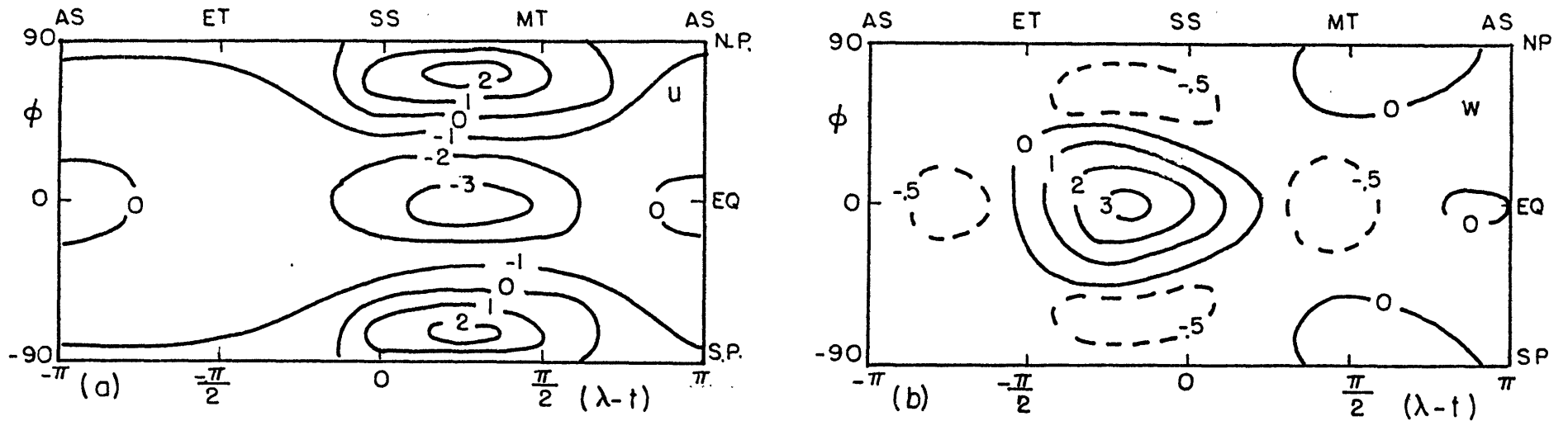


FIGURE 3.9 Horizontal view of the steady state flow for  $M = 4$ : (a) zonal velocity,  $u$ , at the top,  $z = 1$ ; (b) vertical velocity,  $w$ , at  $z = 0.39$ .

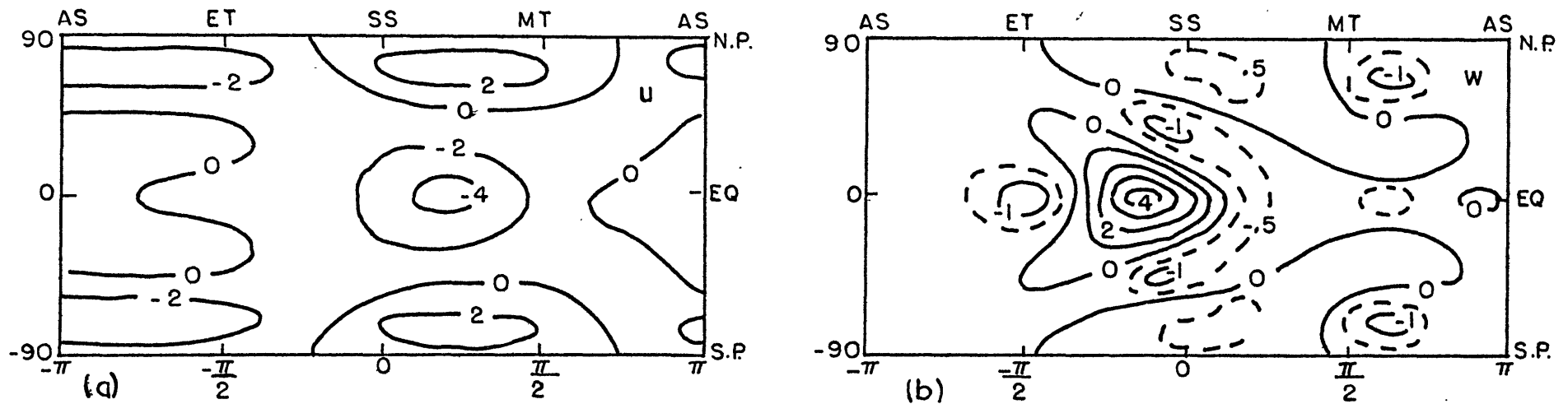


FIGURE 3.10 As in Figure 3.9 except  $M = 6$ .

Most of the flow at the top of the model is clearly retrograde as indicated by the negative values of  $u$ . The strongest retrograde flow occurs at the equator at 900 local time (LT) with a maximum value of  $-3.8$  or  $-15 \text{ m s}^{-1}$ . The prograde flow is restricted to high latitudes in the morning with a maximum value of  $2.4$  or  $9.6 \text{ m s}^{-1}$ . We point out that the prograde flow covers a relatively small part of the planet. The size of this region appears exaggerated because of the map projection. There is also a region of very weak prograde flow at the equator near the antisolar point (local midnight).

For the steady  $M = 6$  case (Figure 3.10a) the overall appearance is quite similar. The main differences are: 1) the strong retrograde flow at the equator occurs a bit later in the morning, at 1000LT, and is more intense with a maximum of  $-4.1$  or  $-16.4 \text{ m s}^{-1}$ ; 2) the region of prograde flow at the equator covers a larger area; 3) in high latitudes there is another relative maximum region of retrograde flow centered at 2100 LT. In both the  $M = 4$  and  $M = 6$  cases the dominance of the retrograde flow is reflected in the horizontally averaged angular momentum. The value is  $-1.8$  for  $M = 4$  and  $-1.2$  for  $M = 6$ .

For the flow after 1.5 SD we see that the overall zonal flow for  $M = 6$  (Figure 3.11a) and  $M = 8$  (Figure 3.12a) are quite similar. The main differences between the 1.5 SD

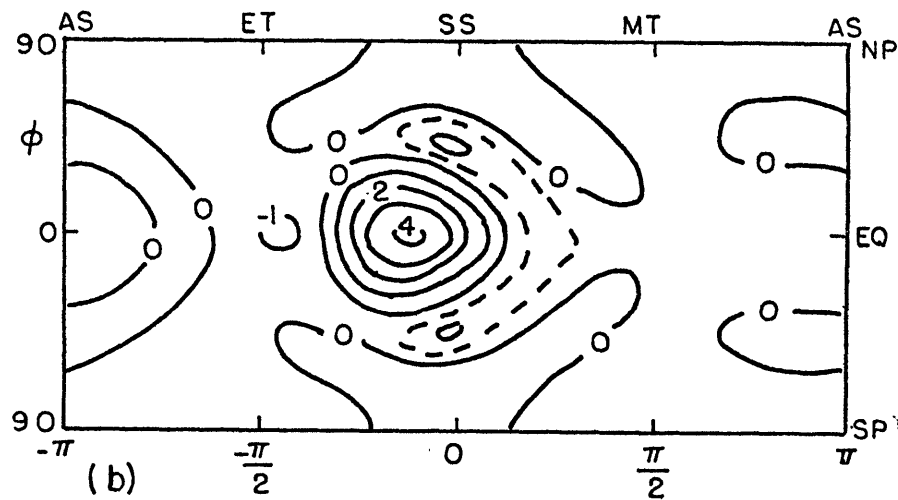
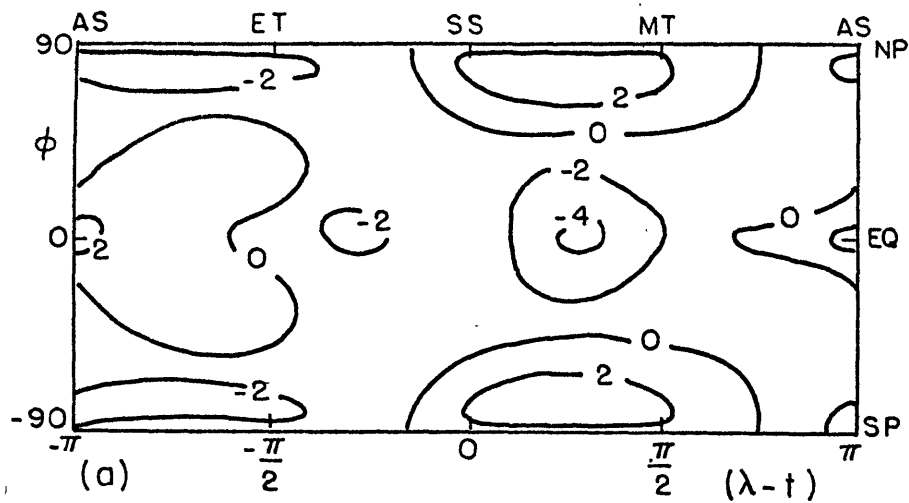


FIGURE 3.11. Horizontal view of the flow after 1.5 solar days for  $M = 6$ : (a) zonal velocity,  $u$ , at  $z = 1$ ; (b) vertical velocity,  $w$ , at  $z = 0.39$

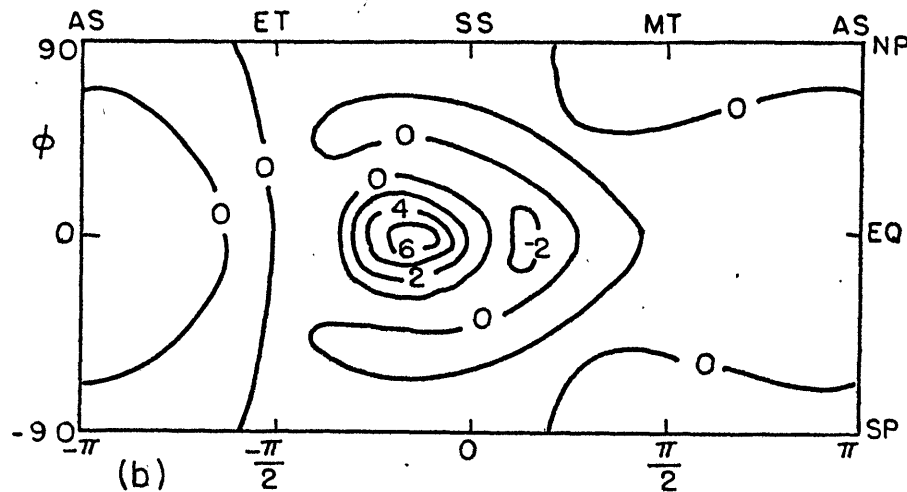
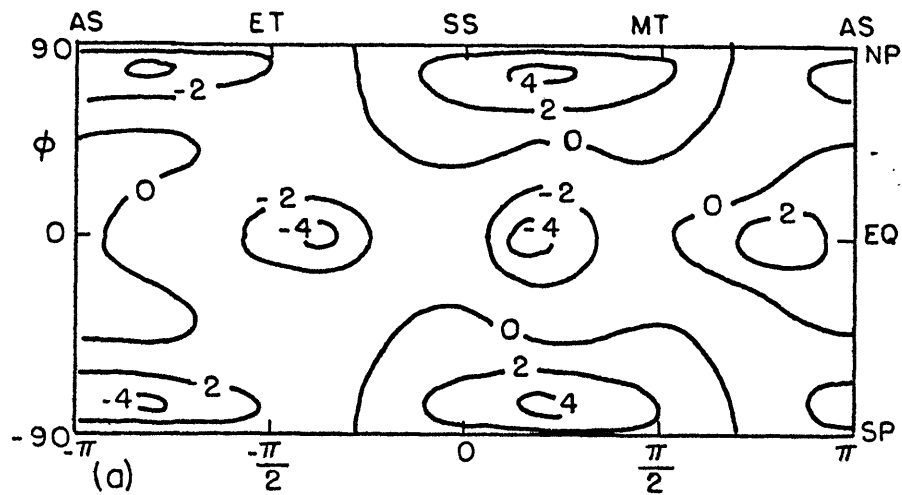


FIGURE 3.12 As in Figure 3.11 except  $M = 8$ .

flow and the  $M = 6$  steady flow are: 1) the appearance of a second region of maximum retrograde flow at the equator at 1630 LT and 2) the maximum values of  $u$  are slightly larger in the 1.5 SD flow. As in the case of the MMC, we find that the differences between  $M = 6$  and  $M = 8$  are not nearly as pronounced as the differences between  $M = 4$  and  $M = 6$ .

We now return to the steady state vertical velocity patterns for  $M = 4$  (Figure 3.9b) and for  $M = 6$  (Figure 3.10b). In both cases, the pattern is dominated by one solar locked region of strong rising motion. A large portion of the rest of the planet experiences relatively weak sinking motion. For  $M = 4$ , the core of rising motion is quasi-elliptical, centered at the equator at 1400 LT, and has a maximum vertical velocity of  $3.2$  or  $1.1 \text{ cm s}^{-1}$ . It is interesting to note that our  $M = 4$  vertical velocity field is remarkably similar to the one in YP solution I (their Figure 18b). Their solution I is analogous to our experiments in the sense that it represents the development of the forced flow from an initial state of rest and neutral static stability. The main differences between their  $w$  field and ours are that their core of rising motion is centered at 1240 LT (i.e., closer to the subsolar point) and their maximum  $w$  is larger than ours by a factor of three. The reason for these differences is probably linked

to the fact that their map is plotted at a height of 56 km above the surface which is right in the midst of the region of strong shortwave absorption and so we might expect the strong vertical motion to be closer to the subsolar point. Recall that our model is forced by boundary heating and thus the location of the core of rising motion is dependent upon the vertical diffusion process.

The  $M = 6$  steady  $w$  field (Figure 3.10b) is a very striking example of planetary scale Y shaped feature. As in  $M = 4$ , the dominant feature is a solar locked core of strong rising motion occurring at 1400 LT. In addition to the very obvious shape difference there are several other important differences between this pattern and the  $M = 4$  case. The  $M = 6$  core is more intense and covers a smaller area. The maximum value here is 4.1 or  $1.4 \text{ cm s}^{-1}$  which is roughly 27% stronger than the  $M = 4$  value. This increase in magnitude and decrease in area indicates that the higher resolution model is better able to represent smaller scale localized features. The other interesting difference is that for  $M = 6$  we see a second V shaped region of weak rising motion indicating that zonal wavenumber 2 is playing a more significant role than in the  $M = 4$  case.

Finally, comparing the  $M = 6$  and 8  $w$  fields after 1.5 SD (Figures 3.11b and 3.12b) we again see the dominant core of rising motion near 1400 LT. As might be expected,

the core for  $M = 8$  is more intense and smaller in area than for  $M = 6$ . We also notice the appearance of two other bow shaped regions of weak rising motion indicating the importance of zonal wavenumbers 1, 2, and 3. We note however that we cannot be sure about the future behavior of the  $M = 8$  fields because of the relatively short integration time. We next turn our attention to the structure of the steady state eddies since we are ultimately interested in their ability to drive the mean zonal flow. In Figures 3.13 and 3.14 we show vertical cross sections of the eddies for  $M = 4$  and 6 respectively. We do not show the  $M = 8$  eddies because of the shorter integration time and the fact that we cannot be absolutely sure that they will converge to a steady state similar to  $M = 6$ . The cross sections for  $\theta'$ ,  $u'$ , and  $w'$  are at the equator while the cross section for  $v'$  is near  $25^\circ$  latitude. All four fields in both figures clearly reflect the dominance of wavenumber 1. The higher order nonlinear interactions are forcing the circulation to concentrate near the subsolar point. This phenomenon is analogous to the effect of the nonlinear interactions on the MMC. By comparing the two figures it is again obvious that the higher truncation allows greater resolution of the nonlinear distortion and concentration of the flow near the subsolar point.



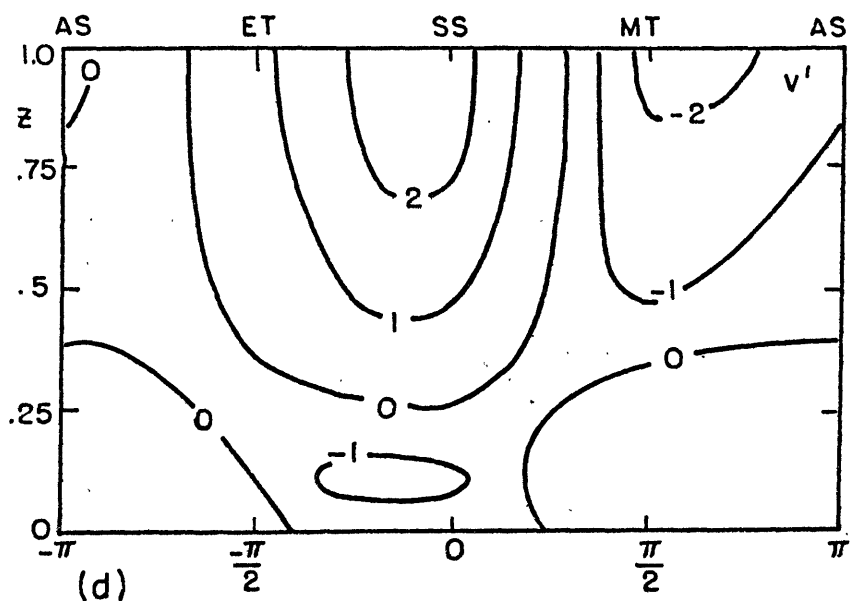
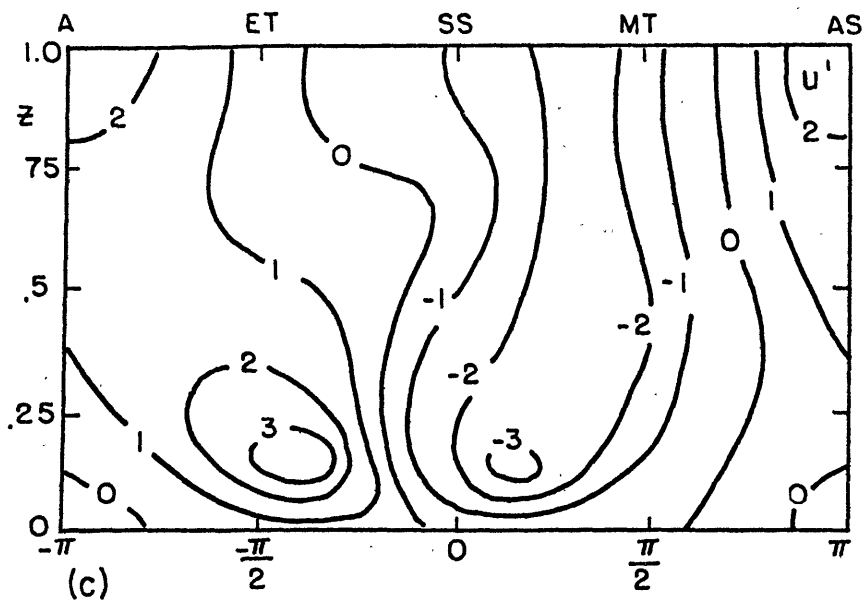
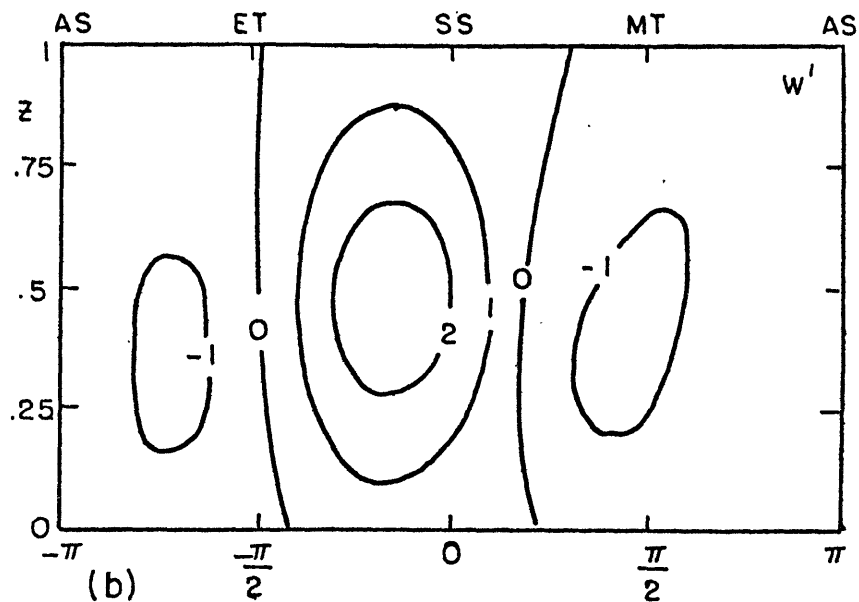
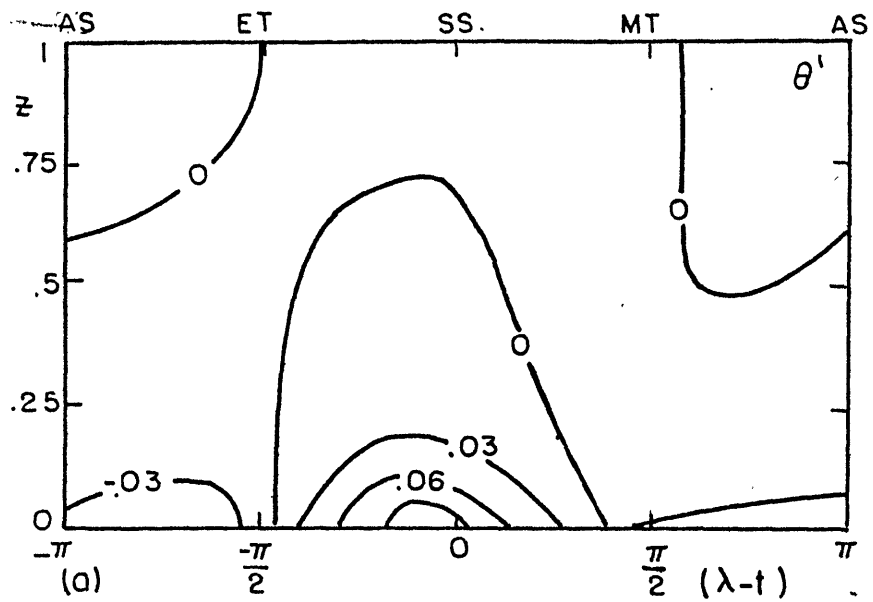


FIGURE 3.13 Steady state eddy fields for  $M = \frac{4}{\lambda}$ : (a)  $\theta'$ , (b)  $w'$ , (c)  $u'$  at the equator, (d)  $v'$  at  $\phi = 25^\circ$ .

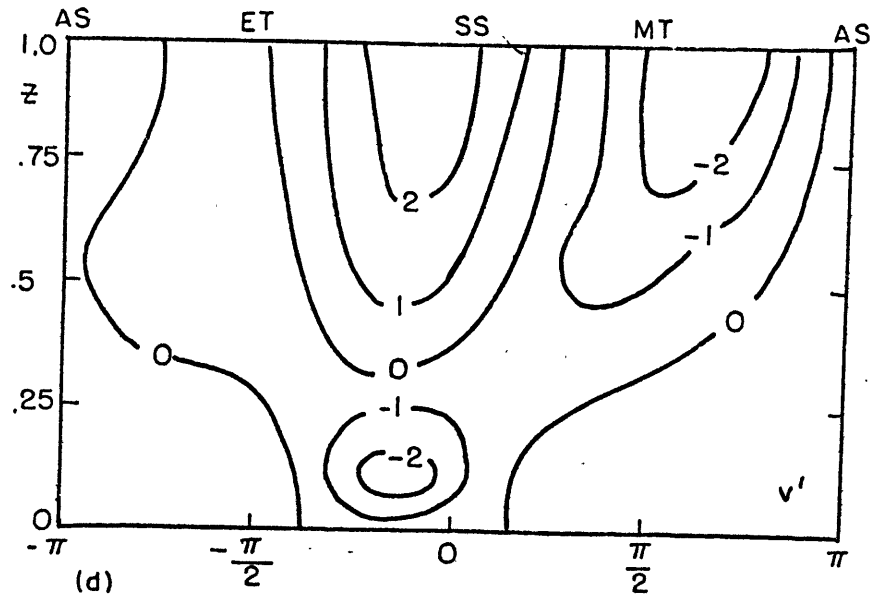
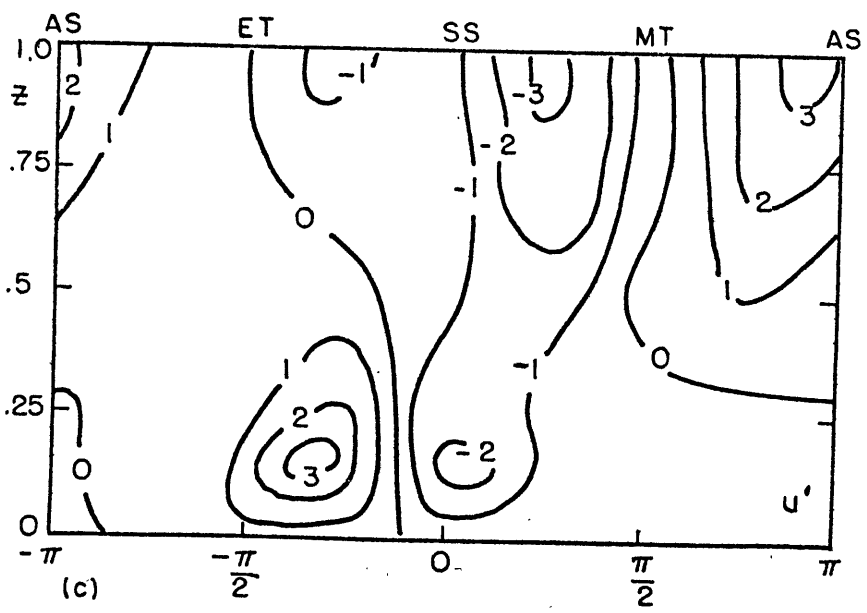
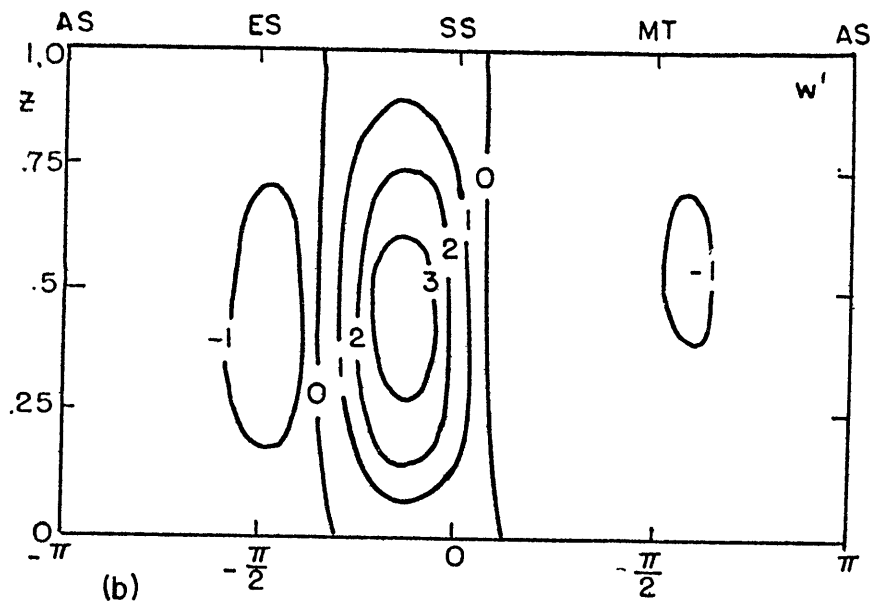
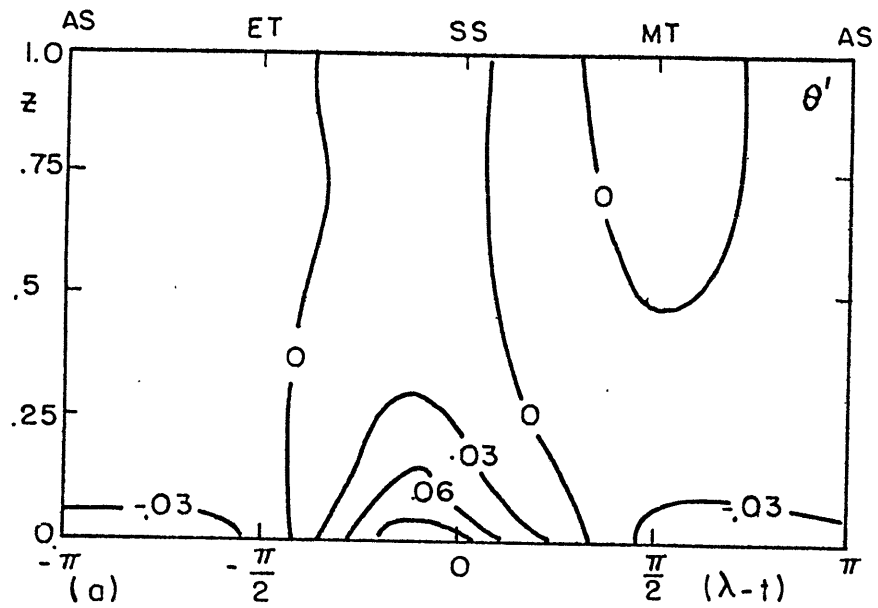


FIGURE 3.14 As in Figure 3.13 except  $M = 6$ .

Starting with  $\theta'$ , we see that the strongest gradients (horizontal and vertical) are confined to the lower boundary layer on the daylight side of the planet. The day to night temperature contrasts are  $0.14$  or  $17^\circ$  K for  $M = 4$  and  $0.16$  or  $19^\circ$  K for  $M = 6$ . Both of these values are significantly larger than their respective meridional contrasts of  $3.8^\circ$  and  $5.5^\circ$  even though the diurnal and meridional heating variations are comparable. The reason for this behavior becomes clear in view of the  $u'$  fields (Figures 3.13 and 3.14c). The diurnal temperature contrasts are closely linked to  $u'$  since  $\bar{u}$  is comparatively small in the lower boundary layer (Figure 3.15). For both  $M = 4$  and  $M = 6$ , in the lower boundary layer,  $u$  exhibits a region of strong horizontal convergence during the afternoon and much weaker flow during the rest of the day. Thus the eddy zonal velocity is maintaining the strong diurnal temperature contrasts on the daylight side of the planet. The maximum temperature at the lowest model level lags behind the heat source by only  $15^\circ$  for both  $M = 4$  and  $6$ . The lag shows only a very modest increase with height, i.e., a very weak retrograde tilt. This is further confirmed by the  $w'$  fields. The point is that in the nonlinear cases, we cannot predict the vertical zonal momentum fluxes from a simple visual inspection of the isotherms and convection cells. We also notice that near the point of maximum  $\theta'$  there is

a region of very weak negative stratification. From our results, we can see that this is not a significant problem i.e., our steady state solutions are not destroyed by small scale convective instability. Clearly the vertical heat diffusion term can account for this sub grid scale convection and thus a parameterized convective adjustment process is not needed in the model.

By comparing  $w'$  for  $M = 4$  (Figure 3.13b) and  $M = 6$  (Figure 3.14b) we once again see the importance of resolution in accurately treating the higher order nonlinear interactions that cause the flow to concentrate in a relatively narrow region. For  $M = 4$ , the core of rising motion has a width of  $120^\circ$  of longitude and a maximum vertical velocity of  $2.7$  or  $0.9 \text{ cm s}^{-1}$ . For  $M = 6$  the corresponding values are  $78^\circ$  of longitude and  $3.8$  or  $1.3 \text{ cm s}^{-1}$ .

Unlike our linearized computations, the eddy circulation pattern is more nonlinear and three-dimensional and cannot be simply described in terms of longitudinal and meridional convection cells. As was mentioned above, for  $M = 4$  and  $6$ , the  $u'$  field exhibits a region of strong convergence in the lower boundary layer in the early afternoon. In both cases, the maximum velocities are  $3.2$  or  $13.6 \text{ m s}^{-1}$ . Near the top of the model we see a region of fairly strong divergence centered around the morning terminator. The main difference between  $M = 4$  and  $M = 6$  appears in this

region where  $M = 6$  shows stronger velocities and a corresponding stronger divergence. For  $M = 4$  the maximum velocity is 2.4 or 9.6  $\text{m s}^{-1}$  while for  $M = 6$  the value is 3.4 or 13.6  $\text{m s}^{-1}$ . We will see in section 3.5 that this seemingly small difference has a very important impact on the kinetic energy spectra (Figures 3.21 and 3.22).

Finally, the meridional eddy flow also exhibits greater activity on the daylight side of the planet. The main effect of increased resolution is once again to produce a narrower region of maximum activity. In both cases the maximum value of  $v'$  is 2.4 or 9.6  $\text{m s}^{-1}$ .

#### 3.4.5 Mean Zonal Velocity

Finally in this section, we have come to the main focus of this thesis -- the mean zonal velocity,  $\bar{u}$ , that is driven and maintained by the moving flame mechanism. In Figure 3.15 we show height-latitude cross sections of the steady state  $\bar{u}$  for truncations  $M = 2, 4,$  and  $6$ . In all three cases we do indeed see a retrograde mean zonal flow with maximum values that are  $O(1)$ . Thus in no case do we find any  $\bar{u}$  that significantly exceeds the speed of the heat source. Recalling that on Venus the 4-day circulation corresponds to a maximum  $\bar{u}$  that is twenty-five times larger than the speed of the sun it appears that it is unlikely that the moving flame mechanism alone can force the 4-day circulation. This is further confirmed by the fact that in

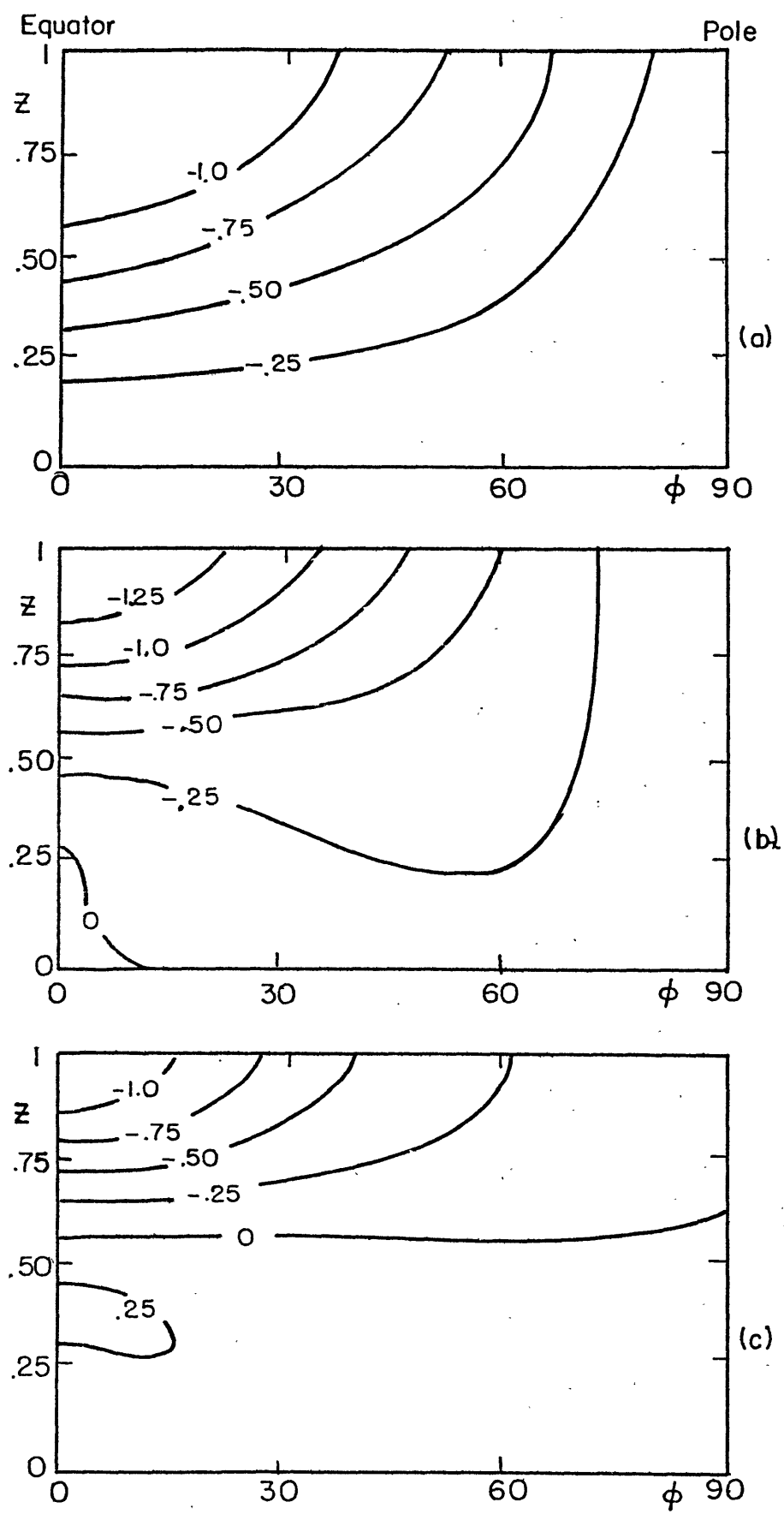


FIGURE 3.15 Vertical cross sections of steady state  $\bar{u}$  for: (a)  $M = 2$ , (b)  $M = 4$ , (c)  $M = 6$ .

our calculations we find eddy and mean velocities that are of the same magnitude which appears to be contrary to the observations of the circulation of the Venus stratosphere. Furthermore, if we assume that our thermal forcing is too weak (even as much as order of magnitude too weak), from our  $M = 2$  parameter study (Figure 3.5) we see that a large increase in  $G$  would result in only a moderate increase in the maximum value of  $\bar{u}$ .

Returning to our results, the cross sections in Figure 3.15 are for  $M = 2, 4, \text{ and } 6$ . In all three cases, the circulation consists of retrograde mean zonal flow with an equatorial jet at the top of the model. For  $M = 2$  (Figure 3.15a) the entire model exhibits retrograde flow. In fact, each model layer is in solid body rotation, i.e.,  $\bar{u}$  varies as  $\cos \phi$ . The maximum value of  $\bar{u}$  is  $-1.2$  or  $-4.8 \text{ m s}^{-1}$ .

For  $M = 4$  (Figure 3.15b) most of the model exhibits retrograde flow except for a small region in the lower one third near the equator. The prograde flow in this region is much weaker than the retrograde flow. The maximum value of  $\bar{u}$  is  $-1.45$  or  $-5.8 \text{ m s}^{-1}$ .

The  $M = 6$  cross section also shows retrograde flow, but in this case it is confined to the top half of the model. However, the prograde flow in the lower half of the model is much weaker than the retrograde flow above. The maximum value of  $\bar{u}$  is  $-1.2$  or  $-4.8 \text{ m s}^{-1}$ .

We can see additional interesting features of the steady state mean zonal flow in Figure 3.16 where we have plotted the vertical profile of  $\bar{u}$  at the equator (Figure 3.16a) and the meridional profile of  $\bar{u}$  at the top (Figure 3.16b). From the curves, it is again immediately obvious that the maximum retrograde mean zonal velocity for all truncations considered at the top of the model near the equator. Considering the vertical profiles (Figure 3.16a) we can now clearly see the region of weak prograde flow in the lower part of the model for the higher truncation cases. It is more pronounced in the  $M = 6$  case. The increase in retrograde  $\bar{u}$  is roughly linear in the interior of the model for all three truncations. The stress free top is also clearly visible in the vertical profiles.

From the meridional profiles of  $\bar{u}$  (Figure 3.16b) we can see that the higher harmonics (with indices  $\geq 4$ ) do indeed play an important role in resolving the structure of the mean zonal flow. As mentioned above, the  $M = 2$  solution represents exactly solid body rotation, i.e.,  $\bar{u}$  varies as  $\cos \phi$ . For  $M = 4$ , the profile deviates slightly from solid body rotation so that  $\bar{u}$  drops off a bit faster than  $\cos \phi$ , especially in midlatitudes.

The  $M = 6$  profile shows a much sharper equatorial jet than  $M = 4$ . Between the equator and  $45^\circ$  latitude,  $\bar{u}$  decreases quite rapidly. The profile then flattens out



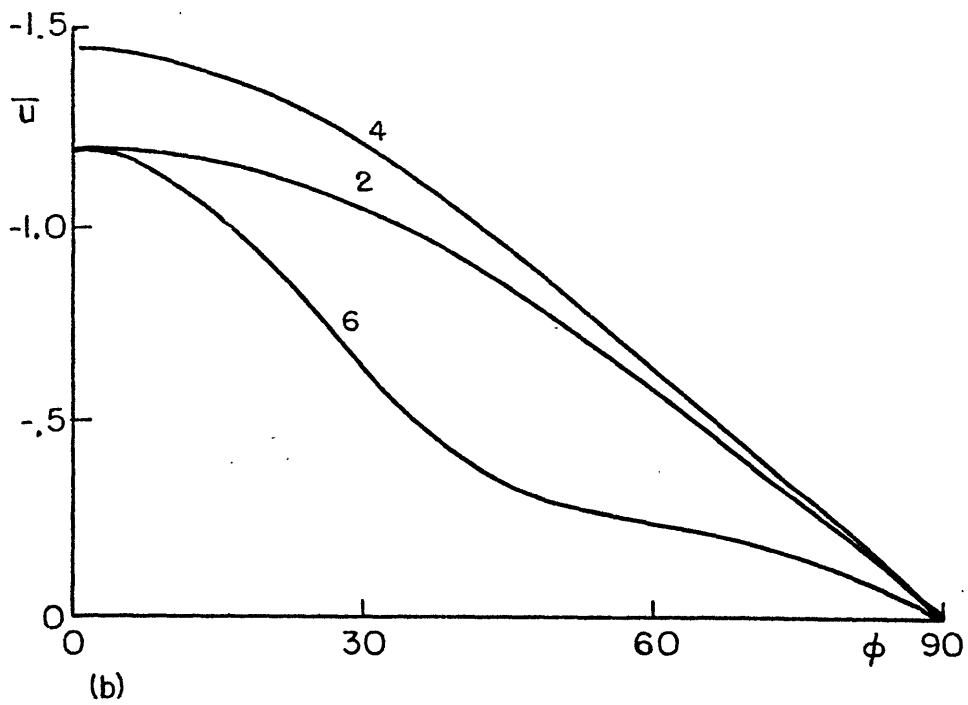
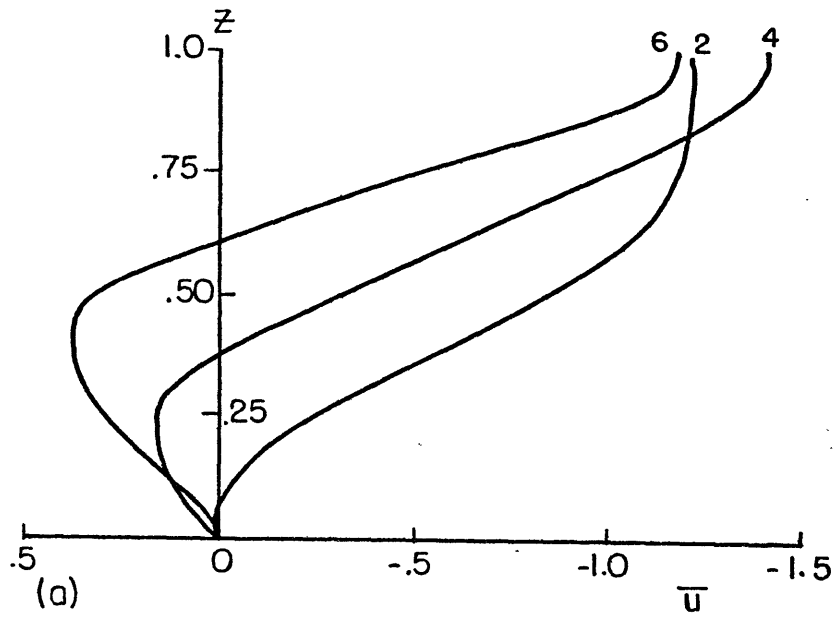


FIGURE 3.16 Profiles of steady state  $\bar{u}$  for  $M = 2, 4,$  and  $6$ : (a) vertical profiles at the equator, (b) meridional profiles at the top.

in high latitudes. The reasons for this behavior will become more apparent later when we discuss the Reynolds stresses (Figures 3.19 and 3.20).

In Figures 3.17 and 3.18 we present the vertical cross sections and the vertical and meridional profiles of  $\bar{u}$  after 1.5 SD for  $M = 4, 6,$  and  $8$ . As in the steady state solutions, we again find that the maximum retrograde mean zonal flow occurs at the top of the model near the equator. The maximum values of  $\bar{u}$  are  $-1.1$  ( $-4.4 \text{ m s}^{-1}$ ),  $-1$  ( $-4 \text{ m s}^{-1}$ ), and  $-0.9$  ( $-3.6 \text{ m s}^{-1}$ ) for  $M = 4, 6, 8$  respectively. We note that the  $M = 4$  and  $6$  values are roughly 80% of their corresponding steady state values.

The cross sections for  $M = 4$  and  $6$  (Figure 3.17a and b) are quite similar in appearance to the steady state cross sections (Figures 3.16 b and c). The main difference is that during this developmental stage, the prograde flow covers a larger area than in the steady state (for both  $M = 4,$  and  $6$ ). For  $M = 8,$  the retrograde flow is confined to the upper part of the model between the equator and  $60^\circ$  latitude. If we may be so bold as to extrapolate in time, we can guess that for  $M = 8,$  the steady state  $\bar{u}$  will consist of retrograde flow in the upper half of the model, except possibly in higher latitudes where there will be very weak prograde flow. The maximum retrograde  $\bar{u}$  will be at the top at the equator and will have a value of approximately  $-5 \text{ m s}^{-1}$ . The lower half of the model will

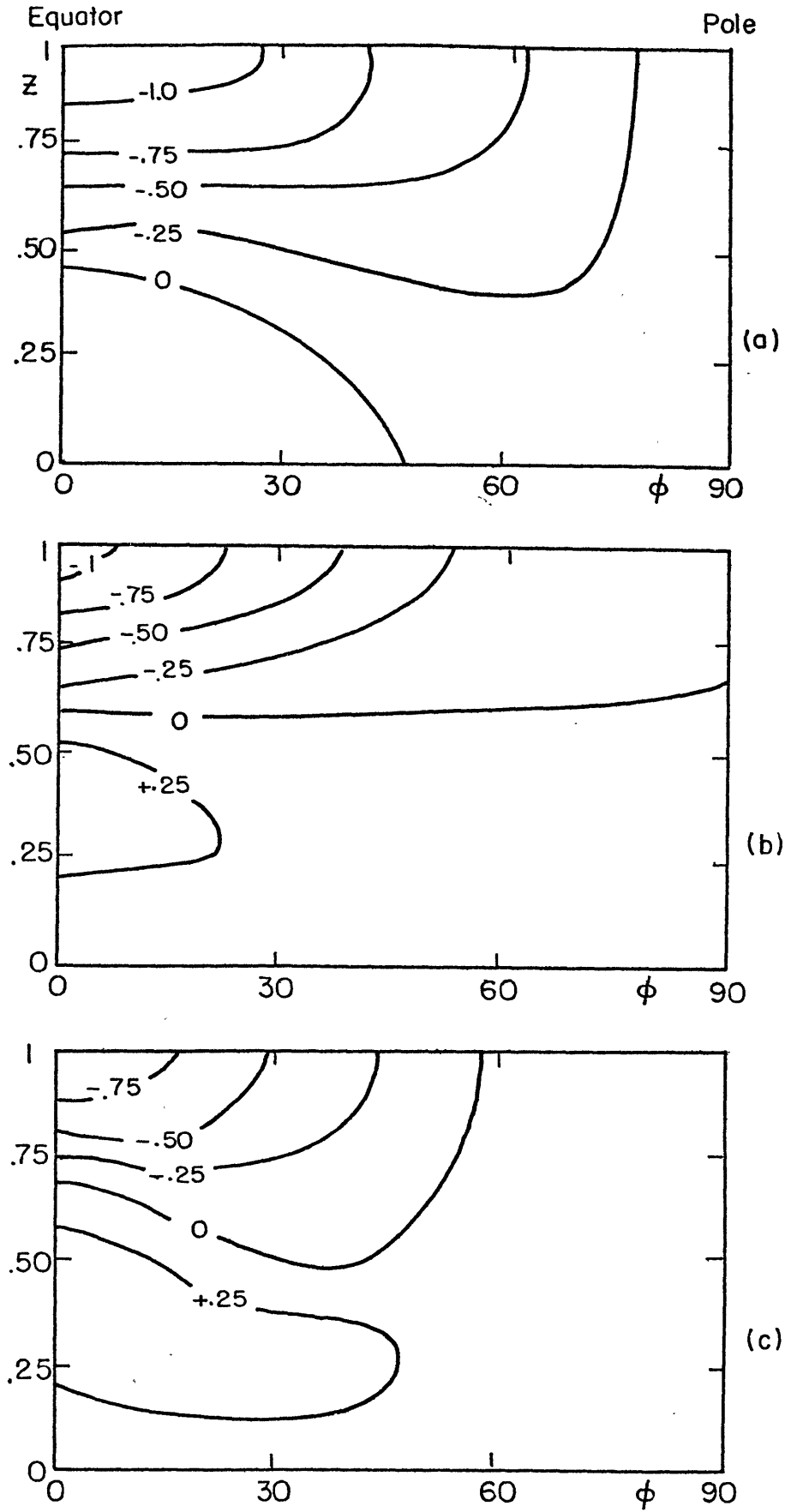


FIGURE 3.17 Vertical cross sections of  $\bar{u}$  after 1.5 solar days for: (a)  $M = 4$ , (b)  $M = 6$ , (c)  $M = 8$ .

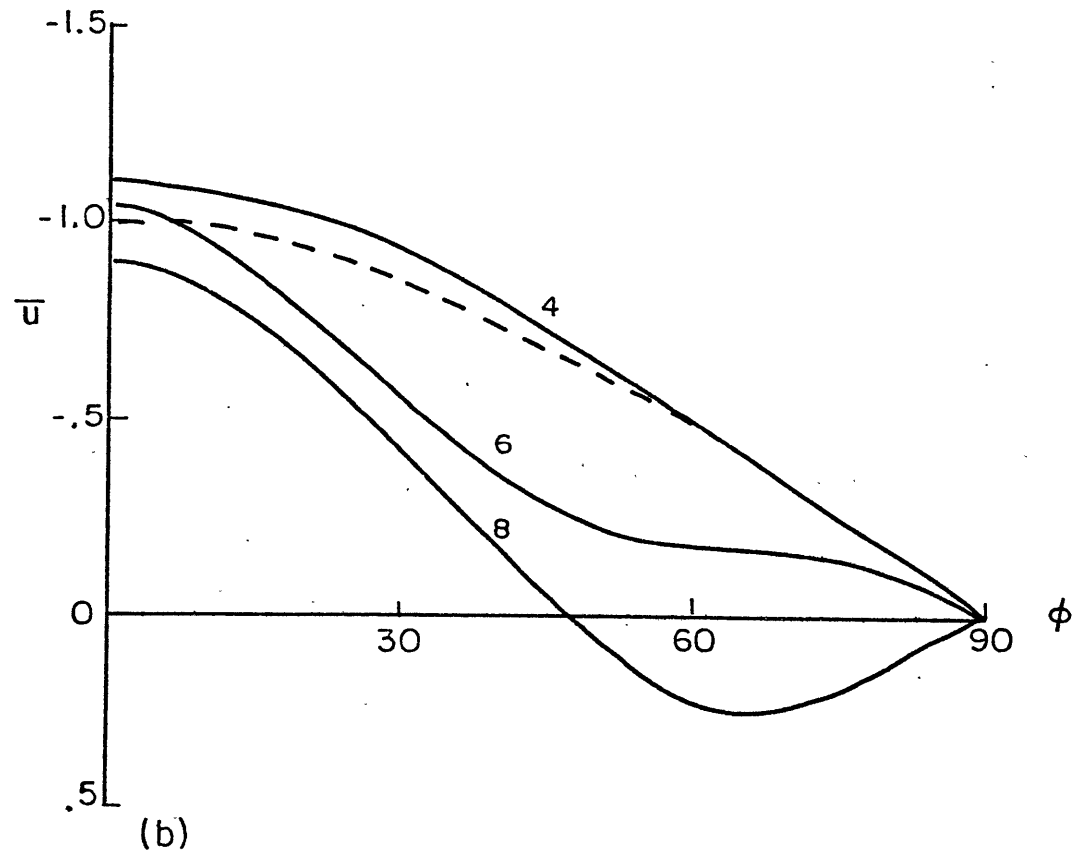
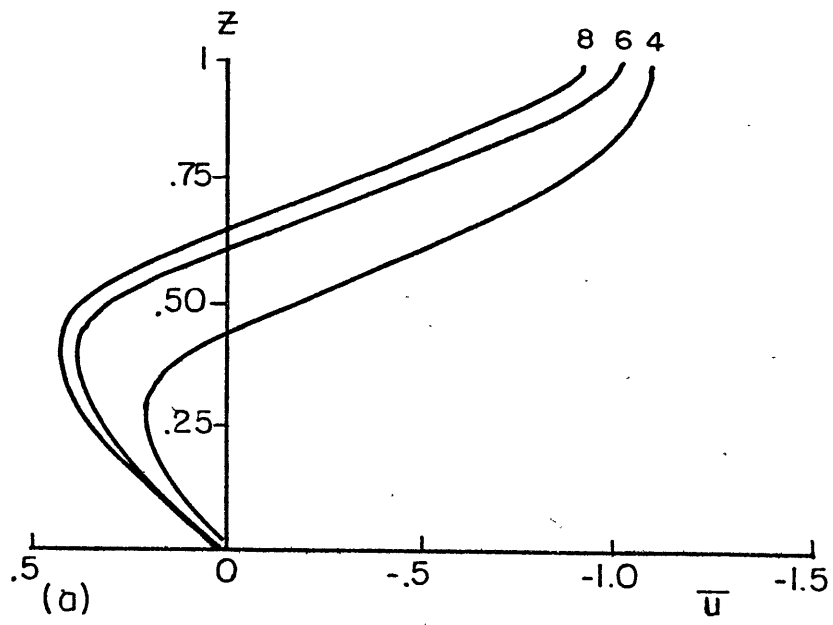


FIGURE 3.18 Profiles of  $\bar{u}$  after 1.5 solar days for  $M = 4, 6,$  and  $8$ : (a) vertical profile at the equator, (b) meridional profile at the top. Dashed line is  $\cos \phi$ .

exhibit weak prograde flow at all latitudes. This description is quite similar to the steady state  $M = 6$  case and is probably very reasonable in view of the similarity between the  $M = 6$  and  $8$  profiles in Figure 3.18 (by similarity we mean that there is a much closer resemblance between  $M = 6$  and  $M = 8$  than there is between  $M = 4$  and  $M = 6$ ).

By comparing the vertical profiles of  $\bar{u}$  at the equator (Figure 3.18a) we find that the differences between  $M = 6$  and  $8$  are quite small as compared to the much more significant differences between  $M = 4$  and  $M = 6$ . We also note that the  $M = 4$  and  $6$  profiles appear quite similar (except in amplitude) to their steady state counterparts. Thus it appears that the 1.5 SD profiles represent a reasonable prediction of the steady state profiles and therefore we might expect the steady state  $M = 8$  profile to be similar to the 1.5 SD  $M = 8$  profile.

As for the meridional profiles (Figure 3.18b) we again see that the  $M = 4$  flow is close to solid body rotation (the dashed line represents  $\cos \phi$  and is included for reference). Both  $M = 6$  and  $8$  show a fairly sharp equatorial jet. In higher latitudes, the  $M = 6$  profile flattens out (as in the steady state) while the  $M = 8$  profile changes sign corresponding to weak prograde flow with a relative maximum near  $65^\circ$  latitude. Had we integrated the  $M = 8$

case for a longer time, we might expect the prograde flow in higher latitudes to further weaken and possibly even change to weak retrograde flow as in the  $M = 6$  case.

In view of the cross sections and profiles of  $\bar{u}$  that we have presented (steady state and 1.5 SD) we point out some interesting similarities and differences between our model results and the observations of the 4-day circulation. The similarities are: 1) the model does produce a retrograde mean zonal flow with an equatorial jet, corresponding to the recent Pioneer Venus results (Rossow et al., 1980); 2) the mean meridional flow at the top is poleward and the maximum value of  $\bar{v}$  is typically smaller than the maximum  $\bar{u}$  by a factor of two or three. On the other hand, the differences between our results and observations are: 1)  $\bar{u}$  is too small by an order of magnitude; 2) the eddy velocity components in our model typically exceed the zonal mean values by a factor of two or three, contrary to observations where  $\bar{u}$  is dominant.

At this point, based on our results we must also conclude that model resolution can have a drastic effect on the details of the resulting flow. In particular it appears that the transition from  $M = 4$  to  $M = 6$  is much more significant than changing from  $M = 6$  to  $M = 8$ . The details of these differences will be discussed in more detail in the next two sections. The main point is that any further

general circulation simulations of Venus must have a resolution of at least  $M = 6$  and thus we must seriously question the validity and relevance of YP computations.

3.4.6 Reynolds Stresses

Through all of our results we have clearly demonstrated that the moving flame mechanism can indeed drive a retrograde mean zonal flow. The final question is: exactly how is this accomplished? The answer can be easily explained in terms of the Reynolds stresses which are simply the angular momentum transport terms in the equations of motion. We are specifically interested in the vertical and horizontal fluxes and the role that each plays in maintaining  $\bar{u}$ . We will focus our discussion on the net angular momentum fluxes defined by:

- 1) net vertical flux across a given height level

$$\int_{-\frac{\pi}{2}}^{\frac{\pi}{2}} \overline{uw} \cos^2 \phi \, d\phi$$

- 2) net horizontal flux across a given latitude circle

$$\int_0^1 \overline{uv} \cos \phi \, dz$$

where the overbar, ( $\bar{\quad}$ ), indicates the zonal mean. We will also be discussing the contribution to the angular momentum transport by the MMC in which case we replace  $\bar{u\bar{w}}$  and  $\bar{u\bar{v}}$  by  $\bar{u\bar{w}}$  and  $\bar{u\bar{v}}$  respectively. Similarly for the contribution by the eddies we replace  $\bar{u\bar{w}}$  and  $\bar{u\bar{v}}$  by  $\overline{u'w'}$  and  $\overline{u'v'}$  respectively (Reynolds stresses).

In Figures 3.19 and 3.20 we show the net vertical and net horizontal angular momentum fluxes for the  $M = 4$  (Figure 3.19) and the  $M = 6$  (Figure 3.20) steady state solutions.

We begin by first recalling that the retrograde flow at the top exhibits an equatorial jet in all cases. For  $M = 4$  the meridional variation of  $\bar{u}$  is close to the profile for solid body rotation. For  $M = 6$ , the meridional profile shows a fairly sharp equatorial jet with  $\bar{u}$  decreasing rapidly between the equator and  $50^\circ$  latitude.

We now compare the vertical Reynolds stresses for  $M = 4$  and 6 (Figures 3.19a and 3.20a). In both figures we show the contributions to the net flux from: 1) the MMC (curve 0), 2) zonal wavenumbers 1 and 2 (curves 1 and 2), 3) all eddies combined (curve E), and 4) the total net flux (dashed line) which is simply equal to  $O + E$ .

For both truncations we can clearly see that the total eddy flux represents an upward transport of retrograde angular momentum. Thus the eddies that are forced by the moving flame type heat flux do indeed produce a retrograde acceleration of the upper part of the model. In linear



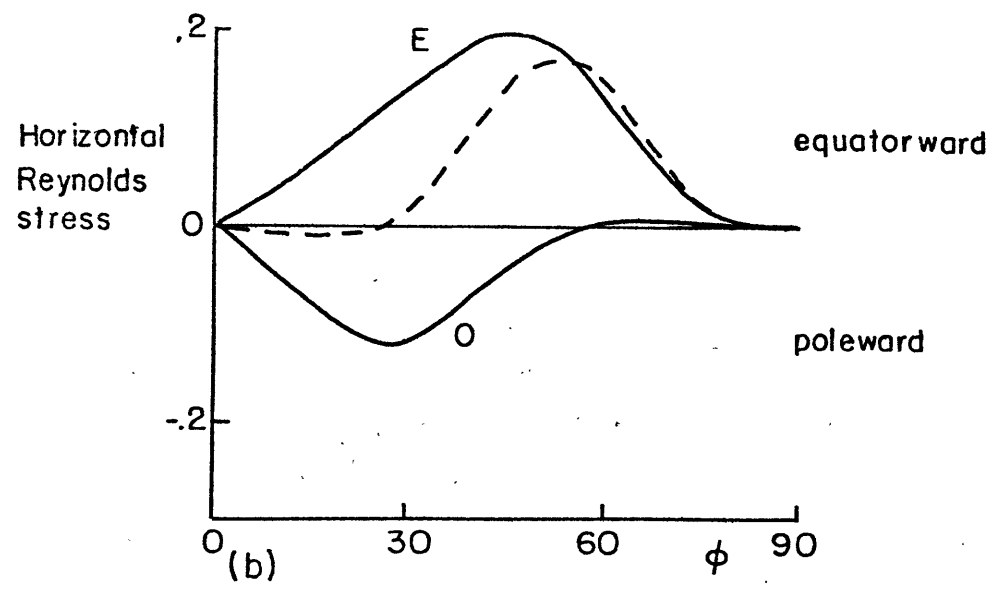
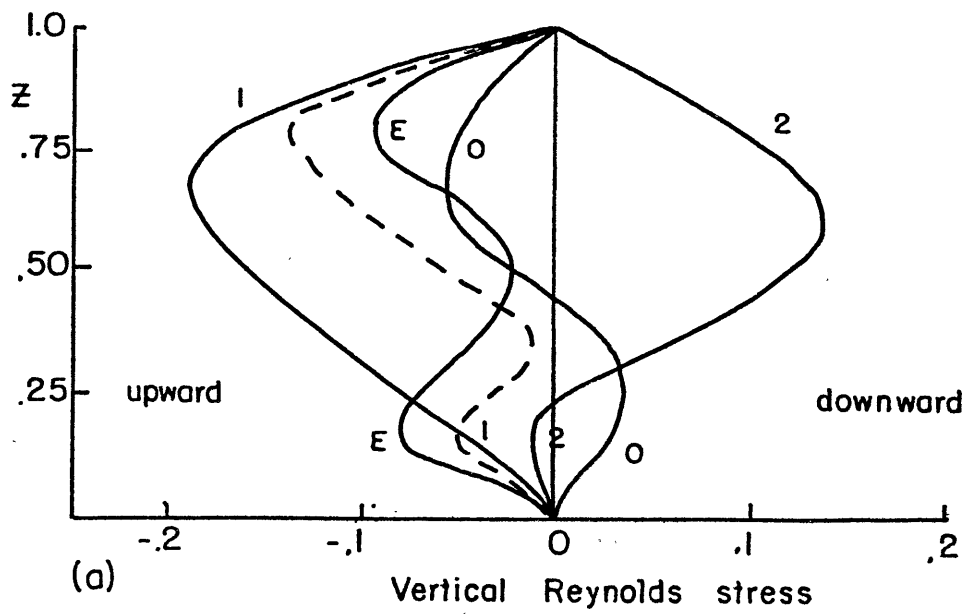


FIGURE 3.19 Angular momentum transports for the steady state  $M = 4$  solution: (a) vertical flux (horizontal averages), (b) horizontal flux (vertically averaged). Curves are labeled as: 0 = MMC, 142 - zonal wavenumbers, E - total eddy (Reynolds stresses), dashed - net flux = 0 + E.

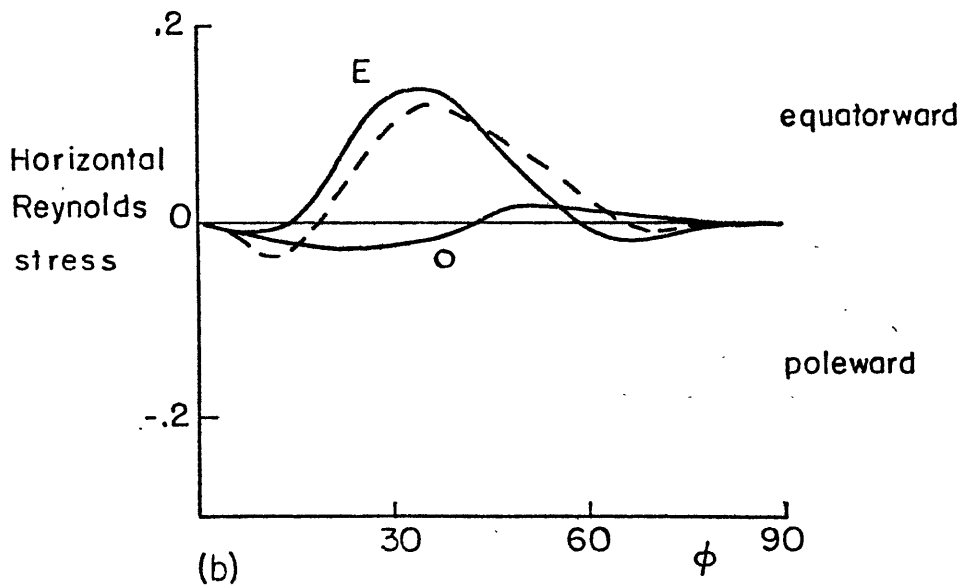
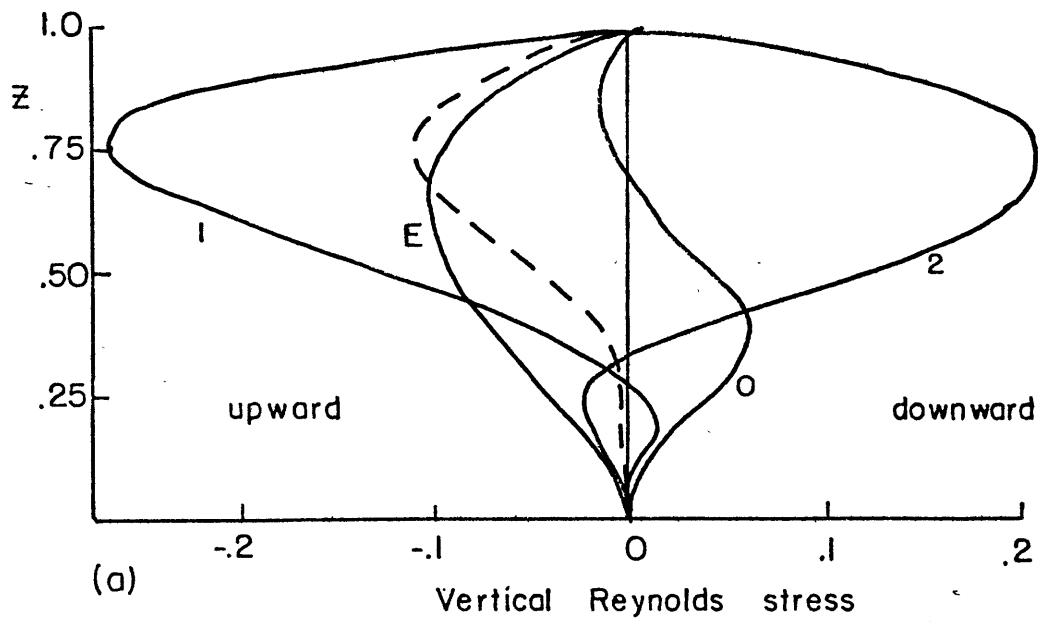


FIGURE 3.20 As in Figure 3.19 except  $M = 6$ .

theory and in our linearized calculations, this conclusion was easily reached based on the tilt of the eddy convection cells. For the current nonlinear calculations, the upward eddy flux of retrograde angular momentum is due to the phase shift of  $w'$  relative to  $u'$  (Figures 3.13 and 3.14), i.e., the core of rapid upward motion is generally correlated with retrograde eddy zonal flow. However, there is no simple and obvious tilt in the convection pattern as in the linear problem.

As a point of interest, we also show the vertical retrograde momentum transport by zonal wavenumbers 1 and 2 (curves 1 and 2 respectively). For both truncations we observe a similar behavior: the moving flame effect (i.e., upward eddy transport of retrograde momentum) is due primarily to zonal wavenumber 1. On the other hand, zonal wavenumber 2 causes a downward flux of retrograde momentum (except in the lowest quarter of the model) and therefore counteracts the desired effect. The total eddy flux is determined primarily by the difference between the contributions from wavenumbers 1 and 2, although for  $M = 6$  it is clear that higher wavenumbers are not negligible.

The major difference between the  $M = 4$  and  $M = 6$  results lies in the relative importance of the momentum transport terms associated with the MMC (i.e., zonal wavenumber 0; curve 0). For both truncations, the overall

structure is similar -- downward flux of retrograde momentum in the lower part of the model and an upward flux in the upper part. However, the difference between  $M = 4$  and  $M = 6$  is the magnitude of the MMC flux and its relative importance in determining the net vertical angular momentum flux (dashed line in figures). In the lower part of the model the  $M = 6$  downward flux is twice as large as the  $M = 4$  downward flux. This explains the larger net upward flux in the lower part of the model for  $M = 4$ .

In the upper part of the model, the difference in the upward MMC fluxes for  $M = 4$  and  $M = 6$  are much more pronounced. The  $M = 4$  flux is larger than the  $M = 6$  flux by a factor of three to four. By comparing the combined effects of the eddies and the MMC in the upper part of the model, we see that for  $M = 4$  the net upward flux of retrograde angular momentum receives two-thirds of its magnitude from the eddies and one-third from the MMC. For  $M = 6$ , the net flux is due almost entirely to the eddies (85% from the eddies and only 15% from the MMC). Thus, we see that the lower spectral truncation of  $M = 4$  results in an overestimate of the importance of the role of the MMC in driving the retrograde mean zonal flow.

We next turn our attention to the horizontal angular momentum fluxes (averaged over height) for  $M = 4$  (Figure 3.19b) and for  $M = 6$  (Figure 3.20b). Here we show the net

flux (dashed line) and the contribution of the MMC (curve 0) and the total contribution of the eddies (curve E). For  $M = 4$ , the MMC provides a poleward flux of retrograde angular momentum between the equator and  $55^\circ$  latitude. The maximum flux occurs near  $27^\circ$  latitude. Such a profile would lead to the development of a mid or high latitude jet. However, balancing this is a strong equatorward eddy flux of retrograde angular momentum with a maximum near  $48^\circ$ . Between the equator and  $30^\circ$  latitude, the MMC flux and the eddy flux are roughly in balance resulting in an almost negligible net poleward flux of retrograde momentum. Beyond  $30^\circ$  latitude, the equatorward eddy flux becomes important and by  $50^\circ$  latitude the net flux curve follows the eddy curve quite closely. The maximum net flux occurs at  $55^\circ$  latitude. This net equatorward flux of retrograde angular momentum is what maintains the equatorial jet profile of  $\bar{u}$  (Figure 3.16b). As in the vertical fluxes, we again find that for  $M = 4$ , the maximum MMC flux is roughly one-half of the maximum eddy flux so that both the role of MMC and the role eddies are comparable in terms of their effect on  $\bar{u}$ .

For  $M = 6$  we see that the MMC provides a poleward flux of retrograde angular momentum between the equator and angular momentum between the equator and  $45^\circ$  latitude and a weak equatorward flux beyond  $45^\circ$ . The eddy

transport is dominated by a strong equatorward flux with a maximum near  $35^{\circ}$ . As in the case of the  $M = 6$  vertical fluxes we again find that the eddy transport is the dominant term in the net flux and the MMC plays only a minor role in the angular momentum balance. The maximum net equatorward transport of retrograde momentum occurs near  $35^{\circ}$  latitude. Since the peak equatorward net flux is  $20^{\circ}$  closer to the equator than in the  $M = 4$  case we now can see why the  $M = 6$  profile of  $\bar{u}$  (Figure 3.16b) shows a sharper jet structure than the  $M = 4$  profile.

In view of these results, we are immediately lead to one conclusion concerning model resolution: the role of the MMC in driving and maintaining the mean zonal flow is severely overestimated in the  $M = 4$  case. Related to this, we point out that YP results also indicated that both the MMC and the large scale eddies play an important role in the angular momentum balance. This agrees with our  $M = 4$  results. Based on the differences between our  $M = 4$  and  $M = 6$  computations we can see that a truncation of  $M = 4$  is not enough to accurately simulate all of the non-linear interactions of even the largest scale waves ( $m=1$  and  $2$ ) and consequently we again must question the validity of YP as being a correct representation of the general circulation on Venus.

### 3.5 Discussion

Before discussing our results, we again want to emphasize that we have investigated only one very specific physical process -- the moving flame mechanism -- in a simplified Boussinesq model. We have not developed a highly complex and detailed general circulation model for Venus. Nevertheless, we do see some interesting similarities and differences among our results, YP results, and observations of Venus. While we cannot make an in-depth comparison between our computations and YP simulations we can compare certain overall features of the two models. We can also make some important and interesting inferences and raise some crucial questions concerning current and future modelling efforts related to Venus.

The discussion that follows in the rest of this section is presented in the same order as the results of the previous section. From a numerical point of view, our problem is complicated from the outset by the inherent relatively long physical time scales. Therefore, to reach any type of steady solution, the model must be integrated for fairly long periods, typically three solar days (corresponding to roughly one terrestrial year). For this reason we are limited in terms of the spatial resolution of the model as well as in terms of the number of possible numerical experiments. Thus we have carried out limited parameter studies for only the lowest order truncation

of  $M = 2$ . The main purpose of these studies is to compare the low resolution nonlinear results to linear theory and to the linearized calculations of Chapter 2. From Figure 3.5 we see that the nonlinear results agree with the linearized results and linear theory to the extent that all three predict an increase in the maximum retrograde  $\bar{u}$  as the thermal forcing parameter,  $G$ , is increased. The main difference is that as the degree of nonlinearity increases, the effectiveness of varying  $G$  becomes less noticeable. According to linear theory, the maximum value of  $\bar{u}$  varies as  $G^2$ . For the low order spectral model, for  $G \sim O(100)$  the maximum  $\bar{u}$  varies as  $G^{1/2}$  while for  $G \sim O(1000)$ , it varies as  $G^{1/3}$ . Thus even if our thermal forcing is too small by an order of magnitude, our maximum  $\bar{u}$  would be off by at most a factor of two.

By comparing Figures 2.13 and 3.6 we see that the dependence of the maximum  $\bar{u}$  upon the thermal frequency parameter,  $2\eta^2$ , is similar for both the linearized and the nonlinear models. The most important feature of these curves is the relative maximum that occurs for  $2\eta^2 \sim O(10)$ . For the linearized calculations the peak is at  $2\eta^2 = 25$  while for the nonlinear calculations the peak is at  $2\eta^2 = 12$ . The most interesting point here is that if the widely used estimate of  $\kappa_v = 10^4 \text{ cm}^2 \text{ s}^{-1}$  is correct, then at the Venus cloud tops we have  $2\eta^2 = 15.5$ . Consequently



for a fixed thermal forcing,  $G$ , the moving flame mechanism exhibits its maximum effectiveness for the estimated Venus value of the thermal frequency parameter.

As mentioned above, because of the relatively high cost of running a fully nonlinear model we were limited as to the number of experiments that could be carried out. Thus after examining the results of the low order truncation parameter studies, we chose values of the dimensionless parameters that seemed reasonable for Venus and concentrated our time and effort on studying the effects of spectral truncation (i.e., spatial resolution). We also note that the spectral truncation is in a sense a measure of the degree of nonlinearity of the model (i.e., higher truncation allows more accurate representation of nonlinear interactions).

In view of our linearized solutions and the results of Stone (1968) the sensitivity of the MMC to spectral truncation is as one might expect. The nonlinear interactions force the Hadley cell to be concentrated near the point of maximum heating (in our case towards the bottom and the equator). For  $M = 4$  (Figure 3.7b) the Hadley cell is centered at  $\phi = 30^\circ$  while for  $M = 6$  (Figures 3.7b and 3.8a) and for  $M = 8$  (Figure 3.8b) it is centered at  $\phi = 22^\circ$ . Thus we again see that the transition from  $M = 4$  to  $M = 6$  is quite significant in terms of the treatment of

nonlinear interactions. The differences between  $M = 6$  and  $M = 8$  are not nearly as pronounced. It is also interesting to note that the MMC reaches a quasi steady state rather quickly -- after  $1 - 1\frac{1}{2}$  SD -- as compared to the mean zonal flow which requires roughly three solar days (the vertical diffusion time scale).

From the horizontal maps of the total flow (Figures 3.9 to 3.12) and the height-longitude cross sections of the eddies (Figures 3.13 and 3.14) it is quite clear that the circulation is dominated by the largest scales of motion -- primarily zonal wavenumbers 1 and 2. Here, the role of the nonlinear interactions is to concentrate the circulation near the subsolar point (local noon). Furthermore, this nonlinear concentration becomes more pronounced as the model resolution (truncation) is increased. This effect is especially noticeable in the vertical velocity patterns shown in parts (b) of Figures 3.9 - 3.14. In all cases, the vertical velocity field is dominated by a relatively narrow core of rising motion near the subsolar point. This feature is analogous to the "mixing region" concept (i.e., an internal vertical boundary layer) introduced by Goody and Robinson (1966) and discussed by Stone (1968) and Kálmán de Rivas (1973). From our figures we can clearly see that the size and intensity of the mixing region is quite sensitive to the model resolution. As an example we consider the eddy vertical velocity fields,  $w'$ , for

M = 4 (Figure 3.13b) and M = 6 (Figure 3.14b). For M = 4 the mixing region has a width of 120° of longitude and a maximum w' of 1.9 cm s<sup>-1</sup>. For M = 6, the width is only 78° of longitude and the maximum w' is 1.3 cm s<sup>-1</sup>.

By comparing the horizontal structure of the total vertical velocity fields (Figure 3.9b for M = 4, Figure 3.10b for M = 6) we see an additional role of the higher truncation -- the ability to capture some important smaller scale details of the circulation. By this we specifically mean the shape of the mixing region. For M = 4 it resembles a distorted ellipse. For M = 6 it appears as a very prominent Y shaped feature with a meridional extent of ± 45 latitude. Furthermore, in the M = 6 map there is a hint of a second Y shaped feature, extending from pole to pole, with its vertex near the morning terminator. The similarities between this pattern and the observed UV features at the Venus cloud tops are quite remarkable. If in fact the dark Y's on Venus are related to convective activity within the clouds, then our solutions seem to imply that these observed phenomena must be at least partially related to the response of the atmosphere to the overhead motion of the sun (i.e., the moving flame effect).

The additional horizontal details that appear in the higher truncation (i.e., M=6 and 8) experiments are related to the assumed form of the diurnal differential heating. A zonal Fourier analysis (Appendix A) of our

heating function (which is analogous to the diurnal variations in solar heating) shows that the bulk of the thermal forcing is confined to those modes that have zonal wavenumbers  $\leq 4$ . Thus to obtain any meaningful results, the resolution (truncation) must be chosen so as to allow the model to accurately simulate all of the important directly forced modes (i.e., those with  $M \leq 4$ ). Clearly in our  $M = 4$  solution and in all of the YP results this criterion is not satisfied since the dissipation terms at the high end of the resolved spectrum are forced to be artificially large to prevent spectral blocking. In our case this is due to the Shapiro filter while in YP this is due to the  $\nabla^4$  diffusion operator. Either way, for  $M = 4$  we can be sure that zonal wavenumbers 3 and 4 are being misrepresented by the model. However, for  $M = 6$  it is very likely that all waves up to  $M = 4$  are treated fairly accurately since our eighth order filter (Figure 3.3) leaves 90% of the amplitude of wavenumber 4 and 99.6% of the amplitude of wavenumber 3. Thus we see significant differences between the  $M = 4$  and  $M = 6$  results but much less significant differences between  $M = 6$  and  $M = 8$ .

Turning our attention to the temperature field (Figures 3.13a and 3.14a) we again notice that the strongest temperature gradients are confined to the lower boundary layer. We also notice that the diurnal temperature contrasts

are larger than the mean equator to pole contrasts (Figures 3.7 and 3.8) by a factor of three. This is surprising since the diurnal and meridional differential heat fluxes are comparable. However, the reason for this behavior is easily understandable in view of the velocity fields.  $\bar{v}$  in the lower boundary layer is consistently equatorward (i.e., the Hadley cell) with dimensionless magnitudes less than one. On the other hand,  $u'$  in the lower boundary layer (Figures 3.13c and 3.14c) exhibits a region of strong convergence on the daylight side of the model with maximum dimensionless magnitudes of three. Thus the strong eddy circulation is maintaining the strong temperature gradients on the daylight side.

Next we turn to the results for the mean zonal velocity. In all cases we find a significant retrograde mean zonal flow with the maximum  $\bar{u} \sim 0(1)$  occurring at the top of the model at the equator. The details of the vertical and meridional profiles of  $\bar{u}$  depend upon the truncation (Figures 3.15 - 3.18). For  $M = 2$   $\bar{u}$  is retrograde at all levels with a meridional profile at each level corresponding to solid body rotation. For  $M = 4$   $\bar{u}$  is retrograde except in a small area near the equator in the lower part of the model. At the top, the meridional profile is very close to solid body rotation. For the higher truncations ( $M=6$  and  $8$ ) the retrograde flow is

confined to the upper half of the model. Also, the higher truncation solutions show a more pronounced equatorial jet. Upon comparing the  $M = 4, 6$  and  $8$  profiles in Figure 3.18 we again see that the differences between  $M = 6$  and  $M = 8$  are much less significant than the differences between  $M = 4$  and  $M = 6$ . And once again we must conclude that  $M = 4$  is insufficient resolution.

By comparing the Reynolds stresses for  $M = 4$  (Figure 3.19) and for  $M = 6$  (Figure 3.20) we immediately notice that the processes that maintain  $\bar{u}$  are different for the two truncations. For  $M = 4$ , both the eddies and the MMC contribute significantly to the angular momentum balance. For  $M = 6$ , the MMC is much less important in maintaining  $\bar{u}$ .

To further confirm our conclusion concerning truncation and the inaccuracies of the  $M = 4$  solution, we have plotted some kinetic energy spectra in Figures 3.21 (steady state solutions) and 3.22 (1.5 SD). These spectra are computed at the top of the model at the equator, i.e., the location of the maximum retrograde mean zonal flow. Since we are considering a point at the equator, the kinetic energy involves only the zonal velocity component,  $u$ . For the spectra the kinetic energy is thus defined as

$$KE = \frac{1}{2} \bar{u}^2$$

By taking advantage of the spectral form of our model we can immediately write

$$KE = \frac{1}{2} \overline{u^2} = \frac{1}{2} \sum_{m=-M}^M u_m \tilde{u}_m$$

so that<sup>a</sup> the contribution of each mode to the spectra is simply

$$(KE)_m = \frac{1}{2} u_m \tilde{u}_m$$

By comparing the results for the various truncations ( $M=2, 4, 6,$  and  $8$ ) we observe one very definite difference between cases with  $M \leq 4$  and those with  $M > 4$ . This difference is the wavenumber of the most energetic mode. It is quite clear that for the lower truncation runs ( $M \leq 4$ ) the mean flow contains the largest portion of the kinetic energy. However, for the higher truncation cases ( $M > 4$ ) zonal wavenumber 1 is the most energetic mode. Once again this truncation related problem is intimately associated with the inability of the  $M \leq 4$  runs to accurately simulate the most important directly forced modes. The zonal Fourier analysis of the diurnal heating contrasts (Appendix A) immediately reveals to us that

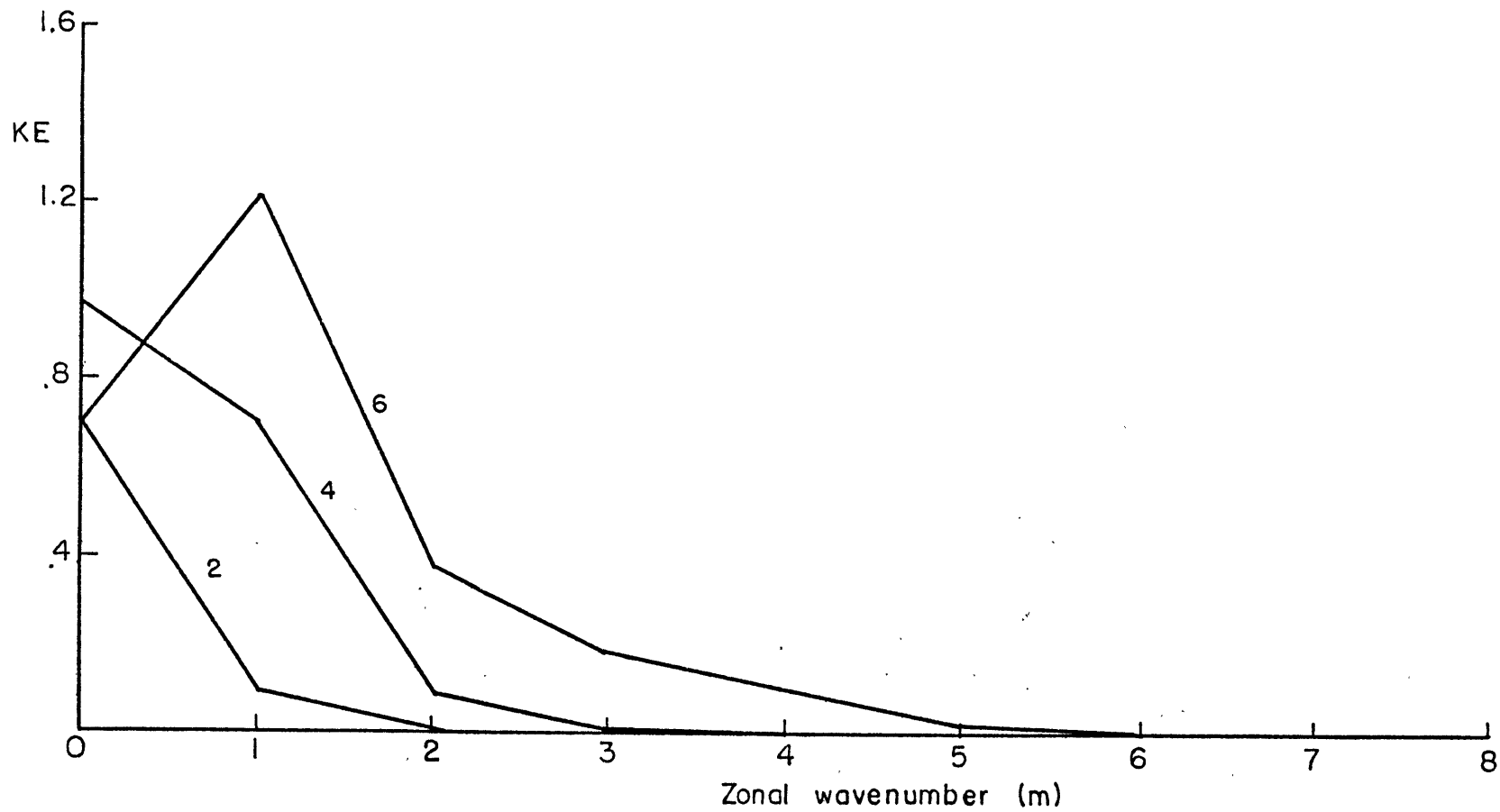


FIGURE 3.21 Kinetic energy spectra at the equator at the top of the model for the steady state  $M = 2, 4,$  and 6 solutions.



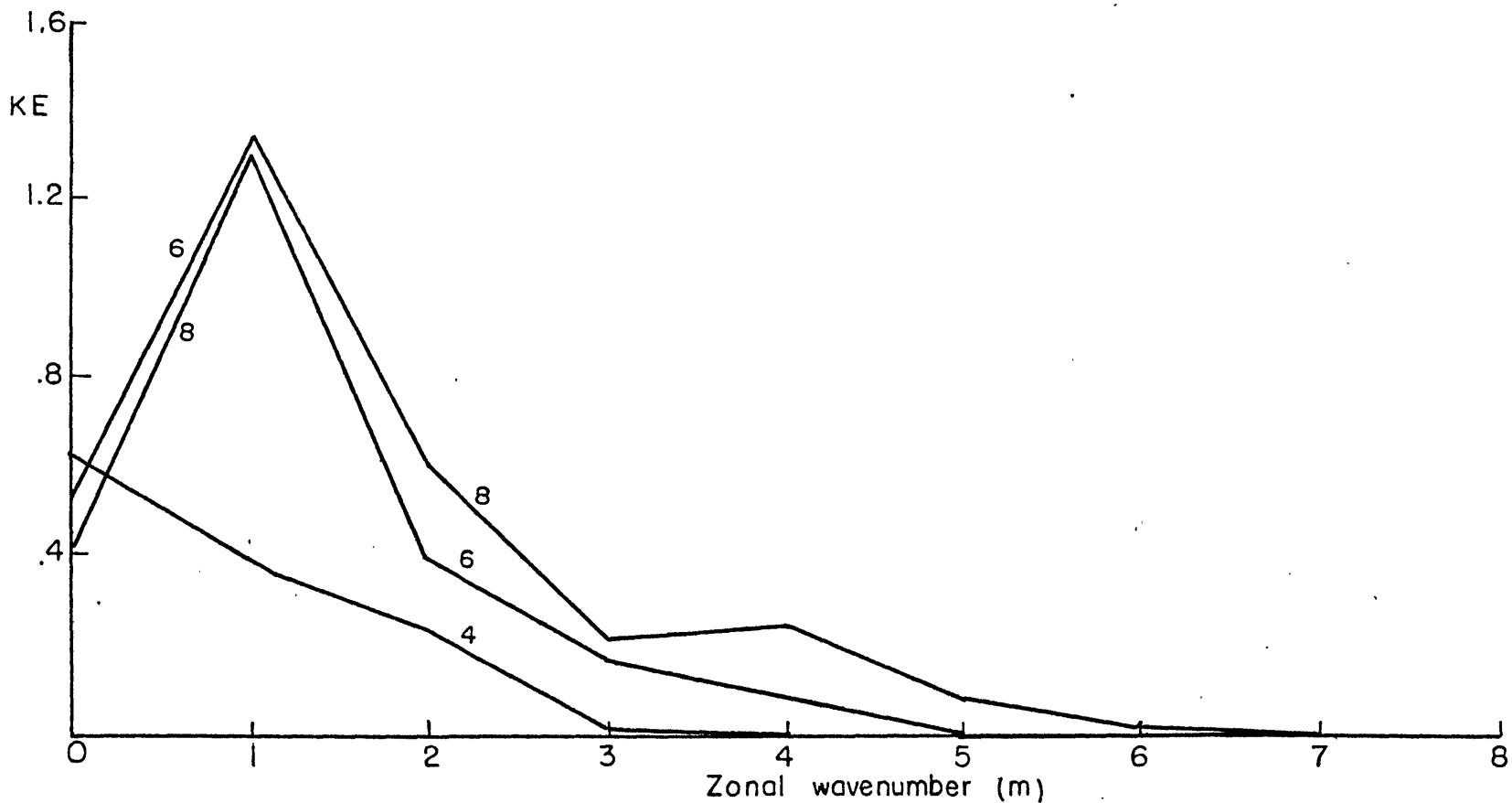


FIGURE 3.22 Kinetic energy spectra at the equator at the top of the model after 1.5 solar days for  $M = 4, 6,$  and  $8.$

the mode subjected to the strongest direct thermal forcing is zonal wavenumber 1. And once again the conclusion is unavoidable: if the forcing for the 4-day circulation is related to the diurnal differential heating then any simulation of the flow must accurately treat all modes with  $M \leq 4$  and therefore the model truncation must be greater than four.

Finally, we would like to say a few more words comparing our results to YP results. We repeat that any direct quantitative comparisons are not possible due to the differences between the two models. However we can make some interesting qualitative comparisons that raise some important questions concerning the validity of the YP simulations and their relevance to Venus. Furthermore we can only compare our results with their solution I (i.e., development of the forced flow from a state of rest).

In general, their velocity components are two to five times larger than ours (theirs are  $25-30 \text{ m s}^{-1}$  while ours are  $6-12 \text{ m s}^{-1}$ ). In view of the different complexities of the two models, these differences are not unreasonable. However, a more valuable comparison is to do an internal check of the results for each model. In their results  $\bar{u}$ ,  $\bar{v}$ ,  $u'$ ,  $v'$  are all of the same order of magnitude. Similarly in our results, all of the horizontal velocity components are all of the same order of magnitude.

Furthermore, for both our results and theirs the horizontal flow is moderately larger than the overhead speed of the sun but not an order of magnitude larger.

In their solution II, they observed a strong retrograde mean zonal flow with  $\bar{u} \simeq -90 \text{ m s}^{-1}$ . This was the product of a finite amplitude instability which they induced by arbitrarily multiplying the  $\zeta_1^0$  mode (after 1.5 SD) by a factor of 36. We also tried this but the model quickly blew up. Alternatively, we multiplied this mode by a factor of six three times over the course of one-half of a solar day. In this case the perturbation of the mean zonal wind disappears rather quickly. Thus the finite amplitude instability observed by YP in their results does not occur in our model and  $\bar{u}$  does not grow to  $100 \text{ m s}^{-1}$  through this mechanism. It is possible that for this instability to occur in our model requires a perturbed value of  $\bar{u}$  greater than some threshold value that we never exceeded.

A more interesting question is why do we observe an equatorial jet in all of our simulations while they observe a midlatitude jet in their solution I. We can tentatively identify two factors that could explain this difference. One is related to truncation, and the other is related to their formulation of the vertical diffusion term and its associated upper boundary conditions.

Concerning the truncation question, we again mention the overestimated role of the MMC in maintaining  $\bar{u}$  in the  $M = 4$  case. YP state that in their solution I the primary forcing for  $\bar{u}$  involves the MMC, planetary rotation, and to a lesser extent the planetary scale waves. It is well-known that a Hadley cell on a slowly rotating planet will transport planetary angular momentum poleward thus leading to the development of a mid or high latitude jet flowing in the same direction as planetary rotation. Furthermore, Kalnay de Rivas (1973) has shown that in a two-dimensional axisymmetric model for Venus a Hadley cell coupled with planetary rotation can force a retrograde high latitude jet of  $10 - 20 \text{ m s}^{-1}$  at the top of the model. If the MMC is the dominant transport mechanism (as indicated in our  $M=4$  case and YP), then it is not surprising that YP observe such a situation and we do not since we have neglected planetary rotation. However, we repeat once again that these results are for  $M = 4$  in which case the role of the MMC has been overestimated. It would be interesting to see if they find similar results for higher truncations. Unfortunately they do not adequately discuss any of their  $M = 6$  simulations.

One puzzling feature of their mid latitude jet is that it only appears in the layer from 55 - 64 km, i.e., at dimensionless heights between 0.86 and 1.0. Below

$Z = .86$  their  $\bar{u}$  field is close to solid body rotation which is the profile we observe. Furthermore, they state that the mid latitude jet only appears much later in the development of the flow. While we do not know exactly what they mean by "later", we can only guess that they mean after 10 solar days. This situation is what leads us to suspect that their  $\frac{\partial^4}{\partial z^4}$  diffusion operator and its associated upper boundary conditions may be contributing to forcing the midlatitude jet in a relatively thin layer near the top. Rossow et al. (1980b) have shown that the additional upper boundary condition specified by YP does not correspond to the assumed stress free top. Furthermore, their mid latitude jet appears only when the integration time (10 SD) approaches the vertical diffusion time scale ( $\sim 12$  SD). Prior to that time, they observe near solid body rotation even at the top of their model. Therefore, based on this evidence we suspect that  $\bar{u}$  in their upper "boundary layer" is being distorted by the erroneous boundary condition while the interior flow, which appears to be insensitive to the error, reflects the correct solution in their model.

## CHAPTER 4

SUMMARY AND CONCLUSIONS

The main goal of this thesis was to investigate the moving flame mechanism in three space dimensions -- i.e., a system which contains both diurnal and meridional heating contrasts of comparable magnitude. The motivation for this problem is to determine whether or not the overhead (diurnal) motion of the sun plays a significant role in driving the circulation of the Venus stratosphere as suggested by Schubert and Whitehead (1969).

To study this process, we constructed two models of different complexities -- a linearized model in Chapter 2 and a nonlinear spectral model in Chapter 3. Both models are Boussinesq and hydrostatic with thermal forcing provided as a heat flux boundary condition at the bottom.

The linearized model (which is simply an extension of previously published two-dimensional models) is written in cartesian coordinates. The two horizontal coordinates are infinite and the flow is assumed to be periodic in both  $x$  and  $y$  with period  $2\pi$ . The linearization consists of neglecting all terms that are quadratic in the eddies except for the Reynolds stress terms in the equation for the mean zonal flow. The relative simplicity of this model allows us to inexpensively: a) examine the first order nonlinear effects (wave-mean zonal flow interaction), and b) carry out

fairly extensive parameter studies.

The most important effect of the nonlinear interactions upon the mean meridional circulation is to concentrate the Hadley cell near the point of maximum heating (i.e., the bottom near the equator). This result was anticipated in view of Stone's (1968) conclusions from his study of the properties of Hadley cells. For the assumed Venus parameter values we found that the maximum mean meridional wind is  $\sim 12 \text{ m s}^{-1}$  and the maximum mean vertical velocity is  $0.39 \text{ cm s}^{-1}$ .

Because of the longitudinal resolution of  $M = 1$ , the linearized eddy circulation consists of a subsolar to anti-solar convection cell. Again due to the resolution the cell shows no longitudinal asymmetries. For the two-dimensional case (no MMC) the eddy convection cell exhibits significant retrograde tilting. In the three-dimensional case the tilt is still retrograde but not as pronounced. The reason for this is that the Hadley cell maintains a stable mean stratification which acts to reverse the tilt of the convection pattern. Nevertheless, the effect of heating from below is the dominant process in terms of determining the retrograde tilt of the convection cell. The maximum eddy velocities are: zonal  $6.8 \text{ m s}^{-1}$ , meridional  $5.6 \text{ m s}^{-1}$ , and vertical  $0.35 \text{ cm s}^{-1}$ .

Consequently, in both cases considered, the eddy circulation produces Reynold's stresses that transport retrograde momentum upward and thus the moving flame mechanism does indeed drive a retrograde mean zonal flow in the upper layers of the model. In the three-dimensional case the Hadley cell is the dominant horizontal momentum transport mechanism. Thus, as one would expect, in this case the maximum retrograde mean zonal wind occurs where the heating is a minimum and has a value of  $-2 \text{ m s}^{-1}$ .

The other purpose of the linearized model was to carry out parameter studies. We are most interested in the dependence of  $\bar{u}$  upon the thermal forcing parameters,  $G$ , and upon the thermal frequency parameter,  $2\eta^2$ . We found that  $\bar{u}$  increases with  $G$ , however as  $G$  becomes large ( $\sim 0(1000)$ ) the effectiveness of increasing thermal forcing becomes less noticeable.

For the  $2\eta^2$  behavior, we found that  $\bar{u}$  reaches a maximum for an intermediate value of  $2\eta^2 = 25$ . For  $2\eta^2 < 25$   $\bar{u}$  drops off quite rapidly while for  $2\eta^2 > 25$  it drops off gradually. It is interesting to note that if our estimated value of  $\kappa_v = 10^4 \text{ cm}^2 \text{ s}^{-1}$  is correct then the Venus value of  $2\eta^2 = 15.5$  is quite close to the peak in the  $2\eta^2$  curve. We note that these parameter dependencies are qualitatively similar to those in previously published linear studies (e.g., Schubert, Young, and Hinch, 1971) in which heat flux



boundary conditions were used. There are two differences between our results and other linear studies. The linear solutions are only valid for relatively small values of  $G$ , i.e., for  $G \lesssim 0(1)$ , while ours are valid for a larger range of values. The other difference is that linear solutions were usually presented as limit solutions for very large and for very small values of the frequency parameter, i.e., for  $2\eta^2 \gg 1$  and  $2\eta^2 \ll 1$ . Since our solutions were obtained numerically (i.e., without any assumptions concerning the value of  $2\eta^2$  and the corresponding asymptotic series expansions of the dependent variables) they are valid for all values of  $2\eta^2$ .

Having completed the linearized study we then proceeded to develop a nonlinear spectral model for spherical geometry. The main goals were to make the simulations more realistic by using spherical coordinates and by allowing for greater horizontal resolution and higher order nonlinear interactions. Because of the high expense of running a nonlinear model we studied particularly the effects of spectral truncation to see what was the minimum resolution necessary to get meaningful results.

For the lowest order truncation,  $M = 2$ , we conducted a limited parameter study and found that the results qualitatively agreed with the linearized results -- the maximum mean zonal wind was retrograde and it increased with the

thermal forcing parameter,  $G$ , and peaked for an intermediate value of the thermal frequency parameter,  $2\eta^2 = 12$ . We must bear in mind however that these results may not necessarily be valid for the higher resolution simulations.

We then chose what seemed to be reasonable estimates of the Venus values of the dimensionless parameters and then carried out experiments for truncations  $M = 4, 6, 8$ . In all cases the mean meridional circulation (MMC) reached a quasi steady state in a relatively short time of 1.5 solar days. For  $M = 4$  and 6 the eddies and the mean zonal velocity reached steady states after roughly three solar days. The  $M = 8$  integration was terminated after 1.5 solar days (i.e., it reached a steady state for the MMC but not for the eddies and  $\bar{u}$ ).

In terms of the MMC, the nonlinear interactions have the same effect as in the linearized model except here they are more pronounced, i.e., they force the Hadley cell to concentrate even more near the point of maximum heating. We also note that the differences between truncation  $M = 4$  and  $M = 6$  are quite significant -- the center of the Hadley cell shifts from  $30^\circ$  latitude ( $M=4$ ) to  $22^\circ$  latitude ( $M=6$  and  $M=8$ ). For all three truncations, the maximum mean meridional velocities are similar with values of  $\lesssim 2.5 \text{ m s}^{-1}$ . The maximum mean vertical velocities are also similar with values of  $\lesssim 0.15 \text{ cm s}^{-1}$ .

Since the spectral model retains higher zonal harmonics (i.e.  $m > 1$ ) we are now able to see the effects of nonlinearity upon the eddy circulation. Interestingly we find an effect analogous to the effect upon the MMC -- i.e., nonlinear interactions force the flow to concentrate near the point of maximum heating. The best example of this is the vertical velocity field which consists of a relatively narrow core of strong rising motion which is centered near 1400 LT at the equator. Most of the rest of the model area exhibits weak sinking motion. As the resolution increases the width of the core decreases and the maximum upward velocity increases (compare figures 3.13 b and 3.14 b). For  $M = 6$  and 8 the resulting  $w$  fields produce y shaped patterns very much like those observed in the ultraviolet cloud top photographs of Venus. We specifically refer the reader to figures 2 u and v and 3a all in Rossow et al. (1980a). We note the remarkable similarity between these photographs and the horizontal map of our  $M = 6$  steady state vertical velocity field (figure 3.10 b).

Turning our attention to the mean zonal flow, we find that the phase shifts between the eddy zonal and vertical velocity components,  $u'$  and  $w'$ , do indeed provide an upward flux of retrograde angular momentum and thus these resulting Reynold's stresses drive a retrograde mean zonal flow in the upper layers of the model. We emphasize here that the

Reynold's stresses are produced by phase shifts and not by any obvious tilting of the convection cells. In all cases considered we found that the maximum retrograde  $\bar{u}$  appears at the top of the model near the equator. The maximum values are  $-5.8 \text{ m s}^{-1}$  for  $M = 4$  and  $-4.8 \text{ m s}^{-1}$  for  $M = 6$ . The most important effect of higher resolution is to allow for a more pronounced equatorial jet structure in the meridional profile of  $\bar{u}$ . We note here that we cannot make any definitive statements concerning the possible role of the barotropic instability mechanism suggested by Rossow et al. (1980a) since our  $M = 6$  and  $M = 8$  runs do contain a few potentially unstable zonal flow modes (those with  $m=0$  and  $n \geq 3$ ) but the hemispheric representation eliminates the most unstable disturbances for those retained zonal flow modes.

We can sum up our results by reviewing our two most important conclusions. First, it appears that the moving flame mechanism does play a role in driving the circulation of the Venus stratosphere. The strongest evidence we have for this is the remarkable similarity between some of our computed Y shaped vertical velocity fields and some of the recent Pioneer Venus cloud top ultraviolet photographs (see discussion and reference above). However, if the effectiveness of the moving flame type forcing is confined to the upper cloud layers then this mechanism alone cannot consistently explain the simultaneous existence of both the

100 m s<sup>-1</sup> retrograde mean zonal winds and much weaker eddy velocities. We base this on the fact that in our results the horizontal eddy and mean velocity components are all of the same order of magnitude. In fact, in our nonlinear results we find that the maximum eddy zonal velocity is  $\sim 12$  m s<sup>-1</sup> which exceeds our maximum mean zonal flow by a factor of 2.5. This is not consistent with the observations of Venus. We therefore must conclude that the 4-day circulation is being driven by other processes that are not explicitly included in our model.

Our second conclusion is important for future modelling efforts. We have clearly shown that  $M=4$  is insufficient resolution for modelling a nonlinear system like Venus. We can quite confidently state that any future simulations of the general circulation of the Venus atmosphere must be able to accurately represent at least the large scale eddies with zonal wavenumbers  $\leq 4$ . This condition requires a resolution of at least  $M=6$  since any numerical dissipation term (e.g., diffusion) will inevitably distort the waves with the highest retained wavenumbers. The observations and analysis presented by Travis (1978) and the barotropic instability cycle proposed by Rossow et al. (1980a) seem to suggest that model truncations may have to be as high as  $M=10$  with global spectral representations of the dependent variables. Considering the current state of numerical modelling, computer technology, and our understanding of Venus

this may indeed turn out to be quite an extensive time consuming undertaking.

REFERENCES

Apt, J., R.A. Brown and R.M. Goody, 1980: The character of thermal emission from Venus. J. Geophys. Res., 85, 7934-7940.

Arakawa, A. and V.R. Lamb, 1977: Computational design of the basic dynamical processes of the UCLA general circulation model. Methods in Computational Physics, V. 17, F. Adler, ed., New York, Academic Press, 174-265.

Belousov, S.L., 1962: Tables of Normalized Associated Legendre Polynomials. New York, Pergamon Press, 379 pp.

Baines, P.G., 1976: The stability of planetary waves on a sphere. J. Fluid Mech., 73, 193-213.

Bourke, W., 1972: An efficient one level primitive equation spectral model. Mon. Weath. Rev., 102, 687-701.

Chalikov, D.V., A.S. Monin, A.S. Safray, V.G. Turikov and S.S. Zilintinkevich, 1975: Numerical simulation of the general circulation of the Cytherean lower atmosphere. Icarus, 26, 178-208.

Counselman, C.C., S.A. Gourevitch, R.W. King, G.B. Lorient and R.G. Prinn, 1979: Venus winds are zonal and retrograde below the clouds. Science, 205, 85-87.

Davey, A., 1967: The motion of a fluid due to a moving source of heat at the boundary. J. Fluid Mech., 29, 137-150.

Dolfus, A., 1975: Venus: Evolution of the upper atmospheric clouds. J. Atmos. Sci., 32, 1060-1070.

Douglas, H.A., P.J. Mason and E.J. Hinch, 1972: Motion due to a moving internal heat source. J. Fluid Mech., 54, 469-480.

Eliassen, E., B. Machenauer and E. Rasmussen, 1970: On a numerical method for integration of the hydrodynamical equations with a spectral representation of the horizontal fields. Inst. of Theor. Meteorology, Univ. of Copenhagen, Report No. 2.

Fels, S. and R. Lindzen, 1975: The interaction of thermally excited gravity waves with mean flows. Geophys. Fluid Dyn., 6, 149-192.

Fultz, D., R.R. Long, G.V. Owens, W. Bohan, R. Kaylor and J. Weil 1959: Studies of thermal convection in a rotating cylinder with some implications for large scale atmospheric motions. Meteor. Monogr., 4, No. 21.

Gierasch, P., 1970: The four day rotation in the stratosphere of Venus. Icarus, 13, 25-33.

\_\_\_\_\_, 1975: Meridional circulation and the maintenance of the Venus atmospheric rotation. J. Atmos. Sci., 32, 1038-1044.

Gold, T. and S. Soter, 1971: Atmospheric tides and the 4-day circulation on Venus. Icarus, 14, 16-20.

Goody, R. and A. Robinson, 1966: A discussion of the deep circulation of the atmosphere of Venus. Astrophys. J., 146, 339-353.

Halley, R., 1686: An historical account of the trade winds and monsoons, etc. Phil. Trans. Roy. Soc. London, 16, 153-158.

Hinch, E.J. and G. Schubert, 1971: Strong streaming induced by a moving thermal wave. J. Fluid Mech. 47, 291-304.

Houghton, J.T., 1977: The Physics of Atmospheres. Cambridge, Cambridge University Press, 203 pp.

Isaacson, E. and H.B. Keller, 1966: Analysis of Numerical Methods. New York, Wiley, 541 pp.

Kálnay de Rivas, E., 1971: The circulation of the atmosphere of Venus. Ph.D. thesis, Dept. of Meteorology, MIT.

\_\_\_\_\_, 1972: On the use of nonuniform grids infinite difference equations. J. Compu. Phys., 10, 202-210.

\_\_\_\_\_, 1973: Numerical models of the circulation of the atmosphere of Venus. J. Atmos. Sci., 30, 763-779.

\_\_\_\_\_, 1975: Further numerical calculations of the circulation of the atmosphere of Venus. J. Atmos. Sci., 32, 1017-1024.

Knollenberg, R.G. and D.M. Hunten, 1979: Clouds of Venus: A preliminary assessment of microstructure. Science, 205, 70-74.



- Kronrod, A.S., 1965: Nodes and Weights of Quadrature Formulas (authorized translation from Russian). New York, Consultants Bureau, 143 pp.
- Lacis, A.A., 1975: Cloud structure and heating rates in the atmosphere of Venus. J. Atmos. Sci., 32, 1107-1124.
- Leovy, C., 1973: Rotation of the upper atmosphere of Venus. J. Atmos. Sci., 30, 1218-1220.
- Machenauer, B. and E. Rasmussen, 1972: On the integration of the spectral hydrodynamical equations by a transform method. Inst. of Theor. Meteorology, Univ. of Copenhagen, Report No. 3.
- Malkus, W.V.R., 1970: Hadley-Halley circulation on Venus. J. Atmos. Sci., 27, 529-535.
- Marov, M., V. Avdnevsky, V. Kerzhanovich, M. Rozhdestrensky, N. Borodin and O. Ryabov, 1973: Measurements of temperature, pressure and wind velocity on the illuminated side of Venus. J. Atmos. Sci., 30, 1210-1214.
- Murray, B., M. Belton, G. Danielson, M. Davies, D. Gault, B. Hapke, B. O'Leary, R. Strom, V. Suomi and N. Trask, 1974: Venus: Atmospheric motion and structure from Mariner 10 pictures. Science, 183, 1307-1315.
- Ogura, Y. and N.A. Phillips, 1962: Scale analysis of deep and shallow convection in the atmosphere. J. Atmos. Sci., 19, 173-179.
- Orszag, S.A., 1970: Transform method for calculation of vector coupled sums: Application to the spectral form of the vorticity equation. J. Atmos. Sci., 27, 890-895.
- Pollack, J.B. and R. Young, 1975: Calculations of the radiative and dynamical state of the Venus atmosphere. J. Atmos. Sci., 32, 1025-1037.
- Prinn, R.G., 1974: Venus: Vertical transport rates in the visible atmosphere. J. Atmos. Sci., 31, 1691-1697.
- Puri, K. and W. Bourke, 1974: Implication of horizontal resolution in spectral model integrations. Mon. Wea. Rev. 102, 333-347.
- Robert, A.J., 1966: The integration of a low order spectral form of the primitive meteorological equations. J. Met. Soc. Japan, 44, 237-245.

Rossow W.B. and G.P. Williams, 1979: Large scale motion in the Venus stratosphere. J. Atmos. Sci., 36, 377-389.

\_\_\_\_\_, A.B. Del Genio, S.S. Limarge, L.D. Travis and P.H. Stone, 1980a: Cloud morphology and motions from Pioneer Venus images. J. Geophys. Res., 85, 8107-8128.

\_\_\_\_\_, S. Fels and P.H. Stone, 1980b: Comments on "a three dimensional model of dynamical processes in the Venus atmosphere." J. Atmos. Sci., 37, 250-252.

Schubert, G., 1969: High velocities induced in a fluid by a traveling thermal source. J. Atmos. Sci., 26, 767-770.

\_\_\_\_\_, and J.A. Whitehead, 1969: Moving flame experiment with liquid mercury: Possible implications for the Venus atmosphere. Science, 163, 71-72.

\_\_\_\_\_, and R.E. Young, 1970: The 4-day Venus circulation driven by periodic thermal forcing. J. Atmos. Sci., 27, 523-528.

\_\_\_\_\_, \_\_\_\_\_, and E.J. Hinch, 1971: Prograde and retrograde motions in a fluid layer: Consequences for thermal diffusion in the Venus atmosphere. J. Geophys. Res., 76, 2126-2130.

Seiff, A., D.B. Kirk, R.E. Young, S.C. Sommer, R.C. Blanchard, J.T. Findlay and G.M. Kelly, 1979: Thermal contrasts in the atmosphere of Venus: Initial appraisal from Pioneer Venus probe data. Science, 205, 46-49.

Shapiro, R., 1970: Smoothing, filtering and boundary effects. Rev. Geophys. Space Phys., 8, 359-387.

Starr, V.P., 1968: Physics of Negative Viscosity. New York, McGraw-Hill, 256 pp.

Stern, M.E., 1959: The moving flame experiment. Tellus, 11, 175-179.

\_\_\_\_\_, 1971: Generalizations of the rotating flame effect. Tellus, 23, 122-128.

Stone, P.H., 1968: Some properties of Hadley regimes on rotating and non-rotating planets. J. Atmos. Sci., 25, 644-657.

\_\_\_\_\_, 1975: The dynamics of the atmosphere of Venus. J. Atmos. Sci., 32, 1005-1016.

Thompson, J., 1892: On the grand currents of atmospheric circulation. Phil. trans. Roy. Soc. London, A183, 653-684.

Thompson, R., 1970: Venus' general circulation is a merry-go-round. J. Atmos. Sci., 27, 1107-1116.

Tomasko, M.G., L.R. Doose, P.h. Smith and A.P. Odell, 1980: Measurements of the flux of sunlight in the atmosphere of Venus. J. Geophys. Res., 85, 8167-8186.

Traub, W.A. and N.P. Carleton, 1975: Spectroscopic observations of Winds on Venus. J. Atmos. Sci., 32, 1045-1059.

Travis, L.D., 1978: Nature of the atmospheric dynamics on Venus from power spectrum analysis of Mariner 10 images. J. Atmos. Sci., 35, 1584-1595.

Whitehead, J.A., 1972: Observations of rapid mean flow produced in mercury by a moving heater. Geophys. Fluid Dyn., 3, 161-180.

*W. R.* Soo, R., 1975: Observations of turbulence in the atmosphere of Venus using Mariner 10 radio occultation measurements. J. Atmos. Sci., 32, 1084-1090.

Young, A.T., 1975: Is the four day "rotation" of Venus illusory? Icarus, 24, 1-10.

Young, R.E., G. Schubert and K.E. Torrance, 1972: Nonlinear motions induced by moving thermal waves. J. Fluid Mech., 54, 163-187.

\_\_\_\_\_, and G. Schubert, 1973: Dynamical aspects of the Venus 4-day circulation. Planet. Space Sci., 21, 1563-1580.

\_\_\_\_\_, and J.B. Pollack, 1977: A three-dimensional model of dynamical processes in the Venus atmosphere. J. Atmos. Sci., 34, 1315-1351.

\_\_\_\_\_, and \_\_\_\_\_, 1980: Reply to comments on "a three-dimensional model of dynamical processes in the Venus atmosphere." J. Atmos. Sci., 37, 253-255.

## APPENDIX A

FOURIER ANALYSIS OF THE DIURNALDIURNAL HEATING FUNCTION

The purpose of this appendix is simply to provide the details of the zonal Fourier analysis of the diurnally dependent differential heat flux defined by equations (2.3.2) and (3.2.17). For simplicity we consider only the diurnal variations as defined by

$$f(\lambda, t) = \begin{cases} \cos(\lambda - t) & |\lambda - t| \leq \frac{\pi}{2} \\ 0 & |\lambda - t| > \frac{\pi}{2} \end{cases} \quad (\text{A.1})$$

where  $\lambda$  is longitude,  $t$  is dimensionless time (scaled by the period of the heat source  $\Omega$ ), and the phase  $\lambda - t$  represents the local time of day measured from a value of zero at local noon. The periodic function defined by (A.1) can be expanded as

$$f(\lambda, t) = \sum_{m=-\infty}^{\infty} f_m e^{im(\lambda - t)}$$

$$f_m = \frac{1}{2\pi} \int_0^{2\pi} f(\lambda, t) e^{-im(\lambda - t)} d(\lambda - t) \quad (\text{A.2})$$

Each coefficient,  $f_m$ , in (A.2) can be rewritten as the sum of a real part plus an imaginary part

$$f_m = \frac{1}{2\pi} \int_{-\frac{\pi}{2}}^{\frac{\pi}{2}} \cos(\lambda-t) \cos m(\lambda-t) d(\lambda-t) - \frac{i}{2\pi} \int_{-\frac{\pi}{2}}^{\frac{\pi}{2}} \cos(\lambda-t) \sin m(\lambda-t) d(\lambda-t) \quad (\text{A.3})$$

from which it is immediately obvious that the imaginary part of  $f_m$  is zero for all  $m$ . Furthermore, we need only evaluate (A.3) for  $m \geq 0$  since  $\cos[-m(\lambda-t)] = \cos m(\lambda-t)$  and thus  $f_{-m} = f_m$ . Upon carrying out the integration, (A.3) becomes

$$f_m = \begin{cases} \frac{1}{\pi} & m = 0 \\ \frac{1}{4} & m = 1 \\ \frac{1}{2\pi} \left[ \frac{\sin(m+1)\frac{\pi}{2}}{m+1} + \frac{\sin(m-1)\frac{\pi}{2}}{m-1} \right] & m \neq 0, \text{ even} \\ 0 & m \neq 1, \text{ odd} \end{cases} \quad (\text{A.4})$$

In Figure A1 we have plotted  $f(\lambda, t)$  as given by (A.1) and its Fourier representation (A.2) truncated at values of  $M = 1, 2, 4$ . From the curves we see that  $M = 2$  represents

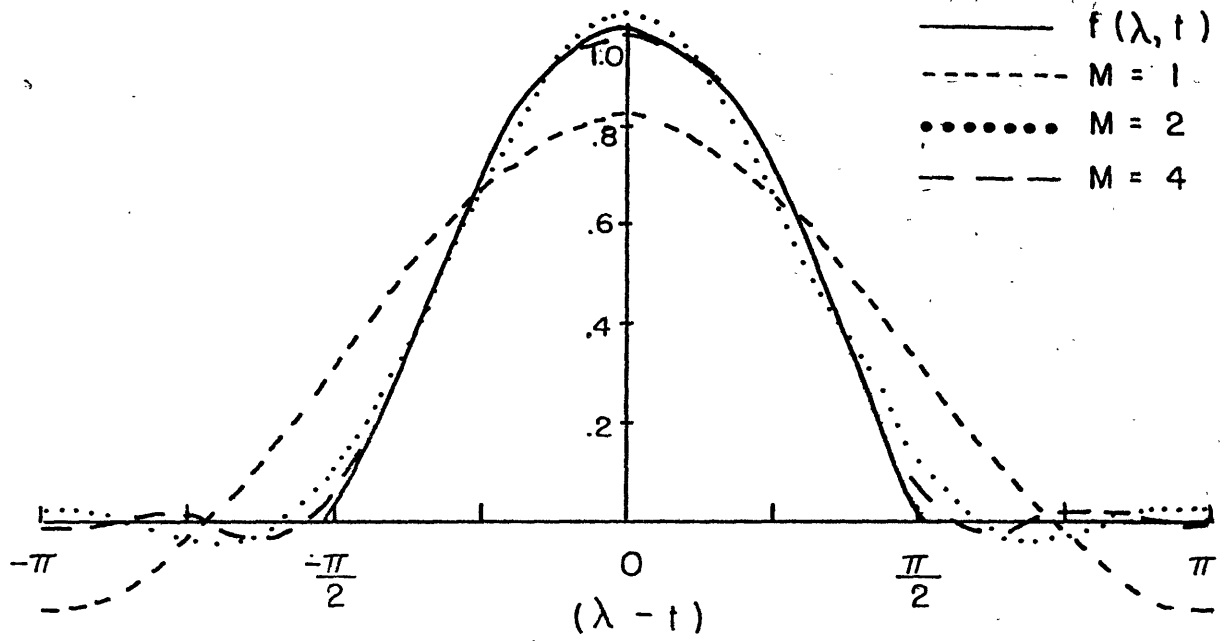


FIGURE A.1  $f(\lambda, t)$  defined by equation (A.1) and its Fourier representative for  $M = 1, 2, \text{ and } 4$ .

significant improvement over  $M = 1$ . The  $M = 4$  curve is nearly indistinguishable from  $f(\lambda, t)$  except in a narrow region around the terminators. Thus we see that the forcing is confined primarily to planetary waves with zonal wave-numbers  $\leq 4$ .

Finally, (A.2) must be slightly modified for use in the spectral model of Chapter 3. The expansion given by (A.2) can be rewritten as

$$\begin{aligned} f(\lambda, t) &= \sum_{m=-\infty}^{\infty} f_m e^{im\lambda} e^{-imt} \\ &= \sum_{m=-\infty}^{\infty} f'_m(t) e^{im\lambda} \end{aligned} \quad (\text{A.5})$$

where the time dependent coefficients are given by

$$f'_m(t) = f_m e^{-imt}$$

and therefore the coefficients for the Fourier expansion in longitude only are given by the product of (A.2) times the appropriate factor of  $e^{-imt}$ .

## APPENDIX B

PHYSICAL CONSTANTS AND DIMENSIONSPARAMETERS FOR VENUS

$a$	$= 6.1 \times 10^8 \text{ cm}$
$c_p$	$= 8.8 \times 10^6 \text{ erg gm}^{-1} \text{ K}^{-1}$
$F_0$	$= 10^4 \text{ erg cm}^{-2} \text{ s}^{-1} \text{ (10W m}^{-2}\text{)}$
$g$	$= 880 \text{ cm s}^{-2}$
$h$	$= 5 \times 10^5 \text{ cm}$
$p_0$	$= 210 \text{ mb}$
$u_0$	$= 400 \text{ cm s}^{-1}$
$Pr$	variable from 0.1 to 1.0 depending on experiment
$R$	$= 1.9 \times 10^6 \text{ erg gm}^{-1} \text{ K}^{-1}$
$T_0$	$= 240^\circ \text{ K}$
$\Delta T$	$= 120^\circ \text{ K}$
$\kappa_H$	$= \text{variable from } 2.9 \times 10^9 \text{ to } 2 \times 10^{10} \text{ cm}^2 \text{ s}^{-1}$ depending on M.
$\kappa_V$	$= 10^4 \text{ cm}^2 \text{ s}^{-1}$
$\nu_H$	$= \kappa_H$
$\nu_V$	$= \kappa_V / Pr$
$\rho_0$	$= 4.6 \times 10^{-4} \text{ gm cm}^{-3}$
$\Gamma$	$= 10^\circ \text{ K/km}$
$\Omega$	$= 6.2 \times 10^{-7} \text{ s}^{-1}$

In the above list, the most uncertain values are the ones for the vertical eddy diffusion coefficients. The value of  $10^4 \text{ cm}^2 \text{ s}^{-1}$  is widely accepted as an appropriate value for



a stable atmosphere. Furthermore, based on the vertical distribution of cloud particles, Prinn (1974) has estimated an upper limit for the vertical eddy diffusion coefficients in the Venus stratosphere. Near the cloud tops, the value he gives is  $2 \times 10^5 \text{ cm}^2 \text{ s}^{-1}$ . In some of our experiments we vary the Prandtl number as part of our parameter studies. Unless otherwise noted we assume a value of  $\text{Pr} = \frac{1}{2}$ . A value of  $\text{Pr} \sim 0(1)$  is appropriate if the dominant transport mechanism is turbulent diffusion. In constructing our model we assumed this to be the case.

Horizontal diffusion terms are included primarily as a numerical tool to control spurious growth of the high wavenumber harmonics. The value of the horizontal diffusion coefficient is chosen according to the truncation -- i.e., as resolution is increased the diffusion coefficient is decreased. The values we use are  $1 \times 10^{10} \text{ cm}^2 \text{ s}^{-1}$  for  $M = 4$ ,  $5 \times 10^9 \text{ cm}^2 \text{ s}^{-1}$  for  $M = 6$  and  $2.9 \times 10^9$  for  $M = 8$ .

Based on the values of the physical constants we can compute the appropriate Venus values of the dimensionless parameters:

$$\text{the Froude number } \mathcal{F} = \frac{gh}{u_o^2} = 2750$$

$$\text{the thermal forcing parameter } G = \mathcal{F} \frac{\Delta T}{T_o} = 1375$$

$$\text{the thermal frequency parameter } 2\eta^2 = \frac{\Omega h^2}{\kappa_V} = 15.5.$$

## APPENDIX C

SURFACE SPHERICAL HARMONICS

In the spectral model in Chapter 3, the horizontal spatial variations are represented by expanding each of the dependent variables in a truncated series of surface spherical harmonics in which the spectral coefficients are functions of time and height only. As shown in (3.3.4), a typical variable can be expressed as

$$\psi(\lambda, \phi, z, t) = \sum_{m=-M}^M \sum_{n=|m|}^M \psi_n^m(z, t) Y_n^m(\lambda, \mu) \quad (C.1)$$

where  $\mu = \sin \phi$ .

The spherical harmonic of order  $m$  and degree  $n$  is defined by

$$Y_n^m(\lambda, \mu) = e^{im\lambda} P_n^m(\mu) \quad (C.2)$$

where

$$P_n^m(\mu) = \left[ \frac{2n+1}{2} \frac{(n-m)!}{(n+m)!} \right]^{\frac{1}{2}} \frac{(1-\mu^2)^{\frac{m}{2}}}{2^n n!} \frac{d^{m+n} (\mu^2-1)^n}{d\mu^{m+n}} \quad (C.3)$$

is the normalized associated Legendre polynomial of order  $m$  and degree  $n$ . The spherical harmonics are the solutions of Laplace's equation on the unit sphere. From (C.2) we immediately see that the order of the harmonic,  $m$ , is simply the zonal wavenumber. The degree  $n$  is the degree of the associated Legendre polynomial and the quantity  $n-|m|$  is the number of nodes between the two poles.

Because of the order of the derivatives in (C.3), the spherical harmonics are defined only when  $n \geq |m|$ . For  $n < |m|$ , the harmonics are exactly zero. The orthonormality condition is given by

$$\frac{1}{2\pi} \int_0^{2\pi} \int_{-1}^1 Y_n^m \tilde{Y}_q^p d\mu d\lambda = \begin{cases} 1 & (p, q) = (m, n) \\ 0 & (p, q) \neq (m, n) \end{cases} \quad (C.4)$$

where  $(\tilde{\phantom{x}})$  stands for the complex conjugate. Given a function  $\psi$  which is expandable in a series of spherical harmonics and the orthonormality condition for  $Y_n^m$ , the expansion

coefficients  $\psi_n^m$  can be obtained by multiplying (C.1) by the appropriate  $Y_n^m$  and integrating over the entire surface of the unit sphere. This procedure can be carried out in two steps. First, we obtain the zonal Fourier coefficients

$$\psi_m(\phi, z, t) = \frac{1}{2\pi} \int_0^{2\pi} \psi(\lambda, \phi, z, t) e^{-im\lambda} d\lambda$$

and then we obtain the harmonic coefficients

$$\begin{aligned} \psi_n^m(z, t) &= \int_{-\pi/2}^{\pi/2} \psi_m(\phi, z, t) P_n^m(\sin\phi) \cos\phi d\phi \\ &= \int_{-1}^1 \psi_m(\mu, z, t) P_n^m(\mu) d\mu \end{aligned}$$

The reality of  $\psi$  require that

$$\psi_{-m} = \tilde{\psi}_m$$

and the definition of the associated Legendre polynomials requires that

$$\psi_n^{-m} = (-1)^m \tilde{\psi}_n^m$$

The horizontal spatial derivatives of the dependent variables are given by the derivatives of the spherical harmonics. From (C.2), the zonal derivative is found to be

$$\frac{\partial Y_n^m}{\partial \lambda} = im Y_n^m \quad (C.5)$$

and from the recurrence relations for the associated Legendre polynomials, the meridional derivative is given by

$$\cos \phi \frac{\partial Y_n^m}{\partial \phi} = (1-\mu^2) \frac{\partial Y_n^m}{\partial \mu} = (n+1) D_n^m Y_{n-1}^m - n D_{n+1}^m Y_{n+1}^m \quad (C.6)$$

where

$$D_n^m = \left[ \frac{n^2 - m^2}{4n^2 - 1} \right]^{\frac{1}{2}} .$$

Finally, since the surface spherical harmonics are solutions of Laplace's equation on the unit sphere, we have a very simple expression for the two-dimensional (horizontal) Laplacian

$$\nabla^2 Y_n^m = -n(n+1) Y_n^m .$$

For computational purposes, the normalized associated

Legendre polynomials and their derivatives are computed once at the beginning of an experiment and then saved on a mass storage device. To generate the polynomials, we begin by computing the non-normalized polynomials ( $P_n^m$  defined by (C.3) without the quantity in the square root, i.e., the normalizing factor). The order of computation is as follows:

- a) the diagonal ( $n=|m|$ ) polynomials are generated from the relations

$$\begin{aligned} P_0^0(\mu) &= 1 \\ P_m^m(\mu) &= (2m-1)(1-\mu^2)^{\frac{1}{2}} P_{m-1}^{m-1}(\mu) \end{aligned} \quad (C.7)$$

- b) the diagonal +1 polynomials ( $n=|m|+1$ ) are generated from the relation

$$P_{m+1}^m(\mu) = (2m+1)\mu P_m^m(\mu) \quad (C.8)$$

- c) all other polynomials for a fixed  $m$  are generated from the polynomials of the two preceding degrees according to

$$P_n^m(\mu) = \frac{2n-1}{n-m}\mu P_{n-1}^m - \frac{(n+m-1)}{n-m} P_{n-2}^m \quad (C.9)$$

d) all of the polynomials are then normalized by multiplying by the appropriate normalization factor

$$\left[ \frac{(2n+1)}{2} \frac{(n-m)!}{(n+m)!} \right]^{\frac{1}{2}} \tag{C.10}$$

Finally, the derivatives of the normalized polynomials are generated from the relation given by (C.6)

$$H_n^m(\mu) = (1-\mu^2) \frac{dP_n^m}{d\mu} = (n+1) D_n^m P_{n-1}^m - n D_{n+1}^m P_{n+1}^m \tag{C.11}$$

where

$$D_n^m = \left[ \frac{n^2 - m^2}{4n^2 - 1} \right]^{\frac{1}{2}}$$

and obviously the first term on the right hand side of (C.11) is zero for  $n = |m|$ .

The values of  $P_n^m$  and  $H_n^m$  are generated in double precision arithmetic (i.e., approximately 16 digits) and the accuracy was checked in two ways. First, we compared our values to those in the tables published by Belousov (1962). The agreement was exact for polynomials of order and/or degree as high as thirty (the maximum degree we computed). Then, we computed the orthonormality integrals

using a Gaussian quadrature (see Appendix D). We point out that a Gaussian quadrature is exact for any polynomial of degree  $\leq 2K-1$  where  $K$  is the order of the quadrature. The values of the integrals computed by this method were correct to sixteen decimal places.



APPENDIX D

TRANSFORM METHOD FOR COMPUTING

NONLINEAR TERMS

Originally suggested by Eliassen et al. (1970) and independently by Orszag (1970), the transform method provides a way to compute the nonlinear terms in the spectral equations of motion without having to explicitly calculate the interaction coefficients. The main advantage of this technique is that it reduces the number of calculations by a factor of roughly  $M^2$  where  $M$  is the truncation wave-number. Basically, the method consists of three steps:

1) transforming the spectral (i.e., spherical harmonic) coefficient of the dependent variables into grid space to obtain grid point values of the variables and/or their derivatives (this step is referred to as the forward transform);

2) multiplying the grid point values of the variables to form the required nonlinear terms (e.g., advection terms);

3) transforming the grid point values of the nonlinear products into spectral space to obtain the required spectral coefficients (referred to as the inverse transform).

The forward transform of step 1 can be further divided into two parts:

1a) transforming the spectral coefficients to zonal Fourier coefficients at the Gaussian latitudes (i.e., latitudes required for a Gaussian quadrature);

1b) transforming the Fourier coefficients to physical grid space consisting of equally spaced longitudes and the Gaussian latitudes.

Steps 1a and 1b are referred to as the forward Legendre and Fourier transforms, respectively. Similarly, the inverse transform of step 3 consists of the two corresponding inverse transforms. For computational purposes, the Fourier transforms (forward and inverse) are carried out by using a Fast Fourier Transform algorithm. Unfortunately, there is no analogous fast Legendre transform so that the forward Legendre transform is carried out by actually summing over the associated Legendre polynomials while the inverse Legendre transform is computed by using a numerical quadrature. For reasons to be explained below, the preferred choice is a Gaussian quadrature.

Machenhauer and Rasmussen (1972) further distinguish between the full transform method and the half transform method. The full transform consists of steps 1a, 1b, 2, and 3 as described above. The half transform consists of the forward Legendre transform, formation of the nonlinear products of the Fourier coefficients at the Gaussian latitudes, followed by the inverse Legendre transform. In our

model, we use the half transform method since it uses less computer time than the full transform for low resolution ( $M < 12$ ) experiments.

We now will demonstrate this method for the thermodynamic equation (3.2.13)

$$\frac{\partial \theta}{\partial t} = -A - B + \frac{1}{2\eta^2} \left[ \frac{\partial^2 \theta}{\partial z^2} + \epsilon_k \nabla^2 \theta \right] \quad (D.1)$$

or in spectral form

$$\frac{\partial \theta_n^m}{\partial t} = -A_n^m - B_n^m + \frac{1}{2\eta^2} \left[ \frac{\partial^2 \theta_n^m}{\partial z^2} - \epsilon_k n(n+1) \theta_n^m \right] \quad (C.2)$$

where the nonlinear advective terms are

$$A = \frac{1}{\cos^2 \phi} \left[ U \frac{\partial \theta}{\partial \lambda} + V \cos \phi \frac{\partial \theta}{\partial \phi} \right]$$

$$B = w \frac{\partial \theta}{\partial z}$$

$$A_n^m = \frac{1}{2\pi} \int_0^{2\pi} \int_{-\frac{\pi}{2}}^{\frac{\pi}{2}} A P_n^m(\sin \phi) \cos \phi \, d\phi \, e^{-im\lambda} \, d\lambda \quad (D.3)$$

$$B_n^m = \frac{1}{2\pi} \int_0^{2\pi} \int_{-\frac{\pi}{2}}^{\frac{\pi}{2}} B P_n^m(\sin \phi) \cos \phi \, d\phi \, e^{-im\lambda} \, d\lambda$$

To obtain the spectral coefficients of the nonlinear terms, one would usually substitute the appropriate expansions, e.g.,

$$\theta = \sum_{m=-M}^M \sum_{n=|m|}^M \theta_n^m P_n^m(\sin \phi) e^{im\lambda}$$

into the expressions for A and B and then carry out the integrations in the expressions for  $A_n^m$  and  $B_n^m$ . The zonal integral is fairly easy to evaluate however the meridional integral will involve the integration of the product of three different associated Legendre polynomials and are quite cumbersome and time consuming. These integrals are the so-called interaction coefficients. The transform method is designed to specifically avoid computing the interaction coefficients. To accomplish this, we begin the transform method by forming the required Fourier coefficients at the Gaussian latitudes. We do this by taking the known spectral coefficients at time  $t$  and summing over the associated Legendre polynomials (the forward Legendre transform),

$$\theta_m(\sin \phi_k) = \sum_{n=|m|}^M \theta_n^m P_n^m(\sin \phi_k)$$

$$L_m(\theta) = \sum_{n=|m|}^M \theta_n^m H_n^m(\sin \phi_k) \quad (D.4)$$

$$\begin{aligned}
 U_m &= \sum_{n=|m|}^{M+1} U_n^m P_n^m(\sin \phi_k) \\
 V_m &= \sum_{n=|m|}^{M+1} V_n^m P_n^m(\sin \phi_k) \\
 W_m &= \sum_{n=|m|}^M W_n^m P_n^m(\sin \phi_k)
 \end{aligned} \tag{D.4}$$

where the subscript  $k$  indicates the  $k$ th Gaussian latitude and the operator  $L_m(\theta)$  is the  $m$ th Fourier coefficient of the meridional derivative operator

$$L(\theta) = \cos \phi \frac{\partial \theta}{\partial \phi} = \sum_{n=|m|}^M \theta_n^m H_n^m(\sin \phi) e^{im\lambda} .$$

Since  $A$  and  $B$  consist of terms that are the products of quantities expanded as truncated zonal Fourier series, then  $A$  and  $B$  can also be expanded as truncated Fourier series with truncation wavenumber  $2M$ , i.e.,

$$\begin{aligned}
 A(\lambda, \phi_k) &= \sum_{m=-2M}^{2M} A_m(\sin \phi_k) e^{im\lambda} \\
 B(\lambda, \phi_k) &= \sum_{m=-2M}^{2M} B_m(\sin \phi_k) e^{im\lambda}
 \end{aligned} \tag{D.5}$$

and the coefficients are given by

$$A_m(\sin \phi_R) = \frac{1}{\cos^2 \phi_R} \sum_{m_1=m-M}^M [i m_1 U_{m-m_1} \theta_{m_1} + V_{m-m_1} L_{m_1}(\theta)]$$

$$B_m(\sin \phi_R) = \sum_{m_1=m-M}^M w_{m-m_1} \frac{\partial \theta_{m_1}}{\partial z} \quad (D.6)$$

Given the Fourier coefficients of the dependent variables in (D.4) it is a simple matter to form the coefficients  $A_m$  and  $B_m$  of the nonlinear terms. Furthermore, we only need to compute  $A_m$  and  $B_m$  for  $0 \leq m \leq M$ . The lower limit  $m = 0$  follows from the fact that  $A_{-m} = A_m$ . The upper limit  $m = M$  is a consequence of the truncation of the time derivative on the left-hand side of (D.2). Since  $\frac{\partial \theta_n^m}{\partial t}$  is truncated at  $m = M$ , we must be consistent and also truncate the right-hand side of (D.2) at  $m = M$ . By consistently truncating the nonlinear terms in this manner we automatically eliminate the problems of aliasing and nonlinear instability that are commonly associated with finite difference models. To complete our computations of the nonlinear terms, we must determine the spectral coefficients  $A_n^m$  and  $B_n^m$  by applying the inverse Legendre transform, i.e.,

$$A_n^m = \int_{-\frac{\pi}{2}}^{\frac{\pi}{2}} A_m(\sin \phi) P_n^m(\sin \phi) \cos \phi \, d\phi$$

$$= \int_{-1}^1 A_m(\mu) P_n^m(\mu) \, d\mu \quad (D.7)$$

$$B_n^m = \int_{-\frac{\pi}{2}}^{\frac{\pi}{2}} B_m(\sin \phi) P_n^m(\sin \phi) \cos \phi \, d\phi = \int_{-1}^1 B_m(\mu) P_n^m(\mu) \, d\mu$$

Recalling that  $A_m(\mu)$  and  $B_m(\mu)$  were formed as products of polynomials of  $\mu$ , we see that the integrands in (D.7) are also polynomials of  $\mu$ . In this case, the integrals in (D.7) can be evaluated exactly with a Gaussian quadrature of order  $K$  (i.e., a  $K$  point quadrature)

$$A_n^m = \int_{-1}^1 A_m(\mu) P_n^m(\mu) \, d\mu = \sum_{k=1}^K A_m(\mu_k) P_n^m(\mu_k) \alpha_k \quad (D.8)$$

provided the integrand  $A_m P_n^m$  is a polynomial of degree  $\leq 2K - 1$  (Isaacson and Keller, 1966). In (D.8) the  $K$  Gaussian latitudes  $(\mu_1, \dots, \mu_K)$  are the zeros of the  $K$ th Legendre polynomial,  $P_K^0(\mu)$ , and  $(\alpha_1, \dots, \alpha_K)$  are the Gaussian weights (values were taken from Kronrod, 1965). The Gaussian quadrature is chosen since it requires fewer points to be exact as compared to any other quadrature formula. Finally, the minimum number of Gaussian latitudes necessary can be determined from the degree of the integrand.  $A_m$  will be at most of degree  $2M + 2$  since  $V_m$  contains polynomials up to  $P_{M+1}^m$  and  $H_M^m$  also contains  $P_{M+1}^m$ . Thus  $A_m P_n^m$  will be at most of degree  $3M + 2$  and the quadrature

will be exact if

$$3M+2 \leq 2K-1$$

and we must therefore have  $K \geq \frac{3M+1}{2}$  Gaussian latitudes (obviously  $K$  must be an integer).

Having obtained the nonlinear contributions to the spectral tendency, the time integration of (D.1) is straightforward since the linear terms are readily evaluated given the spectral coefficients  $\theta_n^m$ . A similar analysis can be carried out for the vorticity and divergence equations with the only difference being the presence of other nonlinear terms in addition to advection.